

MOLECULAR BINDING MECHANISMS OF AQUEOUS Cd AND Pb TO
SIDEROPHORES, BACTERIA AND MINERAL SURFACES

A Dissertation

Submitted to the Graduate School
of the University of Notre Dame
in Partial Fulfillment of the Requirements
for the Degree of

Doctor of Philosophy

by

Bhoopesh Mishra, B.Sc., M.Sc.

Bruce A. Bunker, Director

Graduate Program in Physics

Notre Dame, Indiana

July 2006

MOLECULAR BINDING MECHANISMS OF AQUEOUS Cd AND Pb TO
SIDEROPHORES, BACTERIA AND MINERAL SURFACES

Abstract

by

Bhoopesh Mishra

Recent studies have shown that diverse groups of bacteria adsorb metals to similar extents and uptake can be modeled using a universal adsorption model. In this study, XAFS has been used to resolve whether binding sites determined for single species systems are responsible for adsorption in more complex natural bacterial assemblages. Results obtained from a series of XAFS experiments on pure Gram positive and Gram negative bacterial strains and consortia of bacteria as a function of pH and Cd loading suggests that every bacterial strain has a complex physiology and they are all slightly different from each other. Nevertheless from the metal adsorption chemistry point of view, the main difference between them lies in the site ratio of three fundamental sites only - carboxyl, phosphoryl and sulfide. Two completely different consortia of bacteria (obtained from natural river water, and soil system with severe organic contamination) were successfully modeled in the pH range 3.4 – 7.8 using the EXAFS models developed for single species systems. Results thus obtained can potentially have very high impact on the modeling of the complex bacterial systems in realistic geological settings, leading to further refinement and development of robust remediation strategies for metal contamination at macroscopic level.

In another study, solution speciation of Pb and Cd with DFO-B has been examined using a combination of techniques (ICP, TOC, thermodynamic modeling and XAFS). Results indicate that Pb does not complex with DFO-B at all until about pH 3.5, but forms a totally caged structure at pH 7.5. At intermediate pH conditions, mixture of species (one and two hydroxamate groups complexed) is formed. Cd on the other hand, does not complex until pH 5, forms intermediate complexes at pH 8 and is totally chelated at pH 9.

Further studies were conducted for Pb sorption to mineral surface kaolinite with and without DFO-B. In the absence of DFO-B, results suggest outer sphere and inner sphere sorption of Pb on kaolinite surface at acidic and circumneutral pH conditions respectively. In the presence of DFO-B, bulk sorption studies indicated that Pb sorption is enhanced in the presence of DFO-B around pH 6 and inhibited above pH 6.5. This was confirmed by x-ray fluorescence measurements. Extended XAFS study clearly indicated unwrapping of DFO-B molecule at the surface. Our study has unambiguously recognized it as a "Type A" ternary complex ("Type A" complex means surface-metal-ligand type of interaction). Taken together, bulk adsorption measurements and XAFS experiments represent a powerful approach for determining and modeling metal speciation and adsorption.

CONTENTS

FIGURES	vi
TABLES	xi
ACKNOWLEDGMENTS	xiii
CHAPTER 1: INTRODUCTION	1
1.1 Problem of Environmental Contamination	1
1.2 Scientific Approach to the Problem	3
1.3 Scientific Directions and Interdisciplinary Nature of the Problem	4
1.4 Role of XAFS in Environmental Science	6
1.5 Work Presented in This Dissertation	9
CHAPTER 2: THEORY OF X-RAY ABSORPTION FINE-STRUCTURE SPECTROSCOPY	15
2.1 Introduction	15
2.2 X-ray Absorption Coefficient	16
2.3 Basic Physics of XAFS	18
2.4 Derivation of the EXAFS equation	20
2.4.1 K-edge XAFS Equation of Single Scattering	24
2.5 Effects of Thermal Vibration and Structural Disorder	32
2.6 Many Body Effects	38
2.7 Multiple Scattering	40
CHAPTER 3: XAFS EXPERIMENT AND APPARATUS	43
3.1 Synchrotron Radiation	43
3.2 X-ray Beamlines	53
3.2.1 Monochromator	55
3.2.2 Harmonic Rejection	59
3.2.3 X-Ray Detectors	61
3.2.3.1 Ionization Chambers	61

3.2.3.2	Solid-State Detectors (SSD)	65
3.2.3.3	Bent Crystal Laue Analyzer	67
3.3	Experimental XAFS Detection	69
3.3.1	Transmission XAFS	69
3.3.2	Fluorescence EXAFS	70
3.4	Elimination of Noise in Experiments	76
3.4.1	Harmonics	77
3.4.2	Alignment	77
3.4.3	Linearity	78
3.4.4	Offset	78
3.5	Beamline Alignment	78
CHAPTER 4: XAFS DATA ANALYSIS		80
4.1	Introduction	80
4.2	Data Reduction	81
4.2.1	Aligning Scans	81
4.2.2	Merging of scans	83
4.2.3	Deglitching	84
4.2.4	Determining E_0	85
4.2.5	Pre-edge Background Removal	86
4.2.6	Data Normalization	86
4.2.7	Background Removal	87
4.2.8	Fourier Transform	89
4.3	Qualitative Analysis of XAFS Data	95
4.4	Fitting	96
4.4.1	Philosophy of UWXAFS Package	97
4.4.2	Obtaining the best fit parameters	99
4.4.3	Uncertainties of parameters	103
4.4.4	Using theoretical vs. experimental standards	105
4.5	Avoiding Pitfalls in XAFS Analysis	106
CHAPTER 5: UNIVERSAL ADSORPTION BEHAVIOR OF Cd ONTO BACTERIAL CELL WALLS - A MOLECULAR SPECTROSCOPY APPROACH		108
5.1	Introduction	108
5.2	Methods and Materials	111
5.2.1	Sampling and growth of bacterial consortia	111
5.2.2	Cd Adsorption Experiments	113
5.2.3	XAFS Standards	115
5.2.4	XAFS Measurements	116
5.2.5	XAFS Data Reduction	117
5.3	Results and Discussion	118

5.3.1	Cd adsorption Experiment	118
5.3.2	Standards Compounds for analyzing EXAFS	119
5.3.3	Qualitative Analysis of EXAFS Spectra	122
5.3.3.1	River Water Consortium	122
5.3.3.2	Contaminated Soil Consortium	124
5.3.4	Quantitative EXAFS Modeling	127
5.3.4.1	River Water Consortium	127
5.3.4.2	Contaminated Soil Consortium	131
5.4	Conclusion	137

CHAPTER 6: USING ADSORPTION ISOTHERM MEASUREMENTS TO CONSTRAIN MECHANISMS OF Cd ADSORPTION ONTO *BACILLUS SUBTILIS* AND *SHEWANELLA ONEIDENSIS* BACTERIAL CELL WALLS - INTERGRATING EXAFS AND THERMODYNAMIC MODELING

		140
6.1	Introduction	140
6.2	Methods and Materials	144
6.2.1	Bacterial Growth and Harvest	144
6.2.2	Cd Adsorption Experiments	145
6.2.3	Surface Complex Modeling	146
6.3	Results and Discussions	147
6.3.1	Cd Isotherm Experiment	147
6.3.2	Thermodynamic Modeling of the pH Isotherms	149
6.3.3	X-ray Absorption Fine Structure	151
6.3.4	Qualitative Analysis of XAFS Spectra	151
6.3.5	Quantitative EXAFS Modeling	153
6.4	Conclusion	159

CHAPTER 7: Pb AND Cd SPECIATION IN THE PRESENCE OF MICROBIAL SIDEROPHORE DFO-B: COMBINING X-RAY ABSORPTION SPECTROSCOPY WITH THERMODYNAMIC MODELING

		161
7.1	Introduction	161
7.2	Methods and Materials	164
7.2.1	Speciation Diagrams and Solution Preparation	164
7.2.2	XAFS Measurements	165
7.3	XAFS Data Reduction	168
7.4	Results and Discussion	168
7.4.1	Predicted Solution Phase speciation	168
7.4.2	Measured Solution-Phase Speciation	173
7.4.3	Pb Powder and Solution Standards	174
7.4.4	Cd Powder and Solution Standards	175
7.4.5	Pb-DFO-B samples: EXAFS Analysis and Numerical Fits	178

7.4.6	Cd-DFO-B sample: EXAFS Analysis and Numerical Fits	183
7.4.7	Model vs. measured	184
7.5	Conclusion	185
CHAPTER 8: EFFECT OF BACTERIAL SIDEROPHORES (DFO-B) ON		
	ADSORPTION OF Pb TO CLAY MINERAL KAOLINITE	188
8.1	Introduction	188
8.2	Materials and Methods	189
8.2.1	Mineral and Siderophore Samples Preparation	189
8.2.2	Batch Adsorption Experiments	190
8.2.3	Quantification of sorbed Pb and DFO-B	190
8.2.4	XAFS Standards, Measurements and Data Reduction	192
8.3	Results and Discussion	192
8.3.1	Bulk-Scale Results	192
8.3.2	XAFS Results	196
8.4	Conclusion	205
CHAPTER 9: SUMMARY AND FUTURE WORK		
		207
APPENDIX A: A PRACTICAL GUIDE TO BEAMLINER ALIGNMENT		
		209
A.1	Introduction	209
A.2	Steps of Alignment	209
BIBLIOGRAPHY		
		219

FIGURES

1.1	Transport of metal contaminants. Adapted from talk by Douglas Hunter, Savannah River National Laboratory (SRNL)	2
1.2	Example of metal uptake by surfaces. What can XAFS tell us? Adapted from talk by Douglas Hunter, Savannah River National Laboratory (SRNL)	8
1.3	The "big picture" of Molecular Environmental Science	9
2.1	Plot of the absorption coefficient, $\mu x = \ln\left(\frac{I_0}{I}\right)$, versus incident x-ray energy of the Fe K-edge; Fe foil sample. X-ray Absorption Near Edge Structure (XANES) and Extended X-ray Absorption Fine Structure (EXAFS) regions are shown on the plot.	17
2.2	A schematic of how XAFS works is shown. X-ray is incident on a sample resulting in the ejection of a photoelectron from the core-hole. This photoelectron must return back to the core-hole before its decay for XAFS to happen. (Adapted from Newville's "Fun Slides".)	19
2.3	The principle of XAFS is shown. The absorbing atom is shown by solid red circle and the neighboring atom by green solid circle. The outgoing photoelectron wave from the absorbing atom is shown by solid red lines and the backscattered Photoelectron wave from the neighbor by the dotted lines. These two photoelectron waves interfere to give rise to XAFS oscillations.	20
2.4	Overall scheme of XAFS, showing the difference between XANES and EXAFS. (Adapted from Newville's "Fun Slides")	21
2.5	The scenario in single scattering.	25
2.6	Plot of (a) Scattering amplitude and (b) phase of Fe, O and Pb as a function of the photoelectron wave vector. (Adapted from Newville's "Fun Slides")	26
2.7	Illustration of double scattering path.	41

3.1	Basic structure of a Synchrotron Source [Adapted from the Canadian Light Source (CLS) website] ¹	46
3.2	Comparison between the brilliance of different synchrotron sources. [Adapted from APS website]	50
3.3	Schematic diagram of an insertion device. [Adapted from APS website]	52
3.4	Schematic diagram showing the difference between tapered and untapered undulator beam profile. [Adapted from APS website]	54
3.5	A typical monochromator configuration with parallel plates. [Adapted from APS website]	56
3.6	A gas ionization chamber.	62
3.7	Stern-Heald type Lytle detector used for fluorescence mode XAFS. [Adapted from Lytle detector website]	64
3.8	Schematic diagram of the function the Soller Slits.[Adapted from Steve Heald's XAFS slides, with permission]	65
3.9	Dead Time correction in solid state detector.[Adapted from Steve Heald's XAFS slides, with permission]	67
3.10	Log Spiral Bent Crystal Laue Analyzer.[Adapted from BCLA Manual, with permission]	68
3.11	General and experiment specific alignment for a typical XAFS experiment.	71
3.12	Schematic diagram showing the use of filter in fluorescence mode XAFS. [Adapted from Steve Heald's XAFS slides, with permission]	74
4.1	Steps of XAFS data processing. Raw data is normalized, background subtracted and Fourier transformed.	82
4.2	An oversimplified road map of EXAFS analysis as used in this presentation.	96
5.1	$\chi(k^3)$ data of the river water consortium samples plotted with Cd standards. Data range used for Fourier transforming the data was $2.3 - 9.8k$ (\AA^{-1}).	114
5.2	$\chi(k^3)$ data of the contaminated soil consortium samples plotted with Cd standards. Data range used for Fourier transforming the data was $2.3 - 9.8k$ (\AA^{-1}).	115

¹<http://www.lightsource.ca/files/details.php?id=787>

5.3	Cd adsorption data for the two consortia of bacteria measured using ICP-AES.	118
5.4	Fourier transformed magnitude data of the Cd standard compounds. Notice a systematic decrease in the amplitude of the first shell from hydrated Cd to Cd Phosphate, -sulphate, and -acetate. Cd sulphide has a clear phase shift towards higher value of r	122
5.5	Fourier transformed real part of the Cd standard data plotted over a shorter data range (1.85 – 3.0 Å). Sulphide peak has a phase shift toward higher value of r compared to the acetate peak at about 2.2 Å. Cd acetate has a shallow first shell peak at about 1.9 Å characteristic of destructive interference between O and C shells. Cd sulphate is shown to be slightly shifted toward lower r value at about 2.4 Å. Also notice the kink in Cd phosphate data at about 2.7 Å.	123
5.6	Fourier transformed magnitude data for the river water consortium. Notice the reduction in the amplitude of first shell peak with increase in pH.	125
5.7	Real part of the Fourier transformed river water consortium data plotted over the data range of 1.85 – 3.0 Å. A dramatic change in the peak and a phase shift toward higher r value is seen at about 2.2 Å with increase in pH. This indicates rise in sulphide signal with increase in pH. The lowest and highest pH sample show signature of phosphate binding. The lowest pH sample also shows a phase shift toward lower r value at about 2.4 Å characteristic of sulphate binding.	126
5.8	Fourier transformed magnitude data for the contaminated soil consortium. Notice the reduction in the amplitude of first shell peak with increase in pH. Amplitude of the first shell spectra of this consortium is higher than the spectra of river water consortium.	127
5.9	Real part of the Fourier transformed contaminated soil consortium data plotted over the data range of 1.85 – 3.0 Å. Peak at 2.2 Å in this case is almost on top of each other in contrast to the dramatic changes in This indicates rise absence of sulphide peak in this consortium. All the samples show strong signature of phosphate binding. The lowest pH sample also shows a phase shift toward lower r value at about 2.4 Å characteristic of sulphate binding.	129
5.10	Data and fits of the a) magnitude and b) real part of the Fourier transform of the river water consortium samples.	130

5.11	Data and fits of the a) magnitude and b) real part of the Fourier transform of the contaminated soil consortium samples.	134
6.1	Cell wall of Gram positive bacterium.	142
6.2	Cell wall of Gram negative bacterium.	142
6.3	Cd adsorption isotherm for <i>B. Subtilis</i> . In low concentration regime, a linear relation between the initial and adsorbed Cd is observed. At higher concentration, it deviates from the linear behavior suggesting saturation of sites.	148
6.4	Experimental data and models for different site Cd:C stoichiometry.	151
6.5	Fourier Transform magnitude of the <i>B. Subtilis</i> isotherm data. . .	152
6.6	Real part of the Fourier Transform data of the <i>B. Subtilis</i> isotherm.	153
6.7	Fourier Transform magnitude of the <i>Shewanella</i> isotherm data. . .	154
6.8	Real part of the Fourier Transform data of the <i>Shewanella</i> isotherm.	155
6.9	Fourier transform magnitude of the XAFS data and fits for the <i>B. Subtilis</i> isotherm.	158
6.10	Fourier transform magnitude of the XAFS data and fits for the <i>Shewanella</i> isotherm.	159
7.1	Pb speciation in the presence of DFO-B, modeled by PhreeqC using available binding constants.	170
7.2	Cd speciation diagram in the presence of DFO-B, modeled by PhreeqC using available binding constants.	172
7.3	Comparing Fourier transformed magnitude of the XAFS spectra of Pb-DFO-B at pH 7.5 and 9.0. They completely overlap at each other, indicating that Pb has exact same coordination environment at these two pH conditions.	180
7.4	Pb-DFO-B Fourier transformed magnitude data and fits at pH 3.0, 4.8 and 7.5. Notice the broad first shell at pH 3.0. This is characteristic of hydrated Pb. An increase in the amplitude of second shell can be easily at higher pH values.	183
7.5	Cd-DFO-B Fourier transformed magnitude data and fits at pH 5.0, 8.0 and 9.0. The spectrum at pH 5.0 is similar to hydrated Cd. Higher pH spectra clearly have bigger second shell.	186
7.6	Proposed caged structure of DFO-B with Pb and Cd at higher pH values, same as it is for Zn at high pH values. (Adapted from Neubauer et al. [71])	187

8.1	Pb ²⁺ sorption to kaolinite clay in the presence and absence of DFO-B. Values shown $\mu\text{mol/g}$ and the final pH ($\pm 2\sigma$). Precipitation of Pb ²⁺ is predicted to begin and pH values > 6 and is reflected in the measurements by greater error associated with the extent of Pb ²⁺ sorption.	193
8.2	Speciation diagram of the solution phase at 100 ppm Pb concentration. (Refer to chapter 7 for an explanation of the nomenclature of these molecules).	194
8.3	At the kaolinite surface Pb binds to aluminol surface as edge sharing bidentate inner-sphere around pH 6. Figure shows the Fourier transform data and fit for Pb adsorbed to kaolinite at pH 6.0. Real part of the FT is shown in the inset.	197
8.4	Possible configurations of Pb binding to Al as shown by Barger at el., 1997. XAFS analysis in the present work resulted in the Pb-Al distance of 3.38 Å. Based on the Pb-Al bond distance, an edge-sharing bidentate binding mechanism was proposed for Pb adsorption to kaolinite.	200
8.5	Fourier transformed data and fit for Pb adsorbed to kaolinite in the presence of DFO-B at pH 6.0 (lower graph) and pH 7.5 (upper graph). Real part of the data and fit is shown in the inset. Notice the subtle changes in the data for these two pH values.	201
8.6	Comparison of Pb - DFO-B, -kaolinite, and DFO-B and kaolinite at pH 6.0. Notice the much smaller second shell (C signal) compared to the aqueous phase data. Also notice the differences in first and second shell of Pb adsorbed to pure mineral data.	203
8.7	X-ray Fluorescence data at Pb L ₃ edge showing higher Pb uptake by the kaolinite at pH 6.0 compared to pH 7.5 in the presence of DFO-B.	204
8.8	Real part Fourier transform data for Pb adsorbed to kaolinite in the presence of DFO-B at pH 6.0. Short and long distance O, C and Al paths are shown in the Fig. Notice the interference of all these paths over the data range of $\sim 1.3 - 3.4$ Å.	205

TABLES

5.1	FITTING PARAMETERS OF Cd STANDARDS	119
5.2	PATHS USED FOR FITTING THE UNKNOWN SAMPLES, SHOWING THEIR DISTANCES AND DEBYE-WALLER FACTORS	120
5.3	SIMULTANEOUS FITTING PARAMETERS OF THE NATURAL CONSORTIA SAMPLES	132
5.4	SIMULTANEOUS FITTING PARAMETERS OF THE CONTAMINATED CONSORTIA SAMPLE	133
5.5	FITTING PARAMETERS OF THE HIGHEST PH SAMPLE OF NATURAL AND CONATMINATED CONSORTIA SERIES	135
6.1	FITTING PARAMETERS FOR THE SURFACE COMPLEXATION MODEL DETERMINING SITE STOICHIOMETRY USING NON-ELECTROSTATIC MODEL	150
6.2	XAFS FITTING PARAMETERS FOR THE <i>B. SUBTILIS</i> ISOTHERM SAMPLES	156
6.3	XAFS FITTING PARAMETERS FOR THE <i>SHEWANELLA</i> ISOTHERM SAMPLES	157
7.1	PUBLISHED STABILITY CONSTANTS USED FOR THE PREDICTION OF Pb AND Cd SPECIATION WITH DFO-B	166
7.2	FITTING PARAMETERS FOR Pb STANDARDS	176
7.3	FITTING PARAMETERS FOR Cd STANDARDS	177
7.4	FITTING PARAMETERS OF THE Pb-DFO-B SAMPLES AT PH 3.0, 4.8 and 7.5	182
7.5	FITTING PARAMETERS OF THE Pb-DFO-B SAMPLES AT PH 3.0, 4.8 and 7.5	185
8.1	FINAL PH VALUES AND AMOUNT OF Pb AND DFO-B SORBED FOR EACH OF THE THREE EXPERIMENTAL SYSTEMS. VALUES ARE THE AVERAGE OF TRIPLICATE SAMPLES ($\pm 2\sigma$).	195

8.2	XAFS FITTING PARAMETERS FOR Pb ADSORBED TO KAOLINITE AT PH 6.0	198
8.3	XAFS FITTING PARAMETERS FOR Pb-KAOLINITE-DFO-B SAMPLES AT PH 6.0 AND 7.5	199
A.1	STEP SCAN FOR LYTLE DETECTOR	218
A.2	SCAN SETUP FOR MED	218

ACKNOWLEDGMENTS

First of all, I thank Bruce Bunker (my advisor) for his years of encouragement and support of my graduate education, for his enormous faith in my ability to complete various research projects, and allowing me to pursue a broad and highly interdisciplinary scientific interest. Next I thank Jeremy Fein for introducing me to the world of Environmental Science, and teaching me so much with so much love. I feel privileged to have learnt XAFS analysis from Shelly Kelly, who has been an incredibly patient teacher. Ken Kemner played an extremely important role in inspiring me with wonderful ideas, and giving me some of the best suggestions during the critical years of my Ph.D. Patricia Maurice, with whom I interacted more in the second half of my Ph.D, proved to be a key factor in determining the shape my graduate work. I thank her for her overall guidance and for providing me a wonderful opportunity to learn so much.

Maxim Boyanov was more like what is called a friend, philosopher and guide during all these years. Debdutta Lahiri gave me a head-start by teaching the basics of XAFS experimentation. Endless discussions and beamline support from Igor Vasconcelos and Istvan Robel, who were also one of my best friends at Notre Dame, is highly appreciated. I thank Elizabeth Haack for being a caring friend and productive collaborator, and Hye-Young Lee for making me feel her place my second home at Notre Dame. I am highly indebted to Andrea Asztalos for her enormous support and encouragement during the difficult times of my finishing

up. I am also thankful to my other close friends Zoltan Dezso, Weng-Lee Lim, Erzsebet Ravasz, Smarajit Triambak, Peter Regan, and Raja Chakravorty with whom I shared joy and sorrow and who helped me to maintain my sanity during all these years.

I am grateful to my entire family, specially my brother and sister for providing me the will and independence to go for the dreams of my life. I owe to my parents for believing so much in me and for being by my side in everything I have ever done. My Father has always been an epitome of mental strength to me. Last but not the least, I express my deepest regards to my guru, Professor M. M. R Akhtar, who was not only a compassionate Physics teacher during my undergraduate years but he deeply influenced my thought process and course of life.

Finally I am also thankful to all those who were not the nicest to me. If I met only the nicest people, I would have never understood their importance in my life. I must confess, I have learnt so much from the innumerable failures I had.

CHAPTER 1

INTRODUCTION

1.1 Problem of Environmental Contamination

Surface and sub-surface metal contamination of the environment is a universal problem of immense complexity and great global concern. Since these metal contaminants form chemical complexes, they can be present in many forms ranging from a rather inert state to a highly mobile, toxic, and reactive phase. Their transport properties and toxicity are influenced by their oxidation states, solubility, and sorption processes which in turn are strongly correlated to the chemical and physical attributes of the surrounding medium. Solid-solution interface reactions play a very important role in their transport and bioavailability. Adsorption to mineral surfaces has been relatively well studied due to their amenability to a number of structural characterization methods. But the effect of bacteria and the extra-cellular material associated with them has not been extensively studied, partly due to ignorance about their potential impact and partly due to the complexity involved in studying the mixed bacteria-mineral systems. Many recent investigators have suggested that microorganisms play an important role in metal mobility. In addition, the microenvironment at and adjacent to actively metabolizing cell surfaces can be significantly different from the bulk environment. Thus, to develop a precise mechanistic understanding of the exact reactions taking

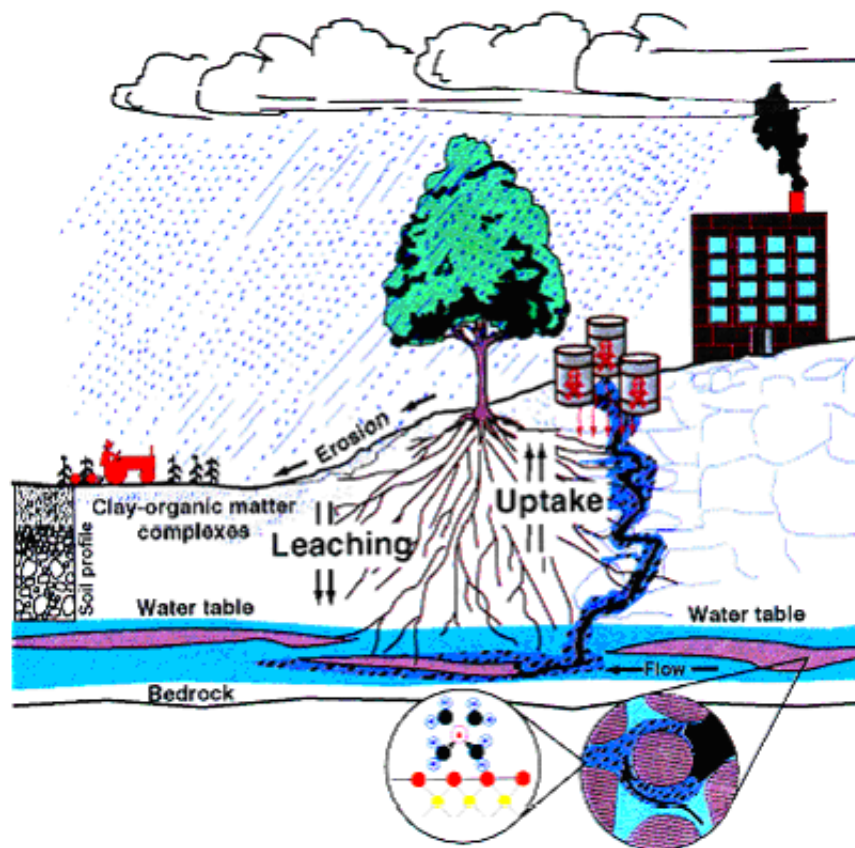


Figure 1.1. Transport of metal contaminants. Adapted from talk by Douglas Hunter, Savannah River National Laboratory (SRNL)

place, the spatial distribution and chemical speciation of contaminants in presence of both mineral and microbe must be characterized at sub-atomic resolution. Understanding and modeling contaminant transport in the environment is not only vital in determining the environmental fate of these contaminants and their relative risk but also in developing remediation strategies as the final goal.

1.2 Scientific Approach to the Problem

The majority of the work done so far has been from a macroscopic viewpoint; however, a detailed understanding of these processes at the molecular-level is now both possible and extremely important. A knowledge of molecular-level transport and chemistry can provide critical information needed to enhance the generality and predictive power of large-scale models, to identify the possible chemical and biological factors influencing contaminant decay rates, or to assess how changes in macroscopic parameters such as temperature might influence modeling parameters. The goal of such research is to address and integrate questions of environmental chemistry on three characteristic length scales: atomic (a few angstroms); microscopic (0.01 – 10 mm); and macroscopic, (0.5 – 1 km). These efforts attack related research questions but from very different perspectives.

One of the main challenges of *molecular environmental science* is accurately modeling bio-geochemical processes; including contaminant transport, mobility and bioavailability, phase partitioning, toxicity, effect of bacterial and mineral surfaces, over the environmentally-relevant range of temperatures, pressure and composition. This requires a reaction based knowledge of chemical form, i.e. *speciation* of contaminants at and adjacent to mineral and microbial micro-environment rather than some empirical derivatives valid for the range of experimental data. To achieve the final goal of developing bio-remediation strategies for contaminated sites, the fundamental mechanisms of transformation and contaminant reactions with changes in physical and chemical conditions must be understood with confidence. Different aspects of microbial-mineral contaminant uptake can be emphasized by using different techniques. Single-component systems are relatively easy to study and provide excellent information about metal-binding mechanisms

and properties. But this is far from real environmental conditions which usually constitute highly heterogeneous systems, and hence cannot be directly applied in field studies. Although studies focused on metal behavior in realistic environmental conditions give good insight about the overall metal distribution, such studies are highly complicated and hence it is hard to decouple different processes involved in the uptake mechanism. This triggers the need to apply a combination of approaches to accurately understand the mechanism of metal distribution and mobility focusing at one aspect at a time. Therefore use of different experimental techniques complementary to each other combined with modeling is commonly used to bridge the gap between bulk scale and molecular level studies.

1.3 Scientific Directions and Interdisciplinary Nature of the Problem

In the initial stages of studies like these, the usual approach is measurement of a macroscopic property dependence on some parameter of the metal (concentration, charge state) or the environment (pH, ionic strength, presence of complexing ligands). Molecular-scale models are then inferred in order to explain the experimental data, and later used to model such systems. In many cases, however, it is desirable to directly determine the atomic structure in order to understand precisely the role of the metal. Techniques such as x-ray diffraction (XRD), atomic force microscope (AFM), electron microscopy (EM), vibrational (infrared and Raman) spectroscopy, and x-ray absorption fine structure (XAFS) spectroscopy are used. Each of them has strengths and limitations and their applicability depends on the nature of the problem at hand. XAFS has the unique capability of providing structural and chemical information about the environment of a certain atom, without the need for long-range order or invasive sample preparation. Amorphous

solids or fluids containing very small amounts of the element of interest can be examined under ambient or controlled conditions. This makes XAFS one of the very few techniques available to study aqueous metal adsorption to organic surfaces.

Synchrotron-based x-ray techniques (such as absorption spectroscopy, micro-fluorescence, and imaging) have advanced considerably over the past few years. This is particularly true for synchrotron radiation facilities such as APS, NSLS, ESRF (to name few of them), where an association of optimal source characteristics with new detectors and computers has opened up new areas of research in addition to improvements in existing techniques. These x-ray techniques find their application to a wide range of topics including physical, medical, material science and engineering subjects. But more recently it has become increasingly important for new areas of study like geophysical, environmental and archaeological sciences. Many new applications of micro focused x-ray beams have been made in the past few years due to significant advances in x-ray sources, optics, detection, and analysis techniques. These developments have resulted in x-ray images with unprecedented spatial, temporal, elemental, and chemical sensitivity. Various techniques including tomography, fluorescence, absorption spectroscopy, and diffraction can be combined for two or three-dimensional microanalysis on the same sample.

In brief, *molecular environmental science* is the fundamental science needed to underpin an understanding of our "environment" and hence is essential to any attempt to predict the behavior of environmental systems. It involves studies of natural fluids, minerals and their surfaces, and how they interact with such fluids. It also involves the interface between inorganic/organic and biological systems (bacteria, plants and higher organisms). It has clear relevance both to the

quality of life and to more profound questions about the role of metals, materials and mineral surfaces in the origin of life and the course of evolution, as well as how human disruption of the environment might influence that course. It integrates traditional macroscopic and microscopic techniques with state-of-the-art molecular-scale approaches such as x-ray absorption spectroscopy, atomic force microscopy, and molecular dynamics modeling.

These topics are highly interdisciplinary, and draw on the techniques of many fields including physics, chemistry, biology, geology, soil sciences, applied mathematics, numerical analysis and computer science. The problems treated in environmental sciences have far-reaching practical implications, and are also of considerable intellectual interest in their own right.

1.4 Role of XAFS in Environmental Science

The mobility and bio-availability of toxic heavy metals and radionuclides in soils and groundwater are controlled by sorption onto mineral surfaces. Metals may sorb by forming surface precipitates, outer-sphere complexes or inner-sphere complexes. We need to understand the mechanisms by which sorption occurs in order to reliably develop thermodynamic and kinetic models of metal solubilities. Using *X-ray Absorption Fine Structure* (XAFS) spectroscopy one can develop a molecular understanding of how metal sorption takes place at bacterial and mineral surfaces and how the sorption mechanisms change with time and during mineral transformations. XAFS analysis allows the determination of the local coordination environment of a metal cation sorbed to a mineral and microbial surface. It has the unique capability of providing structural and chemical information about the environment of a certain atom, without the need for long-range

order or invasive sample preparation. XAFS has the ability to determine atom types and numbers in near vicinity of the atom whose absorption spectrum is being measured, as well as the distance of these atoms from the absorber. The local structural information obtained from XAFS measurements and spectra of appropriately chosen and well-characterized standards enable identification and quantification of the functional groups responsible for the mineral surface complexation. XAFS spectroscopy also serves as a rigorous test for the adsorption models.

Common inorganic and organic ligands found in natural waters can inhibit or enhance cation adsorption on mineral surfaces depending on a number of factors, including the stability of solution complexes relative to surface complexes, the nature of surface complexes formed, the competition between the ligands and cation for surface sites, and the effect of surface charge reduction at low pH by anionic ligands on cation sorption. It is of practical importance to distinguish between the various modes of sorption because the distance of approach and types of bonding of ions to oxide surfaces heavily influence the adsorbing ion's chemical properties and reactivity. Fundamental questions like mode of sorption, molecular structure, and chemical compositions of the system under study can be precisely answered using XAFS. XAFS has emerged as the strongest tool for in-situ characterization of sorption products in ion sorption at solid-aqueous solution interface.

Often, the role of molecular probes is to provide chemical and physical information about the species taking part in the elementary (or overall) reactions which could then be appropriately represented in corresponding reactions to get the rate and/or equilibrium constants. In this context, it is non-trivial to determine the species and stoichiometry of the reactions and whether or not the reaction could be

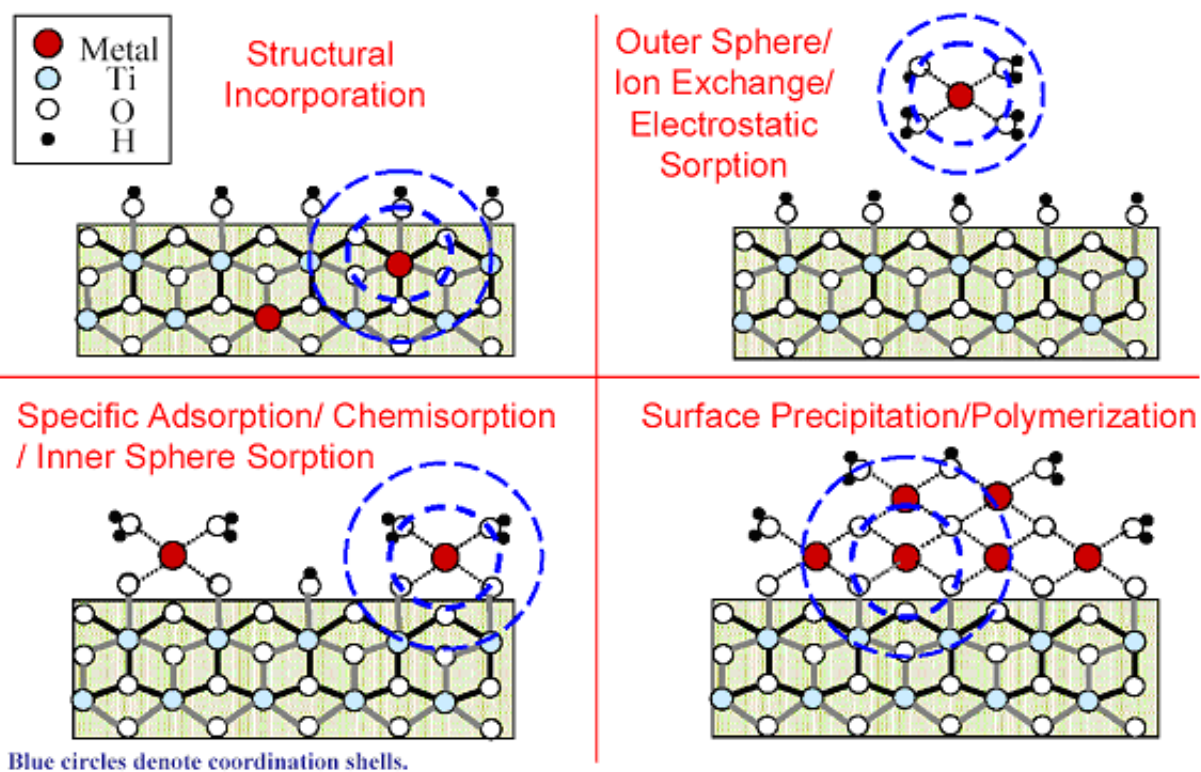


Figure 1.2. Example of metal uptake by surfaces. What can XAFS tell us? Adapted from talk by Douglas Hunter, Savannah River National Laboratory (SRNL)

treated as an equilibrium reaction for the timescale of interest. Making this connection between molecular species (as detected by spectroscopic and microscopic probes) and those chosen to represent macroscopic chemical behavior (based on thermodynamic, kinetic and other bulk measurements) is the crux of using XAFS and applying the information thus obtained to field scale environmental problems.

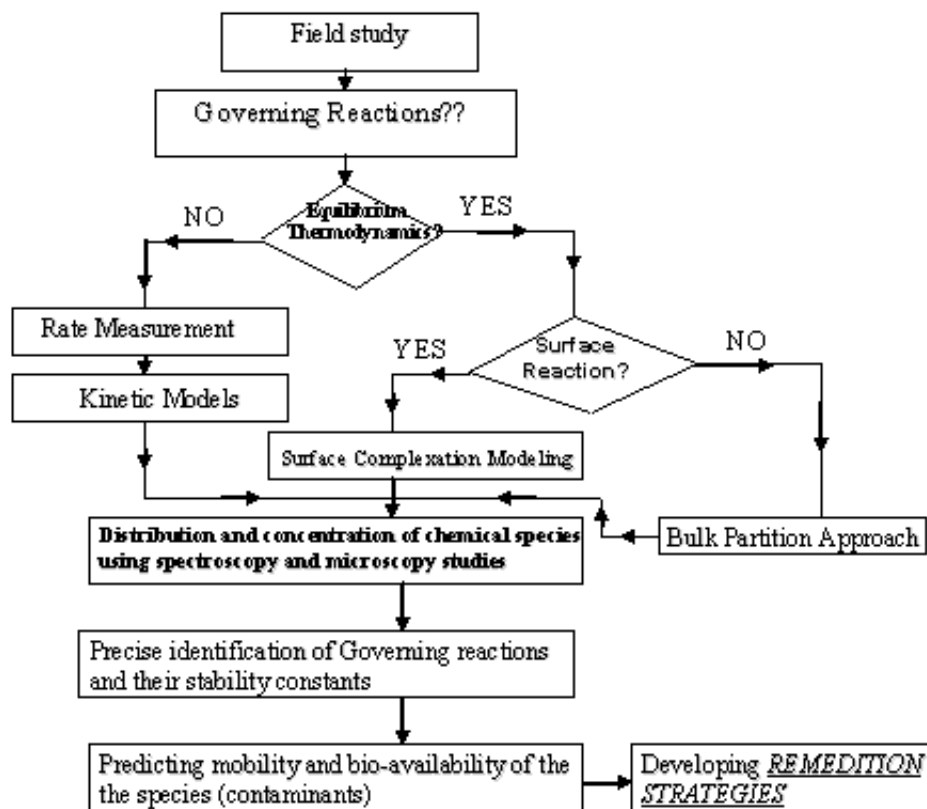


Figure 1.3. The "big picture" of Molecular Environmental Science

1.5 Work Presented in This Dissertation

In this work, XAFS has been applied to the study of contaminant metal complexation with a number of bacterial surfaces, bacterial exudates (siderophores) and 1 : 1 aluminosilicate clay mineral kaolinite. XAFS measurements have been done on heavy and toxic metal contaminants Cd K edge and Pb L₃ edge. Although the XAFS studies are complemented with thermodynamic equilibrium modeling using surface complexation approach in most of the cases, the main focus of this study is the determination of coordination environment and binding mechanism of Cd and Pb sorbed to number of surfaces of environmental interest using state-

of-the-art synchrotron based XAFS spectroscopy.

The study of siderophores is sparked by an interest in both the environmental and potential medical applications. Siderophores are low molecular-weight iron chelating compounds generated by plants, microbes, and even some higher organisms for the acquisition of iron. They are powerful ferric ion-selective chelating agents facilitating active transport of iron for the use of cells. Recent studies have suggested great potential for important therapeutic applications of siderophores. It has been shown that siderophore-drug conjugates can effectively deliver drugs to their target in the pathogen which is otherwise a highly inefficient process. Although siderophores are optimized to acquire Fe, they also have high binding affinities for many more metals. Being strong chelating agents, they play an important role in the transport and bioavailability of metals at contaminated surface and ground water systems. Hence they are an excellent agent for developing bioremediation strategies at environmentally contaminated sites. This study examined chelation property of commercially available trihydroxamate siderophore desferrioxamine B (DFO-B) with Pb and Cd as a function of pH condition. XAFS analysis has been combined with thermodynamic modeling. Neubauer et al. [71] has shown that siderophores inhibited adsorption of Pb to goethite (an Iron oxide mineral) at $\text{pH} > 6.5$, hence enhancing Pb mobility within the approximately neutral to basic pH range. Hepinstall et al. [41] compared the effects of different siderophores (DFO-B, -D, -E) on Pb adsorption to the clay mineral kaolinite as a function of pH. Above 6.5 all the siderophores under investigation inhibited Pb adsorption while they enhanced Pb adsorption around pH 6.0. Discerning the reason behind this pH dependence to enhancement or inhibition of the adsorption of Pb was the main focus the siderophores work. Such a study builds a mechanistic

understanding of hydrobiogeochemical controls on Pb mobility in porous media, enabling us to determine the equilibrium constants determined in sorption studies of such reactions, thus setting the stage for the further improvement of the unified thermodynamic modeling.

In the case of aforementioned bacterial surfaces, Cd binding mechanism to these surfaces has been examined using XAFS. Since adsorption onto bacterial surfaces can control the speciation and distribution of contaminants in many aquatic and near-surface systems, accurate models that describe bacteria-metal interactions are critical to understanding the behavior of heavy metal contaminants and the development of contaminant remediation strategies. An obstacle in modeling realistic systems, however, is that a given bacteria-bearing natural system can contain many different bacterial species.

There are some indications that diverse groups of bacteria adsorb metals to similar extents and suggested that uptake can be modeled using a universal adsorption model. For example, recent studies have shown that individual pure strains of bacteria [25, 56, 78, 113] and artificial mixtures of pure strains of bacteria exhibit broadly similar adsorptive behavior [114]. Similarly, Borrok et al. [12] found that consortia of bacteria grown from a range of uncontaminated soil and water environments exhibit roughly similar affinities for protons and Cd. In contrast, however, Borrok et al. [11] demonstrated that bacterial consortia grown from hydrocarbon-contaminated environments do not exhibit the same relatively narrow range of proton and Cd adsorption behavior that characterizes bacterial consortia from natural environments. The studies by Borrok et al. [11, 12] are based on bulk adsorption experiments only, and do not provide a mechanistic underpinning to explain the observed adsorption commonalities within bacterial

consortia grown from natural environments and pure laboratory cultures; nor do the studies offer a mechanistic understanding of why the commonalities of metal binding onto bacterial consortia do not apply when the bacterial consortia are grown from contaminated environments. Clearly, successful application of a surface complexation approach to quantifying bacterial adsorption of aqueous metal cations onto bacterial consortia requires a detailed understanding of the binding mechanisms and a determination if common mechanisms exist between diverse consortia. That information can be provided directly by using XAFS spectroscopy to identify the surface adsorption sites and to quantify the relative amount of metal bound to each site.

XAFS of fungal cell walls [89], Gram-positive bacteria [13, 47] and Gram-negative bacteria [103] indicate that phosphoryl and carboxyl functional groups are responsible for metal complexation by these three types of microorganisms despite the differences in molecular structure of their exterior surfaces. For example, Sarret et al. [89] examined Zn sorption to fungal cell walls at pH 6 as a function of Zn loading, and the phosphoryl group was shown to be the predominant complexing ligand. Only under the highest Zn loading conditions was the carboxyl group found to contribute to binding. Kelly et al. [47] determined the pH dependence of the cell wall functional groups responsible for the adsorption of aqueous UO_2^{2+} to the Gram positive bacteria *Bacillus subtilis* from pH 1.67 to 4.80. While UO_2^{2+} was found to bind exclusively to phosphoryl functional groups at extremely low pH, an increase in the contribution of the carboxyl functional groups was observed with increasing pH. Similarly, Boyanov et al. [13] reported that Cd binds to the Gram positive bacteria *Bacillus subtilis* predominantly due to phosphoryl binding below pH 4.4, whereas with increasing pH (4.4 – 6.5), adsorption to carboxyl

groups becomes increasingly important. However, at pH 7.8, Boyanov et al. [13] observed the activation of an additional binding site, which was tentatively ascribed as a phosphoryl site with shorter Cd-P distance than the one reported to be active under lower pH conditions. Toner et al. [103] investigated Zn sorption by a bacterial biofilm of Gram negative bacteria *Pseudomonas putida* at pH 6.9, and attributed zinc sorption to the biofilm predominantly to Zn-phosphoryl complexes, with a relatively small contribution from carboxyl-type complexes. Guine et al. [37] reported *sulfhydryl* ligands responsible for Zn adsorption to three Gram negative bacterial strains at low loadings of Zn. However, the characterization of this site was only qualitative in nature, and its quantitative contribution could not be calculated.

The studies discussed above demonstrate that there is spectroscopic evidence that Cd, Zn, Pb and UO_2^{2+} sorption onto microbial biomass is controlled by phosphoryl-, carboxyl-, and perhaps sulfide-type functional groups on cell walls. The possibility that there are only a few types of cell wall binding environments may be the mechanism that causes the similar adsorption behaviors observed for natural bacterial consortia by Borrok et al. [12]. In this study, we test this hypothesis by using XAFS to directly determine the binding environments for Cd using one of the natural consortia tested by Borrok et al. [12]. Furthermore, we attempt to use XAFS experiments to determine the binding mechanisms responsible for the different Cd adsorption behavior that was observed by Borrok et al. [11] for contaminated consortia. These studies are the first to examine metal binding onto complex bacterial consortia. Analogous experiments involving mineral surfaces would likely yield extremely complex XAFS signals that would be difficult to interpret due to the unique binding environment present on each

mineral surface. If bacteria exhibit a more restricted range of adsorption mechanisms, then the XAFS data should demonstrate this directly, and should be able to distinguish binding environments between the two types of bacterial consortia studied.

In order to attempt the XAFS analysis of Cd adsorption to consortium of bacteria from real geologic settings, it was necessary to understand the binding mechanism of Cd adsorbed to a number of pure bacterial strains. To this end, a series of XAFS experiments have been performed as a function of pH and Cd loading to determine the speciation of Cd adsorbed to several pure bacterial strains. These experiments, though the building blocks for the bacterial consortium analysis, served to test and further enhance the existing complexation model for the identification of sites responsible for metal (Cd) binding on those strains and the stoichiometry of the reactions involved.

CHAPTER 2

THEORY OF X-RAY ABSORPTION FINE-STRUCTURE SPECTROSCOPY

2.1 Introduction

A discussion of XAFS should at least briefly outline the landmarks of the historical development of the subject. Fine structure oscillations were first observed by scientists in the 1920's. Early explanation naturally turned to the use of quantum mechanics. However, many of these early developments depended on long-range ordering of the crystal lattice and were demonstrably incorrect for systems such as molecular gases and amorphous materials. An alternate explanation was that the XAFS oscillations were a result of short-range order in a system and depended only on the atoms immediately surrounding the absorbing atom. Although the issue of which was the correct approach was in doubt for many years, by the early 1970's short-range ordering had emerged as the correct theory. A critical step in moving XAFS from curiosity to a powerful analytical tool was when Stern, Sayers, and Lytle noted that the Fourier transform of the XAFS spectrum is a radial distribution function of the near neighbors of the absorbing atom modified by a complex scattering amplitude. This clearly validates the short-range order interpretation of the data.

A logical development of the theory of XAFS begins by a brief discussion on the basic physics behind XAFS and then continues on to examine the more

complicated process of evaluating the theory in order to calculate XAFS spectra. Various approximations, simplifications, and phenomenological additions to the theory will be introduced along the way.

2.2 X-ray Absorption Coefficient

The absorption coefficient, μ , is defined by

$$\frac{dI(x)}{dx} = -\mu I \quad (2.1)$$

where I is the incident x-ray intensity on some homogeneous region and x is the position in the region. The solution of Eq. 2.1 is the familiar exponential relation

$$I = I_0 e^{-\mu(E)x}, \quad (2.2)$$

where I_0 is the incident intensity and $\mu(E)$ is written as a function of the incident photon energy, E , since XAFS is energy dependent.

X-ray absorption spectroscopy measures the absorption of x-rays as a function of x-ray energy $E = \hbar\omega$. If the absorption coefficient is plotted as a function of E , as shown in Fig. 2.1, the experimental data show three general features: (1) an overall decrease in x-ray absorption with increasing energy which can be understood from Fermi's golden rule [88]; (2) the presence of a sharp rise at certain energies called edges. These edges refer to the excitation energies of the inner shell electrons and are characteristic of specific atoms; (3) above the edges, a series of oscillatory structure that modulate the monotonically decreasing absorption, typically by a few percent of the deviation in absorption from the atomic absorption μ_0 . These features have been attributed to the presence of other atoms around the

absorbing atom and by analyzing these oscillations; information about the local environment of the absorbing atom can be derived. The oscillations which occur relatively close to the edge (within about 30 eV) are known as X-ray Absorption Near Edge Structure (XANES). The oscillations well above the absorption edge (≥ 30 eV) are known as Extended X-ray Absorption Fine Structure (EXAFS).

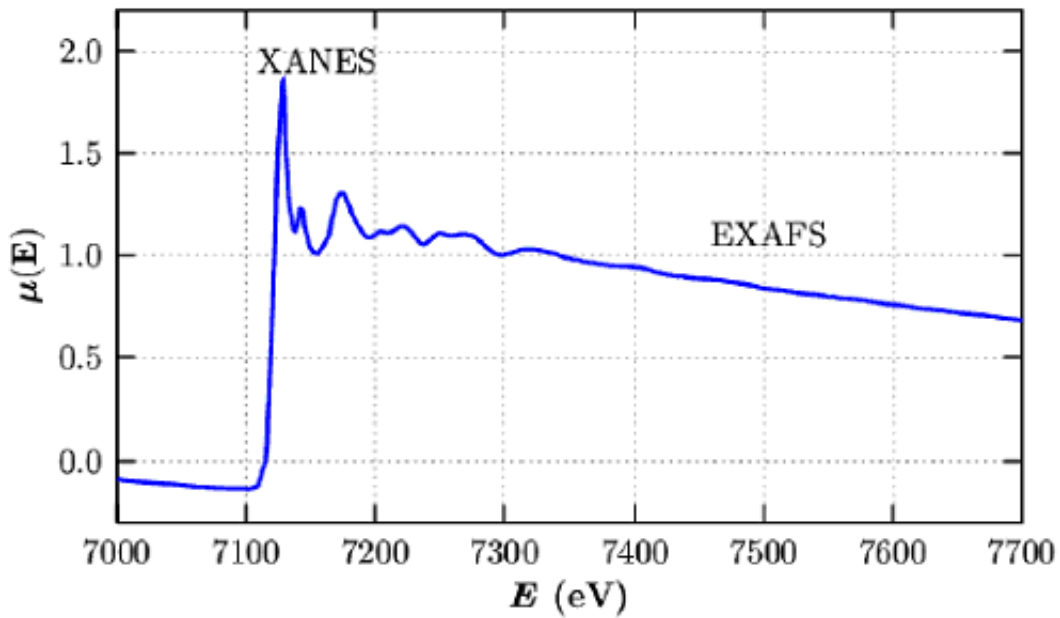


Figure 2.1. Plot of the absorption coefficient, $\mu x = \ln\left(\frac{I_0}{I}\right)$, versus incident x-ray energy of the Fe K-edge; Fe foil sample. X-ray Absorption Near Edge Structure (XANES) and Extended X-ray Absorption Fine Structure (EXAFS) regions are shown on the plot.

It has become clear in recent years that there is no fundamental difference in the physics of EXAFS and XANES, however, interpreting the later is more com-

plicated because some of the approximations used in EXAFS region do not work for XANES. EXAFS and XANES are generally unified under the term "XAFS". The uniqueness of EXAFS as a structural tool stems from the fact that it probes short-range order rather than long-range order and does not require crystalline structure.

2.3 Basic Physics of XAFS

The underlying physics of XAFS can be viewed with a simple picture. EXAFS does not occur for isolated atoms but appears only when atoms are in a condensed state. The absorption edge corresponds to an x-ray photon having enough energy to just free a bound electron in the atom. When the electrons are in the most tightly bound $n = 1$ shell, the edge is called K -edge. For the next most tightly bound shell of atoms, the $n = 2$ shell, the corresponding edges are called the L -edges. X-ray absorption in the photon range up to 40 keV, the range of most importance for EXAFS, is dominated by the photoelectric effect where the photon is completely absorbed, transferring its energy to excite a photoelectron and leaving behind a core hole in the atom. Assuming that all the absorbed photons energy goes into exciting a single core electron, the kinetic energy of the excited photoelectron is given by the difference between the photon energy and binding energy of the electron in the atom. This is shown in the form of an equation given by $\frac{p^2}{2m} = h\nu - E_0$ where the x-ray photon of frequency ν has energy $h\nu$ and E_0 is the binding energy of the photoelectron. For an isolated atom, the photoelectron can be represented as an outgoing wave as shown in Fig. 2.3. The surrounding atoms will scatter the outgoing waves as indicated by the dashed lines. The final state is the superposition of the outgoing and scattered waves. The absorption of

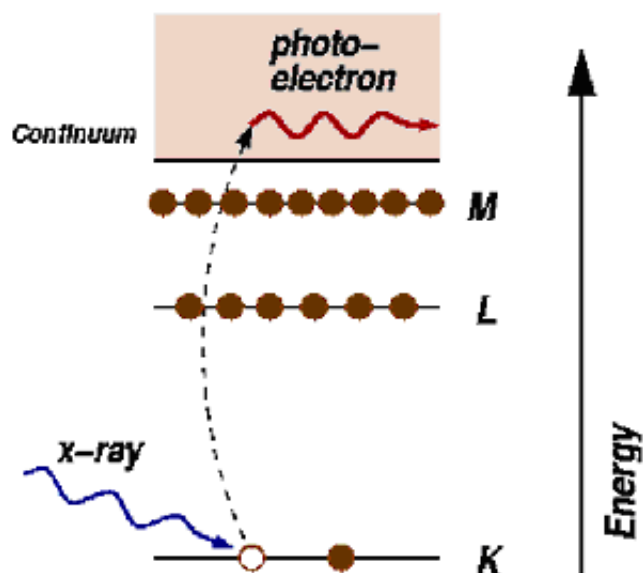


Figure 2.2. A schematic of how XAFS works is shown. X-ray is incident on a sample resulting in the ejection of a photoelectron from the core-hole. This photoelectron must return back to the core-hole before its decay for XAFS to happen. (Adapted from Newville's "Fun Slides".)

x-rays is given quantum mechanically by a matrix element between the initial and final states. In our case, the initial state is the electron in the atomic core and the final state is this electron excited to the escaping photoelectron. The matrix element is large only in the region where the core state has significant probability density - that is, near the center of the absorbing atom. Thus, it is only necessary to determine how the photoelectron is modified by the surrounding atoms at the center of the absorbing atom to determine the modification leading to EXAFS. The backscattered waves will add or subtract from the outgoing wave at the center depending on their relative phase. The total amplitude of the electron wave function will be enhanced or reduced, respectively, thus modifying the probability of the x-ray absorption correspondingly. The way this phase varies with

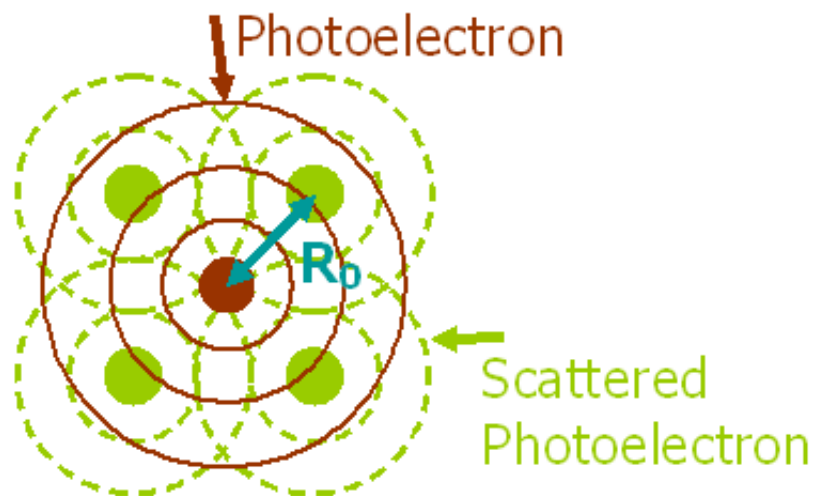


Figure 2.3. The principle of XAFS is shown. The absorbing atom is shown by solid red circle and the neighboring atom by green solid circle. The outgoing photoelectron wave from the absorbing atom is shown by solid red lines and the backscattered Photoelectron wave from the neighbor by the dotted lines. These two photoelectron waves interfere to give rise to XAFS oscillations.

the wavelength of the photoelectron depends on the distance between the central and the backscattering atom. The variation of the backscattering amplitude, as a function of energy of the photoelectron, depends on the type of the backscattering atom. Thus by analyzing EXAFS oscillations, one can derive information about the environment of the central atom.

2.4 Derivation of the EXAFS equation

XAFS is defined as

$$\chi(k) = \frac{\mu(E) - \mu_0(E)}{\mu_0(E)} \quad (2.3)$$

where μ_0 is the slowly varying background absorption from an isolated absorbing atom and other processes. The equation for the absorption coefficient can be

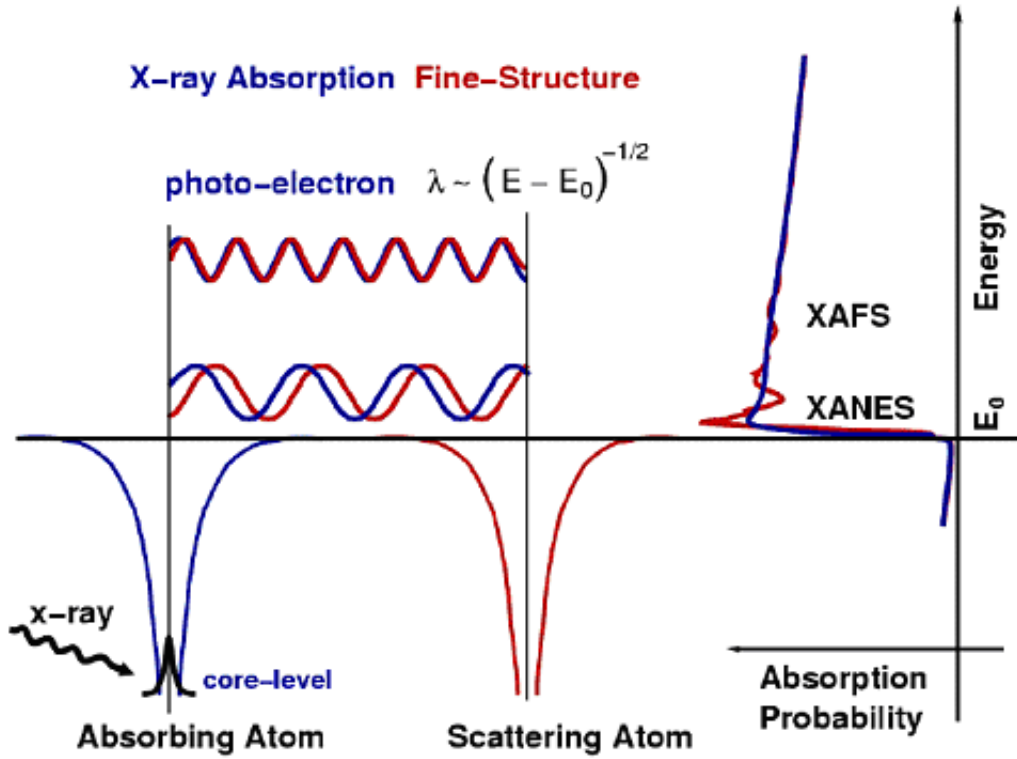


Figure 2.4. Overall scheme of XAFS, showing the difference between XANES and EXAFS. (Adapted from Newville's "Fun Slides")

written in terms of the number density n and the atomic x-ray cross-section σ of the absorbing atom: $\mu = n\sigma$. The probability of a photon being absorbed per unit atom, W , is related to σ through $W = \left(\frac{Nc}{V}\right)\sigma$ where N is the number of photons of a particular energy in a volume V and c is the speed of light. From Fermi's golden rule [88],

$$W = \frac{2\pi}{\hbar} \sum_f |\langle f|H|i\rangle|^2 \delta(E_f - E_i - \hbar\omega). \quad (2.4)$$

Here, H is the Hamiltonian for the electron-photon interaction, $|i\rangle$ and $|f\rangle$ are the initial and final N -electron states, respectively. The delta function ensures

conservation of energy and the summation is carried out over all final states with energy E_f . The electron-photon interaction Hamiltonian H can be written as

$$H = \frac{\vec{P} \cdot \vec{P}}{2m} - \frac{e}{2mc} \vec{A} \cdot \vec{P} - \frac{e}{2mc} \vec{P} \cdot \vec{A} + \frac{e^2}{2mc} A^2 + e\phi, \quad (2.5)$$

where \vec{P} is the electron momentum vector, \vec{A} and ϕ are the vector and scalar potentials of the classical electromagnetic field, respectively. By choosing the Coulomb gauge ($\vec{\nabla} \cdot \vec{A} = 0$), $\phi = 0$ and noting that A^2 term is a factor of e ($\sim 10^{-19}$) smaller than the other terms, and re-writing \vec{A} as a monochromatic transverse wave

$$\vec{A} = A_0 e^{i\vec{q} \cdot \vec{r}} \hat{\epsilon}, \quad (2.6)$$

H reduces to

$$H = -\frac{e}{2mc} A_0 e^{-i\vec{q} \cdot \vec{r}} \hat{\epsilon} \cdot \vec{P} \quad (2.7)$$

where $\hat{\epsilon}$ is the electric field polarization vector of the incident x-rays, \vec{q} is the photon momentum where $q = \frac{\omega}{c} = \frac{E}{\hbar c}$ and \vec{r} is the photoelectron position vector in the initial core electron state. If the exponential in the above equation is expanded in a power series ($1 + i\vec{q} \cdot \vec{r} + \dots$), the $q \cdot r$ term turns out to be of the second order in the expression for W . So if it can be shown that ($qr^2 \ll 1$), the exponential can be approximated by 1. This is known as the *dipole approximation*. With this approximation, H reduces to

$$H \approx -\frac{e}{2mc} A_0 \hat{\epsilon} \cdot \vec{P}. \quad (2.8)$$

Substituting this into the equation for W , we get

$$W = -\frac{2\pi e^2}{\hbar m^2 c^2} A_0^2 \sum_f |\langle f | \hat{\varepsilon} \cdot \vec{P} | i \rangle|^2 \delta(E_f - E_i - \hbar\omega). \quad (2.9)$$

Since

$$\begin{aligned} \vec{P} &= \frac{m}{i\hbar} [\vec{r}, H], \\ |\langle f | \hat{\varepsilon} \cdot \vec{P} | i \rangle|^2 &= -\left(\frac{m}{\hbar}\right)^2 |\langle f | \hat{\varepsilon} \cdot \vec{r} H | i \rangle - \langle f | \hat{\varepsilon} \cdot H \vec{r} | i \rangle|^2 \\ &= -\left(\frac{m}{\hbar}\right)^2 |E_i \langle f | \hat{\varepsilon} \cdot \vec{r} | i \rangle - E_f \langle f | \hat{\varepsilon} \cdot \vec{r} | i \rangle|^2 \\ &= -m^2 \omega^2 |\langle f | \hat{\varepsilon} \cdot \vec{r} | i \rangle|^2 \end{aligned}$$

since E_i and E_f are the eigenvalues of the Hamiltonian H for states $|i\rangle$ and $|f\rangle$ respectively and $\hbar\omega = E_f - E_i$. By using $A_0^2 = \frac{2\pi\hbar c^2 N}{\omega V}$, we further derive

$$\sigma = \frac{4\pi^2 e^2 \omega}{c} \sum_f |\langle f | \hat{\varepsilon} \cdot \vec{r} | i \rangle|^2 \delta(E_f - E_i - \hbar\omega) \quad (2.10)$$

So far, we have been considering the single-electron approximation. It may be noted that following the creation of an electron vacancy in the atom, the potential is slightly changed and other so-called "passive" electrons adjust to this new potential by relaxing to states different from the initial state. By ignoring the further complications involved in a multi-electron model, we can separate the inner product into two parts, i.e., one for the active electron and the other for the $N - 1$ passive electrons. The inner product can then be re-written as

$$\sum_f |\langle f^N | \hat{\varepsilon} \cdot \vec{r} | i^N \rangle|^2 = |\langle f^{N-1} | i^{N-1} \rangle|^2 \sum_f |\langle f | \hat{\varepsilon} \cdot \vec{r} | i \rangle|^2 \quad (2.11)$$

Since the inner product of the $N - 1$ electron states will be less than one, it reduces the amplitude of XAFS. The inner product, $|\langle f^{N-1} | i^{N-1} \rangle|^2$, is often denoted by S_0^2 .

2.4.1 K-edge XAFS Equation of Single Scattering

The configuration of single scattering is shown in Fig. 2.5. In the above derived expression for transition matrix, $\hat{\epsilon} \cdot \vec{r} = r \cos \theta$ and for K-edge absorption, $|i\rangle$ is an s wave without any angular dependence. In order to yield a nonzero matrix element, $|f\rangle$ must have a $\cos \theta$ dependence. This corresponds to $|f\rangle$ having $l = 1$ and $m = 0$ near the origin. The potential is treated in the so-called muffin-tin approximation, where the core potential is considered to be spherically symmetric within a sphere centered about each atom and the potential outside the sphere is averaged to a constant value. The validity and details of the muffin-tin approximation will be discussed later in the chapter. The XAFS equation using this potential model will be first derived [52].

The outgoing part of $|f\rangle$ can be written outside the center atom sphere as the real part of the Hankel function $h_1^+(kr) \cos \theta = [(kr)^{-1} + i(kr)^{-2}] e^{ikr} \cos \theta$. Usually a phase shift factor $e^{i\delta'}$ is added to it in order to account for the central atom potential. However, the phase shift can be set to zero without changing the physics by treating it as an initial phase and multiplying the outgoing wave function by $e^{-i\delta'}$. The outgoing wave function will be scattered by neighboring atom centered at r_j and to the first order, the scattering amplitude will be

$$\Psi_{sc} = h_1^+(kr_j) \frac{e^{ik|r-r_j|}}{k|r-r_j|} \cos \theta_j f(\alpha). \quad (2.12)$$

This is a spherical wave emanating from the backscattering atom with amplitude

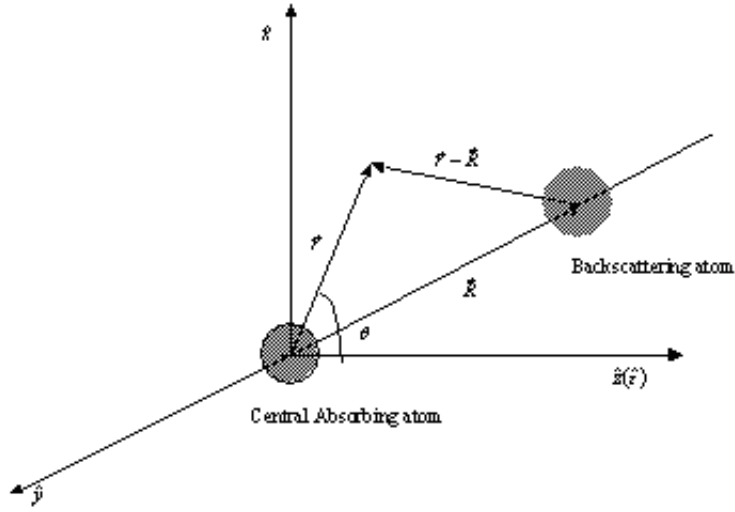


Figure 2.5. The scenario in single scattering.

proportional to the value of the outgoing wave at r_j and a general dependence on the angle α about the direction \vec{r}_j . As this scattered wave penetrates into the spherical core about the central absorbing atom, it will be modified significantly and the interaction can be accounted for exactly by using standard scattering theory. The backscattering amplitudes and the phase-shifts in the central and backscattering amplitudes have been calculated by Lee and Teo [61, 102]. The backscattering amplitudes and phase-shifts for some atoms have been shown in Fig. 2.6*a,b*. It may be noted that the backscattering amplitude and phase-shift for low- Z atoms are featureless over the entire k -range but for atoms with $Z > 40$, there is an increased and added structure at higher k .

The wave Ψ_{sc} can be decomposed into spherical harmonic partial waves about the central atom. Only $l = 1$ and $m = 0$ component contribute since the partial wave will interfere with the outgoing wave that has the same symmetry. Denoting the $l = 1$ and $m = 0$ component of Ψ_{sc} by $\Psi_{sc}^{(1,0)}$, the outside the muffin-tin sphere

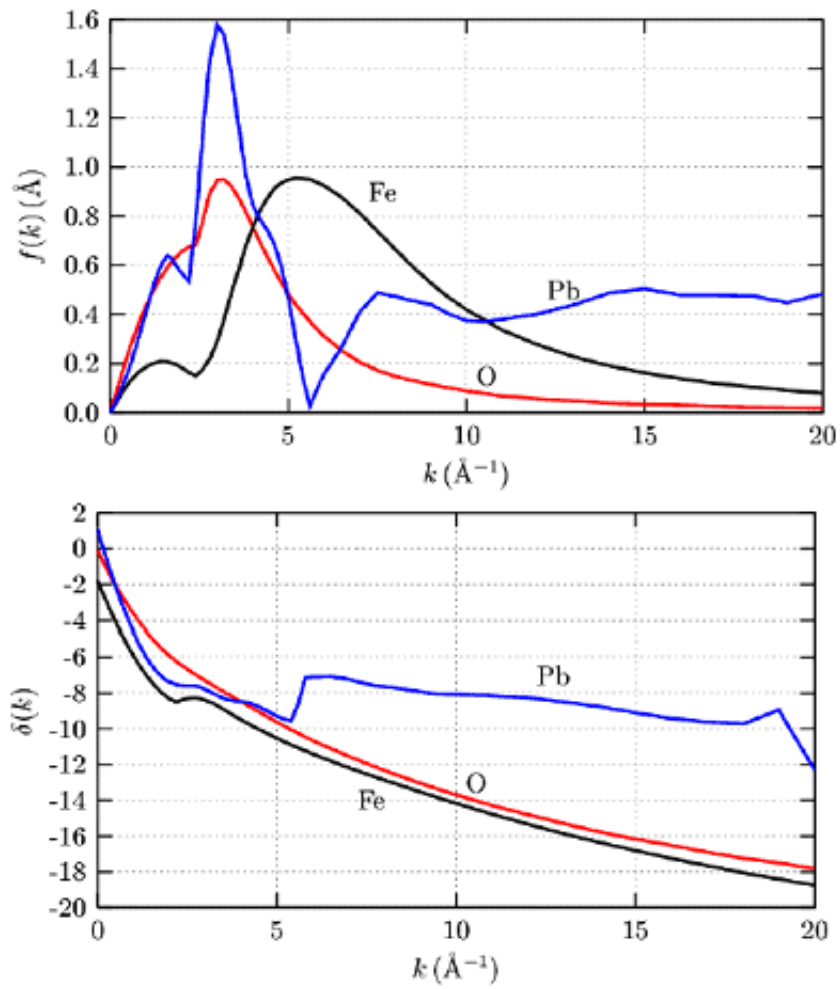


Figure 2.6. Plot of (a) Scattering amplitude and (b) phase of Fe, O and Pb as a function of the photoelectron wave vector. (Adapted from Newville's "Fun Slides")

about the central atom,

$$\Psi_{sc}^{(1,0)} = A(1,0)h_1^-(kr) \cos \theta \quad (2.13)$$

where $h_1^-(kr)$ is the incoming Hankel function for $l = 1$ and $A(1,0)$ is the amplitude of that function present in Ψ_{sc} . The outgoing partial wave produced by the scattering of $\Psi_{sc}^{(1,0)}$ by the central atom potential is then $A(1,0)h_1^+(kr)e^{i2\delta_1} \cos \theta$. The final state $|f\rangle$ is the sum of this outgoing partial wave and the original outgoing wave part of $|f\rangle$ given by

$$|f\rangle = h_1^+(kr) \cos \theta [1 + A(1,0)e^{i2\delta_1}]. \quad (2.14)$$

As $r \rightarrow 0$,

$$\Psi_{sc} \rightarrow h_1^+(kr_j) \cos \theta_j f(\pi) \frac{e^{ikr_j}}{kr_j} \left[1 - ikr \cos \gamma \left(1 + \frac{i}{kr_j} \right) \right] \quad (2.15)$$

where $|\mathbf{r} - \mathbf{r}_j| = (r^2 + r_j^2 - 2rr_j \cos \gamma)^{\frac{1}{2}}$ has been used and Ψ_{sc} has been expanded in Taylor's series to first order in r . The angle γ between \vec{r}_j and \vec{r} in terms of θ and ϕ is given as

$$\cos \gamma = \cos \theta \cos \theta_j + \sin \theta_j \sin \theta \cos \phi. \quad (2.16)$$

By comparing the two expressions and realizing that $Reh_1^+(kr) \rightarrow -\frac{kr}{3}$ as $r \rightarrow 0$,

$$A(1,0) = 3i[(h_1^+(kr_j))^2 \cos^2 \theta_j f(\pi)]. \quad (2.17)$$

Substituting in equation,

$$|f\rangle = h_1^+(kr) \cos \theta [1 + 3i(h_1^+(kr_j))^2 \cos^2 \theta_j f(\pi) \exp(i2\delta_1)] \quad (2.18)$$

and

$$\mu = \mu_0 \{1 - 3\text{Im}[(h_1^+(kr_j))^2 \cos^2 \theta_j f(\pi) \exp(i2\delta_1)]\} \quad (2.19)$$

and

$$\chi(k) = \frac{\mu - \mu_0}{\mu_0} = 3\text{Im}[(h_1^+(kr_j))^2 \cos^2 \theta_j f(\pi) \exp(i2\delta_1 - i\pi)] \quad (2.20)$$

where the minus sign is incorporated as $\exp(-i\pi)$.

Two approximations are made thereafter.

1. In the EXAFS regime, that is 30 eV beyond the edge, the photoelectron has enough energy so that $kr_j \gg 1$ and according to [20]

$$h_1^+(kr_j) \rightarrow \frac{e^{ikr_j}}{kr_j} \quad (2.21)$$

2. The small atom approximation i.e., $\frac{D}{r_j} \ll 1$ where D is the atomic diameter and therefore $f(\pi)$ can be calculated [91] by

$$f_0(\pi) = \sum_l (-1)^l (2l + 1) \sin \delta_l e^{i\gamma_l}, \quad (2.22)$$

where the curvature of the spherical wave is neglected and the incoming and scattered waves can be approximated by plane waves. With these approximations

and summing the contributions from all the backscattering atoms,

$$\chi(k) = 3 \sum_j \frac{m}{2\pi\hbar^2} \frac{t_j(2k)}{(kr_j)^2} \cos^2 \theta_j \sin(2kr_j + \delta_j(k)), \quad (2.23)$$

where

$$t(2k)e^{i\beta} = \frac{2\pi\hbar^2}{m} f_0(\pi) \quad (2.24)$$

and

$$\delta_j(k) = 2\delta_1 + \beta - \pi \quad (2.25)$$

and $t(2k)$ and β are real. In the plane wave approximation, $f_0(\pi)$ is independent of r_j . For polycrystalline samples without a preferred orientation, amorphous solids, samples with cubic or higher symmetry, or unpolarized incident x-rays, the $\cos^2 \theta_j$ term will be averaged over all the neighboring atoms and be replaced by a factor of $\frac{1}{3}$.

In the preceding derivation several approximations have been made. In general the effect of these will be to limit the validity of the derived result to greater than 30 eV above the absorption edge. These approximations are as follows:

Dipole Approximation: $e^{i\vec{q}\cdot\vec{r}}$ was expanded in a power series and noting that the qr term is second order in the transition rate, W , and can therefore be neglected. This approximation is not always good. For deeply-bound atomic states (e.g. more than about 30 keV), quadrupole transitions can sometimes be observed in near-edge structure. This is almost never an important consideration for the extended fine structure. For all the work presented here, this correction is less than 2% or so.

Muffin-tin Approximation: Almost all practical XAFS calculations recently rely on a muffin-tin geometry, which consists of a spherical scattering potential centered on each atom and a constant value in the interstitial region between atoms. The actual potential in a material is evidently more complicated. Near the center of each atom, the charge density of the atomic core will be large and dominate the potential. Hence the potential is approximately atomic-like very close to the nucleus, where the spherical approximation is highly accurate. In the outer regions of the atom and between the atoms, the bonding properties of the material determine the distribution of the charge and the potential is generally anisotropic. In the EXAFS domain, the kinetic energy of the photoelectron is large and the electron is less sensitive to the details of the potential at the outer edges of the atom and in the regions between the atoms. The electron is mainly scattered by the inner parts of the atomic potential and moves more or less freely in the average potential within the flat interstitial region. For this reason, the spherical muffin-tin potential works very well in the EXAFS regime. However, the detail of the potential is much more important for XANES calculations where the photoelectron has low kinetic energy. The details of the potential calculations can be obtained from a review by Rehr and Albers and the references therein.

Plane Wave Approximation: The outgoing spherical wave was replaced by a plane wave in the above derivation. For large kR , the effective curvature of the outgoing wave is much smaller than the effective curvature of the neighboring atomic potential. As the energy of the photoelectron increases, the outgoing electron penetrates more deeply into the core of the neighboring atoms where there is effectively a higher curvature of the atomic potential. This approximation

plainly breaks down at low k (electron momentum). Meaning thereby, PWA is valid if the effective size of the backscattering atom is small compared with the distance between the central and backscattering atoms. At low k , this is not case, because the effective atomic size is about the same as inter-atomic distance. As the k of the photoelectron increases, the effective size of the atom decreases as the photoelectron penetrates deeper into the atom before scattering. At high k the diminishing effective size of the backscattering atom makes the small-atom approximation satisfactory. The errors introduced by this approximation can be largely eliminated by comparing the measured sample to known standard samples with similar coordination chemistry and similar radial distances.

Recent theoretical calculations of XAFS have incorporated a curved-wave formalism to eliminate this source of error. To correct for this, $f(\theta)$ from PWA approximation in the XAFS equation is replaced by $f(\theta) = \sum_l (2l+1) \sin(\delta_l) P_l(\cos \theta) e^{i\delta_l}$ [86]. Convergence with respect to l is controlled by the partial wave t -matrix elements. The mean value of l suitably averaged over t_l , which we call l , is characteristic of the size ρ of the scatterer and is generally much smaller than l_{max} . This maximum value of l may be defined as that for which the classical turning point is outside the range of the scattering potential, i.e. $l_{max} \sim kR_{MT}$ (usually between 10 and 30).

The effect of the breakdown of the small-atom approximation on the phase of EXAFS can be approximately compensated for by a shift of E_0 . Here E_0 is the binding energy of the photoelectron and is related to k by $k = \left(\frac{2m(E-E_0)}{\hbar^2} \right)^{\frac{1}{2}}$. However, E_0 shifts cannot correct for amplitude error introduced by the small-atom approximation. Eliminating the small-atom approximation makes EXAFS less convenient because $t(2k)$ and $\delta(k)$ then depend on r_j in addition to k , and

their tabulation would become prohibitive because of the additional parameter of r_j .

Quasi-Independent Particle Approximation: The preceding analysis has ignored the fact that the remaining $N - 1$ electron states will no longer have the same wave function as the core electron is ejected and correspondingly a hole is created. The effect of this incomplete overlap of the initial and final $N - 1$ electron states, which reduces the measured XAFS amplitudes, has been grouped into the term S_0^2 . This is discussed below in details.

Single scattering Approximation: The derivation of XAFS described above is based only single scattering of the photoelectron. However, multiple-scattering often significantly contributes to the XANES spectra and be significant in the EXAFS regime as well. The multiple-scattering contribution to XAFS will be discussed in another section.

The above derivation is valid for the K or L_1 edge, i.e., for an $1s$ initial state. For a p or d initial state, as may be seen in $L_{2,3}M_{2-5}$ edges, there are two final states possible. Because of this and because of the different final state symmetry, the angular dependence is more complicated and the EXAFS equation is slightly modified. This discussion is beyond the scope of this presentation.

2.5 Effects of Thermal Vibration and Structural Disorder

The preceding derivation, while correct as far as it goes, does not tell the complete story. Each absorbed x-ray photon takes a nearly instantaneous snapshot of the local structure around one atom in the sense that the absorption probability

is based upon the relative positions of the absorbing atom and its neighbors at the time of absorption. Because of the thermal vibration and structural disorder the "snapshots" will each determine a slightly different absorption coefficient for different atoms and at different times. This has the effect of smearing out the absorption spectrum since the measured spectrum is an average of all the individual absorption events.

To model this average, XAFS Debye-Waller (DW) factor is introduced. For the case of small amplitude (or effective Gaussian) disorder, this can be incorporated into the XAFS equation by introducing the term $e^{-k^2\sigma^2}$. The term comes from $\frac{\exp\left(-\frac{(r-R_j)^2}{2\sigma^2}\right)}{(2\pi\sigma^2)^{\frac{1}{2}}}$ which represents the mean square deviation of the bond-length from its mean value R_j . This factor is analogous to that encountered in x-ray diffraction in that it causes an exponential decay of XAFS as a function of energy. There is however a crucial difference between the two. XAFS is sensitive to only the relative distance between the excited atom and the surrounding atom and thus σ^2 represents a deviation in this relative distance while in diffraction, σ^2 represents the mean square deviation of the individual atomic positions from the lattice sites. Thus the XAFS Debye-Waller factor is dependent on displacement correlations as shown in the equation [5]:

$$\langle\Delta_j^2\rangle = \langle(\vec{u}_0 \cdot \hat{R}_j)^2\rangle + \langle(\vec{u}_j \cdot \hat{R}_j)^2\rangle - 2\langle(\vec{u}_0 \cdot \hat{R}_j)(\vec{u}_j \cdot \hat{R}_j)\rangle \quad (2.26)$$

where $\langle\Delta_j^2\rangle$ is the *mean-square-relative displacement* (MSRD), $\langle(\vec{u}_0 \cdot \hat{R}_j)^2\rangle$, $\langle(\vec{u}_j \cdot \hat{R}_j)^2\rangle$ are the *mean-square-displacements* (MSD) $\langle(\vec{u}_0 \cdot \hat{R}_j)(\vec{u}_j \cdot \hat{R}_j)\rangle$ and is the *displacement correlation function* (DCF). This form is useful as we wish to discuss separately the contributions of MSD and DCF.

In a monatomic crystal,

$$\langle \Delta_j^2 \rangle = \frac{\hbar}{NM} \sum_{\vec{q}\lambda} \left(\hat{e}_{\vec{q}\lambda} \cdot \hat{R}_j \right)^2 \frac{1}{\omega_{\vec{q}\lambda}} \coth\left(\frac{1}{2}\beta\omega_{\vec{q}\lambda}\right) \left(1 - \cos(\vec{q} \cdot \vec{R}_j)\right) \quad (2.27)$$

where N is the number of atoms of mass M , and $\hat{e}_{\vec{q}\lambda}$ is the polarization vector for phonons of momentum \vec{q} , polarization λ , and frequency $\omega_{\vec{q}\lambda}$ [36]. The MSD is independent of the average central atom - neighbor distance and determines the decrease in the EXAFS amplitude as a result of the random "total" thermal motions of the atoms along \hat{R}_j . The second term ensures that only the "out-of-phase" thermal motion of the atoms along \hat{R}_j determines the decrease in the EXAFS amplitude. This term is very interesting because of its dependence on R_j and it can be computed, e.g., if a lattice-dynamical force model is available. An attempt has been made by Beni et al. [5] using the Debye Model to calculate the relative weight of the DCF compared to MSD and is found to be 40% at high temperatures for the first shell of fcc and bcc lattice. Hence they cannot be ignored. There are various models for calculating the phonon spectrum. The two models considered mainly for XAFS Debye-Waller factor are 1) Correlated Debye Model based on the Debye approximation of lattice vibrations and 2) Einstein Model based on Einstein approximation of lattice vibrations. The Einstein model approximates all phonon modes with one vibrational frequency ω_E . Given the value for the phonon frequency, the thermal contribution to the Debye Waller factor is given as

$$\sigma_{th}^2 = \frac{\hbar}{M_r \omega_E} \left(\frac{1}{2} + \frac{1}{e^{\frac{\hbar\omega}{k_B T}} - 1} \right), \quad (2.28)$$

where $M_r = \frac{M_1 M_2}{M_1 + M_2}$ is the reduced mass of the absorbing and backscattering

atoms. The Debye Model has a slightly more complicated form given by

$$\sigma_{th}^2 = \frac{\hbar}{2M_r} \int \rho(\omega) \coth\left(\frac{\hbar\omega}{2k_B T}\right) \frac{d\omega}{\omega} \quad (2.29)$$

where

$$\rho(\omega) = \frac{3\omega^2}{\omega_D^3} \left[1 - \frac{\sin\left(\frac{\omega R}{c}\right)}{\left(\frac{\omega R}{c}\right)} \right] \quad (2.30)$$

and $\omega_D = \frac{k_B \Theta_D}{\hbar}$, where Θ_D is the Debye temperature and $c = \frac{\omega_D}{k_D}$ where $k_D = \left(\frac{6\pi^2 N}{V}\right)^{\frac{1}{3}}$. The Debye Model is superior to the Einstein Model for primitive lattices and for second and higher shells of atoms for non-primitive lattices. The Einstein Model is superior for the first shell of non-primitive lattices (where optical phonons are important) and probably for other complicated structures like big molecules or amorphous solids. Since the Einstein model is simpler than the Debye model and still gives results within 10% in most cases, it is more commonly used [52].

The main problem is the isotropy assumption in both of these models and that they are single-parameter models. These methods allow one to calculate σ^2 of a single-scattering path only when all bonds are equivalent, or they may be approximated by a suitable average. In systems that involve highly anisotropic bonds, for example, strong bonds in one plane and weak bonds in the perpendicular axis, neither of these models are able to calculate accurately all single-scattering Debye-Waller factors. This is exactly the situation for a typical three-atom multiple-scattering path: strong bonds (stretching) are vibrationally-coupled with various weaker bonds (bending, etc.). Therefore neither of these two approximations should be used for three- and/or four-atom multiple-scattering Debye-Waller factor calculations in such systems. Moreover, because of the large number of fitting parameters that would be required if all the important multiple-scattering paths

are included and the limited information content of EXAFS spectra, multiple scattering Debye-Waller factors cannot be obtained from the fitting technique. Some *ab initio* calculations have been done in this regard by Dimakis et al. [27]. The approach attempted a calculation of force constants by a variety of self-consistent quantum chemical methods that are available. Good agreement has been observed with those calculated from infrared and Raman frequencies for all cases tested (GeCl₄, GeH₃Cl). An attempt has also been made by Rehr et al. [81] to overcome the isotropy problem of the Correlated Debye and Einstein Models. They have presented a general equation-of-motion method for calculating the Debye-Waller factors in terms of a few local force constants in arbitrary non-periodic systems.

The development for large or non-Gaussian disorder is credited to Stern. The XAFS equation can be re-written as

$$\chi_i(k) = \text{Im} \sum_B A_B(k) G(R_B) \int_B^N P_B^i(r_B) \exp[i(2kr_B + \delta_B(k))] dr_B, \quad (2.31)$$

considering B-type atoms in the i^{th} shell. Here

$$P_B^i(r_B) = \frac{G(r_B) p_B^i(r_B)}{G(R_B)} \quad (2.32)$$

where $p_B^i(r_B) dr_B$ is the probability of finding B-type atom of the i^{th} shell in the range to $r_B + dr_B$ and R_B is the fixed value of r_B . It may be noted that

$$A_B(k) = \frac{m}{2\pi\hbar^2} \frac{t_B(2k)}{k^2} \quad (2.33)$$

and

$$G(r_B) = \frac{\exp\left(\frac{-2r_B}{\lambda}\right)}{r_B^2}. \quad (2.34)$$

Letting $r_B = R_B + \Delta r_B$ and performing the integration over Δr_B ,

$$\chi_i(k) = \sum_B N_B Q_B^i(k) A_B(k) G(R_B) \sin\left(2kR_B + \delta_B(k) + \phi_B^i(k)\right) \quad (2.35)$$

where

$$Q_B^i(k) \exp(i\phi_B^i(k)) = \int_{-\infty}^{\infty} P_B^i(r_B) \exp(2ik\Delta r_B) d\Delta r_B. \quad (2.36)$$

Note that $\phi(k) = 0$ if $P_B^i(R_B + \Delta r_B)$ is symmetric about R_B . General expressions for $Q(k)$ and $\phi(k)$ can be obtained from the cumulant theory [17]:

$$\int P_B^i(r_B) \exp(2ik\Delta r_B) d\Delta r_B = \exp\left(\sum_{n=1}^{\infty} \frac{(2ik)^n}{n!} C_n\right) \quad (2.37)$$

where C_n is the n^{th} order cumulant average. In terms of ordinary averages, the leading cumulants are

$$\begin{aligned} C_1 &= \langle \Delta r_B \rangle \equiv \bar{r}_B - R_B \\ C_2 &= \langle (r_B - \bar{r}_B)^2 \rangle \equiv \sigma_B^2 \\ C_3 &= \langle (r_B - \bar{r}_B)^3 \rangle \\ C_4 &= \langle (r_B - \bar{r}_B)^4 \rangle - 3\sigma_B^4 \end{aligned}$$

The effect of disorder is both a change in the amplitude and a change in the phase of XAFS

$$Q_B^i(k) = \exp \sum_{n=1}^{\infty} \frac{(-1)^n (2k)^{2n}}{(2n)!} C_{2n} \quad (2.38)$$

and

$$2kR_i + \phi_B^i(k) = \sum_{n=0}^{\infty} \frac{(-1)^n (2k)^{2n+1}}{(2n+1)!} C_{2n+1}. \quad (2.39)$$

By expanding the modified probability distribution in terms of cumulants rather

than a power series, convergence is more quickly achieved, requiring only a limited number of terms. Another general approach to the disorder problem has been used by Hayes and Boyce [39]. They assume a particular parameterized form for $P_B^i(r_B)$ and vary the parameters to obtain the best computer fit to the Fourier transform in r -space.

For many materials there can be structural disorder as well as thermal disorder. However XAFS has a limited ability to resolve near-neighbor distances. If the difference in the distances is small enough that their transform peaks are not separable, they are considered to be in the same coordination shell. If this structural disorder is small enough it can be modeled well with the Gaussian Debye-Waller factor. For some region between the two extremes, small disorder and separable shells, it is necessary to consider non-Gaussian disorder. This can arise from structural disorder, anharmonic thermal vibrations, and even from large harmonic thermal vibrations due to the asymmetric $\frac{1}{R_j^2}$ weighting in XAFS.

2.6 Many Body Effects

There are two primary classes of many body effects. The first is the relaxation of the "passive" electrons in the excited atom after the core hole is created. The details of this are often included in the XAFS equation as a constant amplitude reduction factor S_0^2 . This is a good approximation at high energies where the "sudden" approximation is valid. But at low energies the amplitude reduction factor depends on k as it drops from a value of 1.0 at the absorption edge to a high-energy value between 0.7 and 0.9 for most elements.

According to the dipole sum rule, the total absorption must remain the same regardless of the multi-electron effects. There other absorption processes must

compensate for the loss in the primary channel caused by the central-atom amplitude reduction factor. For a sufficiently rapid change in the central atom potential there is a finite probability that one or more electrons will be left in an excited state or in fact ejected from the central atom potential. These are called the "shake-up" and "shake-off" effects, respectively. These multi-electron excitations can still have XAFS associated with them, but they are shifted in energy from the primary channel. Because of the many ways the two electrons may share energy, the XAFS from these processes tend to wash out. This is known as sudden approximation and predicts an S_0^2 which is independent of k . This has been found to be accurate at high excitation energies.

At low excitation energies, one reasons that the escaping photoelectron is moving slowly enough that the induced change in potential on the passive electrons is sufficiently slow that they move adiabatically from the initial state to the final state resulting in an overlap integral of one. As the photoelectron energy increases, one moves continuously from the adiabatic approximation to the sudden approximation at higher energies.

The second class of many-body effects is the effect of the finite lifetime of the excited state. This contributions from both the lifetime of the core-hole and the lifetime of the photoelectrons and can be expressed as a mean-free path, $\lambda(k)$. This term enters the XAFS equation in a different way because of its r -dependence. It expresses the condition that the excited state must last long enough for the photoelectron to travel to the scattering atom and back without losing coherence. This effect can be written as $e^{-2\frac{(r-\Delta)}{\lambda}}$ where Δ has been added phenomenologically to remove double counting of effects already included in S_0^2 . It has been shown that Δ is approximately equal to the nearest-neighbor distance.

The life-time of the excited state, τ , can also be expressed in terms of the mean-free path, $\tau = \frac{\lambda}{\nu}$, where $\nu = \frac{\hbar k}{m_e}$ is the electron velocity. The life-time can be divided further into contributions τ_h from the core-hole lifetime and τ_p from the excited photoelectron where

$$\frac{1}{\tau} = \frac{1}{\tau_p} + \frac{1}{\tau_h}. \quad (2.40)$$

To a good approximation τ_h is independent of the chemical state of the atom since the inner electrons are well shielded from the surrounding atoms. However, the photoelectron lifetime is dependent on the electronic structure of the material, and may not even be isotropic.

2.7 Multiple Scattering

The equation for $\chi(k)$ so far only considers contributions from single scattering where the outgoing photoelectron wave is scattered by one neighboring atom before returning to the central atom. However, as shown in Fig. 2.7, the outgoing photoelectron wave can be scattered by another atom C after being scattered by atom B before returning to the central atom A, rather than directly back to atom A. The total path length of the photoelectron starting from atom A and returning to atom A via backscattering from atoms B and C is given by $R_{total} = R_{AB} + R_{BC} + R_{CA}$. The total phase shift will also be the sum of the phase shifts for each atom. The multiple-scattering path will then peak in the transform at a distance of about $\frac{R_{total}}{2}$ from the central atom. Because multiple scattering paths will always peak at radial distances larger than the first shell, the analysis for the first shell can be considered free of contamination by multiple scattering. However, multiple scattering paths will often interfere with the XAFS of higher

shells. The double-scattering contribution produces a backscattered wave of the form

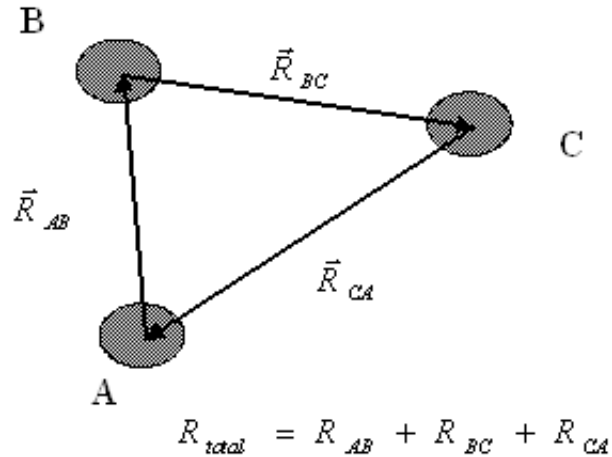


Figure 2.7. Illustration of double scattering path.

$$\frac{F(\theta_B)F(\theta_C) \exp i \left[k(2r_i + r_{BC}) + \delta^{(2)}(k) - \frac{\pi}{2} \right]}{kr_i^2 r_{BC}} \cos \gamma \quad (2.41)$$

where

$$\delta^{(2)}(k) = 2\delta_1 + \beta_B + \beta_C. \quad (2.42)$$

$F(\theta_B)$ is the amplitude of scattering from atom B through an angle θ_B and β_B is the phase introduced by that scattering [52]. The magnitude of the double scattering is about $\frac{F}{r_{BC}}$ times that of single scattering. Since the scattering amplitude is strongly peaked in the forward direction and drops off rapidly with increasing angle, the contribution from scatterings beyond 40° is minimal for typical distances

of $r_{BC} \geq 2 \text{ \AA}$. However, for $\theta \cong 0^\circ$, $F(0)$ peaks and becomes much larger and $\frac{F}{r_{BC}}$ becomes close to 1. Thus double scattering then becomes important. This forward scattering configuration is called the shadowing or focusing effect and is the only case where double scattering is important relative to single scattering in the same shell. For nearly linear arrangement of atoms, the XAFS signal is significantly enhanced by the focusing or shadowing effect of forward scattering amplitude greater than unity.

The forward multiple scattering could be used to determine atom configurations where three atoms are aligned and almost aligned [9]. It has also been used to locate interstitial hydrogen [62]. Normally the backscattering amplitude of hydrogen is very small and does not produce detectable XAFS. However if hydrogen atoms is the intervening atom B between the excited atom A and heavy atom C, the focusing effect is large enough for it to introduce a detectable enhancement of the EXAFS from atom C. In this way hydrogen atom can be located along the line from A to B.

Multiple scattering may also be significant compared with single scattering from a shell farther out. For example, for fcc structure, there are 12 neighbors in the first shell and 6 in the second shell. There will be 48 double scattering paths between the first shell atoms, roughly at about the same distance as the single scattering peak of the second shell. The sheer number will have a significant effect on the XAFS even though each individual path is very weak.

CHAPTER 3

XAFS EXPERIMENT AND APPARATUS

3.1 Synchrotron Radiation

Emission of electromagnetic radiation from charged particle is a direct consequence of the finite velocity of light. When a charged particle is either at rest or has uniform motion, the electric lines of force associated with it are also either at rest or have uniform motion together with the particle. If however the particle is accelerated, so are the field lines radially towards or away from the particle. Since these field lines always point to the location of the particle, they get distorted as the particle assumes new location between the time t and retarded time $t - \Delta t$. It is this *distortion* traveling away from the charged particle at the speed of light that is called *electromagnetic radiation*. The magnitude of these distortions is clearly proportional to the acceleration of the charged particles.

If the charged particles are accelerated in circular motion, the rate of change of transverse velocity is huge as the transverse velocity of the particle increases from zero to very large values in very short time. Thus a circular synchrotron source is most suitable for emission of high intensity radiation (Synchrotron sources, however, are exactly circular as explained below). The intensity and spectrum of the radiation depends greatly on the relativistic factor γ of the charged particle. When the speed of the charged particle approaches the speed of light, special

relativistic effects affect the spectrum as measured in the laboratory frame. The spectrum is shifted to much higher energies, the radiation pattern tilts in the forward direction "the so-called headlight effect", and time structure is introduced to name a few [45, 68]. These phenomena were first observed at a synchrotron and related "storage rings", and now dedicated electron storage rings are built to generate synchrotron radiation. These facilities use technologies developed by particle physicists as well as new techniques and devices to produce x-ray beams for experiments. The major difference from other accelerators is that synchrotron radiation (SR) facilities are designed to enhance SR, not minimize it. They use electrons or anti-electrons (positrons) instead of protons because lighter particles create much more radiation. SR has broad applications in physics, chemistry, biology, engineering, environmental science, geology, soil science, and many other fields. The x-ray sources are complex multi-user facilities providing an excellent environment for cross fertilization between fields.

Although smaller in-house XAFS facilities using conventional Brehmstrahlung sources do exist, SR provides by far the best x-ray source available at present for most applications. This is mainly because it delivers highly collimated beam with very high intensity compared to conventional sources, and the energy is tunable over a wide range. Linear, circular or elliptical polarization of the X-rays can also be realized if required. Above all, high brilliance (high flux per unit solid angle) and small source size plays an important role in making many previously impossible experiments a matter of few hours at newly developed *Third Generation* Synchrotron sources.

Having learnt that a beam of charged relativistic particles can emit synchrotron radiation with interesting properties whenever it is deflected by a magnetic or elec-

tric field, let us take a brief look at the working principle of a modern synchrotron radiation source. In this simple treatment, we consider only magnetic fields for relativistic electron beams since magnetic fields are much more feasible than electric fields to provide the necessary transverse forces to the charged particles. For application and research one would like to have continuous emission of photons which can be accomplished in an electron storage ring (a quasi-circular accelerator).

Electrons are injected into a storage ring, where they circulate for several hours at constant energy serving as the source of continuous synchrotron source. To prevent or lower particle losses due to scattering from residual gas atoms, the storage ring is maintained at ultra-high vacuum (10^{-9} Torr). In the original operations of the APS (Advanced Photon Source) electrons were injected into the ring, and then as some of the electrons were lost from the orbit, the current decayed from approximately 102 mA to approximately 85 mA over a 12-hour period. At that time, more electrons were reinjected to the maximum current. During this injection period, however, the electron energy was lowered and x-ray shutters closed prohibiting experiments. Another problem is that with the beam current change, heat loads on many optical components varied which causes thermal stress and reduced equipment reliability. To address this, the so-called "top-up" mode has been developed at the APS in which some electrons are injected every two minutes without lowering the ring energy to prevent ring current decay. This is technically very difficult; the fact that the machine physicists at the APS were able to accomplish this, and have the beam be extremely stable during each "mini-fill" is a testament to the ongoing developments at the facility.

The purpose of storage ring is not to accelerate electrons to higher energy. Electrons are injected in the linear accelerator using an electron gun and then

accelerated in the booster ring before passing it on to the storage ring. While circulating in the storage ring, electrons emit electromagnetic radiation whenever passing through a magnetic field region. The emitted x-rays are then extracted from the storage ring through long pipes called photon beam lines leading to experimental stations. To establish and sustain an electron beam in a storage ring, many technical components are required. Bending magnets are used to

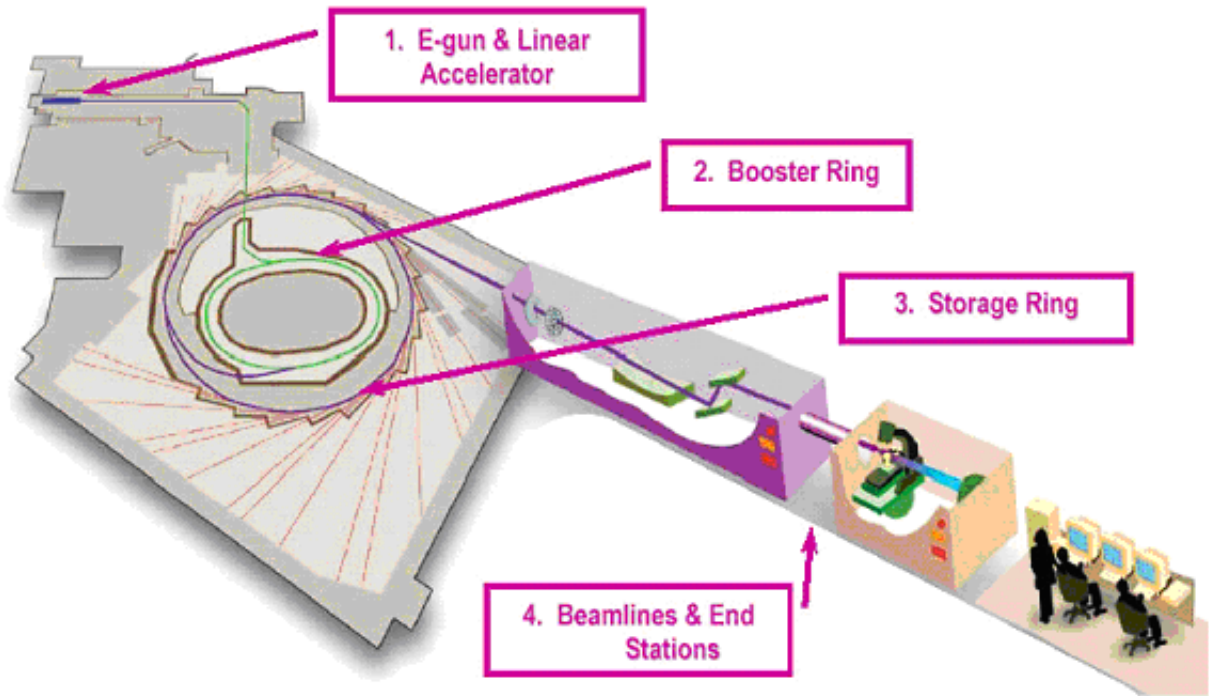


Figure 3.1. Basic structure of a Synchrotron Source [Adapted from the Canadian Light Source (CLS) website]¹

deflect the electron beam in the storage ring. The location and deflection angle

of bending magnets defines the geometry of the storage ring. Bending magnets are arranged in a closed circular ring with a series of straight sections to make space for other components. Bending magnets also serve as sources of synchrotron radiation, although with less collimation and intensity than the insertion devices described below.

Quadrupole magnets are placed in the straight sections between bending magnets, and act like glass lenses in light optics by providing a restoring or focusing force to particles which deviate from the ideal orbit. Further, sextupole magnets are used to correct for the chromatic aberrations caused by focusing errors on electrons of slightly different energies.

To maintain constant energy of the circulating electrons for several hours in storage rings, radio-frequency (RF) cavities are installed along the orbit generating an accelerating electric field synchronized to the arrival of electrons. The acceleration exactly compensates for the energy loss to radiation [57, 68]. The electric fields oscillate at frequencies of the order of 500 MHz and proper acceleration occurs only when electrons pass through the cavity at a specific time which is the reason for the bunched character of the circulating electron beam. The circulating beam is composed of one or more electron clusters, or "bunches", where the distance between bunches is an integer multiple of the RF-wavelength. For the same reason, the circumference of the storage ring must be an integer multiple of the RF-wavelength.

As mentioned earlier, electrons are injected into the storage ring at relativistic speeds. To achieve this, a small linear accelerator and booster is used which accelerates the electrons from the low linear accelerator energy to the operating energy of the storage ring. To reach high beam intensities in the storage ring

many booster pulses are injected.

So far, I gave a qualitative picture of the components used in a traditional synchrotron radiation source. These are characteristic of a second generation synchrotron source. Before proceeding further to the description of newly developed *insertion devices*, lets us understand some basic characteristics of the beam coming from storage ring. Important properties of synchrotron radiation are: 1) Tunability 2) High Flux 3) Collimation 4) Polarization and 5) Time structure.

As it has been pointed out earlier in the text, unlike fixed target sources energy can be tuned over a broad range at a synchrotron source. At APS, most of the beamlines provide an energy range of 4 keV to 40 keV [8]. There are some beamlines which also provide lower energies in the soft x-ray regime, and a number can provide x-rays near 100 keV.

The power radiated in kilowatts for a stored beam of 1 A is derived from Larmor's expression to be

$$S = 88.5 \frac{E^4}{R} = 26.5 E^3 B \quad (3.1)$$

where B is the magnetic field in Tesla, R is in metres and E in GeV [45, 68]. This expression is valid for a single-pole magnet, which can easily be extended for the case of multi-pole magnets. The common figures of merit of synchrotron sources are: (1) the **flux**, which is the number of photons emitted per second per horizontal milliradian into 0.1% bandwidth; (2) the **brightness**, which is flux per vertical milliradian; and (3) the **brilliance**, which is the brightness per unit electron beam area. Comparison between the brilliance of different synchrotron sources (and fixed target sources) are shown in Fig. 3.2.

The emission of electromagnetic radiation originating from the deflection of a

relativistic particle is highly collimated in the laboratory frame of reference. In the vertical, non-deflecting plane, the emission cone angle is of the order of $\frac{1}{\gamma}$. At APS, the value of γ is 13699. Hence the cone angle ($\frac{1}{\gamma}$) is about 73 mrad.

An important parameter is the characteristic energy E_c (also called the critical energy) defined as about one third of the cut-off energy [55]. The spectral distribution of the emitted radiation is given as

$$I(E) \approx \frac{E^{\frac{1}{2}}}{E_c} e^{-\frac{2E}{E_c}} \text{ for } E \gg E_c \text{ and } I(E) \approx E^{\frac{1}{3}} \text{ for } E \ll E_c. \quad (3.2)$$

The beam is also highly collimated with an angular spread

$$\Delta\theta \cong \frac{1}{\gamma} \left(\frac{E_c}{3E} \right)^{\frac{1}{2}} \text{ for } E > E_c \text{ and } \Delta\theta = \frac{1}{\gamma} \left(\frac{E_c}{E} \right)^{\frac{1}{3}} \text{ for } E < E_c \text{ [45, 68]}. \quad (3.3)$$

Another characteristic of the synchrotron radiation is its strong polarization, very close to 100%, in the orbital plane. As the observation angle moves out of the orbital plane the radiation becomes elliptically polarized. An interesting aspect of the polarization is the fact that the components of the radiation always have a phase difference of 90° . Thus the axes of the polarization ellipsoid are always parallel and perpendicular to the orbit plane.

Synchrotron radiation emitted from bending magnets is not necessarily optimized for all experiments. In order to provide the desired radiation characteristics (high flux, high brilliance, small beam size etc) *insertion devices* are placed in the magnet free sections along the orbit. These comprise an array of fixed magnets of alternating N/S polarity.

The alternating magnetic field in the vertical direction imparts an oscillating force in the horizontal plane. The electron oscillates back and forth, causing it

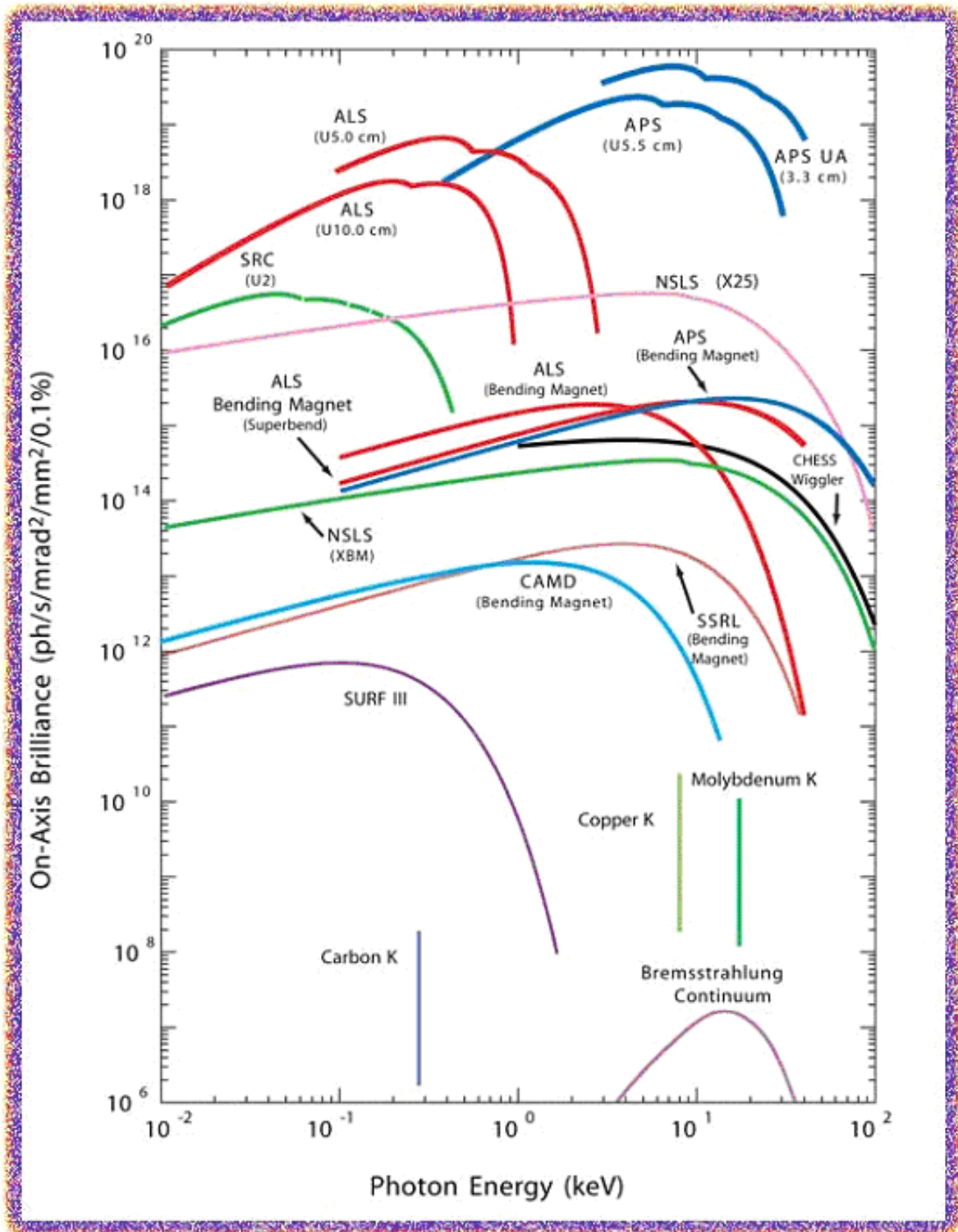


Figure 3.2. Comparison between the brilliance of different synchrotron sources. [Adapted from APS website]

to radiate. Relativistic effects shift the spectrum to high energies. Wigglers and undulators are the two commonly used insertion devices. Wiggler spectra are similar to bending magnets, except they have higher flux and generally a spectrum shifted to higher x-ray energies. In undulators, the electron deflection is small, and the x-rays emitted at the poles interfere with each other, causing the radiated power to be concentrated at specific x-ray energies, and to produce a beam with small divergence. All the XAFS experiments described in this dissertation were conducted at the Advanced Photon Source, Argonne National Laboratory (USA). Most of the experiments were performed at the undulator beamline of the MRCAT (Materials Research Collaborative Access Team) [93], 10-ID at the APS as a CAT member while some preliminary measurements were performed at the bending magnet and undulator beamlines of the PNC-CAT (Pacific Northwest Consortium) as an general user. Difference between undulator and wiggler and their characteristic properties will be discussed in more details in the following section.

Owing to the relatively weak field, the emission angle is small and the radiation cones emitted at each bend in the trajectory overlap, giving rise to a constructive or destructive interference. The situation can be considered somewhat similar to the interference of light by a system of grids. Constructive interference results in one or more spectrally narrow peaks (a fundamental and harmonics) in a beam that is highly collimated in both the horizontal and vertical directions; that is, the beam has a high spectral brightness. Tuning the wavelengths of the harmonics for constructive interference takes place by mechanically adjusting the vertical spacing between the pole tips. The energy of the n^{th} harmonic of the undulator is given by

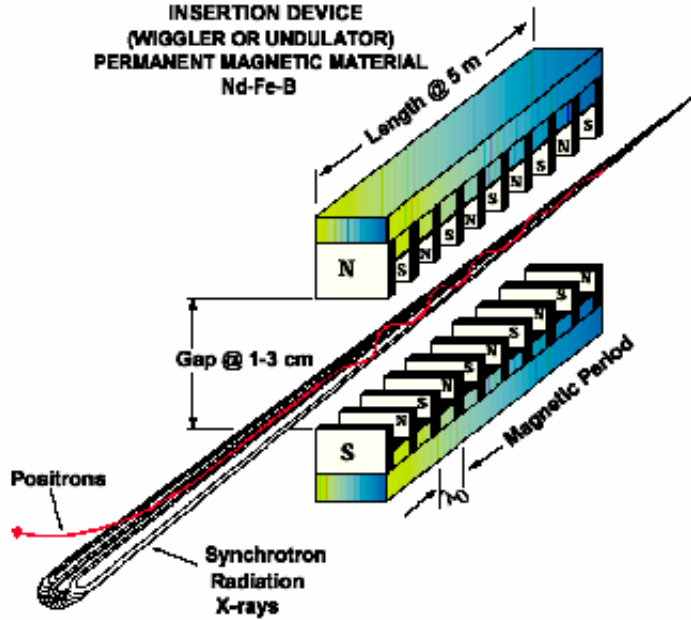


Figure 3.3. Schematic diagram of an insertion device. [Adapted from APS website]

$$E_n = \frac{0.95(E[\text{GeV}])^2 n}{\lambda_u[\text{cm}] \left(1 + \frac{K_{eff}^2}{2} + \gamma^2 \theta^2\right)} \quad n = 1, 2, 3, \dots \quad (3.4)$$

and $K_{eff} = \frac{eB_{eff}\lambda_u}{2\pi mc}$ where B_{eff} is the maximum effective magnetic field and λ_u is the ID period [58, 68]. Properties of an undulator are guided by the value of K_{eff} . If $K_{eff} \ll 1$, first harmonic or the fundamental harmonic is the only harmonic emitted. As K_{eff} increases, the oscillatory motion of the particle in undulator deviates from a pure sinusoidal oscillation. For $K_{eff} > 1$, the transverse motion becomes relativistic, causing a deformation of the sinusoidal motion and the creation of higher harmonics. These harmonics appear at integral multiples of the fundamental radiation energy. Only odd harmonics are emitted along the axis

of the undulator and even harmonics are emitted into an angle $\frac{1}{\gamma}$ with respect to the undulator axis and should ideally have zero intensity along the axis. In practice, however, weak even harmonics along the axis are also found. As the undulator strength is further increased more and more harmonics appear. Since each of them have a finite width due to finite number of undulator periods, all the harmonics finally merge as the upper limit of this situation. This merging of undulator harmonics produces the well known broad spectrum of the wiggler.

For an undulator of the APS, $\lambda_u = 3.3$ cm, number of periods = 72 and $B_{eff} = 0.835$ T at a gap of 10.5 mm [8]. By varying the magnetic gap distance, the first harmonic energy may be tuned up from 4.5 keV to 13.5 keV, which corresponds to a change in K_{eff} from 2.1 to 0.3 V. Brilliance as high as on the order of 10^{18} is generally obtained from the first harmonic, while the third harmonic extends from 10.5 keV to 40 keV [58].

The position of undulator peaks can be tuned by adjusting the undulator gap, which varies the strength of the magnetic field felt by the electrons. Decreasing the gap increases the field, causing a larger deflection, and slightly slowing down the electron's average speed through the undulator. This shifts the spectrum to lower energy.

3.2 X-ray Beamlines

Beamlines prepare the beam for experiments, and protect the users against radiation exposure. They combine x-ray optics, detector systems, computer interface electronics, and computer hardware and software. Typical functions of a beamline include:

- Radiation shielding and safety interlocks

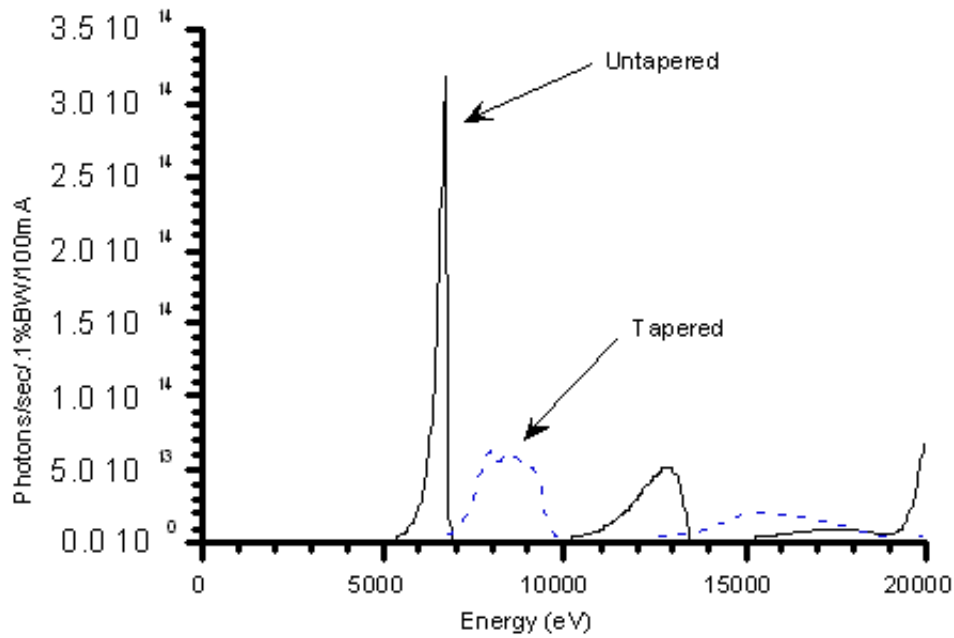


Figure 3.4. Schematic diagram showing the difference between tapered and untapered undulator beam profile. [Adapted from APS website]

- Photon shutters before and after monochromator
- Select specific energies/wavelengths ($E = \frac{hc}{\lambda}$) using *monochromators*
- Focus the beams with *x-ray mirrors*, *bent crystals* or *Fresnel zone plates*
- Define the beams with *x-ray slits*
- *Detectors* measure beam intensity as function of energy
- Electronics amplify signal and interface to the computers
- Computer control and data acquisition system orchestrates motion

of the monochromator and other optics, and reads detectors, and helps remote control alignment of samples

- Comprises other specialized instrumentation as needed.

Details of the beamline optics and other components are described below. This discussion mainly focuses but is not limited to the set up at MRCAT.

3.2.1 Monochromator

For XAFS experiments, the undulator parameters are optimized for maximum and uniform intensity over the desired energy range. Although the undulator spectrum is relatively concentrated in a few energy bands, this is not high-enough energy resolution for our experiments and the beam from the undulator needs to be separated into a single energy or wavelength. This is done by a Bragg crystal monochromator which is based on simple x-ray diffraction: certain lattice plane will diffract x-rays of only a particular energy (or its harmonics) at a particular angle of incidence. The condition is often formulated as "Bragg's Law":

$$2d \sin \theta = n\lambda \tag{3.5}$$

where d is the lattice spacing for the particular plane, θ is the angle of incidence and λ is the wavelength of the diffracted x-ray. The desired wavelength of x-ray is obtained by tuning θ .

A widely adopted monochromator configuration consists of a pair of parallel crystals, usually Si or Ge, which are cut with faces parallel to the (111), (220), or (311) planes, as shown in Fig. 3.5. The first crystal diffracts x-rays with a certain wavelength towards the second crystal. The second crystal further reflects the

x-ray beam into the experimental station. Because of the parallel configuration, the exiting x-ray beam is parallel to the incident one but with a vertical offset of $2l \sin \theta$, where l is the crystal separation.

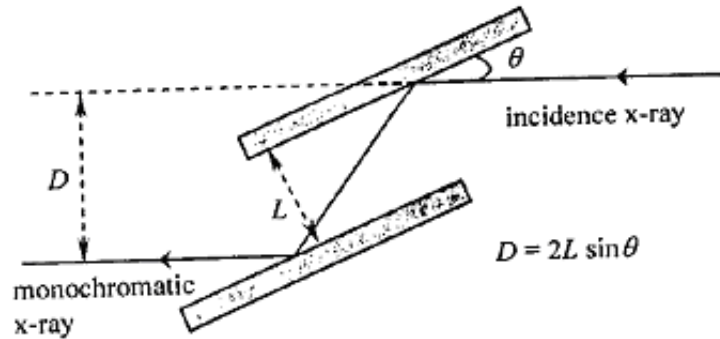


Figure 3.5. A typical monochromator configuration with parallel plates.
[Adapted from APS website]

For different energies, this offset value changes by virtue of change in θ and therefore translation of the sample table height is generally required to ensure that the sample intercepts the same portion of the beam along the whole range of energy scan. In the case of MRCAT, however, the offset is small enough that the shift of the beam is small compared with the beam size and mid-scan translation is not usually necessary.

Another complication is that the two crystals do not mechanically track at exactly the same angle, and some "fine-tuning" of the angle of the second crystal is necessary. This is accomplished by applying small amplitude periodic voltage to a piezoelectric actuator which rocks the second crystal over a portion of rock-

ing curve and translates it horizontally by highly step-reduced motors, and all synchronized by a computer. The reflectivity of a single crystal as a function of incident angle is called a rocking curve. For a perfect crystal the rocking curve has a sharp peak near the Bragg angle θ_B . The width of the rocking curve is given by $\Delta\theta_B \sim \frac{1}{\sin^2\theta_B}$ or $\frac{1}{E^2}$. Using lock-in techniques, a particular relative angle on the rocking curve may be chosen. There are various other monochromator configurations possible, depending on the experiments they are designed for [57].

Heat load issues are important consideration for the choice and design of a monochromator at an undulator beamline. The high thermal and radiation loads at the synchrotron sources call for rugged monochromator crystals. The crystal material should have long lifetime and good thermal conductivity to minimize thermal gradients under the high thermal and radiation loads. It is for this reason that EXAFS beamlines have almost exclusively employed Si and Ge crystals. Si (111) crystals are used for the MRCAT beamline. At a temperature of 125 K, Si has zero coefficient of expansion and therefore gives very stable output energy [50]. The first crystal is kept cooled to this temperature using liquid nitrogen at MRCAT.

One fundamental requirement for the monochromator is rapid tunability since an absorption measurement at a single energy typically requires less than a second. The energy resolution also should be better than or comparable to the lifetime broadening of the absorption edges of interest, which implies

$$\frac{\Delta E}{E} = 1 - 2 \times 10^{-4} \quad \text{for } E = 4 - 30\text{keV}. \quad (3.6)$$

From Bragg's equation,

$$\frac{\Delta E}{E} = \Delta\theta \cot \theta, \quad (3.7)$$

$\Delta\theta$ is determined by source size Δd_1 , the slit size Δd_2 and source-to-monochromator distance L . Higher index planes give better energy resolution. But the intensity is usually lower for higher index planes at lower energies.

One particular problem encountered with a double-crystal monochromator is the possible presence of so-called "glitches". Although the major reflectivity is generally from the lattice planes parallel to the surface, occasionally reflections from oblique lattice planes are allowed, causing a decrease in intensity in the main beam. (Occasionally, these spurious reflections can make it to detectors and the sample.) These effects are minimized by insuring that the detectors are as linear as possible, and can be also eliminated during data processing.

Due to the non-ideal nature of the crystals of the monochromator, often one has to optimize several monochromator parameters, for example, the horizontal angle between them or the vertical distance between them, in order to intercept the beam on the best part of the crystal. The second crystal is 20 cm long and provides an energy range of 4.8 keV to 30 keV from the fundamental reflection and delivers more than 10^{13} photons/second to the experimental hutch.

However, a feedback system tries to compensate for the intensity loss due to crystal imperfections to a certain extent. There is a feedback amplifier prior to the monochromator that monitors the incident beam intensity at each energy point. Any drop in intensity over the measurement time is fed back to the lock-in-amplifier (the second crystal is connected via a piezo to the lock-in-amplifier) which sends out a corresponding feedback or correction signal to the piezo. The piezo is thus always locked into the maximum intensity beam position.

3.2.2 Harmonic Rejection

As mentioned earlier, the beam from the monochromator contains higher harmonics as well as the desired fundamental. Harmonic contamination seriously distorts the XAFS amplitude if the higher energies are not removed. There are two common approaches to harmonic rejection: One technique is deliberately de-tune the two monochromator crystals. Because the rocking curve for harmonics is narrower than for the fundamental, and therefore higher harmonics are greatly suppressed. For a Si (111) crystal at the Cu K edge, the intensity of (333) harmonics is reduced by a factor of 10^3 at the expense of 30% fundamental intensity. The other common approach is to use a "Harmonic Rejection Mirror" downstream of the monochromator. The refractive index in the x-ray energy range is slightly less than 1. The refractive index of a material can be written as:

$$n = 1 - \delta - i\beta \quad (3.8)$$

where δ is proportional to the electron density of the material and β is proportional to the linear absorption coefficient. The negative part of the refractive index accounts for the absorption in the material. Far from an absorption edge, the absorption is small and can be neglected to first order when we consider reflection from a mirror. The refractive index in the x-ray regime being less than one allows for total external reflection for an angle of incidence lower than the so-called "critical angle". Ignoring absorption, the critical angle of reflection for a particular energy E is calculated to be

$$\theta_c \approx \sqrt{\rho}(\lambda). \quad (3.9)$$

where ρ is the electronic density of the material. Therefore, for a particular energy E , the x-ray beam will be totally reflected only at an angle of incidence lower than θ_c and the reflected intensity will suffer a huge drop at higher angles. The sharpness of the drop is determined by several parameters like the surface roughness. Since θ_c can be calculated to be inversely proportional to E , the critical angle of the first harmonic is much higher than that of the higher harmonics. Thus by aligning the mirror at an angle of incidence that is higher than θ_c for the higher harmonic but lower than the θ_c of the fundamental, one can totally reflect the fundamental off the mirror while the higher harmonics will be mostly absorbed.

Usually, there is more than one harmonic rejection mirror in the beamline made of different materials (or a single mirror has different "stripes" deposited on it) with well-separated absorption edges. One of the mirrors is then selected depending on the energy range in question. For example, the ID-10 beamline at APS has a mirror coated with deposited stripes of Pt (L_3 edge = 11.564 keV) and Rh (23.2 keV). For measurements up to 18 keV, the Rh portion of the mirror is used in order to avoid absorption by Pt. On the other hand, for measurements at higher edges, say, 18 keV and above, a Pt stripe is used.

Further optical elements for an XAFS experiment include of the incident intensity monitor in front of the sample, the sample holder (which may be a temperature stage, ultra-high vacuum chamber, etc., depending on the experiment) and the post-sample detectors to measure transmitted or fluorescence signals from the sample. The following section will focus on the various x-ray detectors used for the present XAFS studies.

3.2.3 X-Ray Detectors

Count rate, energy resolution, linearity, and noise are some of the important considerations while deciding the detector to be used for a particular experiment. Two important modes of detector operation are current mode and pulse mode. Current mode operations are used with many detectors when event rates are very high. MSV mode is useful in enhancing the relative response to large amplitude events and finds widespread application in reactor instrumentation. Most applications, however, are better served by preserving information on amplitude and timing of individual events that only pulse mode can provide. The detectors used for the present XAFS measurements were the ionization chamber (current mode) and the solid state detector (pulse mode). Hence only these two detector operation will be discussed in details.

3.2.3.1 Ionization Chambers

The most widely used x-ray detector for XAFS is the ionization chamber because of its higher photon count. These detectors consist of two parallel conducting plates with a potential difference between them. The space between the plates is filled with an inert gas. A parallel plate ion chamber is shown in Fig. 3.6. Usually the incident beam intensity monitor ion chamber in front of the sample has to be optimized for absorption of around 5% (10% for older low flux sources) of the incident flux so that the major fraction of the beam falls on the sample, while the post sample detector should absorb 80 – 90% of the transmitted beam or the fluorescence photons from the the sample for good counting statistics. The gas is selected depending on the energy of the x-rays in question. At higher energy ranges, heavier gas like Ar is a better choice as it has higher absorption coeffi-

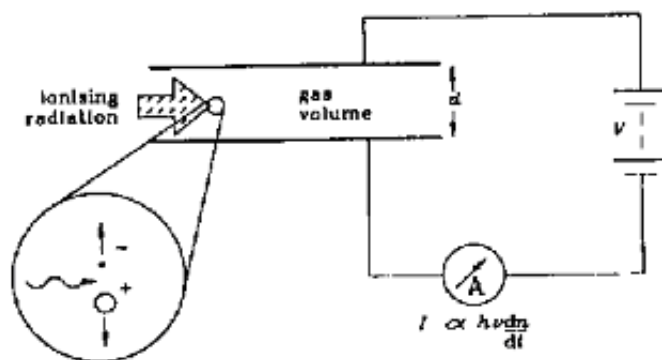


Figure 3.6. A gas ionization chamber.

cients. At lower edges, I_0 chamber usually contains lighter gases like He and N_2 . The post-sample detectors are usually filled with heavier gases like N_2 , Ar, or Kr. As the x-ray photons pass between the plates, some are absorbed and ionize the chamber fill-gas. About one electron-ion pair is created for every 30 eV of the incident x-ray energy. The electrons and ions are separated by the applied field. The total current from the detector is measured with precision current amplifiers. For the current mode, all energy resolution is lost, although the background is expected to be very low in a well-designed experiment, resulting in a minimal degradation in the signal-to-noise ratio.

If the beam is too intense or the applied potential is too low, the ion-electrons are not separated in time to avoid recombination before reaching the collector plates, thus reducing the current output and resulting in a non-linear response. In synchrotron beamlines, the beam intensity is usually large and so the ionization chambers are designed with long collector plates (15 – 30 cm) that are separated by only 1 cm. This allows for a larger volume for absorption and ionization which minimizes recombination. The applied potential is optimized around 1500

V to be in the plateau region of the counter. If the potential is too high, the detector can enter its non-proportional region and behave like a Geiger counter with the primary ions and electrons ionizing further more atoms, resulting in an "avalanche" of total ionization as they travel to the collector plates.

Other than the linearity factor in deciding the dimensions and voltage of the ion chamber, the noise output from the latter also needs to be considered. Noise in ion chambers mainly comes from the electronics and microphonics. Microphonics are vibrations in the collecting plates owing to ambient vibrations. This changes the capacitance of the chamber and gives rise to a current. Microphonics are easily eliminated by employing rigid construction techniques. With commercially-available preamplifiers and current-to-voltage converters, it is easy to obtain a current noise of 10^{-14} A. This corresponds to the signal produced by 200 photons per second, which corresponds to the statistical noise produced by an incident flux of 4×10^4 x-ray photons per second. When the incident flux is significantly greater, the amplifier noise can be ignored. Again at this high signal level, the detector can behave non-linearly.

The ionization chambers for the fluorescence detection are a little different because the fluorescence x-rays are emitted isotropically and are of much lower flux. These detectors are designed to subtend a large solid angle with respect to the sample and consequently, to collect as many fluorescence photons as possible. To this end, the x-rays penetrate through the x-ray-transparent collection plates instead of moving parallel to the plates as in the earlier-described detectors. In this design, a number of internal collector plates at alternate potentials enable a reasonable path length through the detector while keeping the plate separation small to minimize the chance of recombination; a typical fluorescence detector is

shown in Fig. 3.7. The voltage applied in fluorescence chambers is much lower (around 50–300 V) and the plate separation is determined by the estimated range over which an electron could be collected with the available voltage in a reasonable time. The MRCAT beamline has 3-grid and 5-grid fluorescence chambers with a close-coupled and shielded, variable gain, electrometer-type operational amplifier built in. The output of this pre-amplifier can be directly connected to a voltage-to-frequency converter. In most of the XAFS experiments described in the text, 3-grid "Lytle" detector filled with Ar or Kr was used for fluorescence measurements.

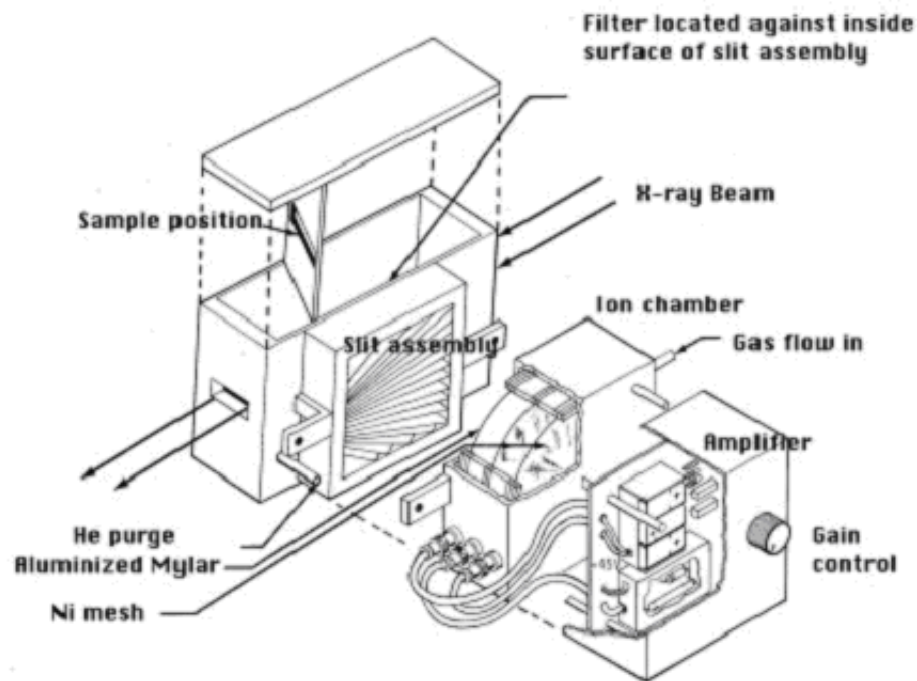


Figure 3.7. Stern-Heald type Lytle detector used for fluorescence mode XAFS. [Adapted from Lytle detector website]

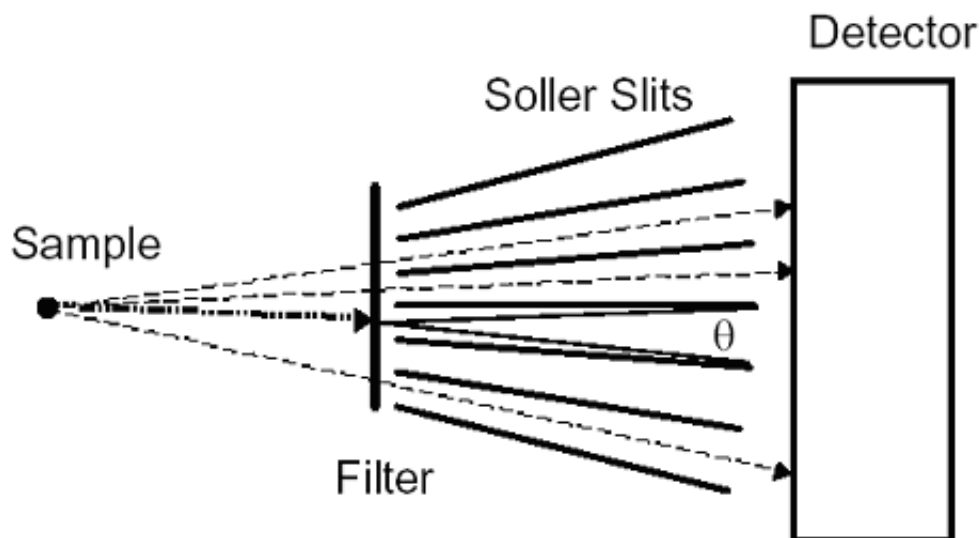


Figure 3.8. Schematic diagram of the function the Soller Slits.[Adapted from Steve Heald's XAFS slides, with permission]

3.2.3.2 Solid-State Detectors (SSD)

The working principal of the solid-state detector also called semiconductor detectors lies in the creation of electron-hole pairs across band-gap under photon-excitation. Both electrons in the conduction band and holes in the valence band may move under the application of an electric field and the charges may be separated similarly to an ion chamber. The small magnitude of the energy required for the electron-hole generation for semiconductors, approximately 3 eV in Si as opposed to approximately 30 eV for gases, is the key to its success in providing the best resolution compared to these other detectors. Therefore, for the same incident photon energy, semiconductors produce an order of magnitude higher

number of charge carriers. For synchrotron beamlines, solid-state detectors using Ge are preferred because of the latter's lower band-gap and higher density and stopping power. The resolution in the hard x-ray regime is about 200 eV. They operate with liquid-nitrogen cooling to minimize thermal creation of charge carriers. These detectors are limited to about 4×10^4 counts per second of which the majority may be thrown as unwanted signal. So even though the detector may be measuring 4×10^4 photons per second, as few as one hundred may be in the desired energy range. The total count rate can be improved by using an array of SSDs, with common configurations having 9, 13, 16, 19, or more elements. Another possible complication associated with solid state detectors are the fluorescence peaks of Ge and Si at 9 keV and 2 keV, respectively.

In all pulse detector systems, there is a minimum amount of time that must separate two events in order to be recorded as separate pulses. This limiting time could be set by the processes in the detector itself or it may arise from the associated electronics. This minimum time separation is usually called the *dead time* of counting systems. Two models of dead time behavior of counting systems have come in common usage: *paralyzable* and *non paralyzable* response [51]. Both these models predict the same first order losses and differ only when true event rates are high. They are in some sense two extremes of idealized system behavior and real counting systems will often display a behavior that is intermediate between these two behaviors. Figure 3.9 shows the dead time response curve of a solid state detector with different dead times. A simple model that is often implemented for dead time correction is $OCR=ICR*\exp(-ICR*DT)$, where OCR and ICR are the output and input count rates, respectively.

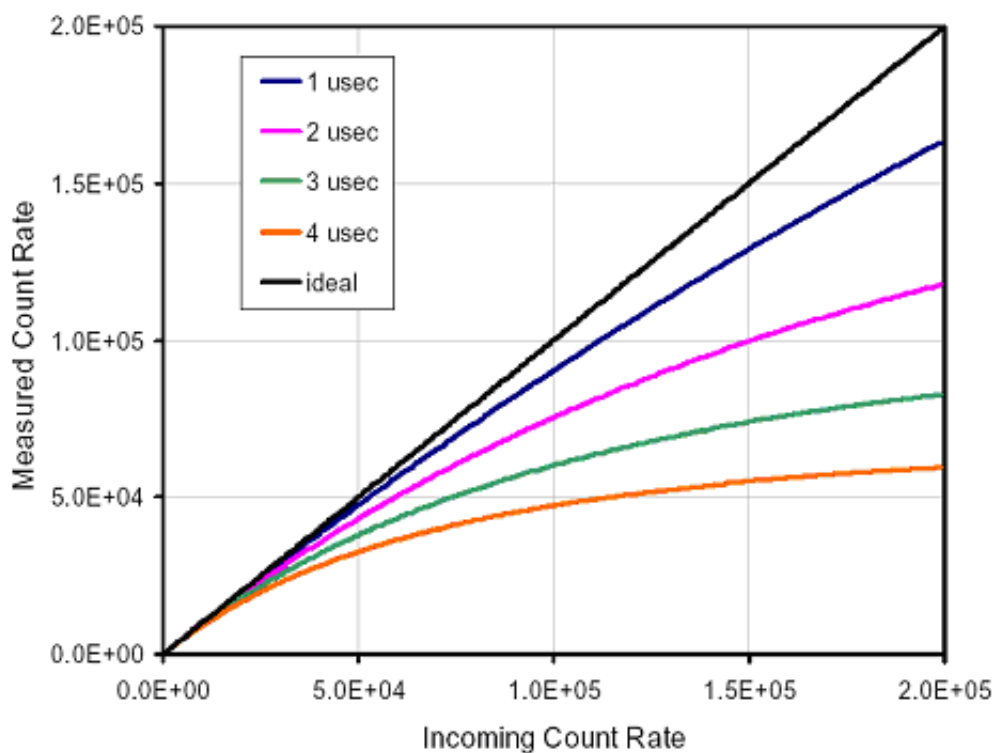


Figure 3.9. Dead Time correction in solid state detector.[Adapted from Steve Heald's XAFS slides, with permission]

3.2.3.3 Bent Crystal Laue Analyzer

Despite the use of dead time corrections, there is always the concern that using a solid state detector could possibly lead to erroneous XAFS analysis resulting in smaller coordination number. Recently there have been several attempts to combine the benefits of an energy selective detector without significant reduction in count rate. *Bent Crystal Laue Analyzer* is such an attempt. BCLA is a device that selects a particular wavelength (or energy) of x-ray photons that radiate from a point-like source, and rejects photons of other energies. Its primary use is to select specific x-ray fluorescence lines emitted from a sample in x-ray fluorescence

experiments. The main benefit of these analyzers compared to conventional solid state detectors is that they reject most of the undesired photons (e.g. scattering and fluorescence from other elements in the sample) before they are detected. In contrast, conventional solid state detectors detect photons of all energies, which saturate the detector in situations where there is a small signal in a large amount of background. The energy resolutions of the BCLAs are also superior to solid state detectors. However this detector has several downsides too. Each analyzer has specific design energy, and they are useful only over a range of 10% variation in the energy. In addition, it works best only when for point sources which is often not the case for aqueous samples.

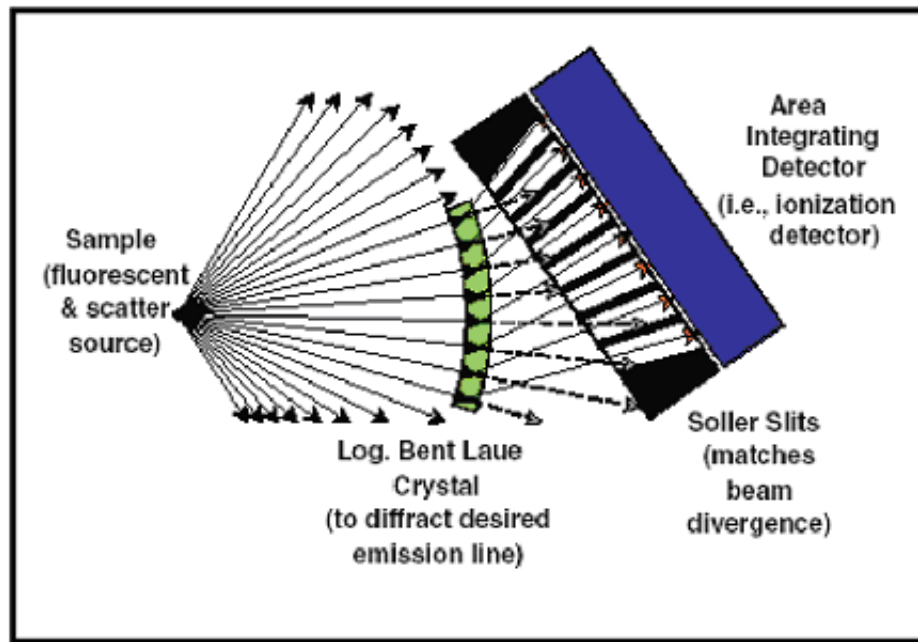


Figure 3.10. Log Spiral Bent Crystal Laue Analyzer. [Adapted from BCLA Manual, with permission]

3.3 Experimental XAFS Detection

The goal of the XAFS experiments is the precise measurement of the absorption coefficient as a function of energy. Since the XAFS is a small part of the total absorption, typically a measurement of absorption coefficient of relative precision better than 10^{-3} is required. Errors in this measurement can degrade or even destroy the XAFS signal. Two main modes of XAFS detection are *Transmission* and *Fluorescence*. Electron yield and optical luminescence etc. are other modes of XAFS detection. While the latter is usually for special cases, the former is a common tool for low energy and surface physics. However, these two modes will not be discussed in details here as they have not been used in for the experimental work presented in this thesis.

Transmission measurements are more straight forward but does require some care to make sure that the beam is well aligned on the sample and the sample is homogeneous. Achieving a noise level of 10^{-3} for fluorescence measurements is certainly possible but can be challenging especially for very low concentration samples. As a rule of thumb, concentrated thin samples are measured in transmission and dilute samples are measured in fluorescence. Since most of the samples of environmental relevance are dilute, most of the samples measured for this study (except of the standard compounds) were measured in fluorescence mode. These two modes of measurements will be discussed in more details in the following section.

3.3.1 Transmission XAFS

In a transmission experiment, the incident and transmitted x-ray intensities are measured with ion chambers. The absorption coefficient is then obtained from

the equation:

$$\mu = \frac{1}{x} \ln \left(\frac{I_0}{I_t} \right) \quad (3.10)$$

where I_0 is the incident intensity and I_t is the transmitted intensity. The phenomenon is shown in Fig. 3.11*b*. The thickness of the sample is usually between two and three absorption lengths. A homogeneous sample with uniform thickness is desired. Small pinholes in the sample or variation in thickness will have a similar effect as a large harmonic content in the beam. Distortions like this are known as "thickness effects". Suppose, a fraction $P(x)$ of the sample area has thickness x , then the absorption equation becomes more generally

$$\exp(-\mu x)_{eff} = \int P(x) \exp(-\mu x) dx \quad (3.11)$$

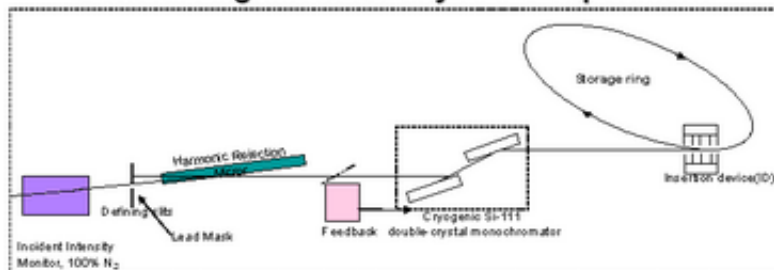
The greater the variation in sample thickness and the higher the absorption coefficient gets, the more the effective absorption coefficient is suppressed. The EXAFS wiggles are squashed down even though the edge step has been normalized and convey the wrong information regarding structure coordination, Debye Waller factor, etc.

3.3.2 Fluorescence EXAFS

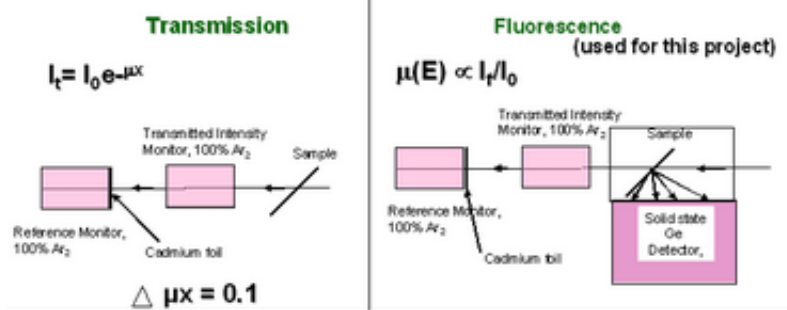
Often transmission mode does not work out the best, especially where the EXAFS signal is only a small fraction of the total absorption. Isolation of the EXAFS from the background in transmission then requires the subtraction of two nearly equal signals, a process requiring very accurate data. In these cases, it is desirable to rather measure processes that are proportional to absorption that is fluorescence and emission of Auger electrons. A fluorescence photon is created

Performing XAFS Experiments

General Alignment for any XAFS experiment



Experiment Specific Alignment



Sample Holder for this Project

- > **Transmission works better for thin concentrated samples.**
- > **Fluorescence works better for dilute samples.**

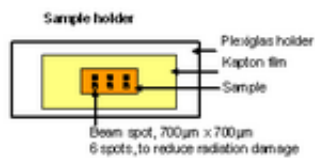


Figure 3.11. General and experiment specific alignment for a typical XAFS experiment.

when an electron from a higher shell jumps to a vacant lower shell, following photo ejection of the electron in the latter shell. An Auger electron is ejected when such a fluorescence photon further ejects another electron. Auger emission and fluorescence are competing processes. Their relative strengths depend on the atomic number of the absorber. For lighter elements, Auger emission is more probable than fluorescence and the reverse holds true for heavier elements. Again, for the same absorbing element, fluorescence is more likely for K -shell holes than L -shell holes. A typical fluorescence experimental setup is shown in Fig. 3.11c. The energy of the fluorescence photons is evidently lower than the corresponding exciting energy edge. The background radiation accompanying the fluorescence signal consists of elastically and Compton scattered radiation and photoelectron-generated bremsstrahlung. The cross-section for scattering, including both elastic and non-coherent Compton Scattering is given by

$$d\sigma = \frac{3\sigma_T}{8\pi} \sin^2 \psi \quad (3.12)$$

where ψ is the angle between polarization direction and the direction of observation, $\sigma_T = \frac{8\pi}{3} \left(\frac{e^2}{mc^2}\right)^2$ [45]. For atoms, the angular distribution of the coherent radiation is modified by interference effects, and is expressed by the atomic form factor. From the equation, it is evident that the scattering is least when the detector is at angle of 45° with respect to the polarization direction. To reduce the effect of elastic scattering, it is therefore desirable that the detector is at angle of 45° . However the usual geometry is with $\psi = 90^\circ$, the above equation is a good estimate of the total scattering cross-section with σ_T replaced by $\sigma_0 = Z\sigma_T$. Then the scattering distribution can be integrated to find the total cross-section of scattering into the detector. For a circular detector of radius R at a distance D

from the sample the result for the horizontal and vertical polarization components is given by

$$\sigma_h = \frac{\sigma_0}{4}(\cos^3 \varphi - 3 \cos \varphi + 2) \quad (3.13)$$

and

$$\sigma_v = \frac{\sigma_0}{8}(4 - 3 \cos \varphi - \cos^3 \varphi), \quad \tan \varphi = \frac{R}{D}. \quad (3.14)$$

The sample bremsstrahlung has been estimated to be

$$N(E) = 2.5 \times 10^{-6} Z I_0 \sigma_t \frac{E - E_x}{E_x} \quad (3.15)$$

where Z is the atomic number of matrix, I_0 the incident flux, σ the photoelectron cross-section at excitation energy E , t is the sample thickness and E_x is the observation energy. The total background is obtained by integrating over the energies accepted by the detector.

To discriminate the background from the fluorescent radiation requires energy resolution. Solid-state detectors offer a solution but they are limited by counting rate. In addition, they are slow, inherently nonlinear at high count rates, expensive, and more complicated to deal with. A reasonable solution to all this is the use of an x-ray filter.

As mentioned earlier, the fluorescent photons have energy lower than the background photons. By choosing a filter material that has an absorption edge that is higher than that of the fluorescence photons but lower than the background, the latter is preferentially absorbed. The situation is shown in Fig. 3.12.

For K edge absorption experiments, a filter material with atomic number $Z - 1$ works best where Z is the atomic number of the absorbing atom in the sample. For the L -edges, $Z - 2$ might work better. The main difficulty with filters is the

re-fluorescence of the filter. However, a suitable set of Soller slits (shown in Fig. 3.7) can be employed to suppress detection of this re-fluorescence. The Soller slit is an array of slits arranged in a geometry such that their focal point is located on the sample position. The filter is located much closer to the detector than the focal point and hence the re-fluorescence from the filter to the detector is negligible. Unfortunately, filters simultaneously attenuate the signal to a certain extent. The

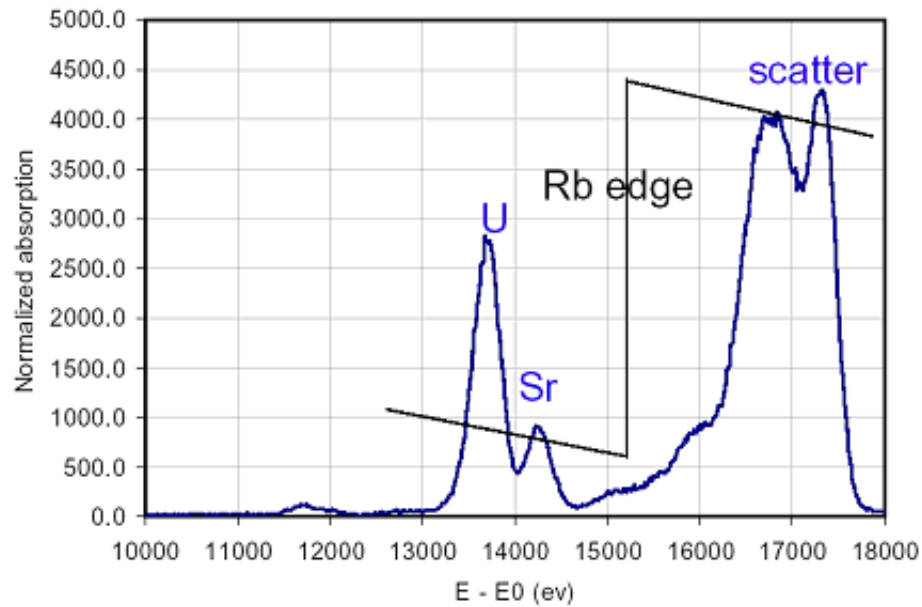


Figure 3.12. Schematic diagram showing the use of filter in fluorescence mode XAFS. [Adapted from Steve Heald's XAFS slides, with permission]

figure of merit of a filter may be assessed by defining the "Quality" Q to be $\frac{\mu_a}{\mu_b}$ where E_a is at the middle of the energy scan range and E_b is the fluorescent energy.

For pure materials of uniform thickness, $Q = 6 - 8$. But practically, it is hard to get such uniform filters and hence Q falls to $4 - 6$. The effect of the Quality factor on the signal to noise ratio can be seen from the effective count rate, given by $N_{eff} = \frac{N_s^2}{N_s + N_b}$ where N_s is the signal count and N_b is the background count rate. If a filter is placed between the sample and the detector, the background is reduced by the filter by a factor of $\exp(-\mu_a x)$ while the signal is reduced by a factor of $\exp(-\mu_b x)$ where x is the thickness of the filter. The re-fluorescence is proportional to the number of photons absorbed and a fraction η makes its way to the detector. Without Soller slits, $\eta = 0.15$ and with the Soller slits, $\eta = 0.02$. Taking into account all these factors and figures, the effective count rate turns out to be

$$\frac{N_{eff}}{N_s} = (1 - \eta) \frac{e^{-\mu_b x} + \gamma}{1 + A \left(\frac{e^{-\mu_a x} + \gamma}{e^{-\mu_b x} + \gamma} \right)} \quad (3.16)$$

where $A = \frac{N_b}{N_s}$ and $\gamma = \frac{\eta}{1 - \eta}$. As can be seen, the effective count rate depends on the effective count rate before the filter, the filter thickness, the filter quality and η . The optimum combination can be derived by setting the derivative of the above equation to 0. For $\eta = 0$ - the ideal case achieved with a solid state detector - the filter thickness is given by $\ln \left[\frac{N_b}{N_s} (Q - 2) \right]$. Thus, if $Q = 3$, N_s should be equal to N_b . If $Q = 4$, N_s should be twice N_b . The best configuration can thus be worked out with filters.

There is another problem in fluorescence measurements arising from systematic error in the case of concentrated samples. As the absorption increases, the penetration depth of the photons decreases thereby sampling fewer numbers of atoms and tending to compensate for the increase in absorption. This results in

a nonlinear distortion of the data. The effective absorption then is given by

$$\mu_{eff} = \frac{\Omega}{4\pi} \varepsilon \frac{\frac{\mu_s(E)}{\sin \theta}}{\left(\frac{\mu(E)}{\sin \theta} + \frac{\mu(E_f)}{\sin \phi} \right)} \quad (3.17)$$

where Ω =solid angle subtended by the detector with respect to the sample, θ = exit angle subtended by the fluorescent beam with respect to the sample, ϕ =entrance angle subtended by the fluorescent beam with respect to the sample, $\mu(E)$ =absorption coefficient of the sample matrix at incident photon energy E , $\mu_s(E)$ absorption coefficient of the atom of interest at energy and ε is the probability for fluorescence emission. For thin samples, the proportionality to the absorption is still maintained. Even for dilute samples, the same kind of deviation is produced if the element of interested is confined in concentrated particles suspended on a dilute matrix. From the conditions for thickness effects, the role of the sample and detection geometry is evident. By attending to the requirements in the experimental configuration, the distortion can be greatly reduced.

3.4 Elimination of Noise in Experiments

In all modes of EXAFS detection technique, it is very important to eliminate noise from the data as much as possible. If the noise in the data has a frequency corresponding to a higher neighbor distance, it gives rise to a spurious peak in r -space which can overlap with the real peak and lead to incorrect fitting. Noise in EXAFS experiments has a number of sources including the unavoidable fluctuation in the number of photons counted by the detector, electronic noise and noise that arises from the sensitivity to the fluctuations of the x-ray beam. The most important of these concerns is sometimes summarized as "HALO": Harmonics,

Alignment, Linearity, and Offset [18].

3.4.1 Harmonics

As mentioned before, a certain fraction of higher harmonics is always present in the spectral content of the incident beam. In order to compensate for the incident beam intensity fluctuations, it is important that the detectors see exactly the same beam in the same way. In the I_0 detector, the incident beam consists mainly of the first harmonic and a certain fraction of higher harmonics. The I_f detector, on the other hand, sees the elastically scattered fundamental and harmonic contents with proportions different from the I_0 detector, plus inelastically scattered beam at a lower energy and of course, the fluorescence photons at a still lower energy. All these add up to give rise to a beam in I_f different than in I_0 . Thus the fluctuations in the I_f beam never cancel out the fluctuations in the I_0 beam, even if the detectors are similar. Methods described earlier are essential to eliminate higher harmonics as much as possible.

3.4.2 Alignment

Misalignment can also become a source of noise. Usually the incident beam is defined by a slit in front of the I_0 chamber. If there is anything on the way of the beam after I_0 chamber especially something non-uniform, be it a wrinkled window, then the post- I_0 detector will certainly see a different fluctuation from that in the I_0 detector and they will not cancel out.

3.4.3 Linearity

Although the incident beam is stable to better than 1% in intensity, high linearity is still essentially for the required data quality. It is required that the detectors and the electronic devices are in their plateau regime of functioning, that is, the output is independent of the voltage applied and it is proportional to the input. When operating with small signals, it is advisable to set an offset of 1 V (out of a maximum of 10 V from the current-to-voltage converters) to maximize linear of the voltage-to-frequency converters. The offset can later be subtracted out from the data to obtain the right signal.

3.4.4 Offset

Finally, it is very important to measure from time to time the "offsets" which is the signal in the different detectors when x-ray beam is off. This offset is due to the manual offset described in Section 3.4.3 plus any residual dark current from the detectors and is subtracted from the data. Fluctuations in I_0 and I_f will not cancel out if the offset is not correct. Sometimes, offsets drift and it is a good idea to check them frequently. If certain detectors are light sensitive, they should be well shielded to avoid the fluctuations of light in the experimental hutch.

3.5 Beamline Alignment

After having talked about the instrumentation and experimental methods for XAFS in some detail, I realize that it can be cumbersome and confusing process. Realizing the importance of alignment and hence better data quality in the least possible time (due to limited and time bound access to SR facilities), I have decided to put a *Practical Guide For Beamline Alignment*. Please refer to Appendix A for

this section.

CHAPTER 4

XAFS DATA ANALYSIS

4.1 Introduction

XAFS analysis sometimes has a mixed reputation, largely because of poorly-trained users using "user friendly" software packages without understanding the mathematical underpinnings of the analysis. As in many techniques, there are a number of pitfalls in EXAFS data analysis and care must be taken to make sure that the numerical results obtained during fitting are robust with change in input parameters. It is easy to have erroneous EXAFS analysis either due to artifacts in the data itself, using an incorrect model for fitting, or minimization to a local instead of global minimum in the analysis. For example, noise in data can give rise to peaks at radial distances similar to higher shell distances. Thus the true peaks get contaminated and incorrect conclusions may be drawn about the coordination environment. The principles of analyzing the data are well-established and steps are nearly standardized in most cases. Nevertheless, a well-planned experiment and considerable analysis experience are required for accurate results, as will be evident from the following discussions of the importance of correct analysis at each stage. While information from nearest neighbors ("first shell") is generally quite straightforward, the work in this dissertation largely involves second- and third-shell structure and is significantly more difficult to analyze and interpret.

The method of data analysis may be broadly divided into two steps: *Data Reduction* and *Fitting*. First step involves reliable and artifact-free procedures to subtract background. The background originates from the atomic absorption of all atoms present in the sample, and is a smooth and monotonically decreasing (above the edge energy) function added to the fine structure oscillations in the data. There are a number of steps involved before a raw data is ready to fit. These steps combined together are commonly called *Data Reduction*, followed by *Fitting*.

4.2 Data Reduction

Steps of data reduction are shown in the Fig 4.1. Although data processing consists of merging of several (or more) scans, deglitching (defined below), determining E_0 , pre-edge background removal, normalization to the edge step, post-edge background removal, and interpolating data to an equally spaced grid in photoelectron wavenumber k , the most critical part of data reduction is subtracting the smooth atomic background from the measured spectrum. Finding the smooth background however, is not always trivial. The procedures presented here are mostly based on chapter 6, "Data Analysis" in [52].

4.2.1 Aligning Scans

A reference foil should always be measured simultaneously while performing XAFS measurements. This reference signal should be aligned with respect to each other first, shifting the edge of the corresponding sample scan by same amount. This ensures same energy grid for each scan. The reference scans should then be merged (explained in next section) and the merged reference should be calibrated

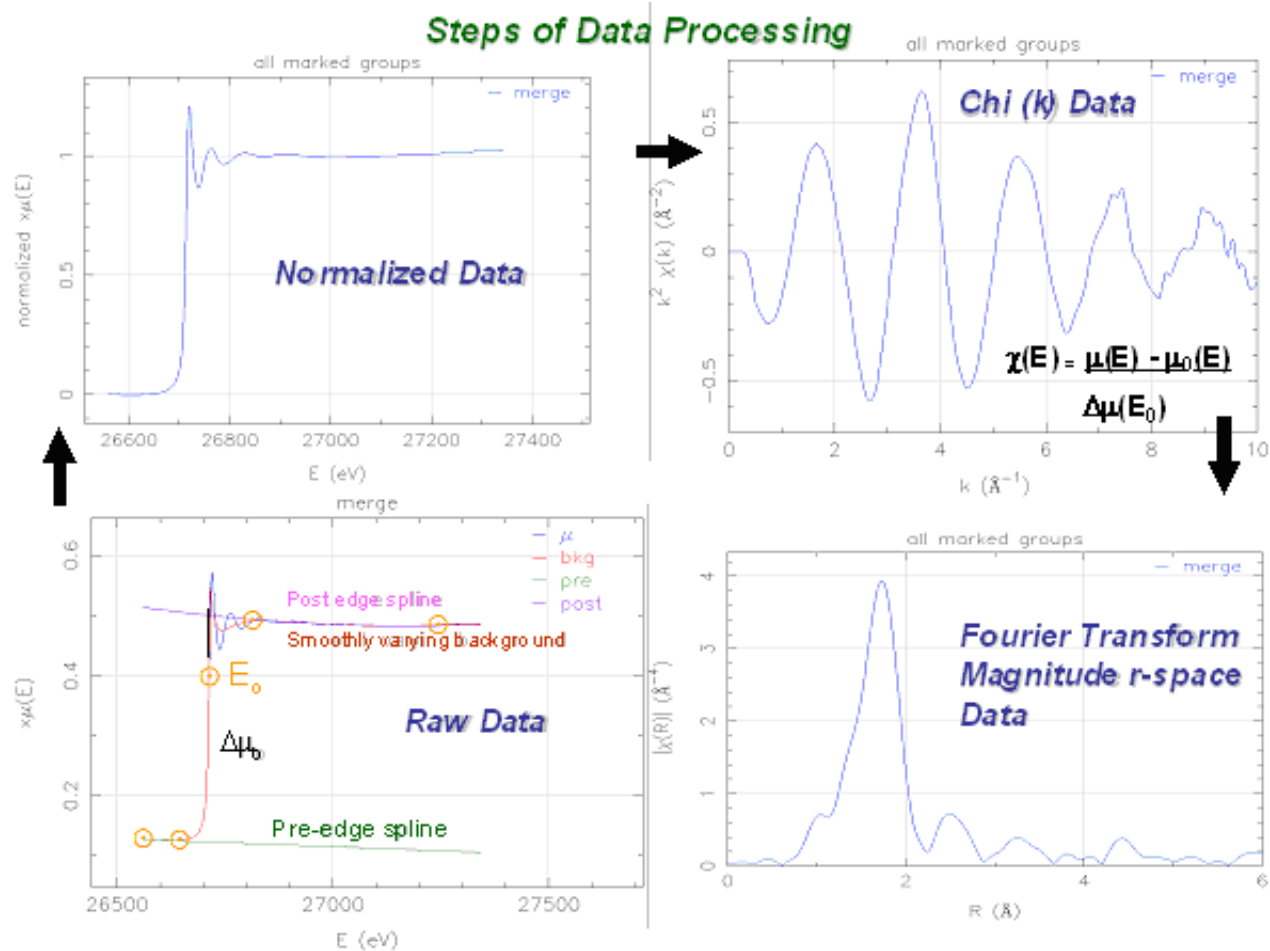


Figure 4.1. Steps of XAFS data processing. Raw data is normalized, background subtracted and Fourier transformed.

to the absolute energy of that central atom in that particular chemical state. The mutually aligned sample scans should be similarly merged and moved in energy by the same value as was required during the calibration of the merged reference. If however, a reference could not be measured simultaneously while measuring XAFS, all the scans must be aligned with respect to each other.

4.2.2 Merging of scans

Depending on the data quality, several scans are typically merged to reduce statistical noise present in the data. However, certain samples tend to change over the period of measurement due to beam induced chemistry (radiation damage). Therefore it is important to check for repeatability of scans before merging. Merging of scans can be done in few different ways.

This procedure could either be merged in k -space, or the raw data itself could be merged. In the first case, the entire process of extracting the XAFS oscillations is completed for each scan and then the oscillations from several scans are merged. If the statistical noise (due to counting statistics) of each individual scan is high, as in the case of dilute samples with relatively short times for each scan, merging the raw data is desirable because the background cannot be subtracted reliably from very noisy data. However if the individual scan are not very noisy as in case of standard compounds or samples with relatively large signal to noise ratio, merging of scan can also be done in k -space. If the data quality is good, merging in either of the two ways does not make any difference. But merging of statistically poor data in χ space could lead to serious systematic errors.

4.2.3 Deglitching

Deglitching is a process that removes sharp artifacts called "glitches" in the raw data. These glitches usually result from the spurious Bragg reflections in the monochromator. When the Bragg condition is accidentally satisfied for the primary wavelength for some reflection plane other than the primary one, part of the beam is reflected in some other direction, resulting in a sharp drop in the experimental incident beam intensity. The glitches show up in the measured XAFS data as sharp peaks and may be many times the larger than the EXAFS signal for dilute samples. Because of their small energy width compared to the EXAFS features of interest, it may seem that glitches are unimportant in further analysis and may be neglected. However, when the data is later Fourier transformed is later taken, the sharp peak has contributions over a broad spectral range and have a non-negligible affect on the data. The background subtraction may also be incorrect because of the presence of these spiky glitches and can change the chi-space spectrum, additionally adding artifacts to the Fourier transform spectrum. For all these reasons, it is generally advisable to remove the worst of the glitches from raw data before further processing.

When a glitch is narrow compared to the width of the XAFS oscillations for all shells of interest, say one data point, it can be removed by a linear interpolation of the data from adjacent points. If the glitch is a few data points wide but still narrower than the XAFS features, a polynomial can be fitted to the surrounding data and interpolated through the glitch region.

If a glitch is present close to the edge, its width becomes comparable to the oscillations since the latter are much narrower here. Instead of removing the glitch and possibly distorting the data, it is advisable to minimize the glitch amplitude

by tweaking around the experimental conditions.

4.2.4 Determining E_0

The photoelectron wave-number k in the XAFS equation is defined with respect to a certain reference or threshold energy E_0 by the relation:

$$k = \sqrt{\frac{\hbar^2}{2m_e}(E - E_0)} \approx \sqrt{0.263(E - E_0)}. \quad (4.1)$$

The threshold energy for the onset of absorption depends on the chemical state of the central atom and the structural symmetry of its surroundings. This can cause E_0 to vary up to a few electron-volts for the same absorbing atom in different samples. Determining the absolute value of E_0 is not critical since the edge energy is often allowed to float as a fitting variable. Usually, the monochromator calibration is checked in every scan with a calibration foil of a pure material whose edge is close to that of the sample. The purpose is to correctly and quantitatively account for any edge shift observed in the different samples. For example, for a radiation-damage-prone sample, the edge might shift from scan to scan and it is important to diagnose if this shift is true or due to a shift in the energy calibration of the monochromator. In practice, E_0 is chosen to be one of the following- the energy at half of the edge step or the position of the maximum of $\frac{d\mu}{dE}$. After the edge energy E_0 is fixed, the scan is divided into two regions: a) the pre-edge region which comprises a background from lower-energy absorption edges and Compton scattering and b) the post-edge region which contains the XAFS oscillations. The pre-edge region extends as a background into the post-edge region and needs to be subtracted before the next step of analysis, i.e. normalization.

4.2.5 Pre-edge Background Removal

The removal of pre-edge background involves fitting of a functional form to the data before the absorption edge and extrapolation of this function to the XAFS data region. Since the pre-edge background is a slowly varying function of energy, it can be fitted to a linear function between 200 eV and 50 eV below the edge and then extrapolated to the post-edge region.

4.2.6 Data Normalization

XAFS, by definition, is given by

$$\chi(E) = \frac{\mu(E) - \mu(E_0)}{\mu_0(E)} \quad (4.2)$$

where $\mu_0(E)$ is the absorption of an isolated atom. To extract and compare the information from different samples, they need to be normalized to the same scale. Other factors remaining same, the normalization constant for different samples reflects the concentration of a particular element in these samples. There are two general approaches to normalization of XAFS data- 1) energy-dependent normalization, or 2) energy-independent normalization. In principal, the normalization should be energy-dependent, as the atomic absorption background typically drops about 20% through an EXAFS scan. Additionally, experimental conditions usually contribute to an *increase* in the normalization for fluorescence or electron-yield measurements. This energy dependence must be taken into account when comparing experiment to theory or comparing different kinds of XAFS data, for example, transmission XAFS and fluorescence XAFS data. Energy-dependent normalization is done after step normalization and extraction of XAFS oscillations by dividing the result out by appropriate energy-dependent background.

Unless required, the normalization is usually energy-independent for simplicity. The usual procedure is to normalize by the *edge step*: the difference in pre-edge and post-edge curves at E_0 . Since $\mu_0(E)$ can never be measured independently or calculated accurately, a more convenient and reasonable replacement of the XAFS equation is

$$\chi(E) = \frac{\mu(E) - \mu_b(E)}{\Delta\mu(E_i)} \quad (4.3)$$

where E_i is systematically chosen at a point near the edge. This point should lie on the background curve for self-consistency. This point should be chosen to be far away from edge to avoid any near edge structure and yet not so far that the absorption cross-section has dropped considerably from its threshold value. Typically, this point lies in the range of 20 – 50 eV above the edge, around which the background is relatively smooth; more precisely it can be chosen to lie at a node of $\frac{d\mu}{dE}$. Finally, the normalization point should be chosen as consistently as possible among the unknown and standard sets used in a particular experiment. Proper selection of the parameters for normalization is critical for minimizing the errors in the measured coordination numbers later.

4.2.7 Background Removal

Extracting the post-edge background function, μ_0 , is the most critical step of background removal, as this function can affect the final conclusions for the structural information.

The XAFS oscillations should be symmetrical about the background line. The background is approximated by a single cubic polynomial over the energy region of interest with the first and last data points, respectively at the beginning and end of the energy range, defined. The polynomial function is solved using these

data points. Generally, this subtraction of a simple cubic polynomial over the entire data range is inadequate, and the background is instead approximated by a series of cubic polynomial functions (a "cubic spline") that are joined at "knots" where the functions and their first derivative are continuous. For a typical dataset, 2 – 5 knots might be necessary. It must be ensured that the data is not distorted by background removal process: Too few knots might not approximate the background oscillation well enough and might show as a low- r peak in the Fourier transform, while too many knots would tend to follow the true XAFS oscillations and reduce the oscillation amplitude. The position of the knots can be varied and the background may also be forced to pass through a certain point in cases of a complicated background fitting, although in practice this is rarely necessary. Once the fitting parameters are fixed, the fitting program tries to adjust the ordinates for the minimization of the mean square error between the data and the polynomial.

Recent efforts to fit the atomic absorption have been attempted by reducing the low- r component of the Fourier transform have been done in the AUTOBK program [76]. The technique is based on the consideration of the background function as that part of the measured absorption that does not contain any structural information. The technique differs from the previously described conventional technique in that (1) no point on the absorption curve is assumed to be on the background curve in the AUTOBK method; (2) whereas conventional background removal method chooses a smooth spline to best fit the whole absorption spectrum, $\mu(E)$, the AUTOBK method chooses the spline to best fit only the low-frequency components of $\mu(E)$; (3) whereas the standard background subtraction is subjective to the number and location of knots that is at the user's disposal, the number

and the abscissas of knots in the AUTOBK method are explicitly determined because of the restrictions put on the background spline from the information content of $\tilde{\chi}(r)$.

$$N_{knots} = \frac{2r_{bkg}\Delta k}{\pi} \quad (4.4)$$

where Δk is the k -range of useful data and r_{bkg} is the upper limit of the low- r region over which the background is to be fit. Typically, r_{bkg} will be about half the distance of the first shell peak. The knots are set to be equally spaced in k -space while the ordinates of the knots are determined by minimizing the difference between data and standard $\tilde{\chi}(r)$ in the low- r region. However, this method has difficulty when leakage from the first shell causes substantial low- r component of $\tilde{\chi}(r)$. In such cases, a suitable standard may be measured to estimate the leakage into the low- r region from the first shell, and this information could be used to reliably subtract the background.

For very noisy data, the conventional background subtraction method tends to do a better job. For most cases, background subtraction from AUTOBK and conventional method are comparable. However, in the case of AUTOBK, the oscillations in k -space turn to be a little more even about the background line. After the oscillations in k -space are extracted by background subtraction, they are Fourier transformed to r -space for fitting to obtain structural information from these oscillations.

4.2.8 Fourier Transform

First of all, it is important to understand what is Fourier transform (FT) and what does it do? I will then explain how we can harness it to our use in EXAFS data analysis. However there are some subtleties associated with doing the FT of

EXAFS data but techniques for dealing with these are well developed. All these issues will be briefly discussed in the following section.

In layman's language, a FT is a frequency filter (not in a true sense though) that transforms a delocalized signal in k -space to a localized signal in r -space. For example, the FT of an infinite sine wave in k -space is a delta function in r -space, and the FT of a step function in k -space is non-localized in r -space. Now, let us review the XAFS equation. It can be represented as

$$\begin{aligned}\chi(k) &= \sum_j |A_j(k)| \sin(2kR_j + \delta_j(k)) \\ &= \sum_j \text{Im}(A_j(k)e^{2ikR_j})\end{aligned}$$

where all the slowly varying functional components of k have been separated as $A_j(k)$,

$$A_j(k) = \frac{N_j}{kR_j^2} S_0^2 F_j(k) e^{-2k^2\sigma_j^2} e^{i\delta_j(k)} \exp \frac{-2(R_j - \Delta)}{\lambda}. \quad (4.5)$$

It is clear from this representation that the sine term is the primary k -dependence term in XAFS spectra. This implies that XAFS signal in k -space is basically a finite sine wave. It is helpful to think of this finite sine wave as a combination of infinite sine wave and a step function. We can then intuitively understand that the FT of this signal will be a peaks at $r = R_j$ corresponding to the sine waves plus the ripple corresponding to a step function. Let us now proceed to get into the mathematical rigor of the problem at hand.

For EXAFS data processing, the Fourier transform of the data is taken over a finite range from k_{min} to k_{max} as

$$\tilde{\chi}(r) = \frac{1}{2\pi} \int_{k_{min}}^{k_{max}} \chi(k) e^{2ikr} dk \quad (4.6)$$

where $k_{min} = 1.5-3.5 \text{ \AA}^{-1}$ and $k_{max} = 10-16 \text{ \AA}^{-1}$ depending on the system under investigation and data quality. The region below 2 \AA^{-1} is usually excluded due to possible complication from multiple scattering and other effects. k_{max} can extend up to any range as long as the signal-to-noise ratio is acceptable. In order to justify the Fourier transform technique mathematically, we should show that the peaks in r -space, resulting from the transform, indeed correspond to the location of the different near neighbors. The Fourier transform of $\chi(k)$ is

$$\tilde{\chi}(r) = \frac{1}{2i} \sum_j \tilde{A}_j(r) * \delta(r - R_j) \quad (4.7)$$

where ” * ” denotes convolution and \tilde{A} the Fourier transform of A . As a trivial example, we may take the case of a Gaussian amplitude to represent $A(k)$. The width of the Gaussian may taken to be Δk and the center at k_0 and we assume for simplicity a phase shift that is linear in k :

$$A(k) = \exp \left[-\left(\frac{k - k_0}{\Delta k} \right)^2 + i(\delta_0 + \delta_1 k) \right]. \quad (4.8)$$

The Fourier transform of this is

$$\tilde{A}(r) = \Delta k \exp \left[-\frac{\Delta k^2}{4} (\delta_1 + 2r)^2 + i(\delta_0 + \frac{k_0}{2} (\delta_1 + 2r)) \right]. \quad (4.9)$$

This results

$$\tilde{\chi}(r) = \frac{\Delta k}{2i} \exp \left[i\delta_0 + ik_0\delta_1 + 2ik_0r - \frac{\Delta k^2}{4} (2r - 2R - \delta_1)^2 \right]. \quad (4.10)$$

The magnitude of this transform is

$$|\tilde{\chi}(r)| = \frac{\Delta k}{2} \exp \left[-\Delta k^2 \left(r - R - \frac{\delta_1}{2} \right)^2 \right] \quad (4.11)$$

Thus it can be seen that in the Fourier transform, a particular inter-atomic distance R shows up as a Gaussian centered at $R + \frac{\delta_1}{2}$. However, in order to realistically evaluate this approach, it is important to know the actual variation of phase δ and amplitude F with k and understand how they affect the transform. For $Z < 50$, the amplitude is relatively smooth over the XAFS data range [61, 102]. But for higher Z atoms, there is additional structure in $F(k)$ which when Fourier transformed gives rise to sidebands about the central frequency in the transform. Although causing spectral broadening and therefore making it somewhat more difficult to isolate a given coordination shell, it generally can be handled in further analysis without problem.

The electronic phase shift $\delta(k)$ due to the central and backscattering atoms is not a linear function of k in most cases and this causes some broadening of the peak. For the vast majority of systems, this broadening due to phase non-linearity is comparable to other contributions to peak-width, such as finite data range.

Other energy-dependent factors include S_0^2 and λ . S_0^2 has only weak k dependence and can therefore be neglected. λ [97], on the other hand, has stronger k dependence through the data range and this may complicate the data analysis [82]. Fortunately, the first shell data are independent of mean free path and are relatively simple. Analysis of higher shell data may be difficult to interpret unless a suitable known material of similar local environment is available for comparison.

Another practical problem associated with the Fourier transforming technique here is due to the finite range. Truncation ripples often interfere with physical

features of interest. For a limited range of k as in our case, $\chi(k)$ may be replaced by $W(k)\chi(k)$ where

$$W(k) = \begin{cases} 1, & \text{if } k_{min} < k < k_{max}; \\ 0, & \text{otherwise.} \end{cases} \quad (4.12)$$

In the transform

$$\tilde{A}(r) = W(r) * A(r - R) \quad (4.13)$$

where $\tilde{W}(r) = \frac{\sin(\Delta kr)}{r} e^{ik_0 r}$, k_0 is the center of transform range and Δk is the width. This is a damped sine function with a peak at $r = 0$. The convolution of $\tilde{A}(r)$ with $\tilde{W}(r)$ results in peak broadening as well as the truncation ripple on the sides of the main transform peak. These ripples can contaminate neighboring peaks. It is possible to reduce the amplitude of truncation ripple at the expense of further peak broadening by using a tapered windowing function of the form

$$W(k) = \begin{cases} \cos^2\left(\frac{k-k_0}{\Delta k}\right), & \text{for } |k - k_0| < \Delta k; \\ 0, & \text{for } |k - k_0| > \Delta k, \end{cases} \quad (4.14)$$

where k_0 and Δk are as defined before. The \cos^2 window (with a "flat top") is often referred to as Hanning function [16]. The transform of this function is given by

$$\tilde{W}(r) = \frac{\sin(\Delta kr)}{r} \frac{\pi^2}{2(\pi^2 - \Delta k^2 r^2)} e^{2ik_0 r}. \quad (4.15)$$

Comparing this with the result of that without window, it is apparent that the truncation ripples die out much faster at large $r - r_0$ using the smooth window, but the central peak is significantly broader. It is often useful to combine a flat

region over the middle of the data range with a Hanning function at the ends, that is:

$$W(k) = \begin{cases} \sin^2\left(\frac{\pi}{2} \frac{k-k_1}{k_2-k_1}\right), & \text{if } k_1 < k < k_2; \\ 1, & \text{if } k_2 < k < k_3; \\ \cos^2\left(\frac{\pi}{2} \frac{k-k_3}{k_4-k_3}\right), & \text{if } k_3 < k < k_4, \end{cases} \quad (4.16)$$

where k_1 , k_2 , k_3 , k_4 delimit three different ranges corresponding to the two end regions and the flat central region.

Therefore, the window function has at least twofold purpose: 1) to weight different portions of the data and 2) to truncate the data smoothly at the ends of the transform range. Low- k data is less reliable because of errors in chemical transferability and other effects. Hence it is useful to put greater weight to the high- k data which de-emphasizes this problem. Truncating the data smoothly minimizes the truncation ripple at the expense of peak broadening.

The type of window function that is most commonly used and has been used in the analysis presented in this thesis is k^w . As mentioned before, a higher value of w emphasizes the higher k region. It is often advisable to compare the various weightings. Because of the differences in the k -dependence of the backscattering amplitude for elements of different Z there is a significant Z dependence in the k or k^3 weighted transforms. A peak with high- Z grows markedly with a higher k weighting and it is thus possible to distinguish between low- Z and high- Z atoms. This is because, for high- Z atoms, the backscattering amplitude is large at higher k and hence when weighted, contributes significantly higher to the transform than the low- Z atoms. After the Fourier transform is extracted, the next step is to fit the r -space data with a reasonable physical model. The scattering functions are calculated from the input model with the program FEFF [73] and are fit to the

data using the fitting program FEFFIT [72].

4.3 Qualitative Analysis of XAFS Data

After having Fourier transforming the XAFS data, it can be compared to standard compounds and some useful information could be gathered about the unknown sample under investigation. In many cases, a great deal of scientific information can be determined by qualitative analysis of the data. It is extremely useful to take a close look at comparison of the FT of the data with standards to predict models used for fitting the data (to be discussed in next section). It is a standard practice to compare the FT amplitudes at different k -weightings to distinguish light from heavy backscatters. Since the scattering amplitude of heavy backscatters extends to higher k -values than the light elements, the higher k -weighting produces a relatively larger amplitude increase for heavier atoms than for the lighter ones. However, the assignment of a peak to a coordination shell and interpretation of the lack of this peak as absence of that shell in magnitude of the FT can lead to erroneous conclusions. Reason for such elusive behavior is that the scaling of the magnitude of the FT is not linear. The backscattering signal from two close shells can interfere destructively in parts of the spectrum in such a manner that there might not be any visual peak. However the FT does combine the contribution of all atoms linearly in real and imaginary parts of the spectra. Looking at the real and imaginary part of the spectra is therefore much more useful and informative. At the same time, it should be emphasized that real and imaginary parts of the spectra do not give any new information as they are related by the Kronig-Kramers relation.

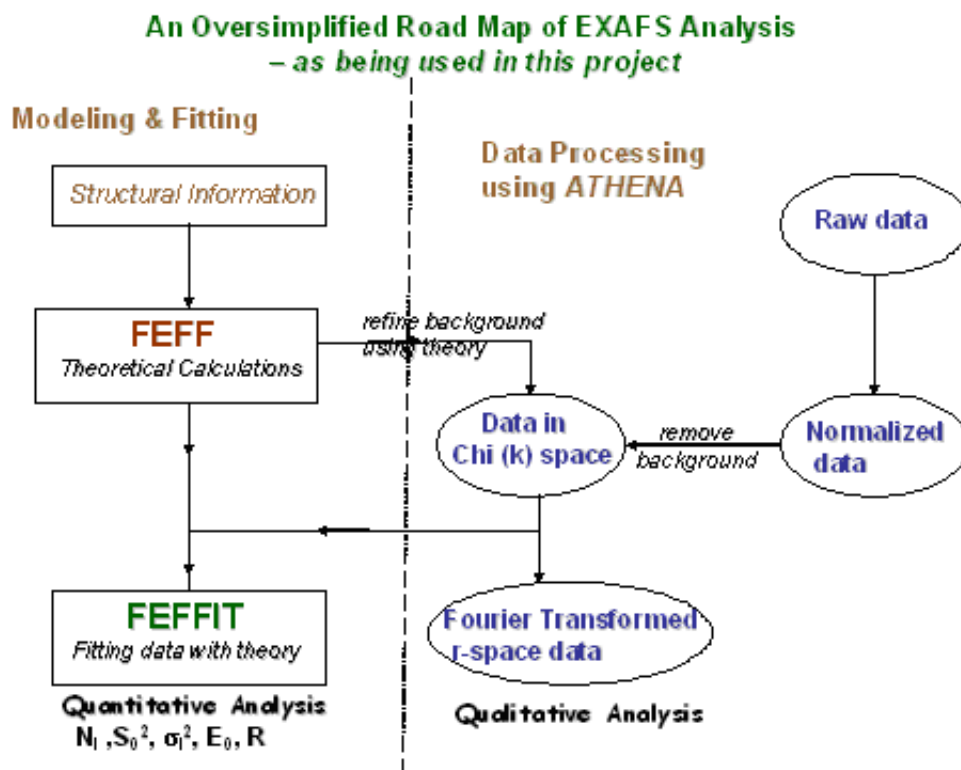


Figure 4.2. An oversimplified road map of EXAFS analysis as used in this presentation.

4.4 Fitting

Until about early 90's, XAFS analysis was traditionally limited to first and second neighbors as there was no reliable way to add multiple scattering (MS) contributions of the photoelectron to the single scattering analysis. Various strategies for simulating theory to fit the experimental data have been implemented. This presentation is mostly based on the UWXAFS package as it has been used for all the analysis implemented in this thesis. It is also the most widely used analysis package. Other two main analysis package are EXCURVE and GNXAS [7, 33, 34]. The strategy of UWXAFS package is well established and has been successfully

implemented to determine the coordination environment of complex systems. The accuracy of the package has also been verified by investigating some known structures. Although this particular suite of programs has been used for this analysis, other competing packages are available and generally well regarded.¹

4.4.1 Philosophy of UWXAFS Package

It is not generally possible to use experimental standards to calibrate MS since a sophisticated theory is needed to predict how the MS varies as the involved atoms are rearranged to obtain the best fit. The FEFF [73] theory has many features that are optimized for use in MS analysis. It has a high accuracy because it employs a Hedin-Lundquist many-body self-energy for the photoelectron and it uses an efficient and rapidly convergent expansion for the propagation of the photoelectron between scatterings which allows rapid calculation of a particular MS path. It preselects only those MS paths which would give a significant contribution. This approach greatly simplifies the necessary calculation and also saves time. FEFF imposes a muffin-tin potential and in earlier versions, ignored charge transfer effects. Recent versions of FEFF, however, calculate self-consistent potentials, greatly improving the E_0 calculation.

One can limit the number of MS paths contributing to the XAFS signal by fitting in r -space. Limiting the number of MS paths has several distinct advantages, not the least of which is in reducing the number of fitting parameters. This is crucial, as it is essential to keep the number of fitting parameters below the number of independent data points. This comes particularly important when dealing with organic/environmental systems as they mostly contain low Z backscatters leading to fast damping of the EXAFS signal. The short data range thus obtained

¹<http://xafs.org/Software>

cannot usually support a full MS analysis unless some of the fitting parameters of the multiple scattering (MS) path could be constrained to be the same or some function of the single scattering (SS). Other advantage of limiting the number of MS paths is that any difference between the fit and data is a direct measure of the quality of fit. This is in contrast to a fit in k -space. There is no obvious limit to the MS paths required for a k -space fit. For example, because higher-order MS contributions damp more quickly with k than lower-order, fitting the low- k portion of the data typically takes MS paths than the high- k portion. If one limits the number of MS paths, as one must because the information content of the data is limited, then the difference between the fit and the data in k -space has two contributions, one from the accuracy of the model used and other from the neglect of the contribution from higher order MS paths. There is no reliable way to separate the two in k -space. This shows a big advantage in r -space fitting: by spectrally isolating shells and MS paths that are not of direct interest, the problem is greatly simplified.

The purpose of the fit to the XAFS data is to determine the structure of the sample under investigation, in particular the coordination environment of the central atom. However just determining the *best fit values* provides only *half* of the necessary information. The other half is the uncertainties in these parameters. It is important to invest as much effort as necessary to calculate these errors accurately.

Finally one needs a criterion to decide if the fit that is obtained is reasonable. Since the fits in general require varying many parameters simultaneously, it is possible that a local minimum may be found instead of the global minimum. Another possibility is that some of the variables are highly correlated and it is

not possible to break these correlations using the available data. Yet another possibility is that a model is chosen which is far from the correct structure and the model does not have enough freedom to allow the necessary variation to reach the correct structure. Issues thus raised will be addressed in the following sections of this chapter.

4.4.2 Obtaining the best fit parameters

r -space fitting is a model-dependent approach that compares FEFF calculations with experimental data. Usually qualitative analysis gives a good idea of the model one should use to simulate the theory. FEFF6 or its newer versions FEFF7 (which includes self-consistent field calculations) or FEFF8 (which further includes circular dichroism and related calculations) is then used to simulate the theoretical XAFS data using an atomic cluster around the absorber. For this one need to specify the x , y , z coordinates of the structure for which simulation is run. This feature of FEFF makes XAFS extremely powerful, as it does not require the unknown samples to be a crystalline or symmetric structure. Any amorphous "mess" can be analyzed as fully as a simple crystalline structure provided a correct model is used for the purpose. Hence choosing this model is of prime importance in the XAFS analysis. However many times paths used fit a particular model is transferable to fit another model having the same central and backscattering atom. This transferability of paths makes it possible to fit a completely unknown sample with known models. Meaning thereby, in many cases, all that is known about the sample is the absorbing atom and possible backscattering atoms, in such cases it is impossible to simulate a FEFF calculation for the sample and hence several known models corresponding to that central atom and

backscattering atom is used on a trial and error basis.

Fitting results are only as good as the structural model, and it is important to examine the quality of fit ("reduced χ^2 ", discussed further below) and the physical parameters to check this. For instance, a ΔR value of 0.5 Å and above is a strong indication of a wrong model. Once the choice of model (the detailed atomic cluster used a first guess) to be used to done, FEFF is used to calculate the backscattering amplitude and phase shift for each individual path that has contribution above a cut-off value (2.5% of the total scattering amplitude is the default). These individual paths are then Fourier transformed to determine their extent in r -space and fit to the data over appropriate range. Usually a shell-by-shell fitting is performed, by varying the structural parameters (R , N , σ , E_0), Fourier transforming it in r -space, comparing it to the FT of the data over the fit range, and adjusting the variables and repeating the process until one gets the best fit. Guessing the initial parameters reasonably close to the actual values is important, so this is usually an iterative process. Usually one starts with shorter fitting range (in r -space) and extends it to longer data range.

The fitting is performed with the Levenberg-Marquardt method of nonlinear least-square minimization [64]. The best figure of merit to judge the quality of the fit is called chi-square noted by χ^2 and is defined by

$$\chi^2 = \sum_{i=1}^N \left(\frac{f_i}{\varepsilon_i} \right)^2 \quad (4.17)$$

where f_i denotes $f(R_i)$ and is defined as

$$f(R_i) = \tilde{\chi}_{data}(R_i) - \tilde{\chi}_{model}(R_i), \quad R_{min} \leq R \leq R_{max}. \quad (4.18)$$

²Note that this χ^2 is totally different from the $\chi(k)$ EXAFS data.

R_{min} and R_{max} define the fitting range in r -space fitting [75, 77]. The function to minimize is denoted by f_i and ε_i is the uncertainty in the function approximated by a constant value due to random fluctuations. The random fluctuations of the data in r -space can be estimated by evaluating the rms value of $\tilde{\chi}(r)$ between 15 and 25 Å, beyond where there should be any structural contribution. N is the number of function evaluations. Since there is one real and one imaginary part at each data point, the number of evaluations is

$$N = \frac{2\Delta r}{\delta r} \quad (4.19)$$

where δr is the grid spacing in r -space and Δr is the fitting range given by $R_{max} - R_{min}$. Since δr is chosen arbitrarily, N has no physical significance and is not the right number if the scale of χ^2 is to be meaningful. The best number to use is the number of relevant *independent* measurements, given by the amount of uncorrelated information in the data. Thus $N_{ind} = N_{info} + 2$. The qualitative arguments for this are (1) that the conjugate Fourier variables are k and $2R$ (2) that since we are measuring the real and imaginary parts of $\tilde{\chi}(r)$, the information must be an even number of points and (3) we must have at least one pair of points, even for an infinitesimally small r -range. Hence χ^2 equation then modifies to

$$\chi^2 = \sum_{i=1}^{N_{ind}} \left(\frac{f_i}{\varepsilon_i} \right)^2 = \frac{N_{ind}}{N} \sum_{i=1}^N \left(\frac{f_i}{\varepsilon_i} \right)^2. \quad (4.20)$$

For fitting, the first and second derivatives of χ^2 are found with respect to each of the variables. These derivatives are used to find the next estimate of the best variables and turn out to be useful for estimating the uncertainties in the variables after the best-fit solution is found.

There is a related figure-of-merit, called reduced chi-square, χ_ν^2 which is equal to $\frac{\chi^2}{\nu}$ where $\nu = N_{ind} - N_{var}$. χ^2 and χ_ν^2 are useful for comparing the quality of different fits. The criterion of the usefulness of a particular variable in the fit is that χ_ν^2 will be lowered for useful variables. In general the fit with lowest χ_ν^2 is considered the best. However, since χ_ν^2 itself has a statistical deviation, the reduction in χ_ν^2 must be larger than the deviation to consider the new fit better than the old one. If the errors are dominated by random fluctuations in the data, χ_ν^2 should be close to 1 with standard deviation of $\sqrt{\frac{2}{\nu}}$. As a criterion for statistically significant fit improvement we can take a reduction in χ_ν^2 by more than a factor of $2\sqrt{\frac{2}{\nu}}$ (twice the standard deviation). In practice however χ_ν^2 is rarely smaller than 10. The likely reason for this is that the estimated uncertainties at high r are lower than in the distance range of interest. However, larger values of χ_ν^2 likely indicate that either the model is a poor representation, the paths used are not right, or there are deficiencies in the FEFF calculations. In order to distinguish between the two cases, i.e. whether a fit is bad or the error is estimation is too low, another figure of merit is defined called the R -factor, denoted by R , which is scaled to the magnitude of the data itself.

$$R = \frac{\sum_{i=1}^N \left\{ \left[\text{Re}(f_i) \right]^2 + \left[\text{Im}(f_i) \right]^2 \right\}}{\sum_{i=1}^N \left\{ \left[\text{Re}(\chi_{data})_i \right]^2 + \left[\text{Im}(\chi_{data})_i \right]^2 \right\}}. \quad (4.21)$$

The R -Factor is the difference between data and fit normalized to the value of the data and does not depend on N , N_{ind} or ε . An R -Factor value within few percent clearly indicates a good fit, meaning that the fit line is agreeing with the data to within a few percent. If for the same fit $\chi_\nu^2 > 10$, we can attribute that to systematic errors causing the misfit to be larger than the random fluctuations,

rather than the actual fit not being good. Typically, an R -Factor of 2% or less, and $10 < \chi_\nu^2 < 100$ indicates a good fit and the structural parameters obtained from FEFFIT can likely be trusted.

The fitting procedures described above have been carried out using FEFFIT for data analysis in this dissertation. Interactive FEFFIT [74], popularly known as IFEFFIT and yet newer software ARTEMIS [84] (also based on IFEFFIT) are also frequently used for XAFS analysis. FEFFIT reads the FEFF calculations and data files and minimizes the sum of squares of the difference between FT of the data and theory by varying the structural parameters.

The new number of independent data points is automatically calculated, and so is χ^2 , χ_ν^2 correlation between different parameters and the uncertainties in the best fit values. It should be emphasized that FEFFIT treats each new data set as an independent measurement. But this not the case when one is fitting the same data for multiple k-weight. Therefore, it overestimates the number of independent data points by as many times as the number of data sets. This should be corrected by scaling the uncertainties reported by FEFFIT. The uncertainties are reported after multiplication by $\sqrt{\chi_\nu^2} = \sqrt{\frac{\chi^2}{\nu}}$, so the correction factor is $\sqrt{\frac{\nu_{multiple}}{\nu_{single}}}$, where $\nu_{multiple} = N_{ind}^{multiple} - N_{var}$ and $\nu_{single} = N_{ind}^{single} - N_{var}$.

4.4.3 Uncertainties of parameters

However, just determining the best values of the structural parameters is only half the necessary information. The other half is the uncertainties in these parameters and their correlations between them, which is critical in evaluating the plausibility of physical models. The uncertainty of a variable is defined as the amount by which a variable can be increased or decreased from its best fit value

and still keep χ^2 below a certain value. If χ_0^2 denotes the χ^2 at the best-fit solution, then for random errors, $\chi_0^2 + 1$ is the criterion. While the uncertainty of a particular variable is calculated, the other variables are allowed to float in order to measure the correlation between the various variables. The correlation is a measure of the amount by which the value of a variable changes in response to the change of another variable from its best-fit value.

The estimates of uncertainties of the variables and the correlations between them are made at the "best fit" condition. It is not sufficient to state universal values for the uncertainties because each analysis requires its own assessment of uncertainties including an estimate of the relative importance of systematic and random errors. Finally one needs a criterion to decide if the fit that is obtained is reasonable. Since the fits, in general, require varying simultaneously many variables, it is possible that a local minimum may be found, instead of the global minimum. Another scenario that may occur is that a model is chosen which is far from the correct structure and the model does not have enough freedom to allow the necessary variation to reach the correct structure. Still another possibility is that some of the parameters employed are highly correlated and it is not possible with the data available to determine these correlated parameters uniquely.

The uncertainties of the variables are provided by the inverse of the curvature matrix (the matrix of the second derivatives) in which the diagonal terms, in fact their square roots; represent the uncertainty of the variables while the off-diagonal terms give the correlations [6].

4.4.4 Using theoretical vs. experimental standards

An advantage of using experimental standards for fitting XAFS data, is that any systematic errors present in the data tend to cancel if the data on the known standard compound and the unknown sample are taken under the same experimental conditions. There are also disadvantages of using experimental standards, however: in that even if a suitable standard is available (which is often not true), it is difficult to extract SS paths in the case of mixed or overlapping shells in the standard, and difficult to determine MS paths under any circumstances. (The use of experimental standards *is* very useful to calibrate theoretical calibrations, however; more below.) However, one needs to be cautious to avoid possible artifacts when using theoretical standards. Because there is no cancellation of experimental or analysis problems, artifacts can arise from background removal, glitches, saturation of detectors, and other measurement pitfalls.

To check on the accuracy of FEFF calculations, known structures should always be measured as a calibration of the calculations. The derived structural parameters should then be compared to results from other techniques such as x-ray diffraction, NMR, etc. In particular, calibration with the reference compounds must always be done for the amplitude reduction factor S_0^2 , which is not calculated in FEFF but instead considered a free parameter. It has been shown (ref) that S_0^2 for a given central atom in a particular chemical state does not change much with change in coordination environment and therefore can be calibrated using a samples of known structure in a similar chemical state. Similarly E_0 , ΔR , σ^2 for each path being used to fit the unknown should also be calibrated with known reference compound. However, these structural parameters are "floated" during fitting of the unknown and such a calibration only provides a signature of the

typical values for that path.

4.5 Avoiding Pitfalls in XAFS Analysis

As mentioned earlier, XAFS analysis is error prone and slightest carelessness could lead to erroneous results. Main sources of pitfalls in XAFS analysis are:

- a. Wrong model
- b. Wrong values because of inadequate treatment of correlations
- c. Underestimation of uncertainties due to neglect of systematic errors

Although an R -factor of 1% or less gives one confidence about being a correct determination of parameters, it does not necessarily guarantee the *best* fit. Locking of parameters could in principle be a local minimum of an entirely wrong model. Different initial guesses of the variables, different fitting ranges and FT ranges, etc., should all be varied to check the robustness of the fit. A robust fit would return the same *best fit values* with such changes. Clearly, the structural parameters should make physical sense for a model to be acceptable. In addition, these parameters should indicate relative small changes from the initial guesses; if the returned parameters show large changes from the initial model, the original model may be a poor approximation. For example, ΔR values greater than 0.5 Å clearly indicate a problem and other structural models should be considered.

Strong correlations between parameters often arise from short data range (typical of dilute samples with low- Z backscatters). For example, coordination number and Debye-Waller factor may be separately determined with sufficient data range, but with a limited range they are strongly correlated: A change in one can be compensated for with a change in the other. One way to deal with this situation is to

use multiple k -weight fitting as the different weights emphasize different regions of the scan. To further improve the situation, multiple data sets of similar samples can be simultaneously fit to break the correlations. Some of the structural parameters can be constrained using additional information about the unknown sample from theoretical calculations or other experimental techniques. Breaking down the correlations between various parameters is however, extremely important to have a meaningful model.

Note that statistical methods for determining errors *do not* work for systematic errors. Error analysis methods can detect some systematic error if done correctly. Systematic errors dominate in most case except for dilute samples where statistical error plays an important role. The trick is to determine the 'statistical uncertainty' in the data by calculating the difference in separate scans or by calculating $\chi(R)$ noise at high $R > 15 \text{ \AA}$. Assuming the data uncertainty used in calculation of the χ_D^2 is not underestimated, if systematic error is negligible, χ_D^2 should be close to 1one. If χ_D^2 is significantly larger than one, further investigation of possible systematic experimental errors or incorrect assumptions of the structural model are advised.

CHAPTER 5

UNIVERSAL ADSORPTION BEHAVIOR OF Cd ONTO BACTERIAL CELL WALLS - A MOLECULAR SPECTROSCOPY APPROACH

5.1 Introduction

Bacteria are present in a wide range of environments. Speciation and distribution of metals in many aquatic and near-surface systems may be affected by metal adsorption onto bacterial surfaces [4, 59, 60]. Despite the importance of these reactions, the chemical reactivity of bacterial surfaces is not well understood. Quantitative models describing bacteria-metal adsorption must be understood for predicting the fate and bioavailability of heavy metal contaminants [106] and for developing remediation strategies [30, 63]. Surface complexation thermodynamic models (SCMs), originally developed to describe the adsorption of metal ions onto mineral surfaces, have recently been applied to describe the adsorption of metals onto bacterial surfaces [31, 32, 40, 79, 80, 112].

However, an obstacle in modeling realistic systems with SCMs is that each natural system of interest likely contains a unique consortium consisting of a large number of bacterial species. If the cell wall functional group sites of each bacterial species exhibit unique adsorption properties, then it would be necessary to determine site densities and binding constants for each site on each bacterial species

of interest. However, recent studies have shown that individual pure strains of bacteria [25, 65, 78, 113] and artificial mixtures of pure strains of bacteria [114] exhibit broadly similar adsorptive behavior. In support of this conclusion, Borrok et al. [12] found that consortia of bacteria grown from a range of uncontaminated soil and water environments exhibit roughly similar affinities for protons and Cd. In contrast, however, Borrok et al. [11] demonstrated that bacterial consortia from hydrocarbon-contaminated environments do not exhibit the same relatively narrow range of proton and Cd adsorption behavior that characterizes bacterial consortia from natural environments. Although the surface complexation models of Borrok et al. [11, 12] adequately account for proton and metal adsorption behavior onto a range of diverse bacterial consortia, we currently do not have a mechanistic understanding of why the broadly robust universality of the metal-complexation properties of bacteria break down to some extent when bacterial consortia from contaminated environments are compared to those from natural-uncontaminated consortia and laboratory cultures. Clearly, successful application of a surface complexation approach to quantifying bacterial adsorption of aqueous metal cations onto bacterial consortia requires a detailed understanding of the binding mechanisms and a determination if common mechanisms exist between diverse consortia. That information can be provided directly by using X-ray absorption fine structure (XAFS) spectroscopy to identify the surface adsorption sites and to quantify the relative amount of metal bound to each site.

XAFS of fungal cell walls [89], Gram-positive bacteria [13, 47] and Gram-negative bacteria [103] indicate that phosphoryl and carboxyl functional groups are responsible for metal complexation by these three types of microorganisms despite the differences in molecular structure of their exterior surfaces. For ex-

ample, Sarret et al. [89] examined Zn sorption to fungal cell walls at pH 6 as a function of Zn loading. Phosphoryl group was shown to be the predominant complexing ligand; only at highest Zn loading carboxyl group was found to be the complexing ligand. Kelly et al. [47] determined the pH dependence of the cell wall functional groups responsible for the absorption of aqueous UO_2^{2+} to a Gram positive bacteria *Bacillus subtilis* from pH 1.67 to 4.80. While UO_2^{2+} was found to bind exclusively to phosphoryl functional groups at extremely low pH (pH 1.67), an increase in carboxyl functional groups was observed with increasing pH (3.22 and 4.80). Similarly, Boyanov et al. [13] reported that Cd binds predominantly to phosphoryl ligands below pH 4.4 to the Gram positive bacteria *Bacillus subtilis*, whereas at higher pH conditions (4.4 – 6.5), adsorption to carboxyl groups becomes increasingly important. However, at pH 7.8, they observed the activation of an additional binding site, which was tentatively ascribed as a phosphoryl site with smaller Cd-P distance than the one reported to be active at lower pH conditions. Toner et al. [103] investigated Zn sorption by a bacterial biofilm of Gram negative bacteria *Pseudomonas putida* at pH 6.9. Zinc sorption to the biofilm was attributed predominantly to Zn-phosphoryl complexes, with a smaller contribution to sorption from carboxyl-type complexes. Given the spectroscopic evidences for Cd, Zn, Pb and UO_2^{2+} sorption by phosphoryl- and carboxyl-type functional groups in Gram positive and Gram negative bacterial cell walls, can we model metal sorption in a consortium of bacteria sampled from natural system using phosphoryl and carboxyl functional groups only? What makes a bacterial consortium sampled from contaminated site different from a bacterial consortium obtained from natural uncontaminated site?

In this study, XAFS has been used to resolve whether binding sites determined

for single species systems are responsible for adsorption in more complex bacterial assemblages. More importantly, this study also aims to examine the key factors responsible for the deviation of contaminated consortia from the general behavior of the uncontaminated natural consortia at molecular scale. To this end, we performed XAFS experiments in order to determine the speciation of Cd adsorbed to a bacterial consortium grown from a river water sample, and a consortium of bacteria cultured from a soil system that was severely contaminated by hydrocarbons.

5.2 Methods and Materials

5.2.1 Sampling and growth of bacterial consortia

The river water sample that was used in this study was collected from the St. Joseph River in South Bend, Indiana, USA. The contaminated soil sample was collected from a manufactured gas plant (MGP) site in Iowa, USA. The clay-rich soils from the MGP site were severely impacted by polycyclic aromatic hydrocarbons that had co-mingled with gasoline range hydrocarbons from a nearby leaky underground storage tank site. The contamination is characterized by visible coal tar and concentrations of benzene, toluene, ethylbenzene, and xylene. All materials used for sample collection including glass jars and lids, and digging scoops were sterilized and sealed in plastic bags before use. The sampling protocol for river water consortium was identical to those described by Borrok et al. [11, 12]. The MGP site soil sample used in this study is the same sample used in previous study by Borrok et al. [11]. The consortium of bacteria obtained from MGP site was regrown for XAFS measurements from the frozen stock that was cultured by Borrok et al. [11].

Approximately 10 g of soil or 10 ml of water from the samples were used to inoculate the chosen broth solution. Bacteria were grown using either trypticase soy broth (TSB) with 0.5% yeast extract or soil broth (SB). SB was made with 250 ml soil extract, 2 g glucose, 1 g yeast extract, and deionized (DI) water (to 1.0 l). Soil extract was made by autoclaving 500 g of soil with 1 l of DI water for 1 h at 15 psi/121°C and decanting the fluid product using Whatman No. 2 filter paper. Inoculated broth solutions were gently shaken at room temperature until they were harvested.

Because a particular set of growth conditions will support growth of only particular types of bacterial species, the bacteria grown for our experiments included only a subset of the total bacterial population present in each environment sampled. For example, if either original sample contained species of strict anaerobes, these would not be represented in the final experimental consortia which was grown under aerobic conditions. However, many individual bacterial species within natural consortia cannot survive repeated inoculations in laboratory growth media [46]. Therefore, by growing the bacteria directly in broth solutions and limiting the number of reinoculations, we expect to have a range of diverse consortia that is at least representative of the diversity which exists in nature. Previous tests of bacterial diversity on consortia grown from these locations using denaturing gradient gel electrophoresis indicated that the river and the MGP consortia exhibited at least six and four bacterial species, respectively, with both exhibiting a mix of Gram-positive and Gram-negative species [11, 12].

5.2.2 Cd Adsorption Experiments

Bacteria were harvested from the growth media by centrifugation, transferred to test tubes, and washed five times in 0.1M NaClO₄ (the same electrolyte used in the experiments). Sodium perchlorate was chosen as the experimental electrolyte because perchlorate does not form complexes to an appreciable extent with Cd under the experimental conditions. During each wash, the bacteria were suspended in fresh electrolyte solution using a vortex machine and stir rod. Bacteria were centrifuged for 5 min at 8000 rpm to form a pellet at the base of the test tube and the electrolyte was discarded. After the final wash, the bacteria were placed in weighed test tubes and centrifuged (7000 rpm at 25°C) for 1 h, stopping three times to decant all supernatant. After 1 h, the weight of the moist bacterial pellet was determined. The weight recorded at this stage is reported throughout this paper and termed the wet weight of the biomass.

In each metal adsorption experiment, 10 g/l of a bacterial consortium was suspended in a pH-neutralized stock solution of 0.1 mol/l NaClO₄ and 30 ppm Cd. After an initial 10 min equilibration time, the bacterial stock solution was divided into individual reaction vessels. The pH of each reaction vessel was adjusted by adding minute aliquots of 1.0 mol/l or 0.1 mol/l HNO₃ or NaOH. After adjustment of the pH, and an additional 2 hr. of reaction time on a rotating rack, the final (equilibrium) pH of each vessel was measured. Previous studies in our laboratory have demonstrated that equilibrium of the adsorption reaction generally occurs in less than 1 hr. and that the adsorption reaction is fully reversible [35]. The individual vessels were then centrifuged, and the resultant supernatant was filtered (0.45 μm) and acidified. The filtered supernatant was analyzed for Cd using an inductively coupled plasma-atomic emission spectroscopy technique with matrix-

matched standards. The concentration of metal adsorbed to bacteria in each vessel was calculated by subtracting the concentration of metal that remained in solution (supernatant) from the original 30 ppm in the stock solution. The biomass pellet formed at the base of each vessel after centrifugation was loaded into slotted Plexiglas holders and covered with Kapton film for XAFS measurements (see description below). All the XAFS measurements were performed within 30 hrs of the adsorption experiment, and the samples were refrigerated until the measurements.

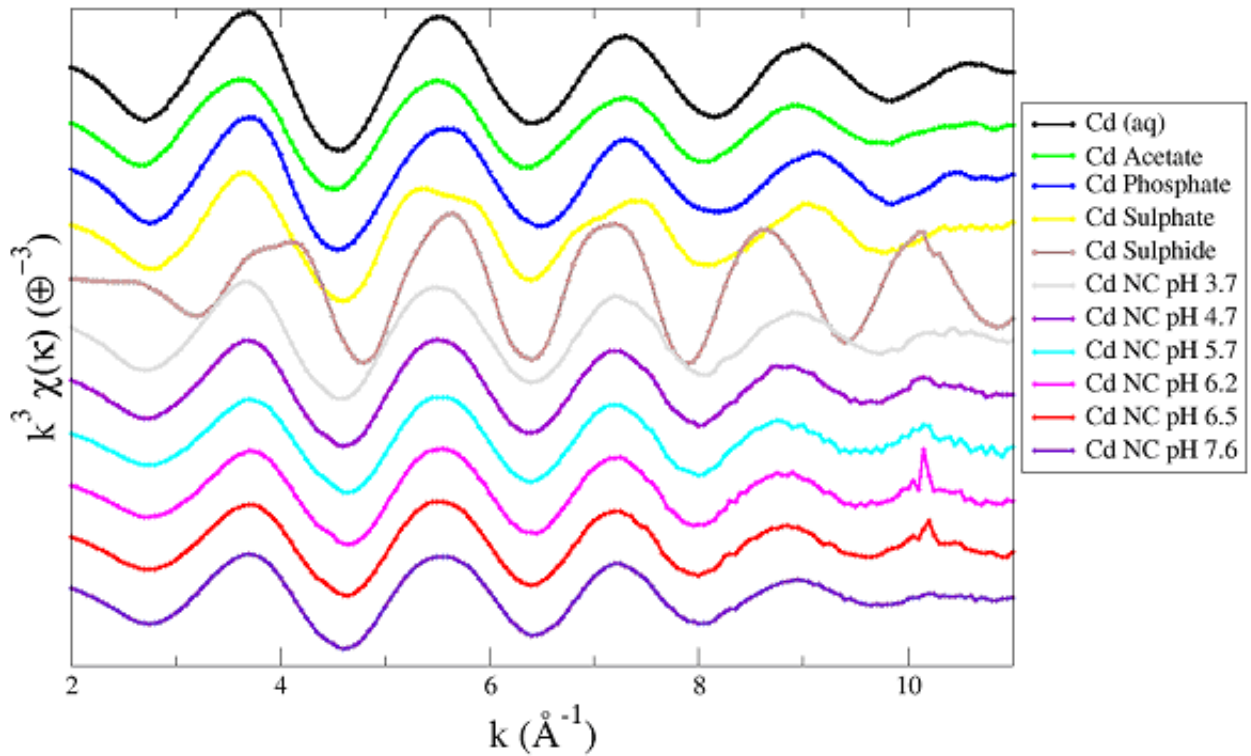


Figure 5.1. $\chi(k^3)$ data of the river water consortium samples plotted with Cd standards. Data range used for Fourier transforming the data was $2.3 - 9.8k$ (\AA^{-1}).

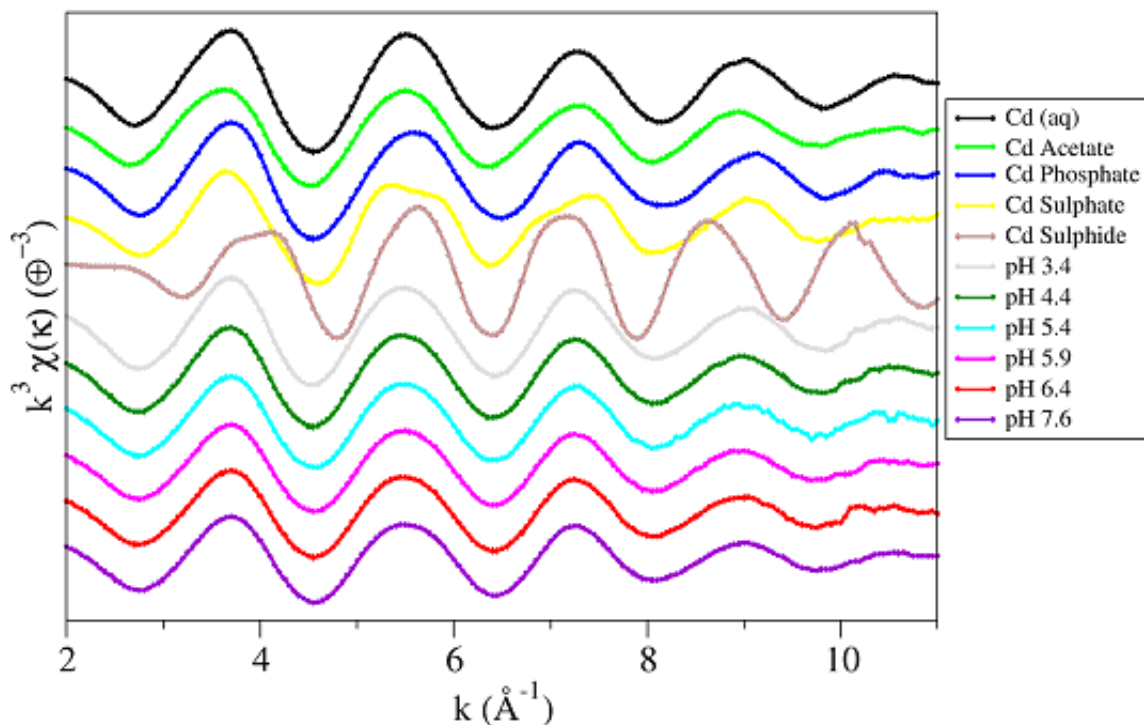


Figure 5.2. $\chi(k^3)$ data of the contaminated soil consortium samples plotted with Cd standards. Data range used for Fourier transforming the data was $2.3 - 9.8k$ (\AA^{-1}).

5.2.3 XAFS Standards

Powder and aqueous Cd standards were used for comparison and theory calibration in the analysis. CdS and CdSO₄ powder standards were prepared from commercially available chemicals (Sigma-Aldrich), after grinding and sieving (~ 400 mesh). The aqueous Cd standards include hydrated Cd, Cd acetate and Cd phosphate solutions. All Cd standards were prepared from 1000 ppm Cd perchlo-

rate stock solution. For hydrated Cd, 0.1 M cadmium perchlorate solution was prepared by diluting the stock solution with 0.1 M sodium perchlorate. For the signature of carboxyl and phosphoryl ligands, 0.1 M aqueous solution of Cd:acetate and Cd:phosphate was prepared in a ratio of 1 : 100 by dissolving appropriate amount of cadmium acetate and cadmium phosphate salts (reagent quality obtained from Alfa Aesar) in 0.1 M sodium perchlorate and diluting the solution to known volume. To shift the equilibrium toward complexed Cd ions, phosphoric acid was added to the Cd phosphate solutions and ammonium acetate was added to the Cd acetate solutions without pH adjustment. Details of this protocol is explained by Boyanov et.al [13].

5.2.4 XAFS Measurements

X-ray Absorption Fine-structure Spectroscopy (XAFS) measurements of Cd K edge (26711 eV) were performed at the MRCAT sector 10-ID beamline [93] at the Advanced Photon Source at Argonne National Laboratory. The energy of the incident X-rays was scanned by using a Si(111) reflection plane of a cryogenically-cooled double-crystal monochromator. The beamline was optimized at the 3rd harmonic of the undulator. The undulator was tapered by approximately 3.54 keV to reduce the variation in the incident intensity to less than 15% over the scanned energy range. Higher harmonics were rejected using Pt-coated mirror. The incident ion chamber was filled with 100% Nitrogen. The transmitted and reference ion chambers were filled with 100% Ar. The fluorescence detector in the Stern-Heald geometry [90] was filled with Kr gas, and Pd filter of six absorption lengths was used to reduce the background signal. The incident X-ray beam profile was 1 mm square. Linearity tests [48] indicated less than 0.1% nonlinearity

for a 50% decrease in incident X-ray intensity. The scans were aligned by the simultaneously collected Cd foil data. The first inflection point was set at 26,711 eV.

Quick scans (continuous-scanning mode of the monochromator with signal sampled every 0.05 eV in the entire scanning range) were used with an integration time of 0.1 second per point. The advantage of using quick-scans is that it reduces the radiation exposure during a single scan (~ 3 minutes per EXAFS scan and < 1 minute/XANES scan). Further XANES was constantly monitored for any possible radiation damage. About 30 to 100 consecutive scans of each sample, depending on the Cd loading were averaged.

5.2.5 XAFS Data Reduction

The data were analyzed using the codes from the UWXAFS package [99]. These programs include ATHENA [85] which is based on AUTOBK [76] to remove the background, FEFFIT [77] to fit the theoretical model to the EXAFS data, and FEFF8 [2] to create the theoretical model. The data sets were aligned and the backgrounds were removed using ATHENA program. The input parameter to ATHENA that determines the maximum frequency of the background R_{bkg} was set to 1.1 Å. The data range used for Fourier transforming the k space data was 2.3 – 9.8 Å⁻¹. Hanning window function was used with a dk of 1.0. Simultaneous fitting of several data sets with multiple k -weighting (k^1 , k^2 , k^3) of each spectrum was performed in r -space. The fitting range for all the data sets was set to 1.2 – 3.4 Å. The simultaneous fitting approach reduces the possibility of obtaining erroneous parameters due to correlations at any single k -weighting.

5.3 Results and Discussion

5.3.1 Cd adsorption Experiment

Cd adsorption experiments on both the bacterial consortia are shown in Fig. 5.3. It can be clearly seen that the contaminated soil consortium exhibits higher Cd uptake at all experimental pH conditions. The parent solution was 30 ppm of Cd in the current study. A bigger contrast in Cd uptake is seen between these two consortia when these experiments are carried out at 10 ppm parent solution [11].

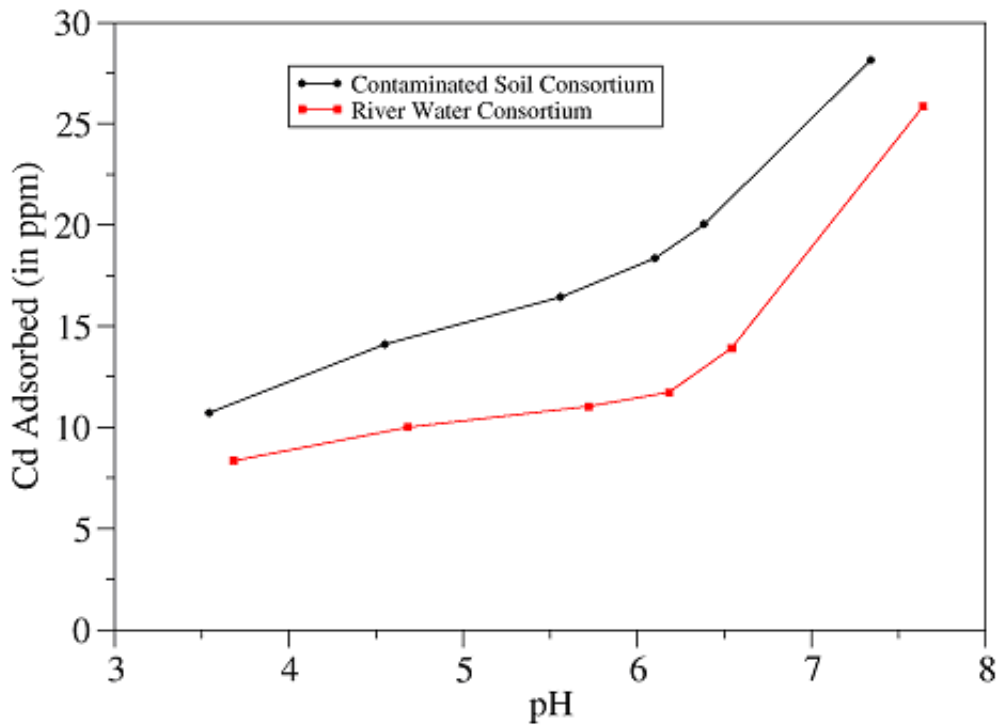


Figure 5.3. Cd adsorption data for the two consortia of bacteria measured using ICP-AES.

TABLE 5.1

FITTING PARAMETERS OF Cd STANDARDS

Standard	Path	N	R(Å)	sig2(10^{-3})
CdClO ₄	Cd-O	6.0 ± 0.18	2.27 ± 0.01	8.8 ± 0.2
	Cd-H	2*No	2.94 ± 0.03	13.7 ± 0.5
CdAc	Cd-O	5.5 ± 0.3	2.29 ± 0.01	10.9 ± 0.9
	Cd-C	2.9 [#]	2.67 ± 0.02	12.8 ± 4
	-C-C-	Nc or 2*Nc	4.26 ± 0.02	15 ± 4
CdPO ₄	Cd-O	5.8 ± 0.3	2.29 ± 0.01	10.5 ± 1.2
	Cd-H	2(No-2Nc)	3.0 ± 0.06	16 ± 9
	Cd-P	1.5 ± 0.3	3.42 ± 0.3	15.0 ± 3.0
CdS	Cd-S	4.0 [#]	2.53 ± 0.02	9.0 ± 1.5
	Cd-Cd	12.0 [#]	4.2 ± 0.01	25.0 ± 4.0

5.3.2 Standards Compounds for analyzing EXAFS

FEFF8, using ATOMS [83] to create an input file for the known crystal structures of Cd-acetate dehydrate, Cd-phosphate and Cd-sulfide, was used to simulate the theoretical XAFS spectra for these standard compounds. For hydrated Cd ion, simple octahedral geometry of water molecules (6 oxygen atoms with 2 hydrogen atoms associated with each oxygen atom) was simulated.

FEFFIT was used to fit the hydrated Cd data with 6 nearest neighbor oxygen in the first shell at 2.28 (± 0.02) Å. The measure of goodness of fit, R -factor

TABLE 5.2

PATHS USED FOR FITTING THE UNKNOWN
 SAMPLES, SHOWING THEIR DISTANCES AND
 DEBYE-WALLER FACTORS

Path	Distance(\AA)	$\sigma^2(\text{\AA}^{-2})$
Cd-O	2.29 ± 0.01	0.0090
Cd-C	2.70 ± 0.03	0.0120
Cd-S	2.53 ± 0.02	0.0090
Cd-P	3.41 ± 0.03	0.0150

and χ^2_{ν} , significantly improved by considering 12 hydrogen atoms in the second hydration shell at $2.9 (\pm 0.08) \text{\AA}$. The coordination environment of the Cd acetate standard was modeled with O and C shells bound to the acetate group. Data were fit with $5.5 (\pm 0.3)$ O atoms in the first shell and 2.9 C atoms in the second shell which is consistent with a bidentate binding mechanism, as is observed in crystal Cd acetate [19]. The Cd-O bond length and Debye-Waller factor were the same as for hydrated Cd. The Cd-C bond distance was found to be $2.67 (\pm 0.02) \text{\AA}$. Cd phosphate solution data were fit with $5.8 (\pm 0.3)$ O atoms in the first shell and $1.5 (\pm 0.3)$ P atoms in the second shell. The Cd-O bond length remained unchanged at $2.28 (\pm 0.02) \text{\AA}$, and the Cd-P bond distance was found to be $3.42 (\pm 0.05) \text{\AA}$. The CdS powdered standard was fit with 4 S atoms in the first shell at $2.53 (\pm 0.02) \text{\AA}$. As can be seen from Fig. 5.1, the second and third oscillations of the Cd sulfide spectrum is clearly phase shifted in χ . The phase shift comes from cadmium bonding to sulfur in the first shell as opposed to

oxygen in all other standards presented here. This phase shift is more obvious in the Fig. 5.4. Note the reduction of the first shell peak in cadmium acetate. In this case, the oxygen atom interferes destructively with the carbon atom leading to this reduction. Since C, P and S are all low Z atoms, the subtle differences in the second shell of the Cd phosphate, -acetate and - sulfate spectra can not be seen clearly from the magnitude of the Fourier transformed data. The blown up real part of the Fourier transformed data, however, brings out the relatively small changes in the second shell of cadmium acetate, -phosphate and - sulfate spectra (Fig. 5.5). Cadmium phosphate has a distinct feature at about 2.7 Å. Distinguishing Cd sulfate from Cd phosphate is not straightforward. There is, however, a small phase shift toward lower r value (left) in the sulfate signal at about 2.4 Å. It would be hard to distinguish the contribution of the sulfate signal from the contribution from Cd phosphate in an unknown sample.

The fitting results of all these standards are compiled in Table 5.1, and are consistent with $S_0^2 = 1$, so this value was set for fitting the bacterial consortia samples. Cd-O, Cd-C, Cd-P and Cd-S are the four important single scattering paths that were used to fit hydrated cadmium, cadmium acetate, - phosphate and - sulfide. Since we have developed a good understanding about the behavior of these four paths, we will try to use only these four paths for the analysis of the unknown bacterial consortia samples. The distances and Debye-Waller factors for these paths are listed in Table 5.2. A Cd-Cd path was also used to fit Cd sulfide spectra, which would be useful for the signature of Cd precipitation in the unknown samples.

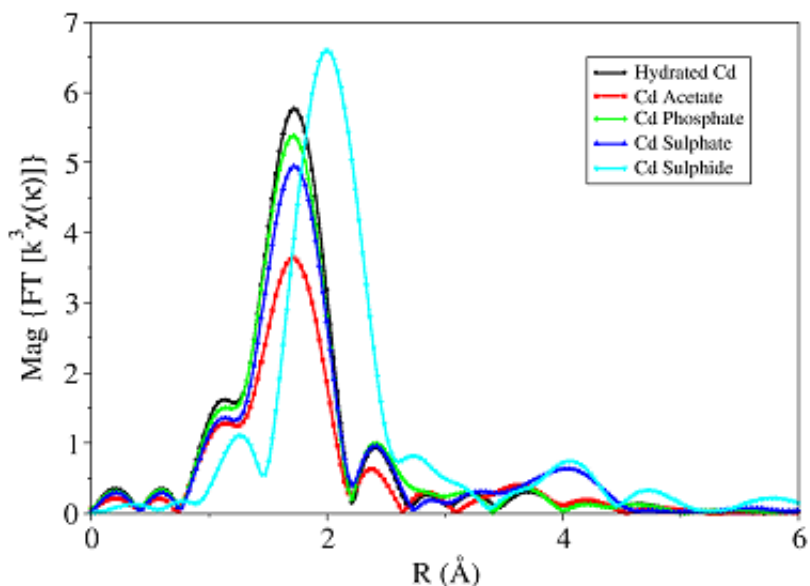


Figure 5.4. Fourier transformed magnitude data of the Cd standard compounds. Notice a systematic decrease in the amplitude of the first shell from hydrated Cd to Cd Phosphate, -sulphate, and -acetate. Cd sulphide has a clear phase shift towards higher value of r .

5.3.3 Qualitative Analysis of EXAFS Spectra

5.3.3.1 River Water Consortium

While we will presently show detailed fitting results, it is useful to look qualitatively at the results first. We used the analysis of EXAFS spectra for the Cd standards described above as a basis for identifying the binding environment of Cd in the bacterial consortia samples. The spectra at pH 3.7 has a phase shift toward lower r value (left) at 2.4 Å, indicating the possibility of Cd-sulfate binding. This is, however, not definitive because the reduction that we observe in the first shell is not as great as the first shell reduction that we observed associated with the spectra of cadmium sulfate. The kink at 2.7 Å suggests Cd-phosphoryl binding. Cd is also found bound to a phosphoryl group at this pH in pure Gram

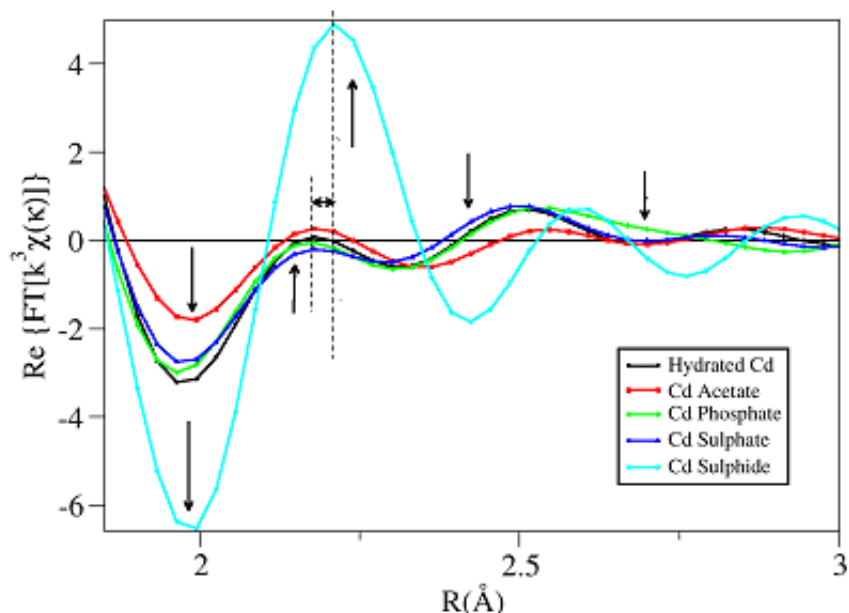


Figure 5.5. Fourier transformed real part of the Cd standard data plotted over a shorter data range (1.85 – 3.0 Å). Sulphide peak has a phase shift toward higher value of r compared to the acetate peak at about 2.2 Å. Cd acetate has a shallow first shell peak at about 1.9 Å characteristic of destructive interference between O and C shells. Cd sulphate is shown to be slightly shifted toward lower r value at about 2.4 Å. Also notice the kink in Cd phosphate data at about 2.7 Å.

positive and Gram negative bacterial strains [13]. The EXAFS spectrum at pH 4.7 has a significant increase in the peak at 2.2 Å, compared to the spectrum at pH 3.7 (Fig. 5.7). This could be indicative of both carboxyl and sulfide binding. A closer look at the first shell strongly suggests the presence of sulfide binding. If the increase in the peak of this spectrum around 2.2 Å was purely due to carboxyl contribution, there would have been an associated reduction in the peak at 1.9 Å (Fig. 5.5, which is clearly not the case. Small shift in this peak at 2.2 Å towards higher r value (right) is also indicative of the sulfide binding. Spectra of pH 5.7 and 6.2 are quite similar, and a further increase in the peak at about 2.2 Å for

these two spectra suggest increasing contribution of the carboxyl and/or sulfide binding at these pH values. Reduction in the peak at 1.9 and 2.2 Å for pH values 6.5 and 7.6 strongly implies decrease in sulfide contribution. A kink at 2.7 Å in the spectra at pH 7.6 clearly suggests an increase in phosphoryl binding at this pH. Increase in phosphoryl contribution around this pH value is consistent with the analysis of pure bacterial strains [13, 69]. Overall the qualitative analysis of the natural consortia of bacteria indicates a phosphoryl binding at pH 3.7, with an increase in the carboxyl and sulfide contribution at pH values 4.7, 5.7 and 6.2. This trend however changes at pH 6.5 and 7.6. At these two pH values a decrease in the sulfide and an increase in the phosphoryl contribution is suggested by the qualitative analysis of EXAFS spectra.

5.3.3.2 Contaminated Soil Consortium

The magnitudes of the Fourier transformed contaminated soil consortium data are shown in Fig. 5.8. A comparison of Fig. 5.6 with Fig. 5.7 shows that the amplitudes of the magnitude of the Fourier transformed data of the contaminated soil consortium are bigger (or higher) than the amplitudes of the magnitude of the Fourier transformed data of the river water consortium at corresponding pH values. The higher amplitudes of the magnitude of the contaminated soil consortium samples suggest that carboxyl contribution to the Cd binding is less important in these samples than it is for the river water consortium samples. It can be seen from Fig. 5.8 that shape of all the Fourier transformed spectra in magnitude space is quite similar between 2.0 and 3.5 Å. In contrast to the spectra of the samples of the river water consortium, which shows dramatic changes in the peak at 2.2 Å in the real space of the Fourier transformed data, the spectra of the contaminated

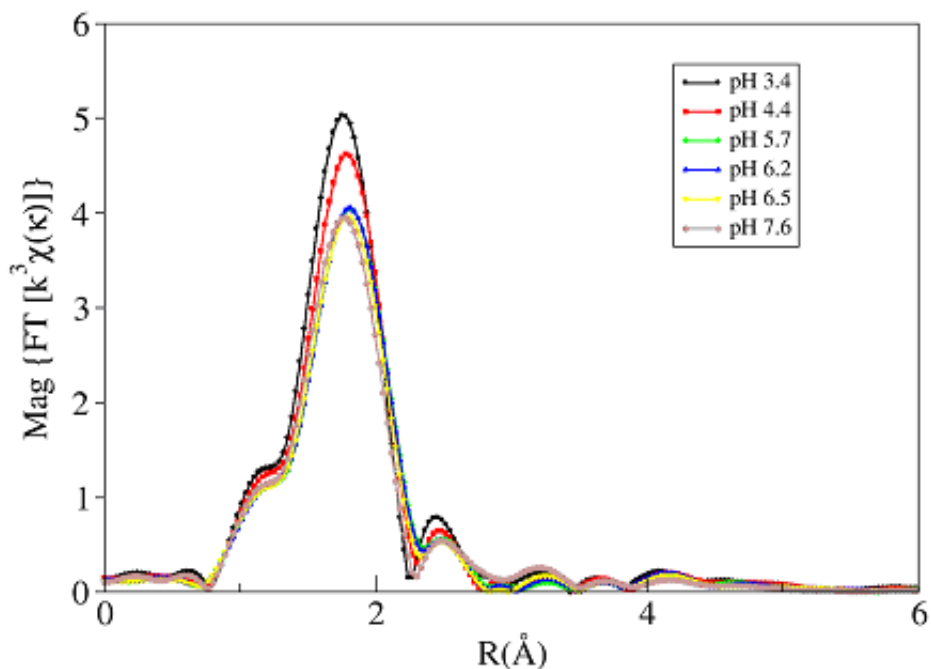


Figure 5.6. Fourier transformed magnitude data for the river water consortium. Notice the reduction in the amplitude of first shell peak with increase in pH.

soil consortium in the real space of the Fourier transformed data (Fig. 5.9) show striking similarity at all the pH conditions. Since the height of the peak at 2.2 Å in the real space of the Fourier transformed data of the contaminated soil consortium is much lower than the corresponding peak heights of the river water consortium samples, possibility of the presence of sulfide bonding can be easily ruled out. A small phase shift toward lower r value (left) in the real space Fourier transformed spectrum of the lowest pH sample, pH 3.4, around 2.4 Å suggests the possibility of sulfate binding at this pH. However, all the spectra of the contaminated soil consortium have a peculiar behavior at about 2.7 Å which strongly resembles the phosphate signature. It is highly likely that phosphoryl group is the dominant

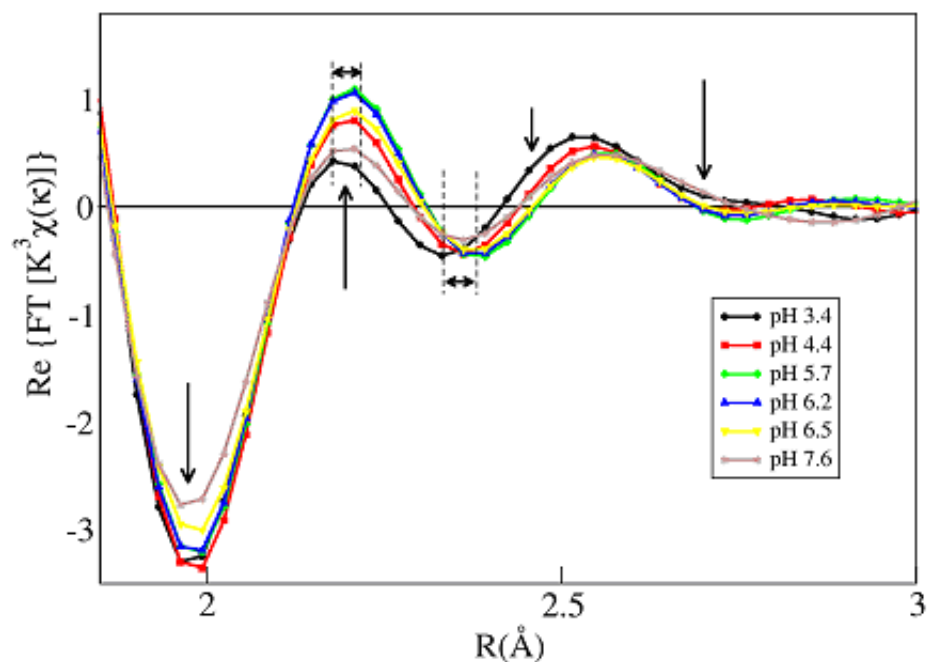


Figure 5.7. Real part of the Fourier transformed river water consortium data plotted over the data range of 1.85 – 3.0 Å. A dramatic change in the peak and a phase shift toward higher r value is seen at about 2.2 Å with increase in pH. This indicates rise in sulphide signal with increase in pH. The lowest and highest pH sample show signature of phosphate binding. The lowest pH sample also shows a phase shift toward lower r value at about 2.4 Å characteristic of sulphate binding.

binding ligand in the entire pH range examined for the soil consortium of bacteria contaminated by hydrocarbons.

It is worth emphasizing here that qualitative analysis of EXAFS spectra can sometimes be deceptive, as interference of signals play an important role in the making of an EXAFS spectrum. A rigorous quantitative modeling is therefore necessary for a precise characterization of the unknown system.

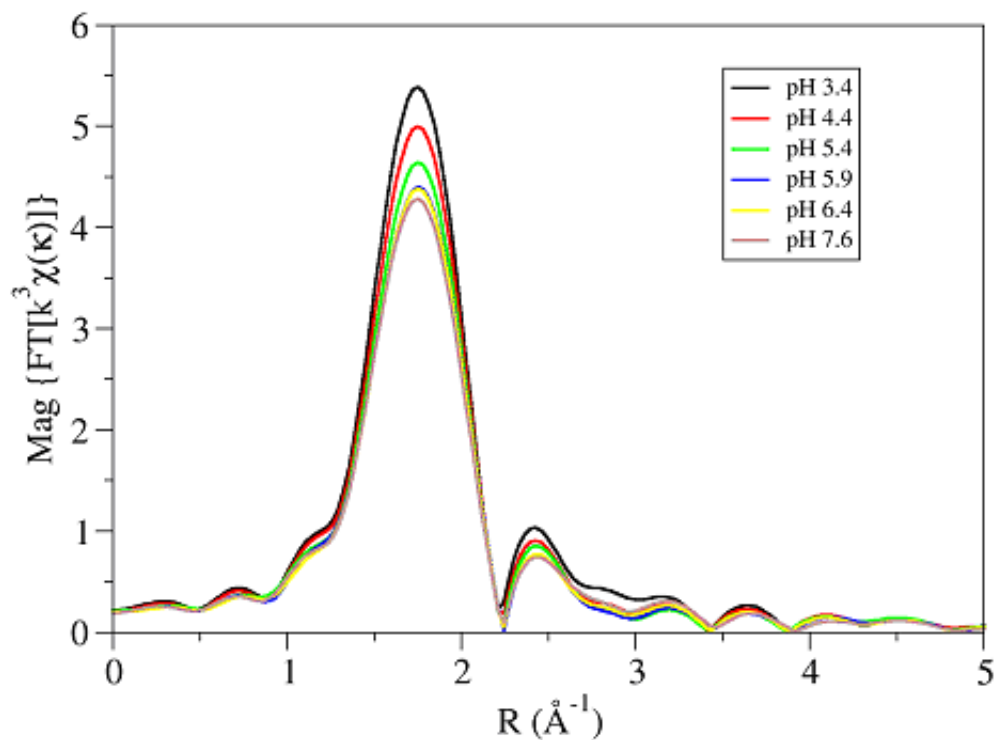


Figure 5.8. Fourier transformed magnitude data for the contaminated soil consortium. Notice the reduction in the amplitude of first shell peak with increase in pH. Amplitude of the first shell spectra of this consortium is higher than the spectra of river water consortium.

5.3.4 Quantitative EXAFS Modeling

5.3.4.1 River Water Consortium

The six river water consortium samples were first fit independently, fitting simultaneously at k weights 1, 2 and 3. Only the four paths (listed in Table 5.2) that were used to fit the Cd standards have been used for fitting the biomass samples. A shell by shell fitting approach was used in which the lower R factor and χ^2_ν values were used as the criteria for the goodness of fit.

The lowest pH sample of the river water consortium, pH 3.7, was attempted

to be modeled as a pure phosphoryl binding to Cd as has been observed in some of the pure Gram positive and Gram negative bacterial strains [13, 69]. But this sample could not be modeled without considering a carboxyl and a sulfide binding to Cd in addition to the phosphoryl binding. Best fit values of the path parameters (σ^2 and ΔR) for this sample were the same (within error bars) as obtained for the Cd standards reported in earlier section. Next four samples at pH values 4.7, 5.7, 6.2 and 6.5 showed a trend of increasing contribution from carboxyl and sulfide binding, with a decrease in phosphoryl binding contribution to Cd. This trend is consistent with the EXAFS modeling of Cd adsorption to Gram negative bacterial cell wall of *Shewanella oneidensis* under similar experimental conditions [69]. Independent modeling of these samples is not the best approach in such a case where relatively small differences have to be brought out as it becomes hard to compare the coordination numbers obtained from independent fits. For instance, small changes in σ^2 could lead to variations in coordination numbers. Hence the spectra at first five pH values were fit simultaneously. Since all these five samples were also fit at k weights 1, 2 and 3 respectively, a total of 15 data sets were fit simultaneously. This fitting procedure puts a rigorous constrain on each other and eliminate the possibility of reaching a local inflection point instead of the global minima. It also breaks down the correlations. In this case, a single ΔE_0 was floated and the ΔE_0 values for the rest of the four samples were set to this value. Similarly only one distance and one Debye-Waller factor was floated for O, C, P and S bonds respectively. The *best fit values* for distances and Debye-Waller factors for these four binding sites are the same (within error bars) as found in standard compounds. The best fit values thus obtained were then set, leaving only 21 parameters to float (ΔE_0 , and coordination number of the four binding

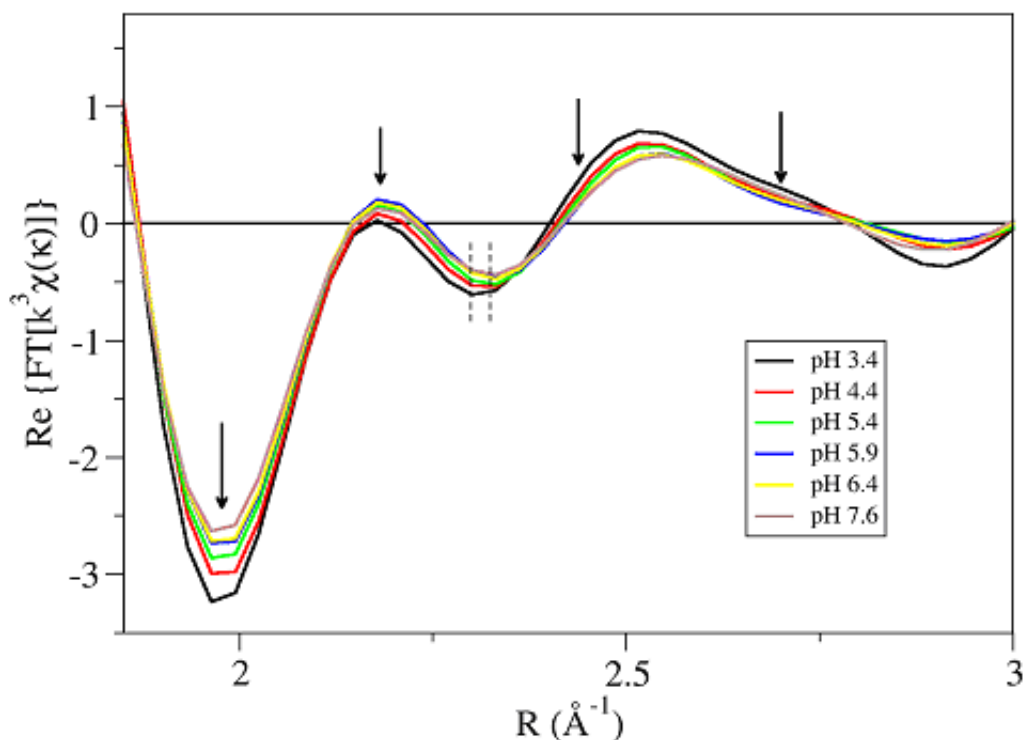


Figure 5.9. Real part of the Fourier transformed contaminated soil consortium data plotted over the data range of 1.85 – 3.0 Å. Peak at 2.2 Å in this case is almost on top of each other in contrast to the dramatic changes in This indicates rise absence of sulphide peak in this consortium. All the samples show strong signature of phosphate binding. The lowest pH sample also shows a phase shift toward lower r value at about 2.4 Å characteristic of sulphate binding.

sites for five samples). Final fitting parameters are shown in Table 5.3.

Sample at pH 7.6 could not be fit with the model developed for samples at other pH conditions. An unusually low ($2 \times 10^{-3} \text{ \AA}^{-1}$) Debye-Waller factor was found for the Cd-P bond, of this sample. This suggests the presence of a different kind of phosphoryl binding at this pH. Boyanov et al. [13] also found similar behavior for Cd adsorption to Gram positive bacterial cell wall of *B. Subtilis* around this pH. A deprotonated phosphoryl group could result in a much tighter binding like

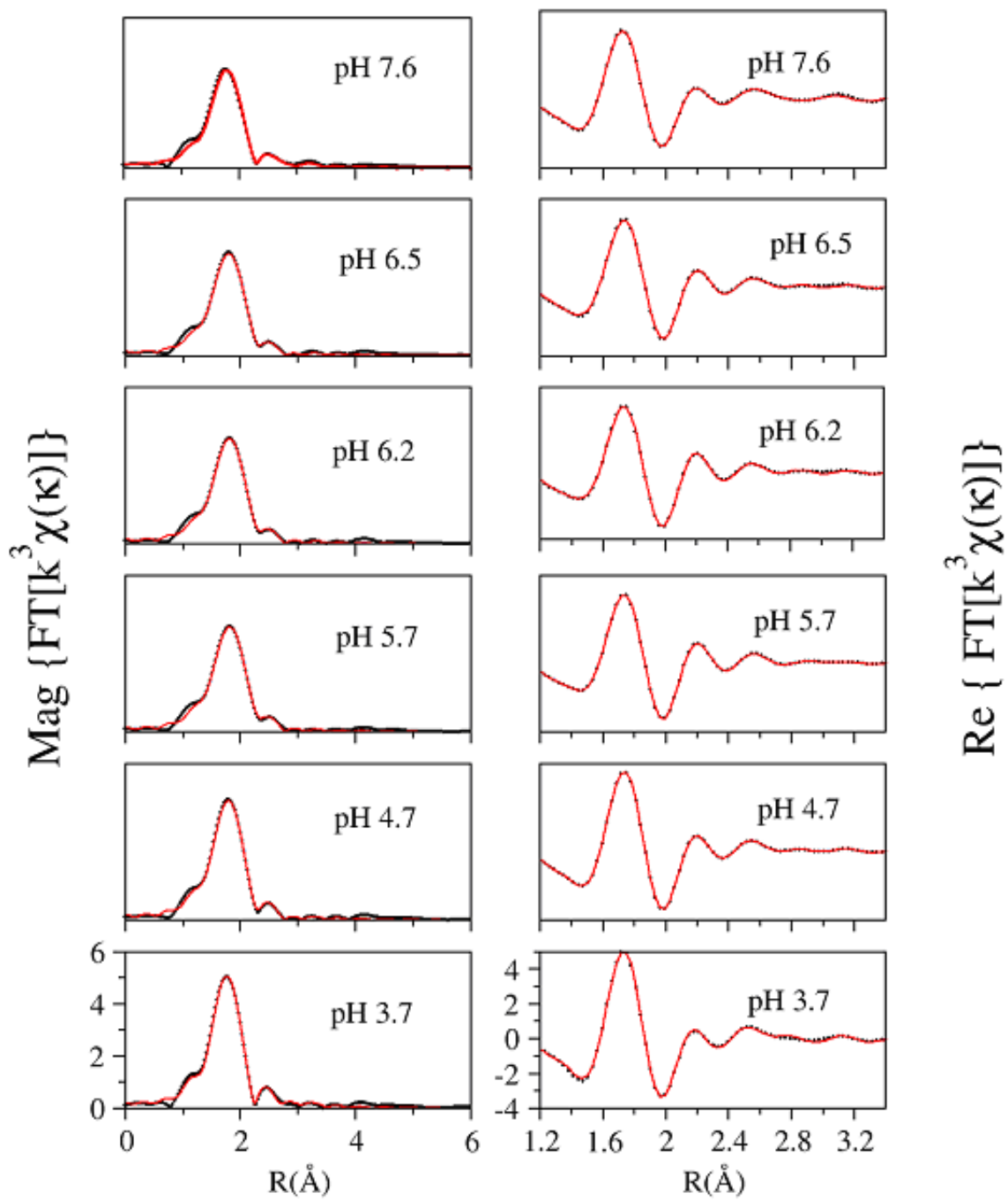


Figure 5.10. Data and fits of the a) magnitude and b) real part of the Fourier transform of the river water consortium samples.

this. Hence such a possibility can not be denied.

Guine et al. [37] reported *sulfhydryl* ligands responsible for Zn adsorption to three Gram negative bacterial strains at low loadings of Zn. However, the characterization of this site was only qualitative in nature, and its quantitative contribution could not be calculated. To this date there is no published literature in the best of our knowledge that quantifies sulfide groups on bacterial surfaces. Our previous work with a number of pure bacterial strains also support carboxyl, phosphoryl and sulfide sites playing key role in Cd adsorption to Gram positive and Gram negative bacterial cell walls [69].

5.3.4.2 Contaminated Soil Consortium

Exact same approach (as described in the previous section) was taken for the EXAFS modeling of the contaminated soil consortium samples. Lowest pH sample was first tried to model as pure phosphoryl binding, but a good fit could not be obtained without considering a carboxyl contribution to Cd in addition to the phosphoryl contribution. Coordination number for P in this sample, however, is 2.5 ± 0.75 , which is unusually high for phosphoryl binding to bacterial systems.

This is likely a case of the EXAFS data not having high enough resolution to distinguish between PO_4 and SO_4 groups. Typical bond length of Cd-S in sulfate group is 3.5 \AA , only 0.08 \AA more than typical Cd-P bond length. In addition, the effective scattering amplitude by these two groups would also be very similar. Hence we are unable to resolve the contribution of SO_4^- from PO_4^- .

Number of oxygen atoms consistently decrease from 5.6 ± 0.10 for the lowest pH sample to 4.6 ± 0.08 for the pH 6.5 sample. Coordination of carboxyl group

TABLE 5.3
SIMULTANEOUS FITTING PARAMETERS OF THE
NATURAL CONSORTIA SAMPLES

	3.7	4.7	5.7	6.2	6.5
N_o	4.91 ± 0.25	4.15 ± 0.20	3.29 ± 0.30	3.33 ± 0.25	3.46 ± 0.24
N_c	0.82 ± 0.45	0.53 ± 0.42	0.80 ± 0.46	0.91 ± 0.49	0.67 ± 0.38
N_s	0.37 ± 0.12	0.78 ± 0.10	1.17 ± 0.12	1.14 ± 0.10	0.89 ± 0.09
N_p	1.45 ± 0.30	0.76 ± 0.28	0.58 ± 0.32	0.65 ± 0.30	0.55 ± 0.2
R_o			$2.29 \pm 0.01 \text{ \AA}$		
R_c			$2.70 \pm 0.03 \text{ \AA}$		
R_s			$2.53 \pm 0.02 \text{ \AA}$		
R_p			$3.36 \pm 0.05 \text{ \AA}$		
ΔE_0			$-2.2 \pm 0.30 \text{ eV}$		
σ_o^2			0.009 \AA^{-2}		
σ_c^2			0.012 \AA^{-2}		
σ_s^2			0.009 \AA^{-2}		
σ_p^2			0.015 \AA^{-2}		

TABLE 5.4
SIMULTANEOUS FITTING PARAMETERS OF THE
CONTAMINATED CONSORTIA SAMPLE

	3.4	4.4	5.4	5.9	6.4
No	5.58 ± 0.35	5.25 ± 0.38	4.80 ± 0.55	4.61 ± 0.36	4.60 ± 0.33
Nc	0.96 ± 0.62	0.93 ± 0.66	0.85 ± 0.82	0.63 ± 0.60	0.71 ± 0.58
Np	2.50 ± 0.75	1.81 ± 0.80	1.53 ± 0.65	1.41 ± 0.60	1.52 ± 0.65
R_o			$2.29 \pm 0.01 \text{ \AA}$		
R_c			$2.68 \pm 0.03 \text{ \AA}$		
R_p			$3.38 \pm 0.05 \text{ \AA}$		
ΔE_0			$-1.5 \pm 1.0 \text{ eV}$		
σ_o^2			0.009 \AA^{-2}		
σ_c^2			0.012 \AA^{-2}		
σ_p^2			0.015 \AA^{-2}		

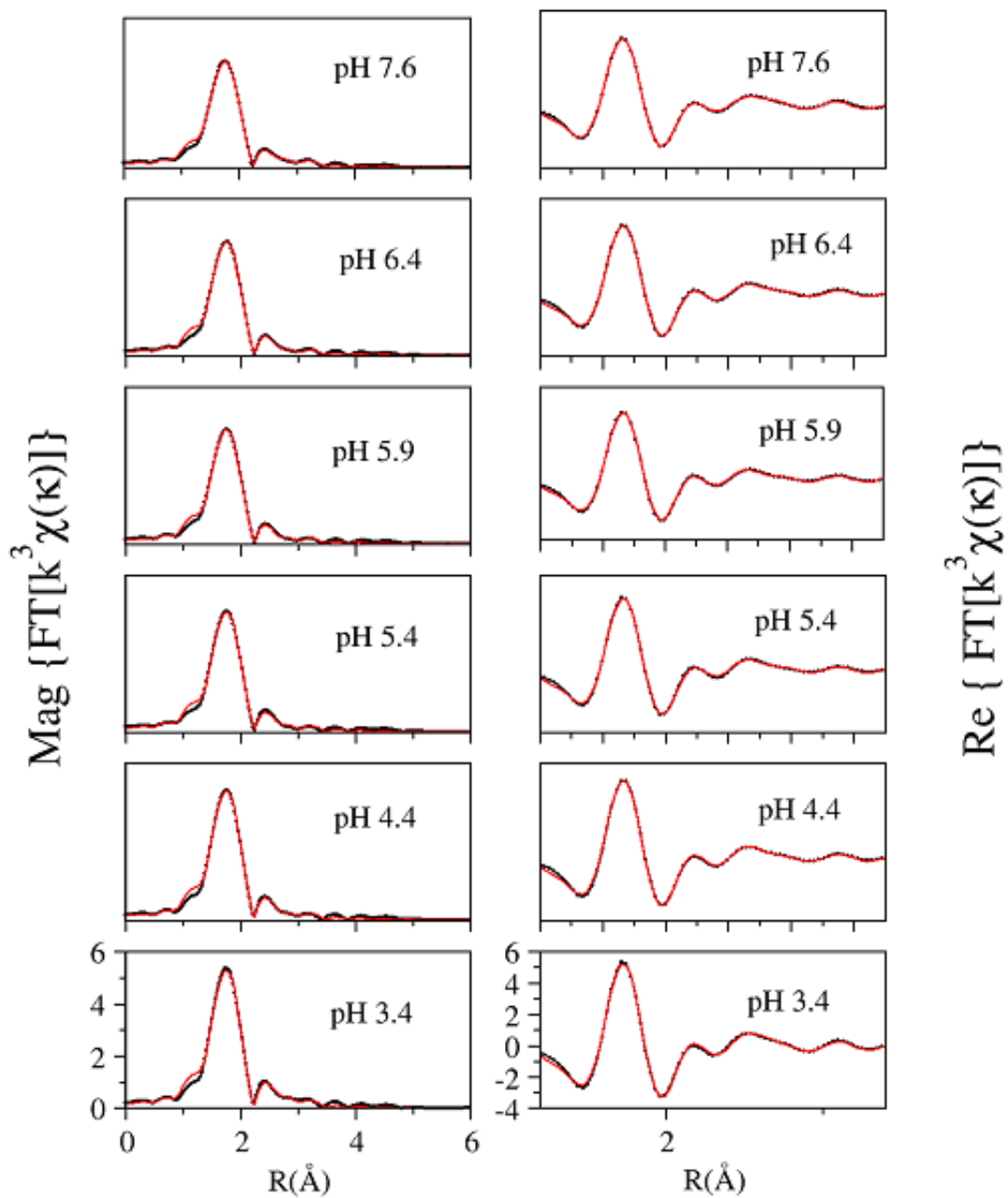


Figure 5.11. Data and fits of the a) magnitude and b) real part of the Fourier transform of the contaminated soil consortium samples.

TABLE 5.5

FITTING PARAMETERS OF THE HIGHEST PH
 SAMPLE OF NATURAL AND CONATMINATED
 CONSORTIA SERIES

	CdNC 7.6	CdCC 7.6
ΔE_0	-0.90 0.30	-1.30 0.25
N_o	4.05 ± 0.22	4.55 ± 0.20
N_c	1.12 ± 0.40	0.62 ± 0.40
N_s	0.30 ± 0.10	
N_p	0.42 ± 0.24	1.12 ± 0.44
R_o	2.29 ± 0.01	2.29 ± 0.01
R_c	2.70 ± 0.03	2.68 ± 0.03
R_p	3.36 ± 0.05	3.38 ± 0.05
R_s	2.53 ± 0.02	
σ_o^2	0.009	0.009
σ_c^2	0.012	0.012
σ_p^2	0.002 ± 0.003	0.010 ± 0.004
σ_s^2	0.009	
R_x is in \AA , σ_x^2 is in \AA^{-2} and ΔE_0 is in eV		

shows a slight decrease but remains roughly the same within error bars ($0.96 \pm 0.30 - 0.65 \pm 0.30$). Coordination number of the phosphoryl group also remains constant ($\sim 1.6 \pm 0.20$) within error bars for the samples at pH 4.4, 5.4, 5.9 and 6.5. Debye-Waller factors and distances for the first five pH samples were the same (within error bars) as the river water consortium and hence also to the Cd standard compounds. Final fitting parameters of the simultaneous fits are shown in Table 5.4.

Unlike the case of river water consortium, the highest pH sample, pH 7.6, fit well with the same model as used for the first five pH samples with slightly lower Debye-Waller factor (0.010 ± 0.004 instead of 0.015 \AA^{-2}). Fitting parameters for the highest pH sample of the river water and contaminated soil consortium are shown in Table 5.5.

The contaminated soil consortium of bacteria showed a rather constant binding mechanism over the pH range examined (pH 3.4–7.6). Consistency of the binding mechanism of contaminated soil consortium is in contrast with the binding mechanism of Cd in the case of river water consortium which shows huge changes in the relative contribution of the three functional groups at each pH value measured. Phosphoryl groups seem to dominate Cd binding to contaminated soil consortium at all pH values. Coordination number of P atoms is also slightly higher than normally observed in the river water consortium. Increased phosphoryl groups might have something to do with change in bacterial physiology in contaminated environments leading to bacterial stress condition. Bacteria are known to produce more EPS under stress conditions, and phospholipids are an important constituent of the EPS. High coordination number of phosphoryl groups could be attributed to such a phenomenon.

In summary this study shows that Cd adsorption to a consortium of bacteria consisting of four to six different species yields a meaningful EXAFS signal over a wide pH range. This observation is non-trivial, as it is hard to imagine that Cd adsorption to a randomly selected four to six different types of surfaces would yield an EXAFS signal which could be coherently modeled over a pH range of 3.4 – 7.6. Such an observation suggests that despite the fundamental differences in the composition of the cell walls of one type of bacteria from another, broadly categorized as Gram positive and Gram negative bacteria, same functional groups are responsible for the reactivity of their surfaces. Since current study examines two different bacterial consortia obtained from completely different geologic settings, it can be easily assumed that this observation is true for bacterial surfaces over a wide variety of physical conditions.

More importantly it has been shown that the river water consortium of bacteria could be modeled using three fundamental sites only - phosphoryl, carboxyl and sulfide, and the contaminated soil consortium has been modeled using phosphoryl and carboxyl sites only. Although it is possible that a sulfate-type group is also present in the contaminated soil consortium but could not be resolved by EXAFS.

5.4 Conclusion

Cd K edge XAFS measurements of Cd adsorption to two different consortia of bacteria clearly indicate that a consortium of bacteria sampled from a real geologic setting can be modeled using XAFS over a wide pH range of 3.4 – 7.6. Results thus obtained are indicative of the universality of the bacterial binding environment. Our result is in agreement with Borrok et al. [12], who showed that consortia of bacteria grown from a wide range of uncontaminated soil and

water environments exhibit roughly similar affinities for protons and Cd. The Cd XAFS data for the river water consortium was modeled using three sites only - phosphoryl, carboxyl and sulfide. Lowest pH sample, pH 3.4, was dominated by phosphoryl and carboxyl binding with small contribution from the sulfide group. A steep rise in sulfide contribution and fall in phosphoryl contribution was observed with an increase in pH, (up to pH 6.5). Carboxyl contribution remained roughly the same over this pH range. The highest pH sample, pH 7.6, could not be fit with the model used for the first five pH samples. At this pH, the river water consortium was dominated by carboxyl and phosphoryl contribution with an unusually low Debye-Waller factor for phosphoryl ligand.

The contaminated soil consortium (sampled from a manufacturing gas plant site) exhibited an increased Cd uptake which is in agreement with the observation of Borrok et al. [11], who demonstrated that bacterial consortia from hydrocarbon-contaminated environments do not exhibit the same relatively narrow range of proton and Cd adsorption behavior as bacterial consortia from natural environments. Cd XAFS data for the contaminated soil consortium was modeled using phosphoryl, and carboxyl groups only. Phosphoryl group was the predominant binding group for the entire range of pH (pH 3.4 – 7.6) investigated. But a possibility of the presence of reduced sulfate groups can not be ruled out. Soft x-ray absorption spectroscopy at S edge would be able to provide more insight about such a possibility. Reason for the deviation in binding mechanism of contaminated consortium from natural consortium is not clear from this study.

Overall, this study suggests that despite the complex physiology of each bacterial strain the adsorption mechanism does not vary much between different strains. From the metal-adsorption chemistry point of view, the main difference lies in the site

ratio of two- three fundamental sites only. Results thus obtained can potentially have very high impact on the modeling of the complex bacterial systems in realistic geological settings, leading to further refinement and development of robust remediation strategies for metal contamination at macroscopic level.

CHAPTER 6

USING ADSORPTION ISOTHERM MEASUREMENTS TO CONSTRAIN MECHANISMS OF Cd ADSORPTION ONTO *BACILLUS SUBTILIS* AND *SHEWANELLA ONEIDENSIS* BACTERIAL CELL WALLS - INTERGRATING EXAFS AND THERMODYNAMIC MODELING

6.1 Introduction

Metal speciation and bioavailability in real geologic settings are dominated by their adsorption onto bacterial surfaces. The large fraction of the metals has been estimated to be associated with the microorganisms under the experimental conditions by Ledin et al. [59]. Bacterial adsorption of aqueous metal contaminants can also augment the mobility of the contaminants in water-rock systems under specific conditions (McCarthy; Lindqvist and Jenkins). Thus, to develop a precise mechanistic understanding of the exact reactions taking place, the spatial distribution and chemical speciation of contaminants in presence of bacterial surfaces must be characterized at atomic resolution. Understanding and modeling contaminant transport in the environment is not only vital in determining the environmental fate of these contaminants and their relative risk but also in developing remediation strategies as the final goal.

While pH dependent studies are important tools for determining the binding constants of ligands responsible for adsorption by bacterial surfaces, pH isotherm

measurements of metal adsorption by them provide more rigorous constraints on the metal:site stoichiometry than do standard pH edge adsorption experiments, and these experiments test if the dominant binding mechanism changes as a function of metal concentration. A constant binding mechanism over a wide range of metal concentrations would allow the use of one set of stability constants to account for the adsorption behavior over the entire range of metal concentration. In contrast, a change in mechanism as a function of metal concentration would require that a number of reaction constants be determined and the metal:site concentration ratio be known more exactly in the natural system of interest for the successful determination of the effects of bacterial adsorption on metal speciation and mobility. Clearly the site stoichiometry of metal:ligand must be modeled for adsorption by bacterial surfaces.

Gram-positive and Gram-negative bacteria are two distinct morphological groups of bacteria with fundamental differences in the structure of their cell walls. The Gram-positive cell wall appears thick and consists of numerous interconnecting layers of the polymer peptidoglycan (Fig. 6.1). Also interwoven in the cell wall of Gram-positive bacteria are teichoic acids. Generally, 60% –90% of the Gram-positive cell wall is peptidoglycan. The Gram-negative cell wall, on the other hand, contains a much thinner, single layer of peptidoglycan which is surrounded by an outer membrane composed of phospholipids, lipopolysaccharide, and lipoprotein (Fig. 6.2). The porous structure of the outer membrane is highly permeable.

Only 10% – 20% of the Gram-negative cell wall is peptidoglycan. Except in unusual cases, teichoic acid, teichuronic acid, and lipoteichoic acid are not found in Gram-negative cell walls. Sherbert [94] showed that LPS of Gram-negative bacteria are the components primary responsible for the anionic character and metal

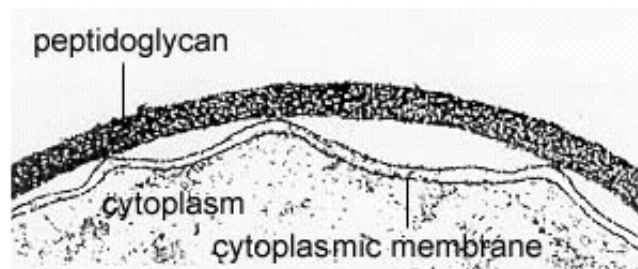


Figure 6.1. Cell wall of Gram positive bacterium. [Adapted from <http://www.cat.cc.md.us/courses/bio141/lecguide/unit1/prostruct/gncw.html>]

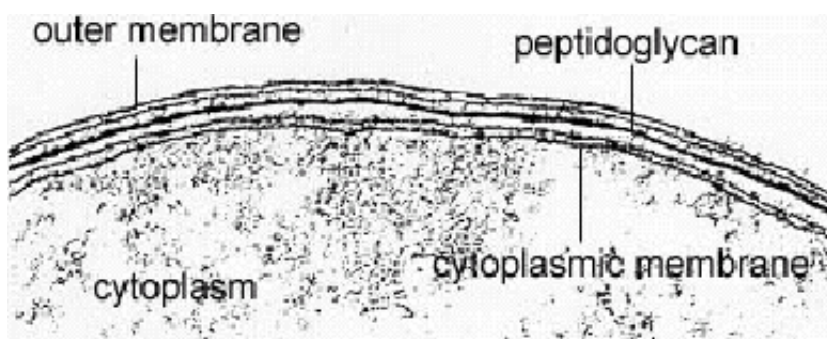


Figure 6.2. Cell wall of Gram negative bacterium. [Adapted from <http://www.cat.cc.md.us/courses/bio141/lecguide/unit1/prostruct/gncw.html>]

binding ability of the cell wall. Extracellular polysaccharides (EPS) are also capable of binding metals. The presence and abundance of EPS depends on the species of bacteria and on the growth conditions. But EPS can often be easily removed with simple mechanical disruption (e.g., centrifugation) or chemical washing (e.g., acid rinse). However, all these results are based only on bulk adsorption data. XAFS measurements at the complexed metal absorption edge can distinguish between the different functional groups proposed to be important in metal uptake, thereby providing additional independent constraints on the stoichiometry of the

adsorption reactions.

Although there are a number of XAFS studies of metal adsorption of bacterial cell walls in the literature, most of them are pH-dependent studies. These studies have shown that phosphoryl and carboxyl functional groups are responsible for metal complexation by Gram-positive bacteria [13, 47] and Gram-negative bacteria [103] despite fundamental differences in molecular structure of their exterior surfaces. They are also in agreement with the results of an infrared spectroscopic study of microbial surface functional groups that confirmed phosphoryl and carboxyl groups as those contributing to the negative surface charge of the bacteria studied in the pH range [108]. There are, however, not enough studies in the literature (only two) showing the change in binding mechanism of metal complexation with bacterial cell wall as a function of metal loading at a given pH. To further complicate the matter, these two results are not consistent. For example, Sarret et al. [89] showed the phosphoryl group to be the predominant complexing ligand on fungal cell walls at pH 6 as a function of Zn loading; only at highest Zn loading was the carboxyl group found to be the complexing ligand. But Guine et al. [37] reported *sulfhydryl* groups responsible for Zn adsorption to three Gram negative bacterial strains at low loadings of Zn. However, the characterization of this site was only qualitative in nature, and its quantitative contribution could not be calculated.

It is clear that the literature lacks data on pH isotherm measurements to reach any consensus about the site stoichiometry of important adsorption reactions on bacterial surfaces. The binding mechanism of different metals needs to be characterized on representative bacterial surfaces. A particular toxic heavy metal, Cadmium, a toxic heavy metal, has become a significant contaminant in many soil

and groundwater systems. Understanding the processes that control the mobility and bioavailability of cadmium in the environment is thus becoming increasingly important.

In this study we have measured pH isotherm curves for Cd adsorption on *Bacillus Subtilis* and *Shewanella oneidensis*, commonly occurring Gram positive and Gram negative bacteria respectively, at circumneutral pH condition (\sim pH 6) as a function of Cd loading over three orders of magnitude (from sub PPM level to 200 PPM). Thermodynamic equilibrium modeling was used to constrain the stoichiometry of the important adsorption reaction using FITEQL [110]. To better understand the molecular-scale adsorption mechanisms and to determine whether the adsorption mechanism changes as a function of Cd loading onto the cell walls, we conducted X-ray Absorption Fine Structure (XAFS) measurements over a wide range of Cd concentrations (1 – 200 ppm for *B. Subtilis* and 3 – 200 ppm for *Shewanella*) at a fixed bacterial concentration of 10 g/l (wet weight).

6.2 Methods and Materials

6.2.1 Bacterial Growth and Harvest

Bacterial growth and wash procedure were followed as described in Fein et al. [31, 32]. A plated colony was transferred from the experimental plate to a sterile 7 ml TSB +0.5% yeast extract broth tube under the laminar flow hood which was then incubated for 24 hours at 32°C in an incubator/shaker. A broth tube was transferred to 1 l of TSB +0.5% yeast extract under laminar flow hood and incubated for another 24 hours at 32°C in an incubator/shaker. The cells were removed from the nutrient medium by centrifugation and rinsed twice with 0.1M NaClO₄ (the electrolyte used in the experiments). Three additional rinses with

0.1M NaClO₄ were performed. The cells were not acid washed in order to avoid excessive disruption of the cell wall structure [12].

6.2.2 Cd Adsorption Experiments

After the final wash, cells were transferred to weighed test tubes and the final moist/wet weight of each bacterial pellet was calculated. Washed bacteria were suspended in 0.1 M NaClO₄ electrolyte to form parent solution of 10 g/l of bacteria (wet weight). NaClO₄ electrolyte was pH adjusted to ~ 6.0 prior to suspending the washed bacteria, so that the bacteria were never exposed to acidic or basic conditions. 1000 PPM of parent Cd solution (99.99% pure as obtained from Alfa-Aldrich) was then pH adjusted to ~ 6.0 . Desired loading of pH adjusted Cd was suspended in the bacterial parent solution and allowed to equilibrate for two hours. Previous studies in Fein's laboratory have demonstrated that equilibrium of the adsorption reaction generally occurs in less than 1 h and that the adsorption reaction is fully reversible (see Fowle and Fein 2000 for a complete discussion). pH was monitored every half an hour and adjusted as required using 1 M HNO₃ and NaOH. Final pH was measured after two hours and the solution was centrifuged. The resultant supernatant was filtered (0.45 μm) and analyzed for Cd using an inductively coupled plasma-atomic emission spectroscopy technique with matrix-matched standards. The concentration of metal adsorbed to bacteria in each vessel was calculated by subtracting the concentration of metal that remained in solution (supernatant) from the original Cd concentration in the stock solution. Finally the homogeneous pellet formed at the base of each vessel was loaded into slotted Plexiglas holders and covered with Kapton film, which was then taken to APS for XAFS measurements. All the XAFS measurements were performed within 30 hrs

of the adsorption experiment, and the samples were refrigerated the entire period.

6.2.3 Surface Complex Modeling

Surface complexation modeling formulates adsorption in terms of the actual reactions that occur at the bacterial surface. For example, the deprotonation of the surface organic functional groups, which gives rise to the negative charge of the cell wall, can be described by the following reaction:



where R represents the bacterium to which each functional group, A, is attached. In addition, interactions between aqueous metal cations (M^{m+}) and deprotonated surface sites on the bacterial cell wall can be represented as:



where x and y represent stoichiometric coefficients that must be determined experimentally. In order to consider bacterial (or mineral) surface sites as thermodynamic chemical components, the electrostatic interactions between the surface electric field and aqueous ions near the surface must be accounted for using the following equation [100]:

$$K = K_{Intrinsic} \exp\left(-\frac{\Delta Z F \Psi}{RT}\right) \quad (6.3)$$

where F and R are Faraday's constant and the gas constant, T is absolute temperature, $K_{Intrinsic}$ represents the equilibrium constant referenced to zero surface

charge, Ψ is the electric potential of the bacterial surface, and ΔZ is the change in the charge of the surface species in the reaction. Absolute species concentrations can be calculated for a range of conditions once the appropriate equilibrium constant values are known. Surface complexation modeling is so named because it explicitly accounts for the adsorbed solute as a "surface complex", or a distinct thermodynamic species with a fixed stoichiometry. A surface complex, like an aqueous complex, has a thermodynamic stability which is described by the equilibrium constant. Clearly, the application of surface complexation modeling requires that reversibility of 6.1 and 6.2 to be demonstrated, and that values of the stoichiometry coefficients (x and y in equilibrium 6.2) and the equilibrium constants must be determined. Using acid/base titrations and metal-bacteria adsorption experiments, deprotonation constants for the important surface functional groups and site-specific thermodynamic stability constants for the important bacterial surface complexes have been determined [32, 112]. Their experimental results indicate that three types of organic functional groups are present and proton-active on the bacterial surfaces. The data constrain the values of the deprotonation constants for the three sites, with values typical of carboxyl ($pK \cong 4.8$), phosphate ($pK \cong 6.9$), and hydroxyl functional groups ($pK \cong 9.4$). Fein et al. [32], Daughney et al. [25] and [24] each find evidence for metal-carboxyl and metal-phosphato bacterial surface complexation.

6.3 Results and Discussions

6.3.1 Cd Isotherm Experiment

The result from the Cd adsorption isotherm experiment for *B. Subtilis* is shown in Fig. 6.3. Similar isotherm curve was obtained for *Shewanella* isotherm (not

shown). A smoothly varying curve was obtained for both the isotherms using ICP. Such a curve rules out the possibility of drastic changes in the binding mechanism or bacterial ligands playing role in Cd uptake as a function of metal loading. However, it was not clear from this result whether a single site or combination of sites play role in Cd binding to bacterial cell wall. Further, thermodynamic equilibrium modeling was used to predict the stoichiometry of the reaction using FITEQL.

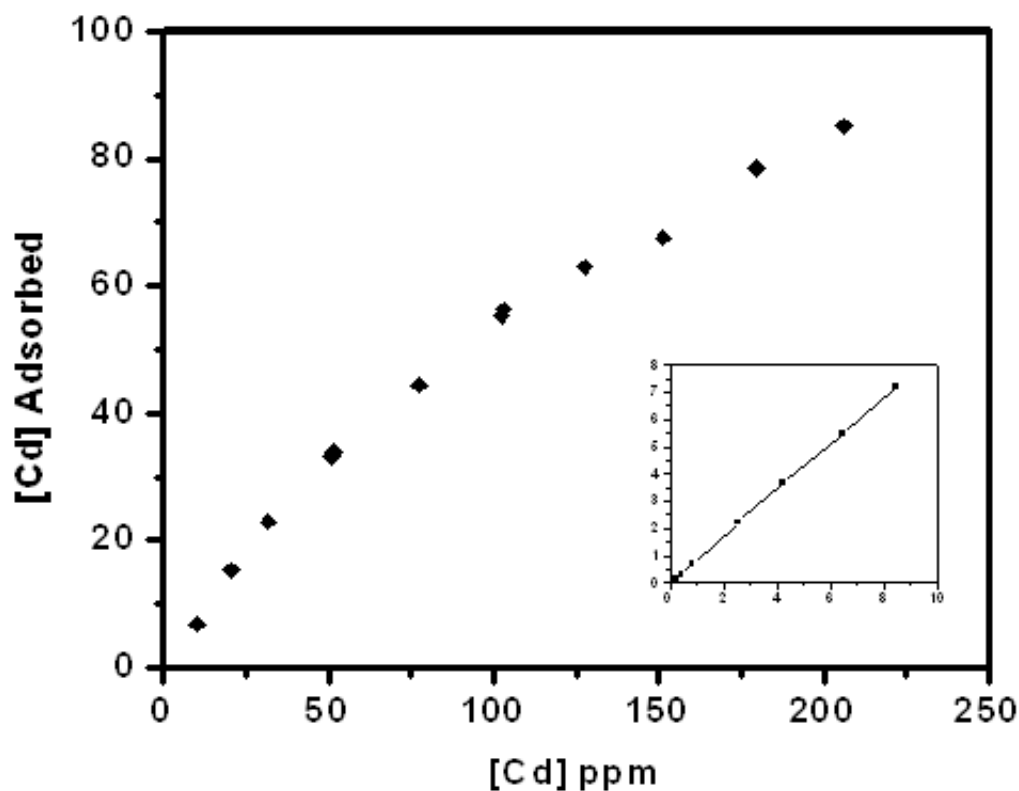


Figure 6.3. Cd adsorption isotherm for *B. Subtilis*. In low concentration regime, a linear relation between the initial and adsorbed Cd is observed. At higher concentration, it deviates from the linear behavior suggesting saturation of sites.

6.3.2 Thermodynamic Modeling of the pH Isotherms

We used FITEQL 2.0 [109] to calculate the best fitting stability constants for the metal-bacterial surface complexes. The application of this code to measurements of metal adsorption onto bacterial surfaces has been described elsewhere in detail [32]. The program accounts for both the aqueous and surface complexation reactions that occur in the experimental systems, and it adjusts the intrinsic stability constants used in the calculations to account for the effects of the bacterial surface electric field.

An attempt to fit the *B. Subtilis* isotherm data with different stoichiometry was made until we obtained an adequate fit to the experimental data. The value of the variance parameter $V(Y)$ from FITEQL's output was used as the criterion to distinguish which model best fits the experimental data:

$$v(y) = \frac{\sum \left(\frac{Y_{calc} - Y_{exp}}{S_{exp}} \right)^2}{n_p n_{II} - n_u} \quad (6.4)$$

where Y_{calc} and Y_{exp} are the calculated and experimental data, S_{exp} is the error associated with the experimental data, n_p is the number of data points, n_{II} is the number of group II components (components for which total and free concentrations are known), and n_u is the number of adjustable parameters. In general, $V(Y)$ values from approximately 1 to 20 indicate excellent fits between a model and experimental data [109].

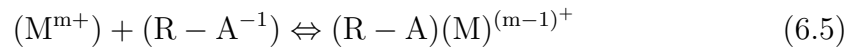
Thermodynamic modeling of the isotherm data was done using surface complexation approach. Cd:carboxyl stoichiometry of 1 : 1, 1 : 2 and 2 : 1 was tried using a non electrostatic model. Results thus obtained are listed in Table 6.1, and the data with models are shown in Fig. 6.4. The $V(Y)$ values, from non-

TABLE 6.1

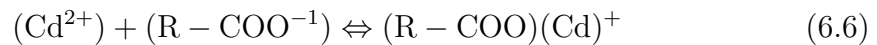
FITTING PARAMETERS FOR THE SURFACE
COMPLEXATION MODEL DETERMINING SITE
STOICHIOMETRY USING NON-ELECTROSTATIC
MODEL

Cd:carboxyl Binding stoichiometry	Equilibrium constant K	Goodness of fit V(Y)
1:1	3.388	10.62
1:2	6.361	320.1
2:1	7.759	174.9

electrostatic models with different stoichiometry, decrease by approximately an order of magnitude for the chosen model. 1 : 1 Cd:carboxyl stoichiometry was clearly the best. This modifies the equation 6.2 to



and more specifically to



Modeling for the *Shewanella* isotherm data is still in progress, and hence could not be included here.

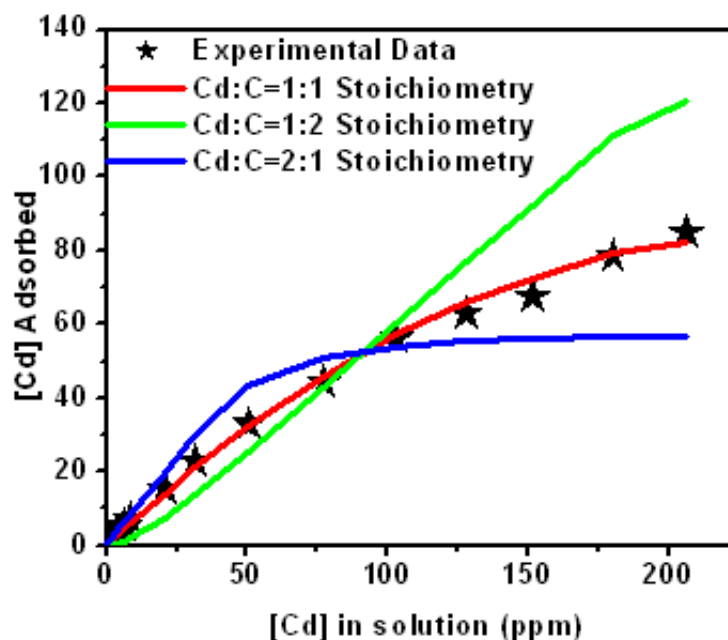


Figure 6.4. Experimental data and models for different site Cd:C stoichiometry.

6.3.3 X-ray Absorption Fine Structure

Please refer to chapter 5 for the details of the XAFS standards, measurements and data reduction processes. A detailed account measurements and data reduction processes have been presented there. Same standard compounds have been used for the analysis of results presented in this chapter.

6.3.4 Qualitative Analysis of XAFS Spectra

Magnitude real part of the Fourier transform data for Cd - *B.subtilis* isotherm is shown in Fig. 6.5 and Fig. 6.6 respectively. A rise in peak at 2.2 Å can be clearly seen in Fig. 6.6. Based on the "fingerprint" of C, P and S binding to Cd from Fig. 5.5, such a rise can be attributed to increasing carboxyl or sulfide

binding to Cd. The two lowest concentration samples, 3.0 and 1.0 ppm, have high amplitude and a phase shift at this peak toward higher r value resembling CdS spectra.

The magnitude real part of the Fourier transform data for Cd - *Shewanella* isotherm is shown in Fig. 6.7. The corresponding real part of the transform over the range of the 2nd and 3rd shells is shown in Fig. 6.8. Dramatic changes can be seen in the real part of the Fourier transform data (Fig. 6.8). Similar arguments, as used for Cd-*B.subtilis* spectra, indicates an increase in sulfide binding contribution with decreasing Cd concentration.

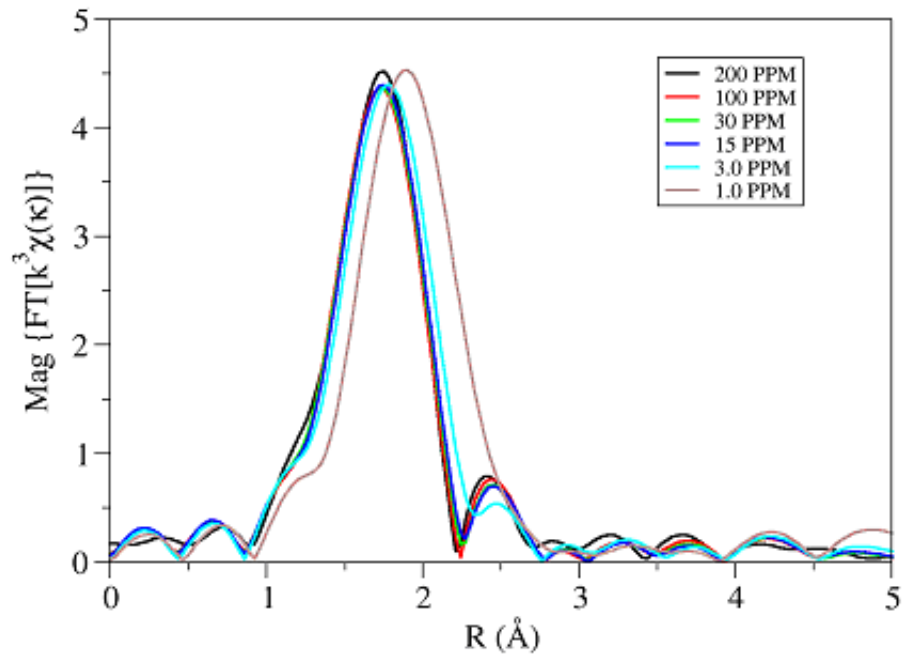


Figure 6.5. Fourier Transform magnitude of the *B. Subtilis* isotherm data.

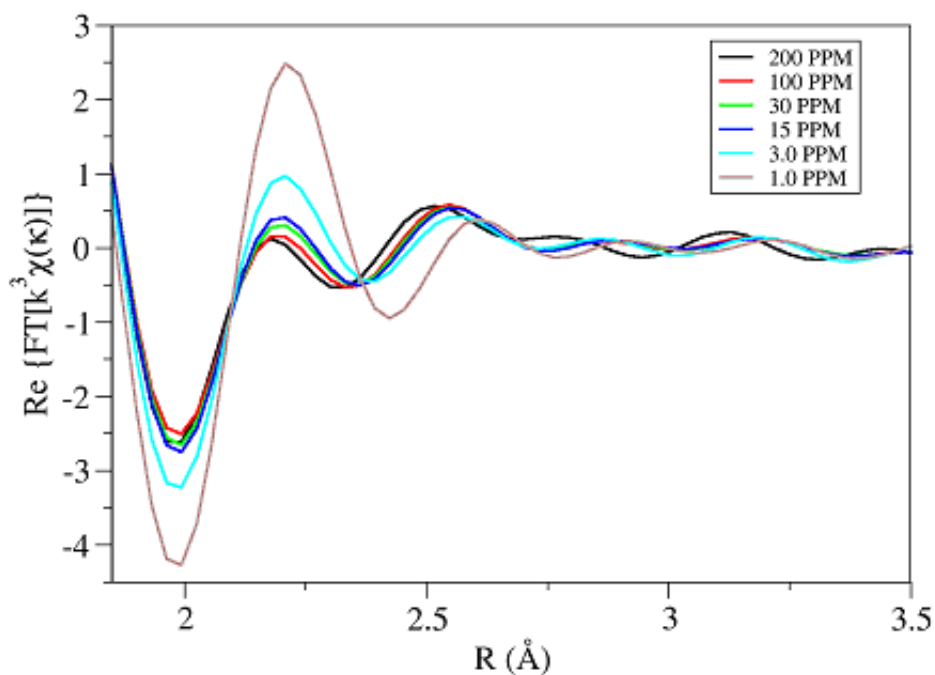


Figure 6.6. Real part of the Fourier Transform data of the *B. Subtilis* isotherm.

6.3.5 Quantitative EXAFS Modeling

The six *B. Subtilis* isotherm samples were fit independently, fitting simultaneously at k weights 1, 2 and 3. Only the four paths (listed in Table 5.2) that were used to fit the Cd standards have been used for fitting the biomass samples. A shell-by-shell fitting approach was used in which the lower R factor and χ^2_ν values were used as the criteria for the goodness of fit. The distances of these four paths were set to the distances obtained for the standards, and the Debye-Waller factors were floated. The best fit values thus returned were the same as found

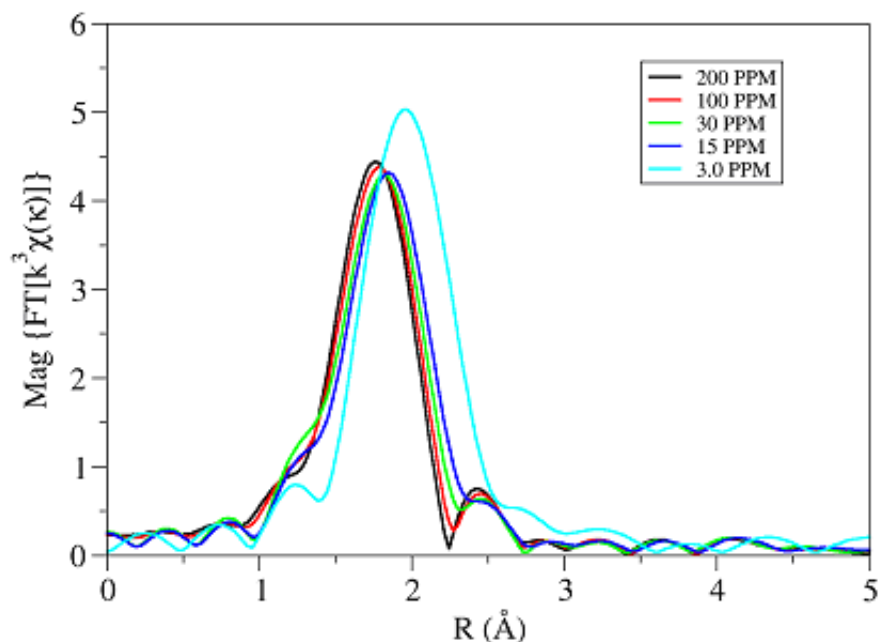


Figure 6.7. Fourier Transform magnitude of the *Shewanella* isotherm data.

in the standards. Hence the Debye-Waller factors were set to the best fit values to reduce the uncertainty and break down the correlations between different parameters. Fitting parameters are listed in Table 6.2. An increase in the number of O atoms in first shell is associated with decrease in S atoms in the first shell with increasing Cd concentration. Carboxyl contribution is constant within error bars but the contribution of phosphoryl group increase with an increase in Cd concentration.

Exact same approach has been adopted for modeling the five samples of the *Shewanella* isotherm. Fitting parameters thus obtained are listed in Table 6.3. A trend similar to the one seen in *B. subtilis* isotherm was also seen in the *Shewanella* isotherm modeling. Sulfide contribution decreases with increasing Cd concentration. Decrease in sulfide contribution was associated with an increase in O atoms

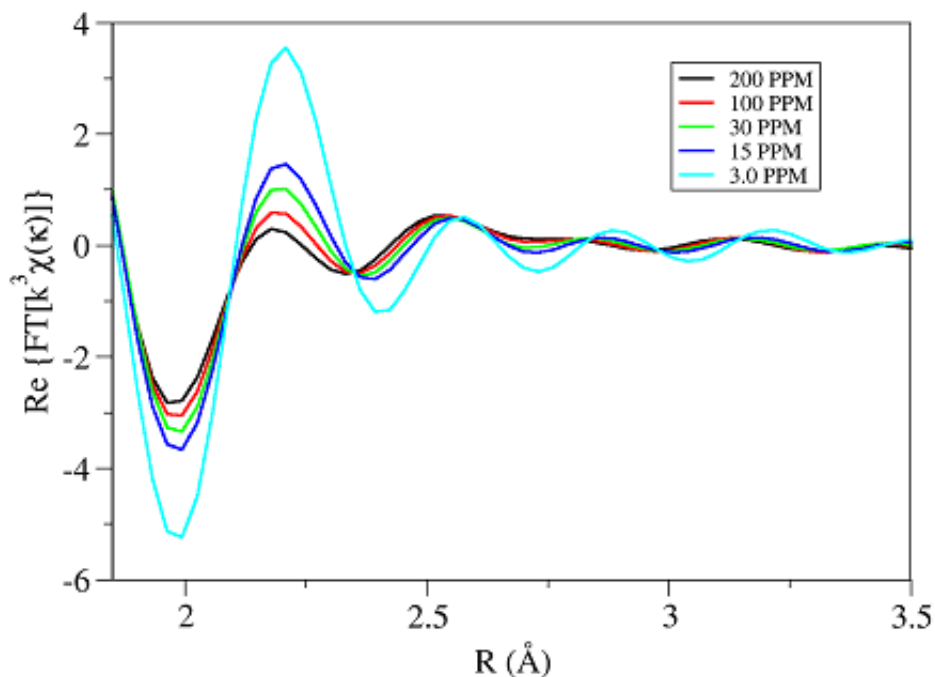


Figure 6.8. Real part of the Fourier Transform data of the *Shewanella* isotherm.

in the first shell. However, the lowest concentration sample in this case, 3.0 ppm Cd, could be fit using S atoms only. Carboxyl contribution remained constant within error bars in all the samples except the lowest concentration sample where no carboxyl contribution was seen. Phosphoryl contribution increased with an increase in the Cd contribution.

In summary, this study shows that a Gram positive and Gram negative bacterial surface could be modeled over two orders of magnitude of Cd concentration using the same path parameters. Although bulk adsorption isotherm and surface complexation modeling data did not exhibit any change in binding mechanism of Cd, XAFS modeling shows three sites are responsible for Cd binding to these two

TABLE 6.2: XAFS FITTING PARAMETERS FOR THE *B. SUBTILIS* ISOTHERM SAMPLES

	1.0	3.0	15	30	100	200
ΔE_0	-1.5 ± 0.26	-2.5 ± 0.88	-2.28 ± 0.20	-2.24 ± 0.16	-2.94 ± 0.42	-2.35 ± 0.18
N_o	1.95 ± 0.16	3.93 ± 0.28	4.67 ± 0.16	4.78 ± 0.12	4.68 ± 0.16	4.93 ± 0.14
N_c	1.22 ± 0.52	1.23 ± 0.62	0.97 ± 0.48	0.89 ± 0.46	0.99 ± 0.60	0.98 ± 0.48
N_s	2.87 ± 0.14	0.98 ± 0.22	0.17 ± 0.14	0.08 ± 0.04		
N_p		0.48 ± 0.34	0.82 ± 0.36	0.82 ± 0.32	1.12 ± 0.40	1.03 ± 0.40
R_o				$2.29 \pm 0.01 \text{ \AA}$		
R_c				$2.70 \pm 0.03 \text{ \AA}$		
R_s				$2.53 \pm 0.02 \text{ \AA}$		
R_p				$3.38 \pm 0.05 \text{ \AA}$		
σ_o^2				0.009 \AA^{-2}		
σ_c^2				0.012 \AA^{-2}		
σ_s^2				0.009 \AA^{-2}		
σ_p^2				0.015 \AA^{-2}		

TABLE 6.3
XAFS FITTING PARAMETERS FOR THE *SHEWANELLA*
ISOTHERM SAMPLES

	3.0	15	30	100	200
ΔE_0	-0.5 ± 1.92	-0.48 ± 0.72	-0.90 ± 0.62	-1.35 ± 0.66	-1.30 ± 0.42
N_o	0.45 ± 0.82	3.18 ± 0.28	3.72 ± 0.22	4.28 ± 0.20	4.68 ± 0.14
N_c		1.17 ± 0.42	1.30 ± 0.56	1.46 ± 0.60	1.40 ± 0.54
N_s	4.10 ± 0.65	1.42 ± 0.14	0.90 ± 0.16	0.45 ± 0.16	
N_p		0.35 ± 0.26	0.58 ± 0.30	0.83 ± 0.30	0.95 ± 0.34
R_o			$2.29 \pm 0.01 \text{ \AA}$		
R_c			$2.70 \pm 0.03 \text{ \AA}$		
R_s			$2.53 \pm 0.02 \text{ \AA}$		
R_p			$3.38 \pm 0.05 \text{ \AA}$		
σ_o^2			0.009 \AA^{-2}		
σ_c^2			0.012 \AA^{-2}		
σ_s^2			0.009 \AA^{-2}		
σ_p^2			0.015 \AA^{-2}		

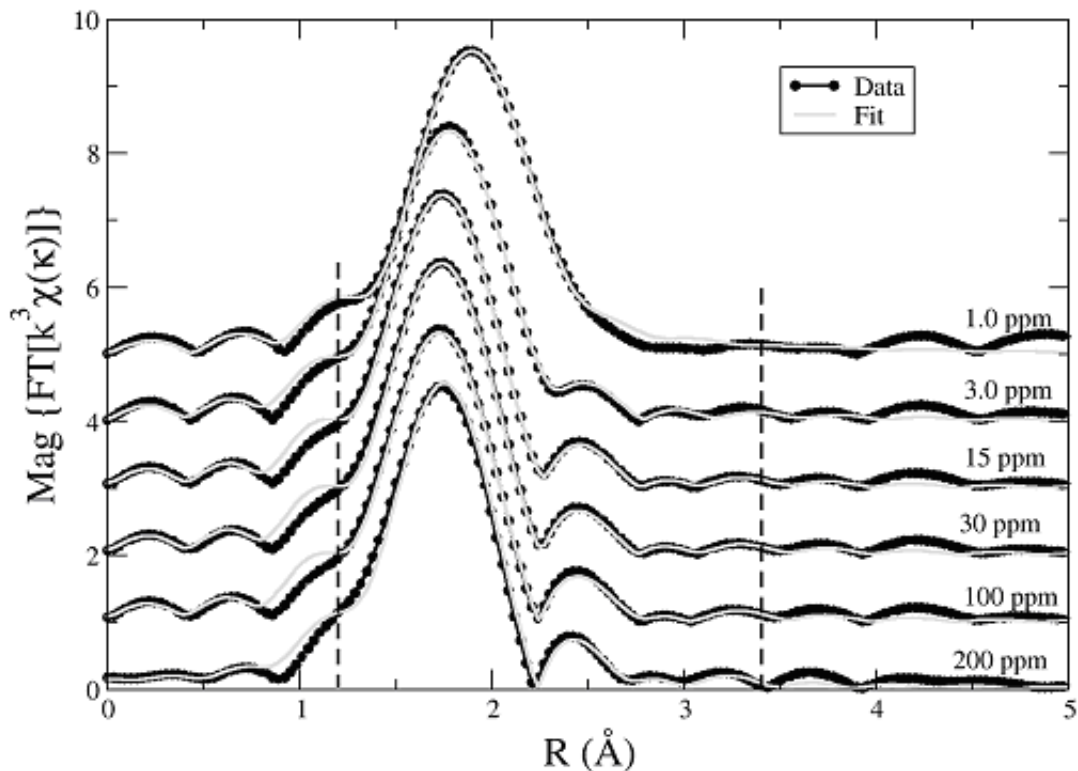


Figure 6.9. Fourier transform magnitude of the XAFS data and fits for the *B. Subtilis* isotherm.

bacterial cell walls. While phosphoryl and carboxyl sites are known to be active at bacterial cell walls, the sulfide site has never been characterized previously. The relative binding contribution of these three sites shows that sulfide sites are the most important sites at low Cd concentrations, followed by carboxyl and phosphoryl sites at medium and high Cd concentrations respectively. Our results indicate that the sulfide sites have very high affinity but are small in number. With increasing Cd loading, these sites are quickly saturated and become relatively less important with an increase in contribution from other two sites. In contrast to previous studies, this work shows that not only the pH condition of the bacterial cell surface is important for predictive modeling of such surfaces but

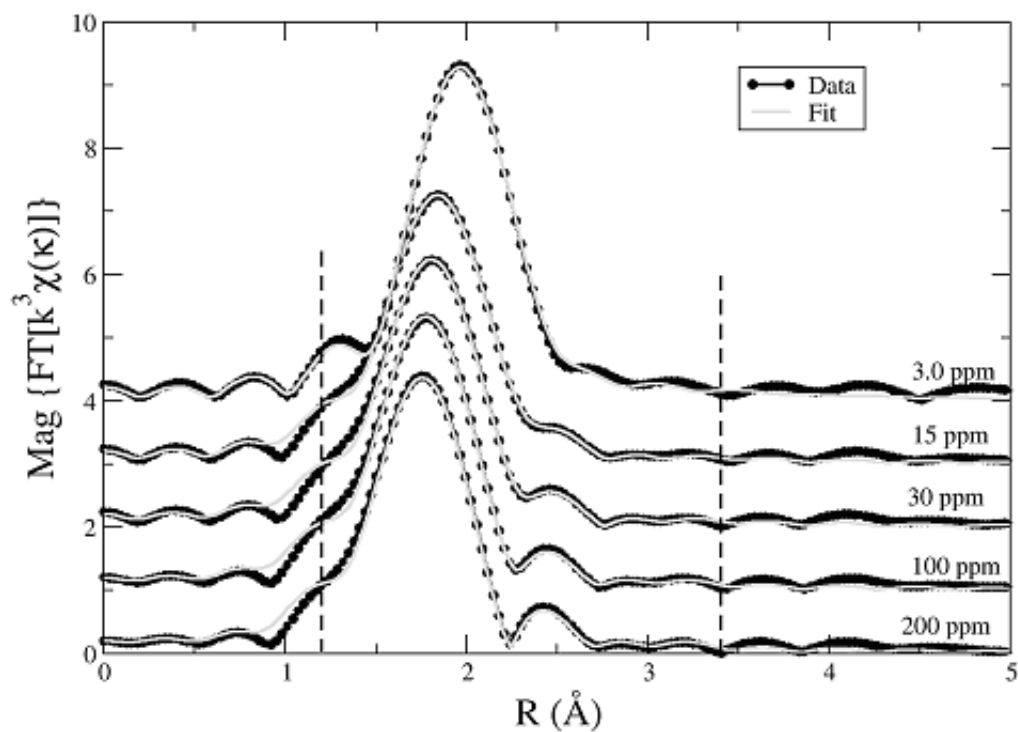


Figure 6.10. Fourier transform magnitude of the XAFS data and fits for the *Shewanella* isotherm.

the metal concentration associated with them also plays a vital role in deciding the important reactions taking place at and adjacent to the organic surfaces and interfaces.

6.4 Conclusion

Thermodynamic modelling was combined with Cd K edge XAFS to examine Cd adsorption to isolated cell walls of commonly occurring Gram positive and Gram negative bacteria, *Bacillus subtilis* and *Shewanella oneidensis MR-1* respectively, as a function of Cd loading at circumneutral pH condition. Thermodynamic equilibrium modeling was used to constrain the stoichiometry of the

important adsorption reaction using FITEQL. The adsorption data was best modeled with a Cd:carboxyl binding site stoichiometry of 1 : 1; however a combination of binding sites could not be unequivocally excluded.

EXAFS confirms predominant carboxyl binding at mid Cd loadings (around 30 ppm) as predicted by the surface complexation model. However, phosphoryl ligands were found to have higher contribution than carboxyl ligands at high Cd loading (100 and 200 ppm). In addition to these, an unexpected sulfide binding was found to completely dominate Cd binding to both these diverse groups of bacterial strains at lower Cd loadings (1 – 15 ppm). XAFS Results suggest that both Gram positive and Gram negative bacterial cell walls have small number of very high affinity sulfide sites which gets masked by carboxyl and phosphoryl sites at higher metal concentrations.

CHAPTER 7

Pb AND Cd SPECIATION IN THE PRESENCE OF MICROBIAL SIDEROPHORE DFO-B: COMBINING X-RAY ABSORPTION SPECTROSCOPY WITH THERMODYNAMIC MODELING

7.1 Introduction

Interactions occurring at the solid-liquid interface affect the fate and transport of metals, and much research has been focused, most recently at the molecular level, on elucidating mechanisms of single or a small number of elements at the surface of specific minerals. In such studies, the solution speciation of the metal ion is generally straightforward and includes products of hydrolysis and/or complexation by carbonate species, depending on the experimental conditions. However in natural environments, metal speciation in solution is likely impacted by the presence of various dissolved organic and inorganic ligands. The phosphate anion and humic and fulvic acids are known to affect the extent of metal sorption at mineral surfaces [28, 38]. Complicating predictions of metal partitioning at the solid-liquid interface in the presence of dissolved ligands is that often the effects are not additive, meaning that metal speciation in the ternary system is not simply the sum of dissolved complexes and those formed between metal and mineral surfaces [92, 107].

Organic ligands in solution of plant and microbial origin can reach relatively

high concentrations at specific locations of high productivity, including the rhizosphere and biofilms. Marine and terrestrial microorganism, algae and fungi produce a group of low molecular weight organic molecules called siderophores to assimilate Fe(III). Siderophore biosynthesis has evolved in response to the very low solubility and slow dissolution kinetics of Fe-bearing minerals at circumneutral pH values, which effectively limits "free" Fe(III) to concentrations that are many orders of magnitude below those required for life [43]. Binding constants of this group of molecules for Fe(III) are extremely high ($10^{25} - 10^{50}$; [1]), and complexation of the metal cation occurs most commonly via hydroxamate, catecholate or α -hydroxycarboxylate functional groups [111]. These molecules have been widely examined because of the known linkage of siderophore biosynthesis by microbial pathogens to virulence [23], their established use in medicine for chelation therapy [10] and more recently, their potential role in active drug transport [105]. However, from a geochemical standpoint, siderophores may be important weathering agents as siderophores enhance the dissolution rates of various Fe-bearing minerals [21, 22, 54, 87]. Further, although siderophore molecules show a high specificity for Fe(III), Brantley et al. [15] have shown that other trivalent and divalent trace metals representing trace structural impurities are leached from hornblende in the presence of siderophores. Relatively high binding constants have been determined for the complexation of divalent cations Pb, Cd, Zn and Cu by the siderophore DFO-B, produced by the bacterium *Streptomyces pilosus*. Siderophore concentrations vary by environment; in bulk soil solutions the concentration of hydroxamate siderophores has been estimated at $10^{-7} - 10^{-8}$ M but are likely higher in the rhizosphere [53]. As such, complexation of toxic non-essential metals, such as Cd and Pb, by siderophores may affect their solution-phase speciation and subsequent

partitioning at the solid-liquid interface.

Studies that have examined the impact of siderophores on divalent metal partitioning to mineral surfaces have done so predominantly in the presence of the siderophore DFO-B. Results for metal sorption to Fe oxides and kaolinite clay have suggested that the overall impact of the presence of DFO-B is to decrease the extent of metal sorption above the zero point of charge of the mineral [41, 54]. For smectite clay, the overall effect is to shift the adsorption edge to lower pH values, and suggests a change in the mechanism of sorption from adsorption at edge sites to exchange at permanent negatively charged sites [71]. The pH values over which the change in uptake behaviour occurs is also the range in which metal-siderophore complexes are predicted based on published stability constants. Thus, likely both the manner in which the metals are complexed by the siderophore as a function of pH and the interactions between siderophores and the minerals themselves dictate the overall effect on metal partitioning. To mechanistically understand these changes, an accurate understanding of the complexes formed between metals and siderophores in solution is needed.

Our goal, thus, was to characterize the complexes of toxic metals Pb^{2+} and Cd^{2+} with the siderophore DFO-B as a function of pH using X-ray absorption spectroscopy. First, speciation diagrams for both metals were predicted using a thermodynamic model and published stability constants. Solutions were then prepared under experimental conditions (pH, metal:siderophore ratio) that corresponded as much as possible to single metal-siderophore complexes. In a subsequent communication [69], the spectroscopic evidence for specific metal-siderophore complexes is used to mechanistically interpret Cd and Pb sorption at the surface of kaolinite.

7.2 Methods and Materials

7.2.1 Speciation Diagrams and Solution Preparation

To measure "signatures" for Pb^{2+} and Cd^{2+} siderophore complexes by XAS, the aqueous-phase speciations for both metals were modeled over the pH range of interest (3 – 10) in the presence of the commercially available trihydroxamate siderophore DFO-B. The thermodynamic model PhreeqC was used with published binding constants (Table 7.1). All speciation diagrams were calculated for ambient conditions (constant CO_2 partial pressure of $10^{-3.5}$), a background electrolyte of 0.1 M NaClO_4 , and addition of Pb^{2+} and Cd^{2+} as nitrate salts ($\text{Pb}(\text{NO}_3)_2$ and $\text{Cd}(\text{NO}_3)_2$ respectively). Experimentally, it was determined that metal concentrations of 10 mM were required for quantitative analysis of metal-siderophore solutions by XAS, thus, all models were run at 10 mM concentrations of Pb^{2+} and Cd^{2+} and metal-siderophore ratios of 1 : 2 and 1 : 10. The resulting speciation diagrams then served as templates for the preparation of solutions. Solutions 10 mM in metal cations and either 20 mM or 100 mM in DFO-B were prepared using solid ($\text{Pb}(\text{NO}_3)_2$ or $\text{Cd}(\text{NO}_3)_2$ (Fisher Scientific) and the commercially available desferrioxamine (DFO-B) mesylate salt (Sigma-Aldrich). The pH values of each solution were adjusted with HNO_3 and NaOH to values that best represented a single metal-siderophore complex. For example, Fig. 7.1 shows solution-phase speciation of Pb^{2+} in the presence of DFO-B; at pH 4.8, the dominant species in solution is Pb^{2+} is $\text{LH}_3\text{Pb}^{2+}$, which represents the complexation of Pb^{2+} by one hydroxamate group of the DFO-B ligand. A total of 4 pH values and metal:siderophore ratios of 1 : 2 and 1 : 10 were chosen to characterize Pb-DFO-B complexes while Cd-DFO-B complexes were characterized at 3 pH values and 1 : 2 metal:siderophore ratio. For all samples analyzed by XAS, beam-induced

changes to the solution chemistry were assessed qualitatively by measuring pH immediately prior to and following the measurement.

Loss of metal and/or siderophore through sorption to bottle walls and/or precipitation was examined in a series of control samples, although precipitation of Pb^{2+} and Cd^{2+} hydroxide and carbonate solids was not predicted. Metal:DFO-B solutions of ratio 1 : 2 and Pb-aHA solutions of 1 : 100 were prepared at all experimental pH values and the concentrations of the metals and siderophores monitored every 48 hours. Metal concentrations were analyzed by inductively coupled plasma mass spectrometry (ICP-OES) after filtering (0.2 μM hydrophobic membrane filters) and acidifying solutions to 2% HNO_3 (v/v). Siderophore (DFO-B and aHA) concentrations were analyzed by total dissolved organic carbon analysis (TOC; Shimadzu TOC-5000). Loss of metals and siderophore was negligible over a 2-week period; comparatively, solutions for XAS analysis were analyzed within 4 days of being prepared.

7.2.2 XAFS Measurements

X-ray Absorption Fine-structure Spectroscopy (XAFS) [encompassing both Extended X-ray Absorption Fine-structure Spectroscopy (EXAFS) and X-ray Absorption Near-Edge Structure (XANES)] measurements were performed at the MRCAT sector 10-ID beamline [93] at the Advanced Photon Source. The beamline optics and setup parameters for the Pb L(III) and Cd K edge XAFS measurements were as follows. The energy of the incident X-rays was scanned by using a Si(111) reflection plane of a cryogenically-cooled double-crystal monochromator. The beamline was optimized for 2nd and 3rd harmonic of the undulator for Pb and Cd measurements respectively. The undulator was tapered by approximately 2.5

TABLE 7.1

PUBLISHED STABILITY CONSTANTS USED FOR THE
PREDICTION OF Pb AND Cd SPECIATION WITH DFO-B

Reaction	Log stability constant ¹
$(\text{DFOB})^{3-} + \text{H}^+ = \text{H}(\text{DFOB})^{2-}$	10.90 ²
$(\text{DFOB})^{3-} + 2\text{H}^+ = \text{H}_2(\text{DFOB})^{-}$	20.48 ²
$(\text{DFOB})^{3-} + 3\text{H}^+ = \text{H}_3(\text{DFOB})$	29.48 ²
$(\text{DFOB})^{3-} + 4\text{H}^+ = \text{H}_4(\text{DFOB})^+$	37.85 ²
$\text{Pb}^{2+} + (\text{DFOB})^{3-} + \text{H}^+ = \text{HPb}(\text{DFOB})$	20.87 ²
$\text{Pb}^{2+} + (\text{DFOB})^{3-} + 2\text{H}^+ = \text{H}_2\text{Pb}(\text{DFOB})^+$	29.73 ²
$\text{Pb}^{2+} + (\text{DFOB})^{3-} + 3\text{H}^+ = \text{H}_3\text{Pb}(\text{DFOB})^{2+}$	35.40 ²
$2\text{Pb}^{2+} + \text{H}(\text{DFOB})^{2-} = \text{HPb}_2(\text{DFOB})^{2+}$	16.29 ²
$\text{Cd}^{2+} + (\text{DFOB})^{3-} + \text{H}^+ = \text{HCd}(\text{DFOB})$	18.8 ³
$\text{Cd}^{2+} + (\text{DFOB})^{3-} + 2\text{H}^+ = \text{H}_2\text{Cd}(\text{DFOB})^+$	26.0 ³
$\text{Cd}^{2+} + (\text{DFOB})^{3-} + 3\text{H}^+ = \text{H}_3\text{Cd}(\text{DFOB})^{2+}$	32.7 ³

¹All stability constants determined at a background electrolyte concentration of 0.1 M.

²Hernlem et al. [42]

³Neubauer et al. [71]

and 3.5 keV respectively to reduce the variation in the incident intensity to less than 15% over the scanned energy range. Higher harmonics were rejected using Rh-coated mirror at the Pb edge and a Pt-coated mirror at the Cd edge. The incident ion chamber was filled with a mixture of 40% Helium and 60% Nitrogen for Pb measurements and 100% Nitrogen for Cd measurements. The transmitted and reference ion chambers were filled with 100% Ar for both edges. The fluorescence detector in the Stern-Heald geometry [98] was filled with Ar gas and an As filter of six absorption lengths was used to reduce the background signal at the Pb L edge. For the Cd edge, Kr gas was used in the fluorescence detector and no filter was required. The incident X-ray beam profile was 1 mm square. Linearity tests [48] indicated less than 0.1% nonlinearity for a 50% decrease in incident X-ray intensity. The scans were aligned by the simultaneously collected Pb and Cd foil data. The first inflection point was set at 13,035 eV for Pb and 26,711 eV for Cd.

Quick scans (continuous-scanning mode of the monochromator with signal sampled every 0.05 eV in the entire scanning range) were used with an integration time of 0.1 second per point. The advantage of using quick-scans is that it reduces the radiation exposure during a single scan (~ 3 minutes per EXAFS scan and < 1 minute/XANES scan). Further XANES was constantly monitored for any possible radiation damage. About 30 consecutive scans of each sample were averaged, and resulting data from all the samples were normalized and background subtracted using ATHENA [83].

7.3 XAFS Data Reduction

The data were analyzed using the codes from the UWXAFS package [99]. These programs include ATHENA which is based on AUTOBK [77] to remove the background, FEFFIT to fit the theoretical model to the EXAFS data, and FEFF8 [2] to create the theoretical model. The data sets were aligned and the backgrounds were removed using ATHENA program. The input parameter to ATHENA that determines the maximum frequency of the background R_{bkg} was set to 1.1 Å. Data range used for Fourier transforming the k space data was 2.3 – 9.8 Å⁻¹. Hanning window function was used with a dk of 1.0. Simultaneous fitting of several data sets with multiple k -weighting (k^1 , k^2 , k^3) of each spectrum was performed in r -space. Fitting range for all the data sets was set to 1.2 – 3.4 Å. Simultaneous fitting approach reduces the possibility of obtaining erroneous parameters due to correlations at any single k -weighting.

At energies slightly above the absorption threshold of the element of interest, the absorption probability is dominated by the absorbing atom's density of states near the Fermi energy. This makes near-edge (XANES) highly sensitive to the valance state, bond type, bond orientation and symmetry. Precise detailed analysis of XANES is not completely developed but comparison with model compounds or between samples of similar coordination environment can reveal some important information about the atom's bond geometry.

7.4 Results and Discussion

7.4.1 Predicted Solution Phase speciation

Speciation diagrams for Pb²⁺ and Cd²⁺ over the pH range 3 – 10 are shown in Fig(s). 7.1 and 7.2, respectively, and illustrate the dramatic effect the presence of

DFO-B has on the solution speciation of both metals. The metal concentrations in these solutions (10 mM) are quite elevated and thus, in the absence of DFO-B, both solution-phase and solid-phase hydroxyl and carbonate species are predicted at alkaline pH values. In the presence of DFO-B, essentially 100% of the nominal Pb^{2+} and Cd^{2+} are complexed by DFO-B at circumneutral pH values and above and the solutions are not saturated with respect to any hydroxide or carbonate solid phase, evidencing the strength of DFO-B as a metal-complexing ligand. Hydroxide and carbonate species of Pb^{2+} and Cd^{2+} do not appear in the speciation diagrams for either metal in the presence of DFO-B because they represented less than 0.2% of the total metal species.

The notation used to designate different metal-siderophore complexes in the speciation diagrams requires some explanation. The DFO-B molecule has four deprotonation sites, each of the three hydroxamate groups and the terminal amine group (pK_a values given in Table 7.1), and the notation that has been used in the literature to represent the fully deprotonated DFO-B molecule is L^{3-} , e.g. Hernlem et al. [42]. Thus, the notation for the fully protonated DFO-B molecule is correspondingly LH_4^+ . In the presence of divalent cations Pb^{2+} and Cd^{2+} , the following species with 1 : 1 stoichiometries are predicted: LH_3M^{+2} , LH_2M^+ and LHM . LH_3M^{+2} represents the complex in which the metal cation (M^{z+}) is bound by both oxygen atoms of one hydroxamate group (i.e. bidentate complex) and the terminal amine group is protonated. This complex forms by exchange of the proton on one hydroxamate group with a Pb^{2+} (or Cd^{2+}) cation. Binding of the metal cation through two hydroxamate groups gives the tetradentate complex LH_2M^+ , and through all three hydroxamate groups gives the hexadentate complex LHM . For Pb^{2+} , the bi-nuclear species $\text{Pb}_2\text{LH}^{+2}$ is also predicted over the pH range of

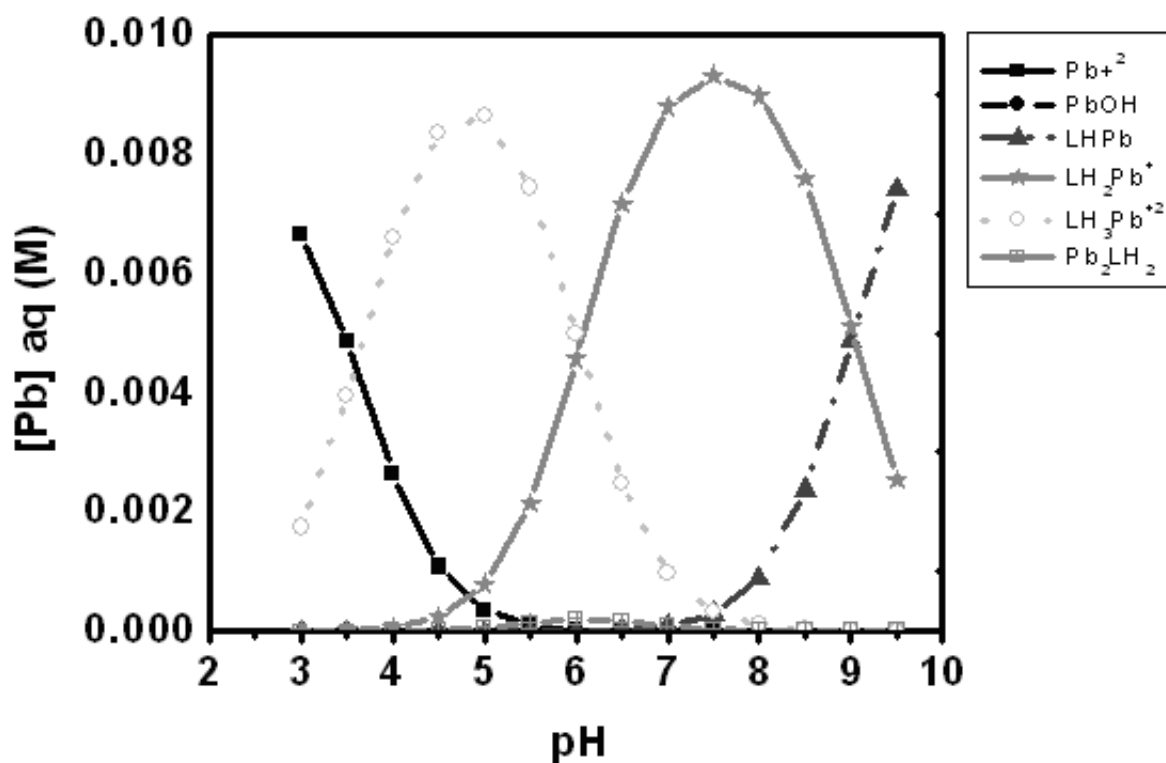


Figure 7.1. Pb speciation in the presence of DFO-B, modeled by PhreeqC using available binding constants.

interest. In this complex, one Pb^{2+} is bound through two hydroxamate groups and the second through the third hydroxamate group of the DFO-B molecule [42]. Again, the notation for all metal-siderophore species assumes a protonated terminal amine group. The model indicates that Pb^{2+} is exchanged for one proton associated with the DFO-B molecule under acidic conditions; the species $\text{LH}_3\text{Pb}^{2+}$ species dominates at pH values 4 – 6 (Fig. 7.1). Tetradentate binding of Pb^{2+} (LH_2Pb^+) occurs at circumneutral pH and the hexadentate species, LHPb , dominates the solution speciation only at pH values > 9 . In contrast, complexation of Cd^{2+} begins only at pH values > 5 (Fig. 7.2). At pH 7 a complex mixture of species roughly equimolar in hydrated Cd^{2+} and all three Cd-DFO-B species is

predicted. Only at pH values > 8 does one species, LHCd, dominate. The predicted complexation behaviours of Pb^{2+} and Cd^{2+} , and specifically the differences in their speciations, reflect differences in their respective chemistries and preferred geometries.

First, before discussion of the differences in speciations of Pb^{2+} and Cd^{2+} are discussed, it must be noted that our structural understanding of metal-siderophore complexes comes almost exclusively from crystallized Fe-siderophore complexes. In the structure of ferrioxamine B (Fe-DFO-B complex), a distorted octahedral geometry occurs about the center Fe(III) cation due to hexadentate binding by all three of the, assymetrical, hydroxamate functional groups [26]. To make possible the hexadentate binding of Fe(III), the DFO-B molecule "wraps" itself around the metal center. The exact conformation of the DFO-B molecule when complexing divalent metals cations as bidentate, tetradentate and hexadentate complexes is not currently known or simulated, so it is the differences in stability constants for those respective complexes between metals that are instructive.

The first difference in complexation behaviours between Cd^{2+} and Pb^{2+} is the greater value for the hexadentate complex for Pb^{2+} versus Cd^{2+} (Table 7.1). The lower relative value for Cd^{2+} is consistent with its lower affinity for hard bases with negatively charged oxygen donor groups. Previous studies have found that the values of monohydroxo complex formation constants (affinity for the hard O donor group of water) and the stability constants for LHM are positively correlated [42, 49]. Further, the difference in values between stability constants for the bidentate, tetradentate and hexadentate complexes are smaller than for Cd^{2+} compared to Pb^{2+} , meaning that the Pb^{2+} forms more stable "intermediate" bidentate and hexadentate complexes. This, in turn, is related to the larger relative size of the

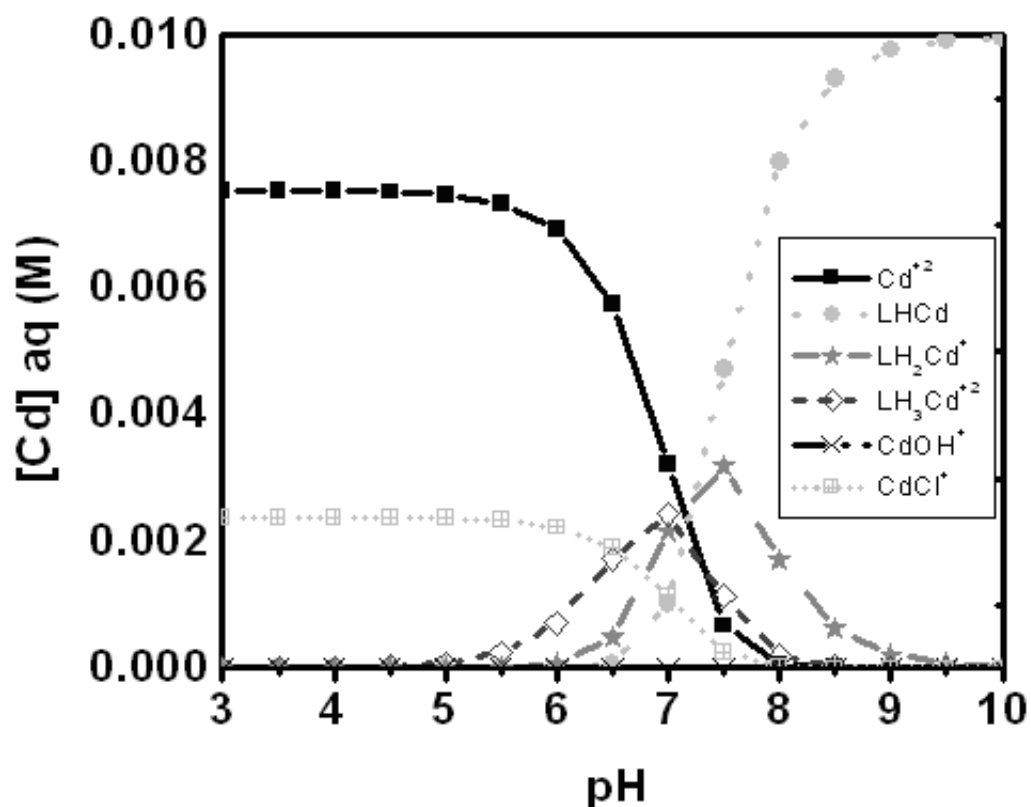


Figure 7.2. Cd speciation diagram in the presence of DFO-B, modeled by PhreeqC using available binding constants.

Pb²⁺ cation with respect to Cd²⁺. Hernlem et al. [42] demonstrated that size did not affect the complexation of metals by DFO-B until the third hydroxamate group binds. Further, Cd²⁺ prefers an octahedral geometry while the coordination surrounding the central Pb²⁺ metal in gas-phase complexes can be wither holo- or hemi-directed depending on the stereochemical activity of the lone-pair [95]. Recent work with and molecular simulations have indicated that the hydrated Pb(II) cation is surrounded by 9 water molecules in a distorted first shell and that a second shell with between 18 – 28 water molecules exists [44]. In contrast, the hydrated Cd²⁺ cation is surrounded in a straightforward manner by six water

molecules in its first hydration sphere and twelve in second shell. Thus, steric considerations and the size of the Pb^{2+} cation may reduce the affinity for the hexadentate Pb-DFO-B species. Further evidence for the different complexation of these metal cations is the work of Kiss and Farkas [49], who observed that as the chain length was decreased for the dihydroxamic acid they were studying, the stability of the complexes formed with Cd^{2+} decreased, while the shortest molecule had the strongest complexation constant with Pb^{2+} . The authors suggested that the lone pair of the Pb^{2+} cation may have resulted in a packed arrangement favoring the smaller molecule.

7.4.2 Measured Solution-Phase Speciation

Metal-siderophore solutions were prepared at specific pH values at which the species of interest of both cations dominated the respective solution speciations. Solutions 10 mM in Pb^{2+} and 20 mM in DFO-B were prepared at pH values 3.0, 4.8, 7.5 to characterize the hydrated (non-siderophore-complexed) cation, the bidentate complex and the tetradentate complex, respectively (Fig. 7.1). At these concentrations of DFO-B and Pb^{2+} the hexadentate LHPb species does not dominate solution until pH values much greater than 9. Thus, a fourth solution was prepared in which was predicted to be 50 : 50 in LH_2Pb^+ and LHPb at pH 9. In this solution the DFO-B concentration was raised to 100 mM and the Pb^{2+} concentration was kept constant at 10 mM. Similarly, solutions 10 mM in Cd^{2+} and 20 mM in DFO-B were prepared at pH values 5.0, 8.0 and 9.0. The nature of Cd^{2+} complexation by DFO-B does not allow for solutions dominated by only one Cd-siderophore complex until very alkaline pH values (> 9), where the LHCd species dominates (Fig. 7.2). Efforts were thus concentrated on determining signatures

for the hydrated Cd^{2+} cation (pH 5) and the caged Cd-DFO-B species (pH 9). At pH 8.0, an approximate 1 : 4 ratio of LH_2Cd^+ and LHCd is predicted; changes in the EXAFS at this pH indicated the presence of two species (as discussed below).

7.4.3 Pb Powder and Solution Standards

Analysis of solid- and solution-phase control samples allows quantitative analysis of the metal-siderophore complexes. Solids PbO and PbO_2 have relatively straightforward local structures for Pb^{2+} and Pb^{4+} , respectively, and measurements of these solids in transmission and at ambient temperature were used to calibrate the theory. The EXAFS was calculated using FEFF8 from the known crystal structures using Pb-O and Pb-Pb paths. The fit (not shown) reproduced the spectral features in the entire fitting range (1.0–4.2 Å) for both solids. Fitting parameters from these two standards are listed in Table 7.2. The S_0^2 was found 0.71 and 0.81 for Pb^{2+} (PbO) and Pb^{4+} (PbO_2) respectively. Based on this, S_0^2 was set to 0.71 in the analysis for all Pb^{2+} samples with oxygen first shell environment. Solution-phase standards for Pb^{2+} consisted of the hydrated Pb^{2+} cation (100 mM Pb^{2+} in 0.1 M NaClO_4) and Pb-acetate complexes (Pb-acetate ratio of 1 : 100) were measured and analyzed as solution-phase Pb standards. Fit results are shown in Table 7.2. The FT of the hydrated Pb^{2+} cation showed a broad and slightly asymmetric peak and which was best fit with a single first O shell from hydration water at 2.55 Å (Table 7.2).

Addition of a third cumulant, which originates from the non-Gaussian disorder associated with the sample, improved the fit to this asymmetric peak. Chemically, the need for this higher disorder term can be rationalized by the presence of the lone electron pair associated with Pb^{2+} . When the fit was attempted without

the third cumulant, reported Pb-O bond length from the fit was 2.49 Å. The inclusion of third cumulant however moves this distance to 2.55 Å, both of which has been reported by previous studies [14]. The coordination number of 9 is in agreement with quantum chemistry calculations [44].

Modeling of the Pb-acetate species, again using PhreeqC and published binding constants, predicted that the species $\text{Pb}(\text{Acetate})_2$ dominates at pH 3.4 and 5 mM Pb^{2+} in 5.0 M acetate (1 : 100 metal:ligand ratio).

Thus, the Pb coordination for measurements of the prepared Pb-acetate standard was modeled with O and C shells from the metal-binding carboxyl group of the acetate ligand. The obtained 4 O atoms in the first shell and 2 C atoms in the second shell are consistent with complexation of the each Pb^{2+} cation by two acetate anion, a bidentate binding mechanism which is observed in crystal Pb acetate.

The Pb-O bond distance in this case is 2.32 Å (Table 7.2), which is significantly shorter than the one reported for hydrated Pb^{2+} (2.55 Å). These two bonds also exhibit a large difference in Debye -Waller factors: The Debye-Waller factor for the shorter Pb-O bond is 0.010 Å² while it is 0.028 Å² for the longer Pb-O bond of the hydrated Pb^{2+} cation. In the rest of the paper the shorter and longer Pb-O interatomic distances will be referred to as Pb-O₁ and Pb-O₂, respectively.

7.4.4 Cd Powder and Solution Standards

Solution standards for Cd^{2+} consisted of hydrated Cd^{2+} ($\text{Cd}(\text{NO}_3)_2$) and Cd-acetate complexes (Cd:acetate ratio of 1 : 100). FEFF8 was used to simulate the simple octahedral geometry of the hydrated Cd^{2+} ion. Data was fit well with 6

TABLE 7.2

FITTING PARAMETERS FOR Pb STANDARDS

Standard	path	N	R(Å)	sig2(10^{-3})	Third
Pb-O (tetra)	Pb-O	4	2.30 ± 0.03	6.8 ± 0.4	
	Pb-Pb	4	3.66 ± 0.09	3.5 ± 0.9	
	Pb-Pb	4	3.80 ± 0.02	3.0 ± 1.3	
	Pb-Pb	4	3.97 ± 0.02	5.4 ± 1.3	
PbO ₂	Pb-O	2	2.14 ± 0.03	3.0 ± 0.3	
	Pb-O	4	2.17 ± 0.03	3.0 ± 0.3	
	Pb-Pb	2	3.35 ± 0.02	6.2 ± 1.9	
	Pb-Pb	8	3.86 ± 0.01	8.0 ± 0.9	
Pb ⁺² (aq)	Pb-O	8.9 ± 0.9	2.56 ± 0.03	27.2 ± 1.8	1.92 ± 0.5
PbAc	Pb-O	3.7 ± 0.2	2.36 ± 0.01	11.0 ± 1.1	
	Pb-C1	2.1 ± 0.2	2.92 ± 0.01	9.0 ± 1.8	
	Pb-C2	Nc1	4.45 ± 0.03	9.0 ± 1.8	
	-C1-C2-	2* Nc1	4.45 ± 0.03	9.0 ± 1.8	
	-C1-C2-C1-	Nc1	4.45 ± 0.03	9.0 ± 1.8	

TABLE 7.3

FITTING PARAMETERS FOR Cd STANDARDS

Standard	path	N	R(Å)	sig2(10 ⁻³)
CdClO ₄	Cd-O	6.0 ± 0.18	2.27 ± 0.01	8.8 ± 0.2
	Cd-H	2*N _o	2.94 ± 0.03	13.7 ± 0.5
CdAc	Cd-O	5.5 ± 0.3	2.29 ± 0.01	10.9 ± 0.9
	Cd-H	2(N _o -2N _c)	3.0 ± 0.06	16 ± 9
	Cd-C	2.9 [#]	2.67 ± 0.02	12.8 ± 4
	-C-C-	N _c or 2*N _c	4.26 ± 0.02	15 ± 4

nearest neighbor oxygen atoms in the first shell at 2.28 Å (Table 7.3). The quality of fit improved by adding 12 hydrogen atoms in the second hydration shell. The Cd-acetate solution (5 mM Cd²⁺, 5.0 M acetate) was modelled with an O and C shell, as for Pb²⁺. The obtained 5.5 (±0.6) O atoms in the first shell and 2.9 (±0.4) C atoms in the second shell is consistent with the bidentate binding mechanism (forming a four-membered C-O-Cd-O ring), observed in crystal Cd acetate. FEFF8 calculations were made for the known crystal structure of Cd acetate dehydrate. The Cd-O bond length and Debye-Waller factor were the same as hydrated Cd. Fit results are shown in Table 7.3. The Cd-C bond distance was found to be 2.70 (±0.05). The S_0^2 were consistent with a value of unity (1) and this value was subsequent fixed in fits of the unknown Cd-DFO-B samples.

7.4.5 Pb-DFO-B samples: EXAFS Analysis and Numerical Fits

Pb-DFO-B solutions were prepared at pH values 3.0, 4.8 and 7.5 at metal:siderophore ratio of 1 : 2, and pH 9 at metal:siderophore ratio 1 : 10. These solutions were predicted to be dominated by the aqueous Pb^{2+} ion, $\text{LH}_3\text{Pb}^{2+}$, LH_2Pb^+ and LHPb , respectively. With increased pH there was significant changes to the EXAFS spectra. At pH 3.0, EXAFS spectra of the Pb-DFO-B solution and that of hydrated Pb^{2+} appear qualitatively the same. The spectrum of Pb-DFO-B at pH 3.0 was fit with 8.8 (± 1.6) water molecules surrounding the Pb ion at the same distance ($2.53 \pm 0.03 \text{ \AA}$; Table 7.4) as reported for hydrated Pb (Table 7.1). As was the case for hydrated Pb, this fit also improved significantly by introducing a shorter distance Pb-O (2.3 \AA) in addition to the longer Pb-O bond. The physical reason for this behavior is unclear. Modeled Pb^{2+} speciation in the presence of DFO-B (Fig. 7.1) predicted approximately 5% of the nominal Pb^{2+} to be complexed by DFO-B ($\text{LH}_3\text{Pb}^{2+}$). However, the EXAFS data does not show the presence of a C/N second shell, which would indicate complexation of the metal by the ligand. Thus, within the limits of resolvability of EXAFS, Pb does not complex with DFO-B at pH 3.0, but instead remains as a hydrated ion.

With an increase in pH to 4.8, there is a clear change in the local environment surrounding Pb^{2+} , observed qualitatively by comparison of the magnitude of the Fourier Transform of the samples at pH 3.0 and 4.8 (Fig. 7.4). The sample at pH 4.8 exhibits a sharper first-shell peak and a more pronounced contribution from higher shells. The fit to this sample included only single scattering paths for O_1 (shorter), O_2 (longer) and C/N, and was restricted in r -space to $1.2 - 3.0 \text{ \AA}$ as no prominent peak was observed beyond this distance. The latter "C/N" path is so named because C and N are not distinguishable by EXAFS, on account of their

similar atomic masses and thus behaviour as backscatterers. The observed EXAFS signal for this sample includes only two distinct peaks because of the interference between the O_2 and both O_1 and C/N paths. The coordination numbers (N) for O_1 and O_2 paths were found to be 2.5 (± 0.42) and 6.6 (± 1.2) respectively. The coordination number of the C/N path was constrained to that of the O_1 , based on the assumption that the metal cations are complexed through both oxygen atoms of one hydroxamate group, thus creating a five-membered ring (C-O-Pb-O-N).

The coordination numbers of the O_1 and O_2 paths, being 2.5 (± 0.42) and 6.6 (± 1.2) respectively, allow (at least) two interpretations of the solution speciation of Pb^{2+} in the presence of DFO-B at pH 4.8. First, a mixture of the hydrated Pb^{2+} cation and PbH_2L^+ could occur, at a ratio of approximately 40 : 60. This ratio was calculated assuming that the Pb^{2+} cation retains ~ 4 waters of hydration at Pb-O interatomic distance of O_2 when complexed by two hydroxamate groups. The second possible solution corresponds to a single Pb^{2+} species, where Pb^{2+} is complexed by one hydroxamate group of DFO-B, LH_3Pb^{2+} , and retains approximately 6 waters of hydration. The second solution is more consistent with the modeled Pb^{2+} speciation, where at pH 4.8 the LH_3Pb^{2+} is predicted to account for approximately 60% of the total Pb^{2+} species. However, the possibility of a mixture of numerous species, where Pb^{2+} , LH_3Pb^{2+} , and LH_2Pb^+ , all contribute to the measured signal cannot be ruled out either. For all possible solutions, however, it is clear that at pH 4.8, at least 60% of the Pb^{2+} is complexed by DFO-B.

At pH 7.5, the local coordination of Pb^{2+} changes still further from the hydrated cation observed at pH 3.0. Best fit values for O_1 was approximately 6 and, again, the coordination number for the C/N path was constrained to this O_1

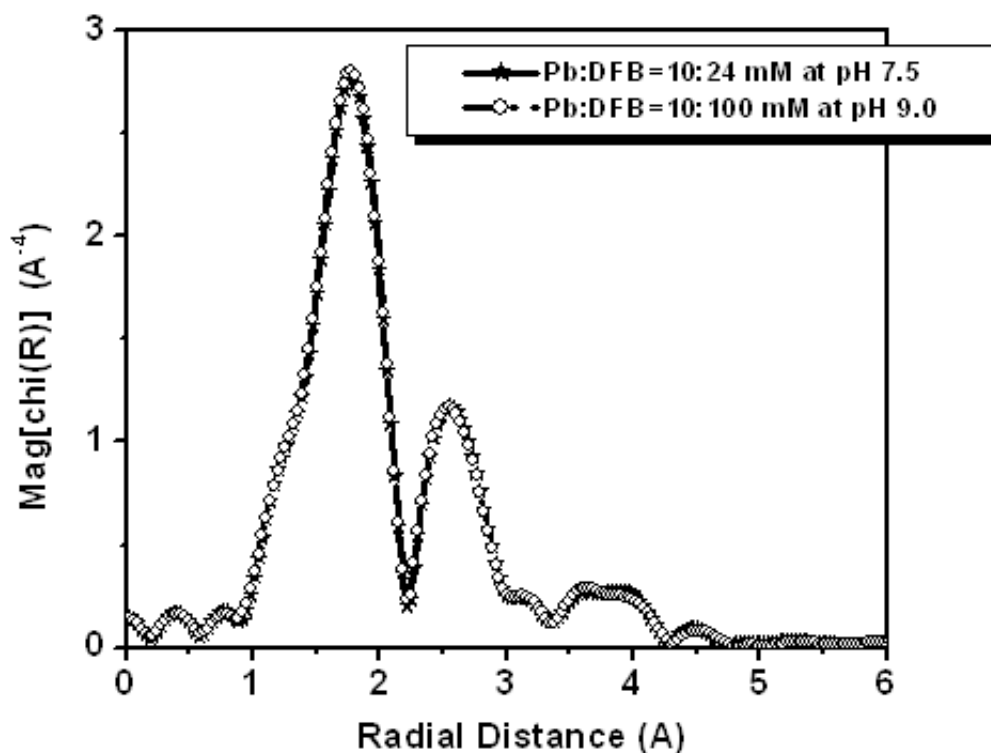


Figure 7.3. Comparing Fourier transformed magnitude of the XAFS spectra of Pb-DFO-B at pH 7.5 and 9.0. They completely overlap at each other, indicating that Pb has exact same coordination environment at these two pH conditions.

value. Although a reasonable fit could be obtained without the inclusion of O_2 ; adding O_2 significantly improved the fit. These results suggest that the dominant species in solution at pH 7.5 is the hexadentate Pb-DFO-B complex, $LHPb$. The presence of O_2 may indicate that even when complexed by three hydroxamate groups of the DFO-B molecule, the Pb^{2+} retains one or two waters of hydration, which are consistent 8 – 9 atoms in the first shell of the hydrated Pb^{2+} cation. Alternatively, a small amount of LH_2Pb^+ may be present in solution. In contrast to the measured Pb^{2+} speciation at pH 7.5, the modeled speciation of Pb^{2+} at this pH value predicted approximately 92% LH_2Pb^+ , but with small contributions

($\leq 3\%$) from other Pb-DFO-B species. A final solution was measured at pH 9 and metal:siderophore ratio of 1 : 10. This solution was predicted to consist of 50% of each LH_2Pb^+ and LHPb. The EXAFS spectra obtained at pH 9 is the exactly the same as that of pH 7.5 (Fig. 7.3). At both pH 7.5 and 9, the modeled Pb^{2+} speciation and that measured by EXAFS differed.

Our results are consistent with the LHPb species dominating at both pH 7.5 and 9, although it is possible but unlikely that Pb EXAFS does not have high enough resolution to distinguish between $\text{LH}_2\text{Pb}^{2+}$ (corresponding to 4 O_1 and 4 C/N) and LHPb (corresponding to 6 O_1 and 6 C/N). The differences between modeled and measured Pb speciation at alkaline pH suggests that the stability constant for the hexadentate Pb-DFO-B complex is stronger than that predicted based on fitting of acid-base titration, from which the published stability constants were derived [42].

We have also observed complexation of Fe as a hexadentate complex outside of the pH range predicted by published stability constants (unpublished data), adding confidence to our interpretation above. Stronger Fe-DFO-B stability constants for the Fe-DFO-B complex have been reported by others [29].

The coordination geometry of the hexadentate Pb-DFO-B complex can be inferred from the EXAFS results presented here. The effect of the lone pair electrons on the coordination chemistry of Pb^{2+} is, as discussed above, dependent on the "activity" of the lone pair and results in either "holodirected" or "hemidirected" coordination geometry. In general, the coordination geometry of Pb^{2+} is hemidirected when the coordination number in the first shell is four or below, and is holodirected at coordination number 8 or above.

For the intermediate coordination numbers (5, 6 and 7), both the coordina-

TABLE 7.4

FITTING PARAMETERS OF THE Pb-DFO-B SAMPLES AT PH 3.0,
4.8 and 7.5

Sample	path	N	R(Å)	sig2(10^{-3})	Third
pH=3	Pb-O ₁	0.89 ± 0.63	2.30 ± 0.03	11.0 ± 1.2	
	Pb-O ₂	8.80 ± 1.52	2.53 ± 0.03	27.2*	2*
pH=4.8	Pb-O ₁	2.5 ± 0.42	2.32 ± 0.02	10.9 ± 1.2	
	Pb-O ₂	6.6 ± 1.20	2.55 ± 0.03	27.2*	2*
	Pb-C	2.5 [‡]	3.17 ± 0.02	8.6 ± 2.1	
pH=7.5	Pb-O ₁	5.8 ± 0.3	2.32 ± 0.01	11.0 ± 1.1	
	Pb-O ₂	1.8 ± 0.8	2.53 ± 0.03	27.2*	2*
	Pb-C	5.85 [‡]	3.19 ± 0.02	7.9 ± 2.7	

tion geometries have been observed and are ligand-dependent. Ideally the bond distances in such cases are Pb-X vs. Pb-ln-X, where X is the ligand and ln is lone pair. The bond distance of Pb-ln-X should be slightly longer than Pb-X. Keeping this in mind, we attempted to fit the first shell at pH 7.5 (which has six O₁ in first shell) using two shells with slightly different bond lengths; in the fitting, forcing this splitting resulted in a markedly worse fit. This is also consistent with two additional water molecules loosely bound to the Pb, making a total of 8 atoms in first shell. We assume that the Pb-DFO-B complex at pH 7.5 and 9.0 have fully caged, symmetric (holodirected) geometry due to overcrowding effect.

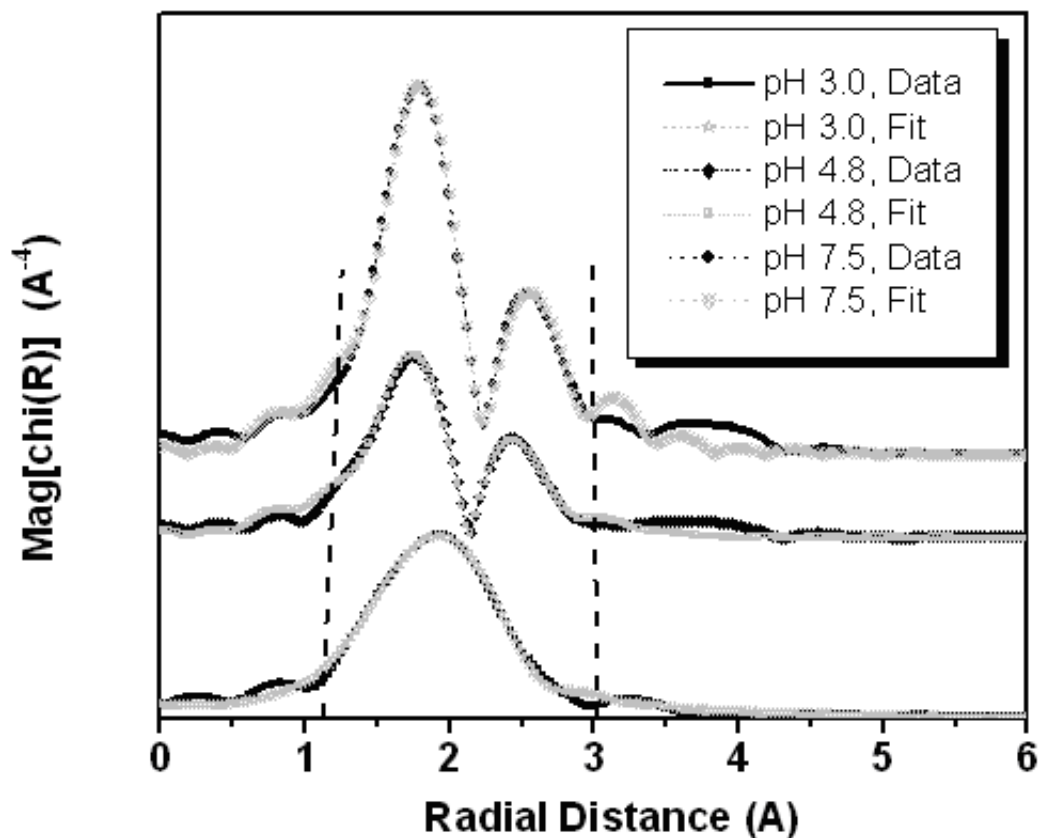


Figure 7.4. Pb-DFO-B Fourier transformed magnitude data and fits at pH 3.0, 4.8 and 7.5. Notice the broad first shell at pH 3.0. This is characteristic of hydrated Pb. An increase in the amplitude of second shell can be easily at higher pH values.

7.4.6 Cd-DFO-B sample: EXAFS Analysis and Numerical Fits

For the Cd-DFO-B solutions, pH values of 5.0, 8.0 and 9.0 were chosen to characterize the hydrated, 1 : 5 mixture of LH_2Cd^+ and LHCd , and LHCd complexes, respectively. The EXAFS spectra at pH 8 and 9 have very subtle differences. At pH 8.0, coordination number of Cd is found to be 5.2 ± 0.2 . The C/N coordination number in the second shell is constrained to be the same as O in the first shell. These results are consistent with a solution consisting of a 2 : 3 ratio (with $\sim 10\%$

error) between LH_2Cd^+ and LHCd , in a ratio of 2 : 3 with about 10% error bar. At pH 9.0, there is a slight increase in coordination number to 5.8 ± 0.2 , which is consistent with a the fully caged hexadentate LHCd complex. To gain confidence in the fitting results of EXAFS spectra so similar in nature, the two data sets (at pH 8 and 9) were fit simultaneously with all the three k weights, having six data sets in total (Fig. 7.5). This approach reduces the correlation between different fitting parameters and makes it much more likely that the best fit value is a global minimum and not some unstable local minima. The correlation between any two parameters was not more than 82%, which is reasonable given the short data range ($k = 2.3 - 10.2 \text{ \AA}^{-1}$). As can be seen from the Table 7.5, all other fitting parameters for these two spectra are the same within error bars. The Cd-C distance reported in this fit is 3.14 \AA and not 2.7 \AA as reported in CdAc standards. This difference in interatomic Cd-C distance arises from the fact that bidentate complexation of Cd^{2+} through one acetate ligand results in a four-membered ring (C-O-Cd-O) while bidentate binding by DFO-B through a hydroxamate group results in a larger five-membered ring (C-O-Cd-O-N).

7.4.7 Model vs. measured

While, within the limits of EXAFS analysis, the speciation of Cd^{2+} was consistent with that predicted using published stability constants, the solution phase speciation for Pb^{2+} measured by EXAFS appears to differ from that predicted. The speciation of Pb^{2+} is presently being assessed by acid-base titration and thermodynamic modeling at the same Pb^{2+} and DFO-B concentrations used in this study. Differences between the observed Pb-DFO-B complexes and those predicted may reflect the different metal:ligand ratios in the solutions on which the

TABLE 7.5

FITTING PARAMETERS OF THE Pb-DFO-B SAMPLES AT PH 3.0,
4.8 and 7.5

Sample	path	N	R(Å)	sig2(10^{-3})
pH=5	Cd-O	6.0 ± 0.25	2.27 ± 0.01	8.9 ± 0.3
	Cd-H	$2*N_o$	2.85 ± 0.03	13.4 ± 0.8
pH=8	Cd-O	5.2 ± 0.3	2.27 ± 0.01	8.6 ± 0.9
	Cd-C	$5.2^\#$	3.10 ± 0.02	4.5 ± 1.4
pH=9	Cd-O	5.8 ± 0.3	2.27 ± 0.01	8.6 ± 0.8
	Cd-C	$5.8^\#$	3.10 ± 0.02	3.8 ± 1.2

stability constants were derived and the solutions of this study. For example, we can not presently rule out the possibility of dimmer formation at high pH and metal:siderophore ratio of 1 : 2, whereby Pb^{2+} bridges two siderophore molecules to give a total of three complexing hydroxamate groups. Such a complex would give the same EXAFS signal as the hexadentate complex.

7.5 Conclusion

Speciation of Pb and Cd was modeled using PHREEQC in the presence of DFO-B using published binding constants. These models were then tested using direct spectroscopic XAFS measurements. Results indicate very strong and completely caged (chelated) structure for Me-DFO-B complex at higher pH values (Fig. 7.6). Pb has particularly sensitive speciation with DFO-B. It does not complex at all with DFO-B until about pH 3.5, but forms a totally caged structure at

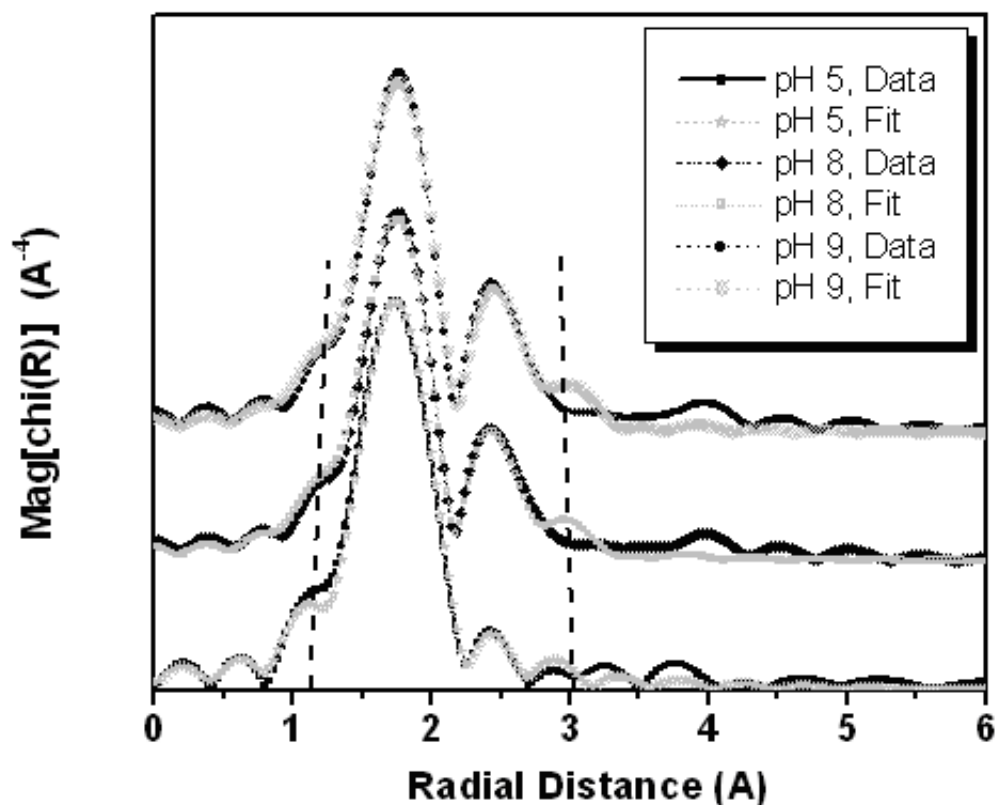


Figure 7.5. Cd-DFO-B Fourier transformed magnitude data and fits at pH 5.0, 8.0 and 9.0. The spectrum at pH 5.0 is similar to hydrated Cd. Higher pH spectra clearly have bigger second shell.

pH 7.5. At intermediate pH conditions, a mixture of species (one and two hydroxamate groups complexed) is formed. Cd, on the other hand, remains as hydrated Cd^{2+} until about pH 6.0, forms a completely chelated structure at pH 9.0, and appears a mixture two different species at pH 8.0. An important observation was that the complete chelation of Pb was observed at a pH value at least two units below that predicted by the equilibrium thermodynamic data. The chelation of Cd was however found as predicted by the model. This underscores the need for a detailed study of metal-siderophore systems using direct measurement techniques

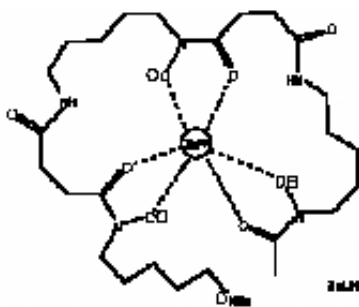


Figure 7.6. Proposed caged structure of DFO-B with Pb and Cd at higher pH values, same as it is for Zn at high pH values. (Adapted from Neubauer et al. [71])

like XAFS.

CHAPTER 8

EFFECT OF BACTERIAL SIDEROPHORES (DFO-B) ON ADSORPTION OF Pb TO CLAY MINERAL KAOLINITE

8.1 Introduction

Siderophores are Fe (III)-specific ligands produced by microorganisms under conditions of Fe stress. In addition to strong binding affinities for Fe, they can also bind a variety of other metals, including Al and Pb and influence the rates of mineral dissolution. A previous study has shown that siderophores inhibited adsorption of Pb to goethite (an Iron oxide mineral) at $\text{pH} > 6.5$ [71], hence enhancing Pb mobility within the approximately neutral to basic pH range. No effect was found on the typically small Pb adsorption at $\text{pH} < 6.5$.

Recently, our collaborating group compared the effects of DFO-B, DFO-D, DFO-E and aHA on Pb adsorption to the clay mineral kaolinite at pH 4.5 to 9, in 0.1 M NaClO_4 , at 22°C, in darkness to avoid possible photoreduction. At $\text{pH} \geq 6.5$ all of the siderophores plus aHA, inhibited Pb adsorption, with inhibition increasing in the order $\text{aHA} < \text{DFOD} < \text{DFOB}$. At lower pH values, all three ligands actually enhanced Pb adsorption, by as much as a factor of 5 under similar conditions. Studying this pH dependence to enhance or inhibit of adsorption is the main focus this study.

More specifically, the aim of this XAFS study is to determine the pH dependent

binding mechanism of Pb (one of the most widespread and hazardous environmental pollutant) adsorbed to kaolinite in the presence and absence of hydroxamate siderophores (desferrioxamineB). This will build a mechanistic understanding of hydrobiogeochemical controls on Pb mobility in porous media, enabling us to do determine the equilibrium constants determined in sorption studies of such reactions, and will set the stage for the further improvement of the unified thermodynamic modeling.

8.2 Materials and Methods

8.2.1 Mineral and Siderophore Samples Preparation

The Clay Minerals Society source clay KGa-1b was used in this study. This well-ordered kaolinite clay originates from Washington County, Georgia [104]. Traces of hallosite are found in association with this sample [101]. The kaolinite was cleaned before use to remove adsorbed organic matter and impurities, as per [101] and [41]. Briefly, the sample is acid washed (pH 3) and the suspension allowed to settle overnight repeatedly until the pH of the supernatant reaches 3. The clay is then rinsed in high purity water (Milli-Q[®] UV; Millipore) until the conductivity of the supernatant reaches $< 300 \mu\text{S}/\text{cm}$, and is freeze-dried. Previous characterization of the cleaned particles indicated a hexagonal micromorphology, crystallographically controlled microtopographic features and a point of zero net proton charge (pHzpc) of 5.1 ± 0.2 [115]. BET surface area of the cleaned particles is $12.1 \text{ m}^2/\text{g}$ measured by N_2 adsorption (SA 3100 volumetric sorption analyzer, Coulter Instruments; Maurice et al. [66]).

The trihydroxamate siderophore desferrioxamine-B (DFO-B) used in this study is available commercially (Sigma Aldrich; mesylate form).

8.2.2 Batch Adsorption Experiments

Pb sorption to kaolinite in the presence and absence of DFO-B was quantified at three initial pH values: 4, 6, and 7.5. Approximately 0.415 g of the pre-cleaned KGa-1b was weighed out into acid-washed 250 ml polypropylene bottles (8 hours in 4% HCl; rinsed 5 times in ultrapure water). Three experimental systems were analyzed: (1) Pb sorption to kaolinite (120 μM Pb^{2+}); (2) DFO-B sorption to kaolinite (240 μM DFO-B); and (3) Pb^{2+} sorption to kaolinite in the presence of DFO-B (120 μM Pb^{2+} and 240 μM DFO-B). All samples were 0.1 M in NaClO_4 with a clay concentration of 2.064 g/l with a final volume of 200 ml. Pb^{2+} was added as $\text{Pb}(\text{NO}_3)_2$ (1000 mg/l Inductively Coupled Plasma-Optical Emission Spectroscopy Standard Solution, Fisher Scientific) and DFO-B from an initial 10 mM stock solution prepared by dissolving the DFO-B powder in ultrapure H_2O . Sample pH was adjusted with 0.1 M NaOH and HNO_3 . Previous studies have indicated that a 2 hour reaction period is sufficient to reach adsorption equilibrium [70, 71], thus the samples were reacted for 2 hours on a rotary shaker and in the dark (to avoid any light-induced Fe^{3+} reduction in the clay). Solid pastes were separated by centrifugation (9000 rpm, 5 minutes; Fisher Scientific Marathon 21000). Samples with Pb^{2+} (Pb-clay and Pb-DFO-B-clay samples) were stored at 4°C for a maximum of 4 days prior XAS analysis.

8.2.3 Quantification of sorbed Pb and DFO-B

The amount of Pb and DFO-B sorbed in each of the samples was calculated as the difference between their initial concentrations (accounting for any changes in final volume due to pH adjustment) and measured final concentrations. Immediately following centrifugation of the batch samples, the supernatants were filtered

(0.2 μM hydrophobic Millipore PTFE filters). Aliquots of the sample for final dissolved-phase Pb concentrations were acidified to 2% in analytical-grade HNO_3 (v/v) and analyzed by Inductively-coupled plasma optical emission spectroscopy (ICP-OES; Optima 3300 XL, Perkin Elmer) using Y as the internal standard (final concentration of 1 ppm) and matrix-matched standards. Prior analysis of Fe, Si, and Al concentrations in samples prepared under the same experimental conditions and DFO-B concentration by ICP-OES indicated that KGa-1b was not dissolved over the reaction time of 2 hours [41]. Specifically, final Si concentrations were below the instrument detection limit (10 ppb), Fe concentrations < 5 ppb, and Al concentrations 5 – 15 ppb.

The concentration of the DFO-B stock solution was confirmed by total dissolved nitrogen (TON) analysis (Shimadzu TOC-5000). Three to five injections per sample were executed until the TON concentration for each sample was $\leq 2\%$ standard deviation. Final DFO-B concentrations in all samples were quantified colorimetrically by complexing dissolved DFO-B in the supernatants with Fe(III) and measuring absorption by UV-vis spectroscopy. The complex between siderophore and Fe(III) is coloured and absorbs strongly between 400 – 500 nm [67]. 3 ml of the sample supernatants were acidified to $\text{pH} \sim 2.7$ by addition of 30 μl 0.2 N high-purity HCl and 20 μl pre-acidified 1.0 M FeCl_3 . The pH of the samples was low enough to promote complexation of Fe by DFO-B, but too low for complexation of Pb by DFO-B, thus Pb-DFO-B complexes did not interfere with DFO-B quantification by complexation of Fe(III). Calibration curves for matrix matched samples (DFO-B in 0.1 M NaClO_4 and DFO-B in 0.1 M NaClO_4 and 120 μM Pb^{2+}) confirmed that the presence of Pb^{2+} did not interfere in the quantification of DFO-B in the solution supernatants.

8.2.4 XAFS Standards, Measurements and Data Reduction

Please refer chapter 7 for these details. Work presented in this chapter is a continuation of chapter 7, so all the protocols for XAFS standards, measurements and data reduction also applies here.

8.3 Results and Discussion

8.3.1 Bulk-Scale Results

The extent of Pb^{2+} partitioning of Pb^{2+} between the solution and solid phase is affected, most dramatically above pH 7, in the presence of DFO-B (Fig. 8.1). In the absence of DFO-B, the extent of Pb^{2+} sorption is pH dependent (Fig. 8.1). A small amount of sorption occurs below the point of zero net proton conditions (pH_{pznpc}), which is likely due to sorption of Pb^{2+} at permanent negatively charged exchange sites resulting from isomorphic substitution in the clay structure. The extent of Pb^{2+} sorption increases above pH 5, which is consistent with a net negative charge on the clay particles above the pH_{zpc} , which has been reported at pH 5.1 [115]. Above pH 6.0, PbOH^+ begins to form in solution and may be the dominant species sorbed at alkaline pH values (> 8). As a result of the relatively high nominal Pb^{2+} concentrations used in these experiments ($120 \mu\text{M}$), the amount of Pb sorbed at pH values above ~ 6.5 reflects both sorption and precipitation (PbCO_3 and Pb(OH)_2). The most significant impact of DFO-B on Pb^{2+} partitioning at the solid-liquid interface was to decrease the extent of Pb^{2+} sorption at pH values > 6.5 (Fig. 8.1). The thermodynamic modeling program PhreeqC was used to predict the speciation of Pb^{2+} in the presence of DFO-B at the nominal concentrations used in these experiments (Fig. 8.2). The model predicts that the solution remains undersaturated with respect to Pb solid phases

(PbCO_3 and $\text{Pb}(\text{OH})_2$) over the entire pH range of interest (3 – 9), and that by pH 7, all the Pb^{2+} is complexed by DFO-B.

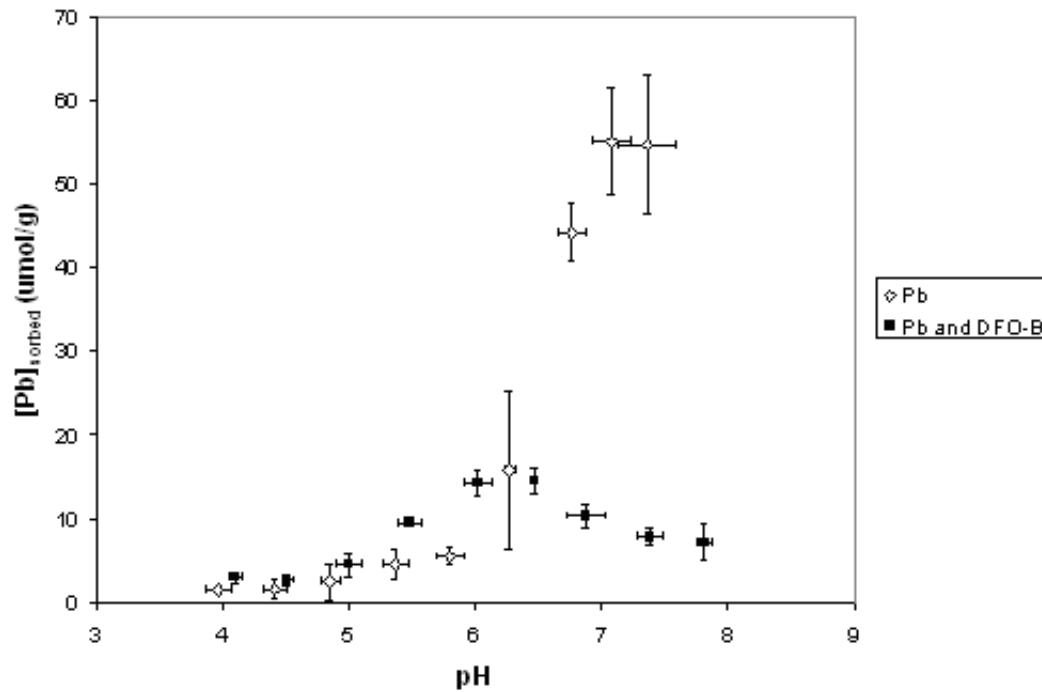


Figure 8.1. Pb^{2+} sorption to kaolinite clay in the presence and absence of DFO-B. Values shown $\mu\text{mol/g}$ and the final pH ($\pm 2\sigma$). Precipitation of Pb^{2+} is predicted to begin and pH values > 6 and is reflected in the measurements by greater error associated with the extent of Pb^{2+} sorption.

Thus, the decrease in the extent of Pb^{2+} partitioning above this pH value suggests a lower affinity of the Pb-DFO-B complex(es) for the surface than Pb^{2+} alone. At acidic pH values, the extent of Pb^{2+} sorption is low and the speciation

diagram suggests that at pH values < 5 , there is only a small amount of Pb^{2+} complexation by DFO-B (Fig. 8.2).

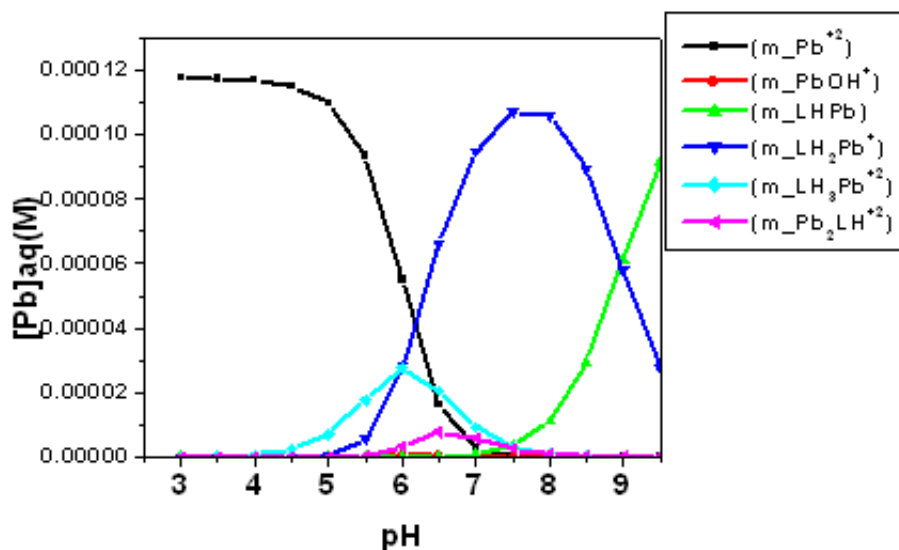


Figure 8.2. Speciation diagram of the solution phase at 100 ppm Pb concentration. (Refer to chapter 7 for an explanation of the nomenclature of these molecules).

Thus, the results are consistent again with a small amount of sorption of Pb^{2+} at permanent negatively charged sites. In a narrow region of pH values, between 5 and 6, a small but significant enhancement of the uptake of Pb^{2+} from solution in the presence of DFO-B is observed. In this pH range, Pb^{2+} is predicted to be complexed by DFO-B through one hydroxamate group, giving the species PbLH_3^{2+} . Increased sorption suggests a higher affinity of this species for the surface

TABLE 8.1

FINAL PH VALUES AND AMOUNT OF Pb AND DFO-B SORBED FOR EACH OF THE THREE EXPERIMENTAL SYSTEMS. VALUES ARE THE AVERAGE OF TRIPLICATE SAMPLES ($\pm 2^*\sigma$).

Experimental System	pH	Pb sorbed ($\mu\text{mol/g}$)	DFO-B sorbed ($\mu\text{mol/g}$)	Pb sorbed/DFO-B sorbed
Pb ²⁺ and Kaolinite	3.99 \pm 0.03	3.2 \pm 1.0		
	6.1 \pm 0.2	4.9 \pm 2.3		
	6.7 \pm 0.1	44.8 \pm 2.5		
DFO-B and Kaolinite	3.97 \pm 0.01		n.s.d ¹	
	5.89 \pm 0.07		2.0 \pm 0.4	
	7.34 \pm 0.06		2.7 \pm 0.2	
Pb ²⁺ , DFO-B and Kaolinite	4.04 \pm 0.03	1.5 \pm 0.7	2.7 \pm 0.1	0.6
	5.95 \pm 0.04	13.7 \pm 3.0	6.7 \pm 0.9	2.1
	7.4 \pm 0.2	6.2 \pm 1.7	4.6 \pm 0.3	1.4

as compared to Pb^{2+} alone.

To mechanistically examine the impact of DFO-B on Pb^{2+} partitioning of Pb^{2+} from solution at the kaolinite surface, sorption of Pb^{2+} to kaolinite in the presence and absence of DFO-B was examined with EXAFS at pH values 4, 6, and 7.5. The extent of Pb^{2+} and DFO-B sorbed in each sample was quantified, as appropriate, and the extent of DFO-B sorption to kaolinite in the absence of Pb^{2+} was also determined at the same pH values. Results are shown in Table 8.1, and are consistent again with sorption of Pb^{2+} to the surface at $\text{pH} < 6$ and precipitation of Pb solid phases at higher pH values in the absence of DFO-B. DFO-B does sorb to the kaolinite to a limited extent in the absence of Pb^{2+} , but in the presence of Pb^{2+} the extent of sorption is increased. The ratio of Pb^{2+} to DFO-B sorbed was calculated for the ternary Pb-DFO-B-kaolinite system. At pH 4.0, more DFO-B is sorbed to the surface than Pb^{2+} while at pH 6 approximately 2 times as much Pb^{2+} is sorbed. At pH 7.5, the Pb:DFO-B ratio approaches unity. These results suggest that at low pH (pH 4), DFO-B and Pb^{2+} may sorb at different sites but as pH increases, and the speciation of Pb^{2+} in solution becomes increasingly dominated by Pb-DFO-B complexes, Pb^{2+} is sorbed predominantly as a Pb-DFO-B complex. Ternary complexes of two types can occur at the clay surface [96]; in the first case the metal cation acts as a bridge between the organic molecule and the surface (Type A) and in the second the organic molecule bridges the surface and the metal cation (Type B).

8.3.2 XAFS Results

EXAFS spectra indicate that when sorbed at the kaolinite surface, Pb^{2+} is bound directly to two oxygen atoms associated with the mineral structure; thus,

Pb^{2+} forms an inner-sphere complex with the kaolinite surface. The coordination number for these nearest neighbors O_1 was 1.88 ± 0.04 at a distance of 2.30 ± 0.01 Å.

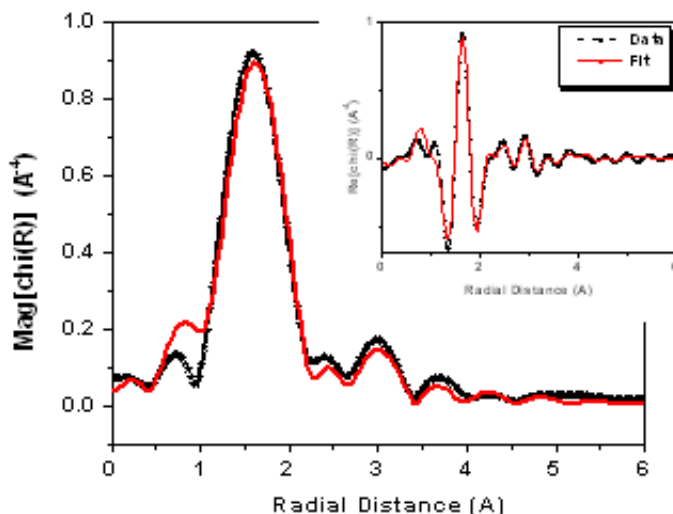


Figure 8.3. At the kaolinite surface Pb binds to aluminol surface as edge sharing bidentate inner-sphere around pH 6. Figure shows the Fourier transform data and fit for Pb adsorbed to kaolinite at pH 6.0. Real part of the FT is shown in the inset.

The Pb-O inter atomic distance of this path is consistent with previously published Pb-O distances for Pb^{2+} sorbed to aluminum oxide as an inner-sphere edge-sharing bidentate complex, whereby Pb^{2+} is bound to two oxygen atoms bound to the same AlO_6 octahedron [3]. A second shell of six (6.04 ± 0.5) ("O₂") oxygen atoms was associated with the adsorbed Pb^{2+} , indicating that Pb^{2+} retains waters of hydration when bound at the mineral surface. A third shell, consistent

with either Al or Si (indistinguishable by EXAFS based on similar atomic mass) occurred at Pb-Si/Al interatomic distance of 3.38 Å. The coordination number for this path is 0.76 ± 0.2 , a value which is consistent with sorption of Pb^{2+} as an edge-sharing bidentate complex.

TABLE 8.2

XAFS FITTING PARAMETERS FOR Pb
 ADSORBED TO KAOLINITE AT PH 6.0

Path	N	R(Å)	sig2(10^{-3})
Pb-O ₁	1.88 ± 0.4	2.30 ± 0.01	11.0 ± 1.2
Pb-O ₂	6.04 ± 0.5	2.53 ± 0.03	$27.2^2\text{C3}=2^3$
Pb-Al	0.76 ± 0.2	3.38 ± 0.03	30.00^4

In the presence of DFO-B, a type-A ternary complex forms, with Pb^{2+} bridging the surface and the DFO-B molecule. At pH 7.5, Pb^{2+} is adsorbed as this complex, and thus, these results will be discussed first. The first shell surrounding Pb is O₁, with a distance of 2.30 ± 0.01 Å and coordination number 4.51 ± 0.3 . This is consistent with Pb^{2+} being bound to the surface of the kaolinite as an edge-sharing bidentate complex, as before, and being bound to the DFO-B molecule through one hydroxamate group, i.e. two Pb-O bonds result from the DFO-B molecule.

TABLE 8.3
 XAFS FITTING PARAMETERS FOR
 Pb-KAOLINITE-DFO-B SAMPLES AT PH 6.0 AND
 7.5

Sample	Path	N	R(Å)	sig2(10 ⁻³)
pH 6.0	Pb-O ₁	2.96 ± 0.5	2.30 ± 0.01	11.0 ± 1.2
	Pb-Al	0.89 ± 0.2	3.38 ± 0.03	30.00 [#]
	Pb-C	1.40 ± 0.5	3.16 ± 0.03	12.00 [#]
	Pb-O ₂	3.20 ± 1.0	2.55 ± 0.03	27.2*(C3=2)
pH 7.5	Pb-O ₁	4.51 ± 0.8	2.30 ± 0.01	11.0 ± 1.2
	Pb-Al	1.15 ± 0.2	3.38 ± 0.03	30.00 [#]
	Pb-C	1.50 ± 0.4	3.15 ± 0.03	12.00 [#]

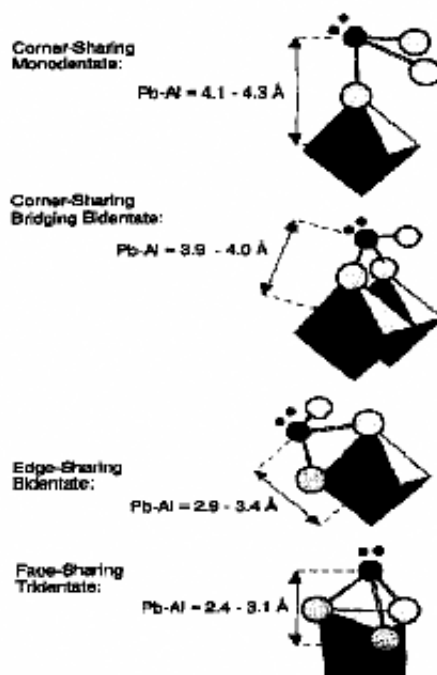


Figure 8.4. Possible configurations of Pb binding to Al as shown by Barger et al., 1997. XAFS analysis in the present work resulted in the Pb-Al distance of 3.38 Å. Based on the Pb-Al bond distance, an edge-sharing bidentate binding mechanism was proposed for Pb adsorption to kaolinite.

Our previous work examining the complexes of Pb^{2+} and DFO-B in solution (refer to chapter 7) determined that the Pb-O interatomic distance when bound to DFO-B was 2.30 Å. Again, the second shell has Pb-Al/Si interatomic distance consistent with the edge-sharing bidentate complex and a third C/N shell from the siderophore. At pH 6.0, EXAFS results are consistent with Pb adsorption both as hydrated Pb^{2+} (edge-sharing bidentate complex) and as a Pb-DFO-B ternary complex, in 40 : 60 ratio. This result is consistent with the bulk results which indicated that approximately two times as much Pb^{2+} is sorbed at this pH value compared to DFO-B.

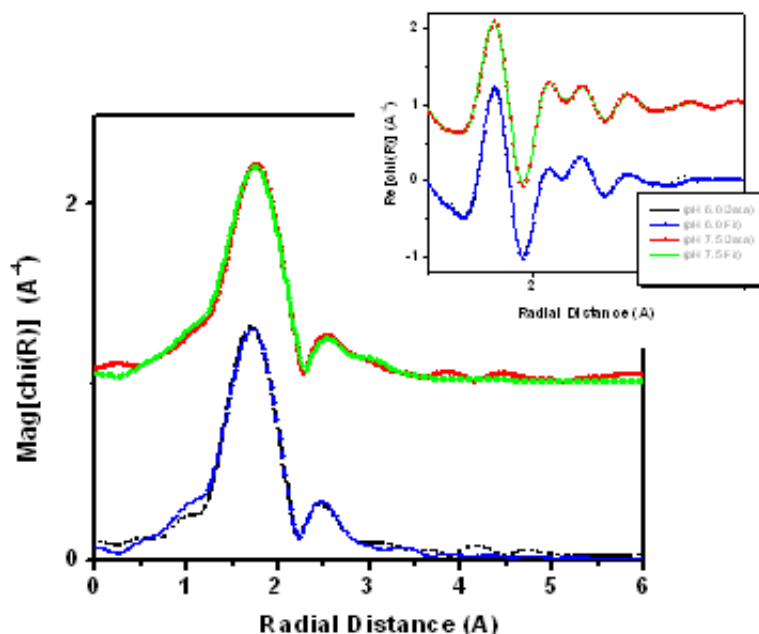


Figure 8.5. Fourier transformed data and fit for Pb adsorbed to kaolinite in the presence of DFO-B at pH 6.0 (lower graph) and pH 7.5 (upper graph). Real part of the data and fit is shown in the inset. Notice the subtle changes in the data for these two pH values.

This work is novel in demonstrating the formation of a ternary complex at the surface of kaolinite clay. Further, it demonstrates the potential of DFO-B, not only to impact the extent of Pb^{2+} sorption, but the type of surface species formed. Our results show that the mechanism of Pb^{2+} sorption to kaolinite, as an inner-sphere edge-sharing bidentate complex, does not change in the presence of DFO-B. Also, the results from EXAFS as well as bulk-scale chemistry studies suggest that the PbLH_3^{2+} species has the highest relative affinity for the surface, compared with Pb^{2+} alone and to the other Pb-DFO-B species. When bound as a ternary complex, Pb^{2+} is bound to the siderophore through one hydroxamate group, and when complexed in solution as PbLH_3^{2+} , it is also bound by only one

hydroxamate group. Thus, it is possible that, in the narrow pH range where PbLH_3^{2+} is predicted to occur and be the predominant dissolved-phase Pb-DFOB species (pH 5 – 6), the structure of DFO-B affords some added stability to the Pb-kaolinite complex. At higher pH values, where the Pb^{2+} is predicted to be bound by two or three of the DFO-B hydroxamate groups, bonds between Pb^{2+} and the siderophore molecule would have to be broken to allow the formation of the observed ternary complex. The decreased extent of Pb sorption at higher pH values suggests that this "unraveling" of the Pb-DFO-B complex and adsorption at the surface is not energetically favorable. Overall, the presence of siderophore serves to increase the solution-phase concentrations and thus potential mobility of Pb^{2+} at circumneutral pH values and above. Our results may have important implications for metal toxicity to micro-organisms; however, the bioavailability of siderophore- Pb^{2+} complexes is currently unknown.

In summary, a combination of bulk-adsorption measurements and XAFS has been used to show that Pb interacts strongly with a common bacterial siderophore DFO-B, and the presence of DFO-B has a pH dependent effect on the adsorption of Pb to kaolinite.

While DFO-B forms a caged structure with Pb alone at pH 7.5, it forms a ternary complex with Pb in the presence of kaolinite at this pH value. The formation of ternary complex in the case of Pb is in contrast to the results for Cd. Although, DFO-B forms a caged structure with Cd in the aqueous phase at pH 9 (refer to chapter 7), it does not show any signature of ternary complex formation with Cd in the presence of the kaolinite surface at the same pH value. XAFS results unambiguously show that Pb-DFO-B-kaolinite ternary complex is a type-A ternary complex; meaning thereby the configuration of this complex is such that

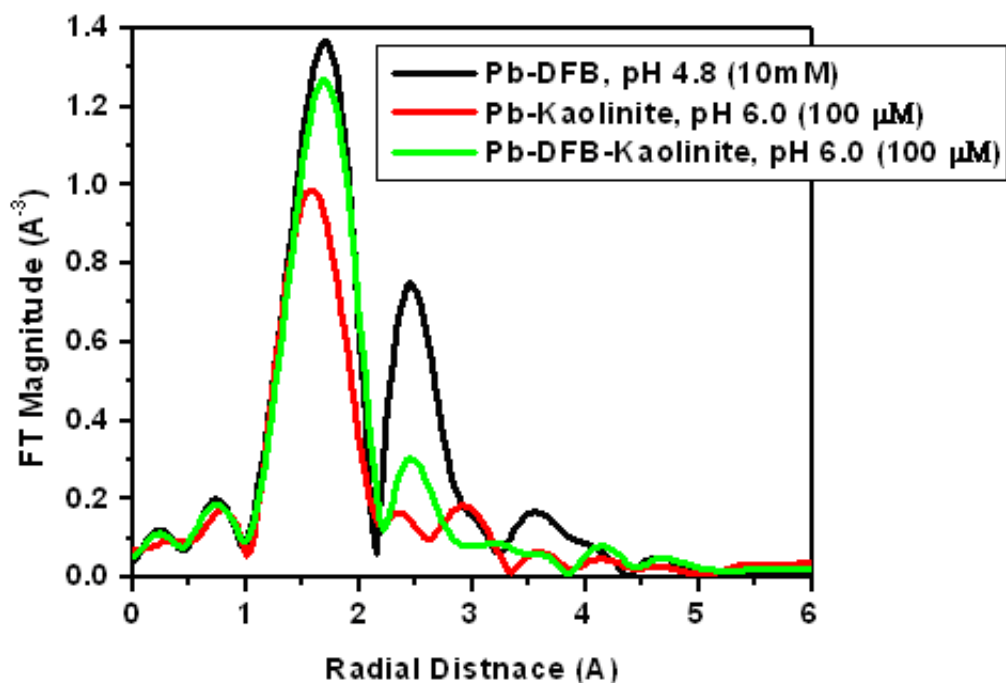


Figure 8.6. Comparison of Pb - DFO-B, -kaolinite, and DFO-B and kaolinite at pH 6.0. Notice the much smaller second shell (C signal) compared to the aqueous phase data. Also notice the differences in first and second shell of Pb adsorbed to pure mineral data.

a Pb atom comes between the kaolinite surface and DFO-B molecule. Resolving the details of this configuration is not straightforward however. XAFS results also indicate that DFO-B unwraps itself (see the comparison of aqueous, mineral and composite phases at pH 6.0 in Fig. 8.6) when in the caged structure of Pb-DFO-B comes in contact with the kaolinite surface. DFO-B, however, does not have high affinity for kaolinite surface in the absence of Pb. The reason for such a behavior of DFO-B is not clear from this study. Other complementary techniques such as Molecular Dynamics simulations might help to have a better understanding of this behavior. X-ray fluorescence results show that in the presence of DFO-B, kaolinite has higher uptake of Pb at pH 7.5 than pH 6.0 (shown in Fig. 8.7). However,

X-ray Fluorescence Spectra

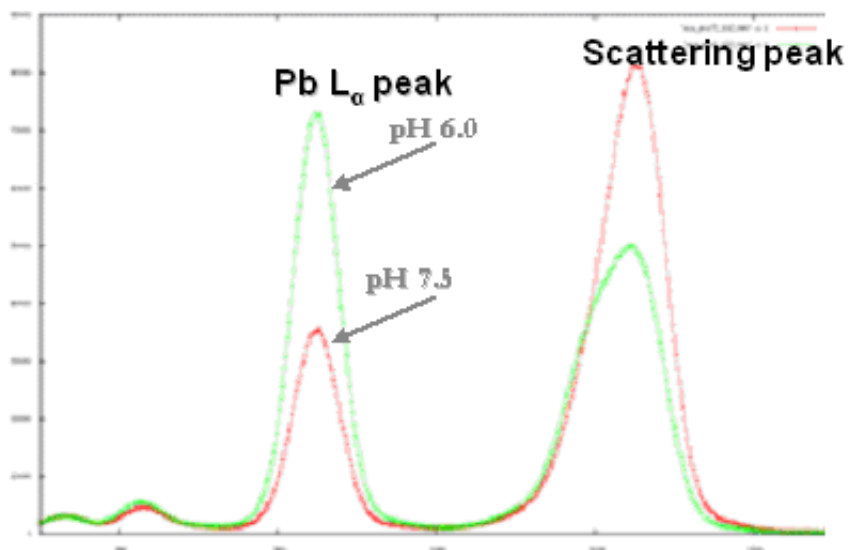


Figure 8.7. X-ray Fluorescence data at Pb L₃ edge showing higher Pb uptake by the kaolinite at pH 6.0 compared to pH 7.5 in the presence of DFO-B.

XAFS results indicate similar binding mechanism of Pb to DFO-B and kaolinite at these two pH values. The main difference at these two pH values was that at pH 6.0, Pb retained part of the hydration sphere (Table 8.3), while at pH 7.5 a reasonably good fit was obtained without including the contribution of water molecules attached to Pb. It is worthwhile mentioning that in the XAFS analysis, contribution from four different low Z (atomic number) backscatterers has been accounted for in relatively short fitting range. As can be seen from Fig. 8.8, all these paths have strong interference with each other, so there is a possibility of paths compensating for each other's contribution thereby adding to uncertainties. The sub-molar concentration of Pb in a matrix of light backscatterers (O, C, N, Al/Si) in these samples further complicates the collection of higher data range.

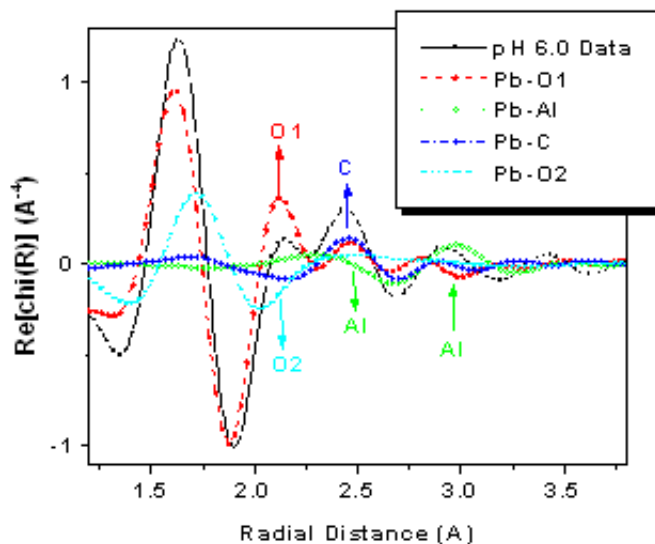


Figure 8.8. Real part Fourier transform data for Pb adsorbed to kaolinite in the presence of DFO-B at pH 6.0. Short and long distance O, C and Al paths are shown in the Fig. Notice the interference of all these paths over the data range of $\sim 1.3 - 3.4 \text{ \AA}$.

8.4 Conclusion

Results of solution speciation of Pb and Cd with commercially available trihydroxamate siderophore desferrioxamine B (DFO-B) has been shown in chapter 7. In continuation to solution speciation of Pb, further studies were conducted for Pb sorption to mineral surface kaolinite (1 : 1 aluminosilicate) with and without DFO-B. In the absence of DFO-B, results suggest outer sphere and inner sphere sorption of Pb on kaolinite surface at acidic and circumneutral pH conditions respectively.

In the presence of DFO-B, bulk sorption studies indicated that Pb sorption is enhanced in the presence of DFO-B around pH 6 and inhibited above pH 6.5. This was confirmed by x-ray fluorescence measurements. Extended XAFS results

study clearly indicated unwrapping of the DFO-B molecule at the surface (while DFO-B does not interact strongly with kaolinite surface in the absence of Pb). Our study has unambiguously recognized it as a "Type A" ternary complex ("Type A" complex means surface-metal-ligand type of interaction). Taken together, bulk adsorption measurements and XAFS experiments represent a powerful approach for determining and modeling metal speciation and adsorption.

CHAPTER 9

SUMMARY AND FUTURE WORK

Work presented in this dissertation mainly deals with the XAFS study of complexation and adsorption of heavy metal contaminants (Cd and Pb) on siderophores, and bacterial and mineral surfaces. XAFS was used to probe the detailed local structure (coordination environment and binding mechanism) of the above mentioned metal ions. Two independent classes of experiments were performed. The first set of experiments involved Cd adsorption to bacterial cell walls under various pure bacterial strains and consortia of bacteria from both uncontaminated and contaminated sites. The second set of experiments involved Pb and Cd speciation with siderophores, the clay mineral kaolinite, and the composite siderophores-mineral system.

For the Cd-bacteria work, at least a dozen of individual experiments were successfully carried out to study Cd adsorption on Gram-positive, Gram-negative, and consortia of bacteria as a function of Cd concentration and pH conditions. Overall, this study suggests that despite the complex physiology of each bacterial strain, the adsorption mechanism does not vary much between different strains. From the metal-adsorption chemistry point of view, the main difference lies in the site ratio of two-three fundamental sites only. Results thus obtained can potentially have very high impact on the modeling of the complex bacterial systems in realistic geological settings, leading to further refinement and development

of robust remediation strategies for metal contamination at macroscopic level.

The second class of experiments revealed that heavy metal ions like Pb and Cd are strongly sequestered by siderophores at higher pH values (7.5 for Pb and 9.0 for Cd). Their strong affinity for metal ions makes them an excellent agent for developing bioremediation strategies at environmentally contaminated sites. They also affect metal uptake by clay minerals such as kaolinite by formation of ternary complexes with metals and mineral surface. The solution speciation as found by XAFS analysis showed errors in predictions of thermodynamic modeling using available binding constants. This underscores the need for a detailed study of metal-siderophore systems using direct measurement techniques like XAFS.

Future directions for Cd-bacteria work would be to use XAFS for testing the competitive adsorption on Cd on a composite bacterial and mineral surfaces. Using such studies it can be directly seen whether the fate and bioavailability of the contaminant metal ions in the environment are dominated by the presence of bacterial surfaces or mineral surfaces. Since the experimental evidence did not match the predicted speciation of metals for the siderophores work, more XAFS experiments should to be conducted to build a better database for metal-siderophores interaction. Such studies may also have strong implications in medical applications.

APPENDIX A

A PRACTICAL GUIDE TO BEAMLINER ALIGNMENT

A.1 Introduction

The alignment procedure described here is based on but not limited to MR-CAT, sector-10 ID beamline at APS where most of the experiments presented in this thesis was performed. A general sketch for the steps of alignment has been outlined for a typical XAFS experiment. This alignment procedure would be valid for any ID (insertion device) beamline. Omitting few steps involving the ID optics will make it suitable for any BM (bending magnet) beamline too.

A.2 Steps of Alignment

Note down the previous parameters, like $m\omega$, $m\chi$, $m\pi$, normal and mirror positions. Also note down the gain and offset of all amplifiers, and amplitude, phase, frequency, sensitivity and offset of the feedback. Open up all the slits; raise the mirror vertically to take it out of the beam.

- Getting the best beam
 - ★ Couple the monochromator with undulator (*set id_ev_enabled 1*)
 - ★ Start moving the energy up to the desired value in steps of 1000 eV or 2000 eV. Keep monitoring the $I_{feedback}$ and properly adjust $m\omega$

and normal on the way to make sure you don't lose the beam. You can watch this on a Fluorescence screen.

- ★ Change the undulator harmonic and monochromator plan as necessary for this.
- ★ 1st harmonic goes from 4.5 to 12 keV
- ★ 2nd harmonic should be used from 12 to 16 keV. (Some times people have used 2nd harmonic for 19 keV at MRCAT but it is not usual)
- ★ 3rd harmonic should be used for 16 to 32 keV. (Beyond 32 keV will need 5th harmonic).
- ★ *Si(111) mono plane works fine for all energies up to 32 – 33 keV.*
- ★ After reaching the required energy value, play with normal to make sure that the beam is sitting in the "Plateau Region". For this jock the normal both ways by about 500 – 600 in steps of 50 and pick up a position where changing normal either way by few hundred does not change the $I_{feedback}$. Also notice the beam profile, choose a normal position which has nice beam profile and feedback system locks in nicely. For this you might have to play with feedback amplitude and phase. Don't play with feedback frequency unless you have to, and if you do, adjust the sensitivity of feedback accordingly. Normally you should not need to play with the offset but you might want to change it and improve beam stability if it is noisy.

- Check mchi angle alignment

For this take a burn at 6 keV and 12 keV (make sure you are at 1st harmonic of the undulator else the heat load might damage the monochromator).

There should not be any diagonal movement of the beam. If there is any, beamline support should take care of this. As a rule of thumb, try to avoid messing with mchi. Feedback signal should be between 0.2 V and 2.0 V (normally). Turn the following knobs:

- ★ Gain : 1×10^6 to 1×10^9
 - ★ Use a scatterer like kapton tape or Al foil for $E > 11$ keV (scattering from air is not enough at higher energies).
 - ★ Gas : 100% Argon
- For Non-Tracking Mode
 - ★ Decouple the monochromator from the undulator. Scan I_o using direct beam by setting the Average_Energy somewhere in the middle of the scan range. This should show you a well shaped undulator harmonic. If not, change the offset of the undulator energy to sit at the upslope of the harmonic profile. (Upslope varies slower than downslope).
 - ★ Reduce the scan range to more relevant range for your measurements. Play with the Taper and center of undulator (by fixing Average_Energy of undulator) to get a good idea of what "taper and Av_energy" combination gives you a relatively flat I_o (I_o should not change by more than 15% in the scan range for your measurements). For this you may have to re-adjust the normal too. If you see any abnormal behavior of the beam profile (including beam instability) and/or shape of harmonic at this stage, report to the beamline staff and ask them to fix it. *Whatever you are getting so far is the raw beam.*

- ★ *PS: Increasing Taper makes I_0 flatter but kill intensity, so here is a compromise between the two, which you want to optimize according to your experimental needs.*
 - ★ Note the undulator and monochromator setting that seems to work the best and **record them**.
- For Tracking Mode: If for some reason you want to work in tracking mode. Ignore the step mentioned above. Set taper to 0.5, and bandwidth to 2 or 3. However, I don't personally prefer to work in scanning (tracking) mode (at least at MRCAT) for several reasons.
- Mirror Alignment
 - ★ Put a fluorescence screen before the slit. Lower the mirror and until you see the mirror starts cutting down the beam. Tilt the mirror to be able to see a well separated direct and reflected beam.
 - ★ Adjust the mirror strip, Rh strip works better for $E < 18$ keV and Pt for $E > 18$ keV. *Couple the monochromator to the undulator (**set `id_ev_enabled 1`**), even if you plan to work in non-tracking mode.*
 - ★ Flatten the mirror (mabs mirror_tilt 0).
 - ★ Take out the fluorescence screen.
 - ★ Readjust the mirror height until it cuts I_0 in half.
 - ★ Go to $E_2 + 1000$, or desired cut-off energy.
 - ★ Do mirror scans (mirror_tilt) at E_1 , E_2 , $E_2 + 1000$ eV and $E + 2000$ and so on. Plot these scans together and determine the angle where I_0 starts dropping off sharply for each of the scans. Set the mirror angle

such that you have a relatively flat intensity for scan range, but really low intensity for much higher energies.

★ Block the direct beam by lowering the top slit placed after the mirror and before I_o ion chamber.

- $E1$ =Lowest energy from where scan will be started. (Edge energy -200 eV)

- $E2$ =Highest energy required for the EXAFS scan. (Edge energy $+800/1000$ eV)

★ Adjust the mirror height to maximize the reflected beam intensity. For this you have to make sure that the beam does not walk off the mirror at either ends of the scan. This can be done as follows:

★ Go to $E1$ and move the mirror up (in steps of 300 Micro-meter) and see if the beam walks off the mirror. Move the mirror down by few steps and go to $E2$. Again 1st move the mirror down to see if the beam is walking off. Then move it up and finally place the mirror at such a position that the beam is well placed at either extremes of the energy scan. This is based on the assumption that beam moves vertically up at higher energies.

★ *Go back to the monochromator and undulator settings if working in non-tracking mode.*

- Post Mirror Alignment

Adjust rail height so that the beam passes almost through the center of all the detectors and ion chambers (I_o , I_t and I_{ref}). Do an I_o energy scan again (with slits wide open, except the top slit which was lowered to cut the direct

beam) to make sure that the reflected beam does not change by more than 15 – 20% over the scan range. If it does, then you need to re-adjust the taper and Av_energy to bring it back to 15 – 20% over scan range. It is worthwhile to spend some time on this part.

- Slit Scans

- ★ Close the vertical slits to the required size. (*600 – 900 μm is a typical size*) and keep the horizontal slit size 1500 μm . Do vertical slit scans at $E1$, $E1 + 200$, $E1 + 400$, $E1 + 600$, $E1 + 800$, $E1 + 1000$ eV. Over plot these scan and set the center at the position where beam profile looks the best.

- ★ Now close the horizontal slit size to 900 μm and keep the vertical size small ~ 900 μm . Do a horizontal scan for $E1$, $E1 + 300$, $E1 + 600$, $E1 + 900$. Over plot these scan and set the center to the positions where beam profile looks the best.

- ★ Take a burn before these slits, block the direct beam by a lead mask.

- Energy and Time scan for I_o

Scan I_o (energy scan). Get satisfied with the change of I_o over scan range and the shape of I_o . Set the energy to about 300 eV above the edge energy and do a time scan (you are scanning the time noise in I_o at a fixed energy). Time noise in I_o should not be more than 1%. **If the time noise in I_o is more than 1.5%**, there is something wrong with the alignment. Either the monochromator parameters, feedback, gas in I_o , mirror or slits - one or more of them are not optimized properly. If you don't know what is the screw-up, **start over!!!**

- Six Spots

If everything looks fine and you want to measure a sensitive sample and you may want to move your sample from one spot to another (as in a sample which might have beam induced chemistry going on), have **six spots** within the Lytle Holder. Set the stage such that beam passes through the center of the Lytle holder. Set the hsmx and hsmx motor positions to zero. Note down the position of these six spots, use them for moving sample from one spot to another.

- Energy calibration

- ★ Measure XANES of the foil (or any standard compound if the foil is not available) of the edge you are going to measure. Find the inflection point by looking at the first derivative of the XANES spectra. Set the energy to that value (value of energy at the inflection point). Set the position of the energy to the value of that edge energy. (Command: **Set mot energy position 26711.14** (for Cd K edge)).

- ★ Also set the E_0 position to your edge position (**Set var edge_energy 26711.14**). Setting the edge energy position is not required for quick scans but is extremely important for step scans.

- Measuring Foil as Reference

Now take the foil and stick it in front of the I_{ref} detector such that the beam hits it properly.

- Check linearity (for Fluorescence measurements)

- ★ It is always good to start the measurement with a known sample (or standard compound). Best way to troubleshoot for linearity is to mea-

sure a known structure of roughly the same concentration as your samples are going to be).

- ★ Stick that known structure (or the unknown sample if any known structure at that concentration is not available) in the ion chamber for fluorescence measurement (that is what would be required most of the time) in Stern-Heald geometry (more commonly known as Lytle detector). Set a time scan at any chosen energy (typically ~ 300 eV above the edge), attenuate I_o by 50% using attenuating filter, and look for change in $\frac{I_f}{I_o}$.
- ★ Time noise in $\frac{I_f}{I_o}$ should not be more than 0.1%, and change in $\frac{I_f}{I_o}$ with 50% change in I_o should not be more than 0.2%.
- ★ For Transmission measurements, linearity is not an issue. It is always good for transmission *If you are using Solid-State detector (more commonly called MED as in Multi-element detector), 2 – 3% non-linearity in $\frac{I_f}{I_o}$ with 50% change in I_o is typical).*

- Rule of Thumb

- ★ If the change in I_o over scan range is less than 20%
- ★ If time noise in $\frac{I_f}{I_o}$ is less than 0.1%
- ★ If non-linearity in $\frac{I_f}{I_o}$ is less than 0.2% YOU ARE READY TO START MEASURING XAFS
- ★ Try Z-1 or Z-2 filters of various absorption lengths to improve the signal to noise ratio. Start crunching data and enjoy sleepless nights. Do energy scan, time scan, and linearity check every time you change a sample (or even if you change spot on the same sample if you want to

be more careful) to make sure that the systematic errors are consistent for all your measurements. Reduce the data and analyze it as much as you can at the beamline itself. This is the only way to make sure that your measurements are useful.

- Scan setup (Quick scan; My Favorite)
–200 – 800 eV at 0.5 step size, with 0.1 sec integration time \sim 200 seconds/scan. There are several advantages of using quick scan. First of all it is amazingly fast. This helps to keep the measurement away from some systematic errors which creep in due to long scans. Repeatability between scan is usually great, so it is much easier to identify the bad scans and throw them away. My personal experience is that random errors rather than systematic errors (compared to step scans or MED scans) dominate in sample measured in quick scan mode.

Add 5 sec dead time for each point, about 17 minutes in this case. This makes the scan setup for about 91 minutes per scan.

TABLE A.1

STEP SCAN FOR LYTLE DETECTOR

Interval	Step size	# of steps	Integration time	Total time
-200 - -20	5 eV	36	2 sec	72 sec
-20 - +30	0.5 eV	100	5 sec	500 sec
+30 - 9K	0.1K	62	8 sec	496 sec
9K - 14K	0.1K	50	12 sec	600 sec
Total:			1668 sec \sim 29 minutes	

TABLE A.2

SCAN SETUP FOR MED

Interval	Step Size	Integration time	Total time
-150eV - -20eV	10 eV	5 sec	65 sec
-20eV - +40eV	0.5 eV	12 sec	1440 sec
+40eV(k=3.24) - k=9	0.1k	25 sec	1440 sec
9k - 14k	0.1k	30 sec	1500 sec

BIBLIOGRAPHY

- [1] A. Albrecht-Gary and A. Crumbliss, *Coordination chemistry of siderophores: Thermodynamics and kinetics of iron chelation and release*. Number 35 (1998).
- [2] A. Ankudinov, B. Ravel, J. Rehr and S. Conradson, Real-space multiple-scattering calculation and interpretation of x-ray-absorption near-edge structure. *Phys.Rev.B*, 58(12): 7565–7576 (1998).
- [3] J. Bargar, G. Brown and G. Parks, Surface complexation of Pb(II) at oxide-water interfaces .1. XAFS and bond-valence determination of mononuclear and polynuclear Pb(II) sorption products on aluminum oxides. *Geochimica et Cosmochimica Acta*, 61(13): 2617–2637 (1997).
- [4] S. Barns and S. NierzwickiBauer, *Microbial diversity in ocean, surface and subsurface environments* (1997).
- [5] G. Beni and P. Platzman, Temperature and Polarization Dependence of Extended X-Ray Absorption Fine-Structure Spectra. *Phys.Rev.B*, 14(4): 1514–1518 (1976).
- [6] P. Bevington, *Data Reduction and Error Analysis for the Physical Sciences*. McGraw-Hill Company, New York (1969).
- [7] N. Binsted and S. Hasnain, State-of-the-art analysis of whole X-ray absorption spectra. *Journal of Synchrotron Radiation*, 3: 185–196 (1996).
- [8] H. Bizek, The Advanced Photon Source List of Paramteres. Technical report, Argonne National Laboratory (1996).
- [9] J. Boland, S. Crane and J. Baldeschwieler, Theory of Extended X-Ray Absorption Fine-Structure - Single and Multiple-Scattering Formalisms. *Journal of Chemical Physics*, 77(1): 142–153 (1982).
- [10] B. Borgias, A. Hugi and K. Raymond, Isomerization and Solution Structures of Desferrioxamine-B Complexes of Al-3+ and Ga-3+1. *Inorganic Chemistry*, 28(18): 3538–3545 (1989).

- [11] D. Borrok, J. Fein and C. Kulpa, Cd and proton adsorption onto bacterial consortia grown from industrial wastes and contaminated geologic settings. *Environmental Science & Technology*, 38(21): 5656–5664 (2004).
- [12] D. Borrok, J. Fein and C. Kulpa, Proton and Cd adsorption onto natural bacterial consortia: testing universal adsorption behavior. *Geochimica et Cosmochimica Acta*, 68(15): 3231–3238 (2004).
- [13] M. Boyanov, S. Kelly, K. Kemner, B. Bunker, J. Fein and D. Fowle, Adsorption of cadmium to *Bacillus subtilis* bacterial cell walls: A pH-dependent X-ray absorption fine structure spectroscopy study. *Geochimica et Cosmochimica Acta*, 67(18): 3299–3311 (2003).
- [14] M. Boyanov, J. Kmetko, T. Shibata, A. Datta, P. Dutta and B. Bunker, Mechanism of Pb adsorption to fatty acid langmuir monolayers studied by X-ray absorption fine structure spectroscopy. *Journal of Physical Chemistry B*, 107(36): 9780–9788 (2003).
- [15] S. Brantley, L. Liermann and T. Bullen, Fractionation of Fe isotopes by soil microbes and organic acids. *Geology*, 29(6): 535–538 (2001).
- [16] E. Brigham, *The Fast Fourier Transform*. Prentice-Hall, Englewood Cliffs, NJ (1974).
- [17] G. Bunker, Application of the Ratio Method of EXAFS Analysis to Disordered-Systems. *Nuclear Instruments & Methods in Physics Research*, 207(3): 437–444 (1983).
- [18] G. Bunker, XAFS tutorial documents (1997).
- [19] R. Caminiti, P. Cucca, M. Monduzzi, G. Saba and G. Crisponi, Divalent metal-acetate complexes in concentrated aqueous solutions - An X-ray diffraction and NMR spectroscopy study. *Journal of Chemical Physics*, 81: 543–551 (1984).
- [20] P. Chattopadhyay, *Mathematical Physics*. Wiley Eastern (1990).
- [21] S. Cheah, S. Kraemer, J. Cervini-Silva and G. Sposito, Steady-state dissolution kinetics of goethite in the presence of desferrioxamine B and oxalate ligands: implications for the microbial acquisition of iron. *Chemical Geology*, 198(1-2): 63–75 (2003).
- [22] C. Coccozza, C. Tsao, S. Cheah, S. Kraemer, K. Raymond, T. Miano and G. Sposito, Temperature dependence of goethite dissolution promoted by trihydroxamate siderophores. *Geochimica et Cosmochimica Acta*, 66(3): 431–438 (2002).

- [23] S. Dale, A. Doherty-Kirby, G. Lajoie and D. Heinrichs, Role of siderophore biosynthesis in virulence of *Staphylococcus aureus*: Identification and characterization of genes involved in production of a siderophore. *Infection and Immunity*, 72(1): 29–37 (2004).
- [24] C. Daughney and J. Fein, The effect of ionic strength on the adsorption of H^+ , Cd^{2+} , Pb^{2+} , and Cu^{2+} by *Bacillus subtilis* and *Bacillus licheniformis*: A surface complexation model. *Journal of Colloid and Interface Science*, 198(1): 53–77 (1998).
- [25] C. Daughney, J. Fein and N. Yee, A comparison of the thermodynamics of metal adsorption onto two common bacteria. *Chemical Geology*, 144(3-4): 161–176 (1998).
- [26] S. Dhungana, P. White and A. Crumbliss, Crystal structure of ferrioxamine B: a comparative analysis and implications for molecular recognition. *Journal of Biological Inorganic Chemistry*, 6(8): 810–818 (2001).
- [27] N. Dimakis and G. Bunker, Ab initio single- and multiple-scattering EXAFS Debye-Waller factors: Raman and infrared data. *Phys.Rev.B*, 58(5): 2467–2475 (1998).
- [28] D. Dzombak, W. Fish and F. Morel, Metal Humate Interactions .1. Discrete Ligand and Continuous Distribution Models. *Environmental Science & Technology*, 20(7): 669–675 (1986).
- [29] D. Edwards, S. Nielsen, A. Jarzecki, T. Spiro and S. Myneni, Experimental and theoretical vibrational spectroscopy studies of acetohydroxamic acid and desferrioxamine B in aqueous solution: Effects of pH and iron complexation. *Geochimica et Cosmochimica Acta*, 69(13): 3237–3248 (2005).
- [30] A. Esposito, F. Pagnanelli, A. Lodi, C. Solisio and F. Veglio, Biosorption of heavy metals by *Sphaerotilus natans*: an equilibrium study at different pH and biomass concentrations. *Hydrometallurgy*, 60(2): 129–141 (2001).
- [31] J. Fein, Quantifying the effects of bacteria on adsorption reactions in water-rock systems. *Chemical Geology*, 169(3-4): 265–280 (2000).
- [32] J. Fein, C. Daughney, N. Yee and T. Davis, A chemical equilibrium model for metal adsorption onto bacterial surfaces. *Geochimica et Cosmochimica Acta*, 61(16): 3319–3328 (1997).
- [33] A. Filipponi and A. Di Cicco, X-ray-absorption spectroscopy and n-body distribution functions in condensed matter. II. Data analysis and applications. *Phys.Rev.B*, 52(21): 15135– (December 1995).

- [34] A. Filipponi, A. Di Cicco and C. R. Natoli, X-ray-absorption spectroscopy and n-body distribution functions in condensed matter. I. Theory. *Phys.Rev.B*, 52(21): 15122– (December 1995).
- [35] D. Fowle and J. Fein, Experimental measurements of the reversibility of metal-bacteria adsorption reactions. *Chemical Geology*, 168(1-2): 27–36 (2000).
- [36] E. Gruneisen and E. Goens. *Zeits.f.Physik.*, 29: 141 (1924).
- [37] V. Guine, L. Spadini, G. Sarret, M. Muris, C. Delolme, J. Gaudet and J. Martins, Zinc sorption to three gram-negative bacteria: Combined titration, modeling, and EXAFS study. *Environmental Science & Technology*, 40(6): 1806–1813 (2006).
- [38] Z. Guo, F. Guo and Z. Tao, Effects of phosphate and ionic strength upon uranium(VI) sorption onto alumina as a function of pH. *Radiochimica Acta*, 94(4): 223–228 (2006).
- [39] T. Hayes and J. Boyce, *Solid State Physics*. Number 37, Academic, New York (1982).
- [40] L. He and B. Tebo, Surface charge properties of and Cu(II) adsorption by spores of the marine Bacillus sp. strain SG-1. *Applied and Environmental Microbiology*, 64(3): 1123–1129 (1998).
- [41] S. Hepinstall, B. Turner and P. Maurice, Effects of siderophores on Pb and Cd adsorption to kaolinite. *Clays and Clay Minerals*, 53(6): 557–563 (2005).
- [42] B. Hernlem, L. Vane and G. Sayles, Stability constants for complexes of the siderophore desferrioxamine B with selected heavy metal cations. *Inorganica Chimica Acta*, 244(2): 179–184 (1996).
- [43] L. Hersman, A. Huang, P. Maurice and J. Forsythe, Siderophore production and iron reduction by *Pseudomonas mendocina* in response to iron deprivation. *Geomicrobiology Journal*, 17(4): 261–273 (2000).
- [44] T. Hofer and B. Rode, The solvation structure of Pb(II) in dilute aqueous solution: An ab initio quantum mechanical/molecular mechanical molecular dynamics approach. *Journal of Chemical Physics*, 121(13): 6406–6411 (2004).
- [45] J. Jackson, *Classical Electrodynamics*, volume Second. Wiley Eastern (1989).

- [46] T. Kaeberlein, K. Lewis and S. Epstein, Isolating "uncultivable" microorganisms in pure culture in a simulated natural environment. *Science*, 296(5570): 1127–1129 (2002).
- [47] S. Kelly, K. Kemner, J. Fein, D. Fowle, M. Boyanov, B. Bunker and N. Yee, X-ray absorption fine structure determination of pH-dependent U-bacterial cell wall interactions. *Geochimica et Cosmochimica Acta*, 66(22): 3855–3871 (2002).
- [48] K. Kemner, B. Bunker, A. Kropf, H. Luo, N. Samarth, J. Furdyna, M. Weidmann and K. Newman, Atomic Rearrangement at ZnTe/CdSe Interfaces. *Phys.Rev.B*, 50(19): 14327–14335 (1994).
- [49] T. Kiss and E. Farkas, Metal-binding ability of desferrioxamine B. *Journal of Inclusion Phenomena and Molecular Recognition in Chemistry*, 32: 385–403 (1998).
- [50] G. Knapp, M. Beno, C. Rogers, C. Wiley and P. Cowan, Solution to the high heat loads from undulators at third generation synchrotron sources: Cryogenic thin-crystal monochromators. *Review of Scientific Instruments*, 65(9): 2792–2797 (1994).
- [51] G. Knoll, *Radiation Detection and Measurement*, volume 3. John Wiley & Sons (1999).
- [52] D. Koningsberger and D. Prins, editors, *X-ray Absorption: Principles, Applications, Techniques, XAFS, SEXAFS and XANES*. Wiley, New York (1988).
- [53] S. Kraemer, Iron oxide dissolution and solubility in the presence of siderophores. *Aquatic Sciences*, 66(1): 3–18 (2004).
- [54] S. Kraemer, S. Cheah, R. Zapf, J. Xu, K. Raymond and G. Sposito, Effect of hydroxamate siderophores on Fe release and Pb(II) adsorption by goethite. *Geochimica et Cosmochimica Acta*, 63(19-20): 3003–3008 (1999).
- [55] S. Krinsky, M. Perlman and R. Watson, *Handbook on Synchrotron Radiation*. Number 1, North-Holland, Amsterdam (1983).
- [56] E. Kulczycki, F. Ferris and D. Fortin, Impact of cell wall structure on the behavior of bacterial cells as sorbents of cadmium and lead. *Geomicrobiology Journal*, 19: 553–565 (2002).
- [57] C. Kunz, *Topics in Current Physics*. Number 10, Springer-Verlag (1979).

- [58] B. Lai, A. Khounsari, R. Savoy, L. Moog and E. Gluskin, Undulator A Characteristics and Specifications. Technical report, Argonne National Laboratory (1993).
- [59] M. Ledin, C. Krantz-Rulcker and B. Allard, Microorganisms as metal sorbents: comparison with other soil constituents in multi-compartment systems. *Soil Biology & Biochemistry*, 31(12): 1639–1648 (1999).
- [60] M. Ledin and K. Pedersen, The environmental impact of mine wastes - Roles of microorganisms and their significance in treatment of mine wastes. *Earth-Science Reviews*, 41(1-2): 67–108 (1996).
- [61] P. Lee and G. Beni, New Method for Calculation of Atomic Phase-Shifts - Application to Extended X-Ray Absorption Fine-Structure (Exafs) in Molecules and Crystals. *Phys.Rev.B*, 15(6): 2862–2883 (1977).
- [62] B. Lengeler, Lattice Site Location of Hydrogen by Use of Extended X-Ray Absorption Fine-Structure. *Physical Review Letters*, 53(1): 74–77 (1984).
- [63] L. Macaskie and G. Basnakova, Microbially enhanced chemisorption of heavy metals: A method for the bioremediation of solutions containing long lived isotopes of neptunium and plutonium. *Environmental Science & Technology*, 32(1): 184–187 (1998).
- [64] D. Marquardt, An Algorithm for Least-Squares Estimation of Nonlinear Parameters. *Journal of the Society for Industrial and Applied Mathematics*, 11(2): 431–441 (1963).
- [65] R. Martinez, D. Smith, E. Kulczycki and F. Ferris, Determination of intrinsic bacterial surface acidity constants using a donnan shell model and a continuous pK(a) distribution method. *Journal of Colloid and Interface Science*, 253(1): 130–139 (2002).
- [66] P. Maurice, Y. Lee and L. Hersman, Dissolution of Al-substituted goethites by an aerobic *Pseudomonas mendocina* var. bacteria. *Geochimica et Cosmochimica Acta*, 64(8): 1363–1374 (2000).
- [67] J. Meyer, A. Stintzi, V. Coulanges, S. Shivaji, J. Voss, K. Taraz and H. Budzikiewicz, Siderotyping of fluorescent pseudomonads: characterization of pyoverdines of *Pseudomonas fluorescens* and *Pseudomonas putida* strains from Antarctica. *Microbiology-Uk*, 144: 3119–3126 (1998).
- [68] A. Michette and C. Buckley, *X-Ray Science and Technology*. Institute of Physics, Bristol and Philadelphia (1993).
- [69] B. Mishra and B. Bunker.

- [70] U. Neubauer and G. Furrer, The use of voltammetry for sorption studies of heavy metals on mineral surfaces in presence of the siderophore desferrioxamine B. *Analytica Chimica Acta*, 392(2-3): 159–173 (1999).
- [71] U. Neubauer, B. Nowack, G. Furrer and R. Schulin, Heavy metal sorption on clay minerals affected by the siderophore desferrioxamine B. *Environmental Science & Technology*, 34(13): 2749–2755 (2000).
- [72] M. Newville, FEFFIT: Using FEFF to Model XAFS data (1998).
- [73] M. Newville, EXAFS analysis using FEFF and FEFFIT. *Journal of Synchrotron Radiation*, 8: 96–100 (2001).
- [74] M. Newville, IFEFFIT: interactive XAFS analysis and FEFF fitting. *Journal of Synchrotron Radiation*, 8: 322–324 (2001).
- [75] M. Newville, B. Boyanov and D. Sayers, Estimation of uncertainties in XAFS data. *Journal of Synchrotron Radiation*, 6: 264–265 (1999).
- [76] M. Newville, P. Livins, Y. Yacoby, J. Rehr and E. Stern, Near-Edge X-Ray-Absorption Fine-Structure of Pb - A Comparison of Theory and Experiment. *Phys.Rev.B*, 47(21): 14126–14131 (1993).
- [77] M. Newville, B. Ravel, D. Haskel, J. Rehr, E. Stern and Y. Yacoby, Analysis of Multiple-Scattering Xafs Data Using Theoretical Standards. *Physica B*, 209(1-4): 154–156 (1995).
- [78] B. Ngwenya, I. Sutherland and L. Kennedy, Comparison of the acid-base behaviour and metal adsorption characteristics of a gram-negative bacterium with other strains. *Applied Geochemistry*, 18(4): 527–538 (2003).
- [79] A. Plette, M. Benedetti and W. vanRiemsdik, Competitive binding of protons, calcium, cadmium, and zinc to isolated cell walls of a gram-positive soil bacterium. *Environmental Science & Technology*, 30(6): 1902–1910 (1996).
- [80] A. Plette, W. Vanriemsdijk, M. Benedetti and A. Vanderwal, Ph Dependent Charging Behavior of Isolated Cell-Walls of A Gram-Positive Soil Bacterium. *Journal of Colloid and Interface Science*, 173(2): 354–363 (1995).
- [81] A. Poiarkova and J. Rehr, Multiple-scattering x-ray-absorption fine-structure Debye-Waller factor calculations. *Phys.Rev.B*, 59(2): 948–957 (1999).
- [82] C. Powell, Attenuation lengths of low-energy electrons in solids. *Surface Science*, 44(1): 29–46 (July 1974).

- [83] B. Ravel, ATOMS: crystallography for the X-ray absorption spectroscopist. *Journal of Synchrotron Radiation*, 8: 314–316 (2001).
- [84] B. Ravel and M. Newville, Athena, Artemis, Hephaestus: Data Analysis for X-Ray Absorption Spectroscopy Using Ifeffit. *Journal of Synchrotron Radiation*, 12: 537–541 (2005).
- [85] B. Ravel, E. Stern, R. Vedrinskii and V. Kraizman, Local structure and the phase transitions of BaTiO₃. *Ferroelectrics*, 206(1-4): 407–430 (1998).
- [86] J. Rehr and R. Albers, Scattering-Matrix Formulation of Curved-Wave Multiple-Scattering Theory - Application to X-Ray-Absorption Fine-Structure. *Phys.Rev.B*, 41(12): 8139–8149 (1990).
- [87] D. Rosenberg and P. Maurice, Siderophore adsorption to and dissolution of kaolinite at pH 3 to 7 and 22 degrees C. *Geochimica et Cosmochimica Acta*, 67(2): 223–229 (2003).
- [88] J. Sakurai, *Advanced Quantum Mechanics*. Addison Wesley, New York (1967).
- [89] G. Sarret, A. Manceau, L. Spadini, J. Roux, J. Hazemann, Y. Soldo, L. Eybert-Berard and J. Menthonnex, Structural determination of Zn and Pb binding sites in *Penicillium chrysogenum* cell walls by EXAFS spectroscopy. *Environmental Science & Technology*, 32(11): 1648–1655 (1998).
- [90] D. Sayers, S. Heald, M. Pick, J. Budnick, E. Stern and J. Wong, X-Ray-Beam Line at the Nsls for X-Ray Absorption Studies in Material Science. *Nuclear Instruments & Methods in Physics Research*, 208(1-3): 631–635 (1983).
- [91] L. Schiff, *Quantum Mechanics*, volume 3. McGraw-Hill, New York (1968).
- [92] B. Schroth and G. Sposito, Effect of landfill leachate organic acids on trace metal adsorption by kaolinite. *Environmental Science & Technology*, 32(10): 1404–1408 (1998).
- [93] N. C. L. L. W. P. P. K. A. K. A. B. B. K. K. D. P. D. R. K. J. Segre, C.U.; Leyarowska, The MRCAT insertion device beamline at the Advanced Photon Source. In *Synchrotron Radiation Instrumentation: Eleventh U.S. National Conference*, volume 521, pages 419–422, American Institute of Physics, New York (2000).
- [94] G. Sherbert, *The biophysical characterization of the cell surface*. Academic Press, London (1978).

- [95] L. Shimoni-Livny, J. Glusker and C. Bock, Lone pair functionality in divalent lead compounds. *Inorganic Chemistry*, 37(8): 1853–1867 (1998).
- [96] G. Sposito, *The Chemistry of Soils*. Oxford University Press, New York (1989).
- [97] E. Stern, B. Bunker and S. Heald, Many-Body Effects on Extended X-Ray Absorption Fine-Structure Amplitudes. *Phys.Rev.B*, 21(12): 5521–5539 (1980).
- [98] E. Stern and S. Heald, *Handbook of Synchrotron Radiation*. Number 1b, North-Holland, Amsterdam (1983).
- [99] E. Stern, M. Newville, B. Ravel, Y. Yacoby and D. Haskel, The Uwxafs Analysis Package - Philosophy and Details. *Physica B*, 209(1-4): 117–120 (1995).
- [100] W. Stumm and J. Morgan, *Aquatic Chemistry*, volume 3rd. Wiley-Interscience, New York (1996).
- [101] S. Sutheimer, P. Maurice and Q. Zhou, Dissolution of well and poorly crystallized kaolinites: Al speciation and effects of surface characteristics. *American Mineralogist*, 84(4): 620–628 (1999).
- [102] B. Teo and P. Lee, Ab initio calculations of amplitude and phase functions for extended x-ray absorption fine structure spectroscopy. *Journal of the American Chemical Society*, 101(11): 2815–2832 (1979).
- [103] B. Toner, A. Manceau, M. Marcus, D. Millet and G. Sposito, Zinc sorption by a bacterial biofilm. *Environmental Science & Technology*, 39(21): 8288–8294 (2005).
- [104] H. Van Olphen and J. Fripiat, *Data Handbook for Clay Materials and Other Non-Metallic Minerals*. Pergamon Press, Oxford, U.K. (1979).
- [105] A. Vergne, A. Walz and M. Miller, Iron chelators from mycobacteria (1954-1999) and potential therapeutic applications. *Natural Product Reports*, 17(1): 99–116 (2000).
- [106] B. Volesky, Detoxification of metal-bearing effluents: biosorption for the next century. *Hydrometallurgy*, 59(2-3): 203–216 (2001).
- [107] L. Warren and E. Haack, Biogeochemical controls on metal behaviour in freshwater environments. *Earth-Science Reviews*, 54(4): 261–320 (2001).

- [108] J. Wei, A. Saxena, B. Song, B. Ward, T. Beveridge and S. Myneni, Elucidation of functional groups on gram-positive and gram-negative bacterial surfaces using infrared spectroscopy. *Langmuir*, 20(26): 11433–11442 (2004).
- [109] J. Westall, FITEQL, a computer program for determination for chemical equilibrium constants from experimental data. Technical report, Oregon State University (1982).
- [110] J. Westall, Modeling of Surface Coordination Reactions - Determination of Reaction Stoichiometries and Equilibrium-Constants from Experimental-Data. *Abstracts of Papers of the American Chemical Society*, 205: 64–GEOC (1993).
- [111] G. Winkelmann, *CRC Handbook of Microbial Iron Chelates*. CRC Press, Boca Raton, FL (1991).
- [112] H. Xue, W. Stumm and L. Sigg, The binding of heavy-metals to algal surfaces. *Water Res.*, 22: 917–926 (1988).
- [113] N. Yee and J. Fein, Cd adsorption onto bacterial surfaces: A universal adsorption edge? *Geochimica et Cosmochimica Acta*, 65(13): 2037–2042 (2001).
- [114] N. Yee and J. Fein, Quantifying metal adsorption onto bacteria mixtures: A test and application of the surface complexation model. *Geomicrobiology Journal*, 20(1): 43–60 (2003).
- [115] Q. Zhou, *Surface characteristics and dissolution kinetics of two standard kaolinites*. Ph.D. thesis, Kent, OH (1996).